



UNIVERSITY OF SOUTHERN QUEENSLAND

$C^2$ -ELEMENT RADIAL BASIS FUNCTION  
METHODS FOR SOME CONTINUUM MECHANICS  
PROBLEMS

A dissertation submitted by

**DUC-ANH AN-VO**

B.Eng. (Hon.), Ho-Chi-Minh City University of Technology, Vietnam, 2005

M.Sc. (Hon.), Toyohashi University of Technology, Japan, 2007

For the award of the degree of

**Doctor of Philosophy**

February 2013

# Dedication

*To my parents*

*Thanh Vo-Kim and Dung An-Bang*

*and*

*The woman in my life*

*Thach Huynh*

# Certification of Dissertation

I certify that the ideas, experimental work, results and analyses, software and conclusions reported in this dissertation are entirely my own effort, except where otherwise acknowledged. I also certify that the work is original and has not been previously submitted for any other award.

---

Duc-Anh An-Vo, Candidate

---

Date

## ENDORSEMENT

---

Prof. Nam Mai-Duy, Principal supervisor

---

Date

---

Prof. Thanh Tran-Cong, Co-supervisor

---

Date

---

Dr. Canh-Dung Tran, Co-supervisor

---

Date

# Acknowledgments

I would like to acknowledge my supervisors Professor Nam Mai-Duy, Professor Thanh Tran-Cong and Dr Canh-Dung Tran for their effective guidance, constant support and encouragement throughout. I deeply appreciate their knowledge and patience to answer any question I have asked and correct my manuscripts. They are indeed wonderful supervisors.

In addition, I would like to thank A/Prof. Armando A. Apan, Mrs Juanita Ryan (Faculty of Engineering and Surveying), Ms Katrina Hall (Office of Research and Higher Degrees), Mr Martin Geach (P9 operational officer) for their kind support; Dr Andrew Wandel and Dr Kazem Ghabraie for offering me teaching assistant positions.

I am grateful to numerous friends and people, whom I have not mentioned by name, for their invaluable help during the course of my study.

My candidature was at all possible owing to a Postgraduate Scholarship from the University of Southern Queensland and Scholarship supplements from Faculty of Engineering and Surveying and Computational Science and Engineering Research Centre. These financial supports are gratefully acknowledged.

Finally, I am indebted to my parents, my brother and my wife for their unconditional support, love and encouragement.

# Abstract

This work attempts to contribute further knowledge to high-order approximation and associated advanced techniques/methods for the numerical solution of differential equations in the discipline of computational science and engineering. Of particular interest is the numerical simulation of heat conduction, highly non-linear flows and multiscale problems. The distinguishing feature in this study is the development of novel local compact 2-node integrated radial basis function elements (IRBFEs) and their incorporation into the subregion/point collocation formulations based on Cartesian grids. As a result, a new class of  $C^2$ -continuous methods are devised, representing a significant improvement on the usual  $C^0$ -continuous methods. Incorporation of the new  $C^2$ -continuous methods into the development of a high-order multiscale computational framework provides advantageous features compared to other multiscale frameworks available in the literature, including (i) high rates of convergence and levels of accuracy; and (ii) converged  $C^2$ -continuous solutions of two-dimensional multiscale elliptic problems.

Firstly, a new control-volume (CV) discretisation method, based on Cartesian grid and IRBFEs, for solving PDEs is proposed. Unlike the standard CV method (Patankar 1980), the flux values at CV faces are presently estimated with high-order IRBF approximations on 2-node elements and the solution is  $C^2$ -continuous across the interface between two adjacent elements. Only two RBF centres (a smallest RBF set) associated with the two nodes of the element are used to construct the approximations locally leading to a very sparse and banded system matrix. Moreover, a wide range of RBF-widths can be

---

used to effectively control the solution accuracy. Secondly, the proposed 2-node IRBFEs are incorporated into the subregion and point collocation frameworks for the discretisation of the streamfunction-vorticity formulation governing the fluid flows. Several high-order upwind schemes based on 2-node IRBFEs are developed for highly non-linear flows. Thirdly, the ADI procedure (Peaceman and Rachford 1955, Douglas and Gunn 1964) is applied to enhance the efficiency of the proposed methods. Especially novel  $C^2$ -continuous compact schemes based on 2-node IRBFEs are devised and combined with the ADI procedure to yield optimal tridiagonal system matrices on each and every grid line. Such tridiagonal matrices can be solved effectively and efficiently with the Thomas algorithm (Fletcher 1991, Pozrikidis 1997). Finally, the proposed  $C^2$ -continuous CV method is employed in a multiscale basis function approach to develop a high-order multiscale CV method for the solution of multiscale elliptic problems.

Accuracy, stability and efficiency of the proposed methods are verified with extensive numerical results.

# Papers Resulting from the Research

## Journal Papers

1. **D.-A. An-Vo**, N. Mai-Duy, T. Tran-Cong (2010). Simulation of Newtonian-fluid flows with  $C^2$ -continuous two-node integrated-RBF elements, *SL: Structural Longevity*, 4(1):39 – 45.
2. **D.-A. An-Vo**, N. Mai-Duy, T. Tran-Cong (2011). A  $C^2$ -continuous control-volume technique based on Cartesian grids and two-node integrated-RBF elements for second-order elliptic problems. *CMES: Computer Modeling in Engineering and Sciences*, 72(4):299 – 335.
3. **D.-A. An-Vo**, N. Mai-Duy, T. Tran-Cong (2011). High-order upwind methods based on  $C^2$ -continuous two-node integrated-RBF elements for viscous flows. *CMES: Computer Modeling in Engineering and Sciences*, 80(2):141 – 177.
4. C.-D. Tran, **D.-A. An-Vo**, N. Mai-Duy, T. Tran-Cong (2011). An integrated RBFN based macro-micro multi-scale method for computation of visco-elastic fluid flows. *CMES: Computer Modeling in Engineering and Sciences*, 82(2):137 – 162.
5. **D.-A. An-Vo**, N. Mai-Duy, C.-D. Tran, T. Tran-Cong (2013). ADI

method based on  $C^2$ -continuous two-node integrated-RBF elements for viscous flows. *Applied Mathematical Modelling*, 37:5184 – 5203.

6. **D.-A. An-Vo**, C.-D. Tran, N. Mai-Duy, T. Tran-Cong (2013). RBF-based multiscale control volume method for second order elliptic problems with oscillatory coefficients. *CMES: Computer Modeling in Engineering and Sciences*, Accepted 21/01/2013.
7. **D.-A. An-Vo**, N. Mai-Duy, C.-D. Tran, T. Tran-Cong (2013). A  $C^2$ -continuous compact implicit method for parabolic equations, submitted.

## Conference Papers

1. **D.-A. An-Vo**, D. Ngo-Cong, B.H.P Le, N. Mai-Duy, T. Tran-Cong (2010). Local integrated radial-basis-function discretisation schemes. *The ICCES Special Symposium on Meshless & Other Novel Computational Methods (ICCES-MM'10)*, 17-21/Aug/2010, Busan, Korea Republic. ICCES Journal, Tech Science Press (ISSN 1933-2815).
2. **D.-A. An-Vo**, N. Mai-Duy, T. Tran-Cong (2011). IRBFEs for the numerical solution of steady incompressible flows. *ICCES: International Conference on Computational & Experimental Engineering and Sciences*, 16(3) 87 – 88, 2011.
3. **D.-A. An-Vo**, C.-D. Tran, N. Mai-Duy, T. Tran-Cong (2011). IRBFN-based multiscale solution of a model 1D elliptic equation. In *Boundary Element and Other Mesh Reduction Methods XXXIII*, 241 – 251. ISSN 1743-355X (invited).
4. C.-D. Tran, T. Tran-Cong, **D.-A. An-Vo** (2011). A macro-micro multiscale method based on RBFNs control volume scheme for the Non-Newtonian

fluid flows. *The 1<sup>st</sup> International Conference on Computational Science and Engineering*, 19-21/Dec/2011, HCM city, Vietnam (invited).

5. **D.-A. An-Vo**, N. Mai-Duy, C.-D. Tran, T. Tran-Cong (2012). Modeling strain localisation in a segmented bar by a  $C^2$ -continuous two-node integrated-RBF element formulation. In *Boundary Element and Other Mesh Reduction Methods XXXIV*, 3 – 13. ISSN 1743-3533 (invited).
6. **D.-A. An-Vo**, C.-D. Tran, N. Mai-Duy, T. Tran-Cong (2012). RBF computation of multiscale elliptic problems. *ICCES-MM'12*, 2-6/Sep/2012, Bubva, Montenegro (keynote lecture).

# Contents

Dedication	i
Certification of Dissertation	ii
Acknowledgments	iii
Abstract	iv
Papers Resulting from the Research	vi
Acronyms & Abbreviations	xv
List of Tables	xvii
List of Figures	xxii
Chapter 1 Introduction	1
1.1 Motivation . . . . .	1

---

1.2	Problem definition . . . . .	2
1.3	Review of multiscale methods . . . . .	3
1.3.1	Mathematical homogenisation method . . . . .	4
1.3.2	Heterogeneous multiscale method . . . . .	7
1.3.3	Multiscale finite element method . . . . .	10
1.4	Discussion . . . . .	12
1.5	Radial basis functions (RBFs) . . . . .	15
1.6	Objectives of the present research . . . . .	17
1.7	Outline of the Dissertation . . . . .	18

**Chapter 2 Two-node IRBF elements and a  $C^2$ -continuous control-volume technique 21**

2.1	Introduction . . . . .	22
2.2	Brief review of integrated RBFs . . . . .	26
2.3	Proposed $C^2$ -continuous control-volume technique . . . . .	27
2.3.1	Interior elements . . . . .	29
2.3.2	Semi-interior elements . . . . .	30
2.3.3	Incorporation of IRBFEs into the control-volume formulation . . . . .	33
2.3.4	Inter-element $C^2$ continuity . . . . .	36

---

2.4	Numerical results . . . . .	37
2.4.1	Function approximation . . . . .	38
2.4.2	Solution of ODEs . . . . .	39
2.4.3	Solution of PDEs . . . . .	48
2.5	Concluding remarks . . . . .	58

**Chapter 3 High-order upwind methods based on  $C^2$ -continuous two-node IRBFEs for viscous flows** **59**

3.1	Introduction . . . . .	60
3.2	Governing equations . . . . .	62
3.3	Two-node IRBFEs . . . . .	64
3.3.1	Interior elements . . . . .	64
3.3.2	Semi-interior elements . . . . .	65
3.4	Proposed $C^2$ -continuous subregion/point collocation methods . .	65
3.4.1	Discretisation of governing equations . . . . .	66
3.4.2	Approximations of diffusion term . . . . .	67
3.4.3	Approximations of convection term . . . . .	69
3.4.4	$C^2$ continuity solution . . . . .	72
3.5	Numerical examples . . . . .	72

3.5.1	Lid-driven cavity flow . . . . .	74
3.5.2	Flow past a circular cylinder in a channel . . . . .	87
3.6	Concluding remarks . . . . .	93

**Chapter 4 ADI method based on  $C^2$ -continuous two-node IRBFs for viscous flows 96**

4.1	Introduction . . . . .	97
4.2	Two-node IRBFs . . . . .	100
4.3	Derivation of $C^2$ -continuous ADI method . . . . .	101
4.3.1	ADI scheme for N-S equations on a Cartesian grid . . . . .	101
4.3.2	Proposed $C^2$ -continuous IRBFE-ADI method . . . . .	103
4.4	Numerical examples . . . . .	107
4.4.1	Square cavity . . . . .	108
4.4.2	Triangular cavity . . . . .	120
4.4.3	Discussion . . . . .	124
4.5	Concluding remarks . . . . .	126

**Chapter 5 A  $C^2$ -continuous compact implicit method for parabolic equations 128**

5.1	Introduction . . . . .	129
-----	------------------------	-----

5.2	Proposed compact 2-node IRBF schemes . . . . .	132
5.2.1	$C^2$ -continuous compact schemes on a uniform grid . . . . .	134
5.2.2	$C^2$ -continuous compact schemes on a nonuniform grid . . . . .	136
5.3	Application to parabolic equations . . . . .	139
5.3.1	One-dimensional problems . . . . .	140
5.3.2	Two-dimensional problems . . . . .	142
5.4	Numerical examples . . . . .	145
5.4.1	Example 1: one-dimensional problem . . . . .	146
5.4.2	Example 2: rectangular domain problem . . . . .	153
5.4.3	Example 3: circular domain problem . . . . .	158
5.4.4	Example 4: a non-linear problem . . . . .	163
5.5	Discussion . . . . .	178
5.6	Concluding remarks . . . . .	178

**Chapter 6 RBF-based multiscale control volume method for second order elliptic problems with oscillatory coefficients** 180

6.1	Introduction . . . . .	181
6.2	Problem definition . . . . .	184
6.3	Multiscale finite-element methods (MFEM) . . . . .	184

---

6.4	Multiscale finite volume method (MFVM) . . . . .	185
6.5	Proposed RBF-based multiscale control volume method . . . . .	192
6.5.1	Two-node IRBFEs . . . . .	193
6.5.2	Proposed method for 1D problems . . . . .	194
6.5.3	Proposed method for 2D problems . . . . .	199
6.6	Numerical results . . . . .	211
6.6.1	One-dimensional examples . . . . .	213
6.6.2	Two-dimensional examples . . . . .	220
6.7	Concluding remarks . . . . .	233
<b>Chapter 7 Conclusions</b>		<b>240</b>
7.1	Research contributions . . . . .	240
7.2	Suggested work . . . . .	246
<b>Appendix A Analytic forms of integrated MQ basis functions</b>		<b>248</b>
<b>Appendix B Analytic forms of 2-node IRBFE basis functions in physical space</b>		<b>250</b>
<b>References</b>		<b>252</b>

# Acronyms & Abbreviations

1D-IRBF	One-dimensional Integrated Radial Basis Function
2D-IRBF	Two-dimensional Integrated Radial Basis Function
ADI	Alternating Direction Implicit
BEM	Boundary Element Method
C2NIRBFM	Compact 2-node Integrated Radial Basis Function Method
CD	Central Difference
CFD	Computational Fluid Dynamics
CM	Collocation Method
<i>CM</i>	Convergence Measure
CPU	Central Processing Unit
CV	Control Volume
CVM	Control Volume Method
DGM	Discontinuous Galerkin Method
DRBF	Differentiated Radial Basis Function
ETCM	Explicit Treatment of Convection Method
FD	Finite Difference
FDM	Finite Difference Method
FE	Finite Element
FEM	Finite Element Method
FSS	Fine Scale Solver
FVM	Finite Volume Method

---

HMM	Heterogeneous Multiscale Method
HOC	High-Order Compact
IRBF	Integrated Radial Basis Function
IRBFE	Integrated Radial Basis Function Element
LCR	Local Convergence Rate
LHS	Left Hand Side
LR	Line Relaxation
MD	Multidomain
MFEM	Multiscale Finite Element Method
MFVM	Multiscale Finite Volume Method
MHM	Mathematical Homogenisation Method
MQ	Multiquadric
N-S	Navier-Stokes
ODE	Ordinary Differential Equation
PDE	Partial Differential Equation
PR	Peaceman and Rachford
RBF	Radial Basis Function
RHS	Right Hand Side
SVD	Singular Value Decomposition
UW	Upwind

# List of Tables

2.1	List of semi-interior elements and their characteristics. . . . .	33
2.2	ODE, Problem 1, Dirichlet boundary conditions: rates of convergence $O(h^\alpha)$ for $\phi$ and $\partial\phi/\partial x$ for several large $\beta$ values and semi-interior element types. . . . .	45
2.3	ODE, Problem 1, Dirichlet-Neumann boundary conditions: rates of convergence $O(h^\alpha)$ for $\phi$ and $\partial\phi/\partial x$ for two semi-interior element types. . . . .	45
2.4	ODE, Problem 2, Dirichlet boundary conditions: rates of convergence $O(h^\alpha)$ for $\phi$ and $\partial\phi/\partial x$ for several $\beta$ values and semi-interior element types. . . . .	46
2.5	ODE, Problem 2, Dirichlet and Neumann boundary conditions, $D3-N2$ treatment: rates of convergence $O(h^\alpha)$ for $\phi$ and $\partial\phi/\partial x$ for several $\beta$ values. . . . .	46
2.6	PDE, Problem 1 and Problem 2: Rates of grid convergence $O(h^\alpha)$ for the field variable and its first-order partial derivatives, (1): standard CVM. . . . .	55

3.1	Lid-driven cavity flow, IRBFE-CVM, $Re = 100$ : extrema of velocity profiles on the vertical and horizontal centrelines of the cavity. [★] is Ghia et al. (1982) and [★★] is Botella and Peyret (1998). . . . .	79
3.2	Lid-driven cavity flow, IRBFE-CVM, $Re = 1000$ : extrema of the vertical and horizontal velocity profiles through the centrelines of the cavity. [★] is Ghia et al. (1982) and [★★] is Botella and Peyret (1998). . . . .	80
3.3	Lid-driven cavity flow, IRBFE-CVM, $Re = 1000$ : percentage errors relative to the spectral benchmark results for the extreme values of the velocity profiles on the centrelines. Results of upwind central difference (UW-CD), central difference (CD-CD) and global 1D-IRBF-CVM are taken from Mai-Duy and Tran-Cong (2011a). . . . .	81
3.4	Lid-driven cavity flow, IRBFE-CM, $Re = 1000$ : effects of $\beta$ on the solution accuracy. The present results at the “optimal” value (i.e. about 3) with a grid of $51 \times 51$ are in better agreement with the benchmark spectral results than those by 1D-IRBF-CM using the same grid and by FDM using a much denser grid. [★] is Mai-Duy and Tran-Cong (2009b), [★★] is Ghia et al. (1982), and [★★★] is Botella and Peyret (1998). . . . .	82
3.5	Flow past a circular cylinder in a channel, IRBFE-CVM, $\gamma = 0.5$ : The critical Reynolds number $Re_{crit}$ for the formation of the steady recirculation zone behind the cylinder. . . . .	91

3.6	Flow past a circular cylinder in a channel, $\gamma = 0.5$ , $Re = 60$ : minimum velocity $u_{min}$ and its position on the centreline, and the length of recirculation zones behind the cylinder ( $L_w$ ). It is noted that the case of $Re = 60$ and $\gamma = 0.5$ here is equivalent to the case of $Re = 45$ and $\gamma = 0.5$ in Singha and Sinhamahapatra (2010). . . . .	91
4.1	Square cavity flow: computational times. . . . .	113
4.2	Square cavity flow: extrema of the vertical and horizontal velocity profiles along the centrelines of the cavity. % denotes percentage errors relative to the benchmark spectral results (Botella and Peyret 1998). Results of the global 1D-IRBF-C, FDM and Benchmark are taken from Mai-Duy and Tran-Cong (2009b), Ghia et al. (1982) and Botella and Peyret (1998) respectively. . . . .	115
5.1	One-dimensional problem, Dirichlet boundary conditions only, $N = (21, 23, \dots, 63)$ , $\Delta t = 0.001$ : condition numbers of the system matrix and relative $L_2$ errors of the approximate solution $\phi$ at $t = 1$ for various values of $h$ by the 3-point FD method and the present compact 2-point IRBF method ( $\beta = 231$ ). LCR stands for local convergence rate. . . . .	148
5.2	One-dimensional problem, Dirichlet and Neumann boundary conditions, $N = (21, 23, \dots, 63)$ , $\Delta t = 0.001$ : condition numbers of the system matrix and relative $L_2$ errors of the approximate solution $\phi$ at $t = 1$ for various values of $h$ by the 3-point FD method and the present compact 2-point IRBF method ( $\beta = 231$ ). LCR stands for local convergence rate. . . . .	151

- 
- 5.3 Rectangular domain problem, Dirichlet boundary conditions only,  $N_x \times N_y = (21 \times 21, 23 \times 23, \dots, 63 \times 63)$ ,  $\Delta t = 0.001$ : condition numbers of the system matrix on a grid line and relative  $L_2$  errors of the approximate solution  $\phi$  at  $t = 1$  for various values of  $h$  by the 3-point FD method and the present compact 2-point IRBF method ( $\beta = 124$ ). LCR stands for local convergence rate. 155
- 5.4 Circular domain problem,  $N_x \times N_y = (21 \times 21, 23 \times 23, \dots, 51 \times 51)$ ,  $\Delta t = 0.001$ : maximum condition numbers of the system matrix on a grid line and relative  $L_2$  errors of the approximate solution  $\phi$  at  $t = 0.05$  for various values of  $h$  by the present compact 2-point IRBF method ( $\beta = 330$ ). LCR stands for local convergence rate. . . . . 161
- 5.5 Lid-driven cavity flow: extrema of the vertical and horizontal velocity profiles along the centrelines of the cavity. % denotes percentage errors relative to the benchmark spectral results (Botella and Peyret 1998). Results of the FDM are taken from Ghia et al. (1982). . . . . 172
- 6.1 One-dimensional example 1,  $\varepsilon = 0.01$ , Strategy 1:  $L_2$  errors of the field variable, its first and second derivatives. It is noted that the set of test nodes contains 10,001 uniformly distributed points. LCR stands for local convergence rate. . . . . 216
- 6.2 One-dimensional example 1,  $\varepsilon = 0.01$ , Strategy 2:  $L_2$  errors of the field variable, its first and second derivatives. It is noted that the set of test nodes contains 10,001 uniformly distributed points. LCR stands for local convergence rate . . . . . 217

---

6.3	One-dimensional example 2, $\varepsilon = 0.01$ , Strategy 1: $L_2$ errors of the field variable, its first and second derivatives by the present method. It is noted that the set of test nodes contains 100,001 uniformly distributed points. LCR stands for local convergence rate. . . . .	221
6.4	One-dimensional example 2, $\varepsilon = 0.01$ , Strategy 2: $L_2$ errors of the field variable, its first and second derivatives by the present method. It is noted that the set of test nodes contains 100,001 uniformly distributed points. LCR stands for local convergence rate. . . . .	222
6.5	Two-dimensional example 1: $L_2$ errors of the field variable, its first and second derivatives. LCR stands for local convergence rate. . . . .	227
6.6	Two-dimensional example 2, $\varepsilon = 0.1$ : $L_2$ errors of the field variable, its first and second derivatives. LCR stands for local convergence rate. . . . .	235
6.7	Two-dimensional example 2, $\varepsilon = 0.01$ : $L_2$ errors of the field variable, its first and second derivatives. LCR stands for local convergence rate. . . . .	236

# List of Figures

1.1	Exact solution of problem (1.22)-(1.24) for $\epsilon = 0.01$ : (a) field variable, (b) its zoomed part, (c) its first-order derivative, (d) its second-order derivative. . . . .	14
2.1	A domain is embedded in a Cartesian grid with interior and semi-interior elements. . . . .	28
2.2	Schematic outline for 2-node IRBFE. . . . .	29
2.3	Schematic outline for a control volume in 2D. . . . .	34
2.4	Function approximation: Approximation for functions (left) and their first-order derivative (right) by using one IRBFE only. It can be seen that the present two-node IRBFE is able to produce non-linear behaviours (i.e. curved lines) between the two extremes.	40
2.5	Function approximation ( <i>continued</i> ), trigonometric function: Approximations for the function (left) and its first-order derivative (right). . . . .	41
2.6	Control volumes associated with interior and boundary nodes in 1D. . . . .	42

2.7	ODE, Problem 1, Dirichlet boundary conditions, $n = 9$ : Comparison of the exact and approximate solutions for $\phi$ and $d\phi/dx$ by the present $D1-D1$ strategy (left) and the standard CV method (right). . . . .	43
2.8	ODE, Problem 1, Dirichlet boundary conditions: $h$ -adaptivity studies conducted with several values of $\beta$ for the $D1-D1$ strategy. It is noted that results with $\beta = (5, 10, 15)$ are undistinguishable. . . . .	44
2.9	ODE, Problem 1, Dirichlet boundary conditions: Effects of types of semi-interior elements on the solution accuracy for $\beta = 15$ . . . . .	44
2.10	ODE, Problem 1, Dirichlet boundary conditions: $\beta$ -adaptivity studies conducted with $n = 9$ (left) and $n = 153$ (right) for three boundary treatment strategies. . . . .	47
2.11	ODE, Problem 1, Dirichlet and Neumann boundary conditions: Effects of types of semi-interior elements on the solution accuracy for $\beta = 1$ (left) and $\beta = 15$ (right). It is noted that plots have the same scaling and results by the two boundary treatment strategies are undistinguishable. . . . .	48
2.12	ODE, Problem 2: Exact solution (a) and its first-order derivative (b). . . . .	49
2.13	ODE, Problem 2, Dirichlet boundary conditions: $h$ -adaptivity studies conducted with $\beta = 1$ (left) and $\beta = 15$ (right). . . . .	50
2.14	ODE, Problem 2: $\beta$ -adaptivity studies conducted with $n = 103$ (left) and $n = 383$ (right) for three different semi-interior element strategies. . . . .	50

2.15 ODE, Problem 2, Dirichlet and Neumann boundary conditions: <i>h</i> -adaptivity (left) and $\beta$ -adaptivity (right) studies for the <i>D3-N2</i> strategy. . . . .	51
2.16 Half control volume associated with a boundary node in 2D. . .	51
2.17 PDE, Problem 1, rectangular domain, Dirichlet boundary con- ditions: <i>h</i> -adaptivity studies for the <i>D1-D1</i> (left) and <i>D2-D2</i> (right) strategies. . . . .	52
2.18 PDE, Problem 1, rectangular domain, Dirichlet and Neumann boundary conditions: <i>h</i> -adaptivity studies conducted with $\beta = 1$ and $\beta = 15$ for the <i>D1-N2</i> strategy. . . . .	53
2.19 PDE, Problem 2: Geometry and discretisation. Boundary nodes denoted by $\circ$ are generated by the intersection of the grid lines and the boundary. . . . .	57
2.20 PDE, Problem 2, circular domain, Dirichlet boundary conditions: the solution accuracy using the <i>D1-D1</i> strategy and $\beta = 15$ . . .	58
3.1 Lid-driven cavity flow, IRBFE-CVM, $Re = 1000$ , grid = $81 \times 81$ , solution at $Re = 400$ used as initial guess: convergence be- haviour. Scheme 1 using a time step of $3 \times 10^{-4}$ converges re- markably faster than the no-upwind version using a time step of $7 \times 10^{-6}$ . It is noted that the latter diverges for time steps greater than $7 \times 10^{-6}$ . <i>CM</i> denotes the convergence measure as defined by (3.38). . . . .	74

- 3.2 Lid-driven cavity flow, IRBFE-CM,  $Re = 1000$ , grid =  $81 \times 81$ , solution at  $Re = 400$  used as initial guess: convergence behaviour. Scheme 2 and Scheme 3, using a time step of  $3 \times 10^{-4}$  and  $10^{-4}$ , respectively, converge remarkably faster than the no-upwind version using a time step of  $8 \times 10^{-6}$ . It is noted that the latter diverges for time steps greater than  $8 \times 10^{-6}$ .  $CM$  denotes the convergence measure as defined by (3.38). . . . . 75
- 3.3 Lid-driven cavity flow, IRBFE-CVM,  $Re = 3200$ , grid =  $91 \times 91$ , solution at  $Re = 2000$  used as initial guess: convergence behaviour. Scheme 1 using a time step of  $10^{-4}$  converges remarkably faster than the no-upwind version using a time step of  $8 \times 10^{-7}$ . It is noted that the latter diverges for time steps greater than  $8 \times 10^{-7}$ .  $CM$  denotes the convergence measure as defined by (3.38). . . . . 76
- 3.4 Lid-driven cavity flow, IRBFE-CVM: velocity profiles on the vertical (left) and horizontal (right) centrelines at different grids, results by Ghia et al. (1982) were obtained at a grid of  $129 \times 129$ . [\*] is Ghia et al. (1982) and [\*\*] is Botella and Peyret (1998). . . . . 83
- 3.5 Lid-driven cavity flow, IRBFE-CVM: velocity profiles on the vertical (left) and horizontal (right) centrelines at different grids, results by Ghia et al. (1982) were obtained at a grid of  $129 \times 129$ . [\*] is Ghia et al. (1982) and [\*\*] is Botella and Peyret (1998). . . . . 84
- 3.6 Lid-driven cavity flow, IRBFE-CVM: stream and iso-vorticity lines for several  $Re$  numbers and grid sizes. The contour values are taken to be the same as those in Ghia et al. (1982) and Sahin and Owens (2003) respectively. . . . . 85

3.7	Lid-driven cavity flow, IRBFE-CVM: stream and iso-vorticity lines for several $Re$ numbers and grid sizes. The contour values are taken to be the same as those in Ghia et al. (1982) and Sahin and Owens (2003) respectively. . . . .	86
3.8	Flow past a circular cylinder in a channel: schematic representation of the computational domain. . . . .	87
3.9	Flow past a circular cylinder in a channel, IRBFE-CVM, $\gamma = 0.5$ , $Re = 60$ , grid = $367 \times 62$ , solution at $Re = 35$ used as initial guess: convergence behaviour. Scheme 1 using a time step of $2 \times 10^{-4}$ converges faster than the no-upwind version using a time step of $10^{-4}$ . It is noted that the latter diverges for time steps greater than $10^{-4}$ . $CM$ denotes the convergence measure as defined by (3.38). . . . .	88
3.10	Flow past a circular cylinder in a channel, IRBFE-CM, $\gamma = 0.5$ , $Re = 60$ , grid = $367 \times 62$ , solution at $Re = 0$ used as initial guess: convergence behaviour. Scheme 3 using a time step of $10^{-4}$ converges faster than the no-upwind version using a time step of $5 \times 10^{-5}$ . It is noted that the latter diverges for time steps greater than $5 \times 10^{-5}$ . $CM$ denotes the convergence measure as defined by (3.38). . . . .	89
3.11	Flow past a circular cylinder in a channel, IRBFE-CVM, $Re = 0$ , grid = $367 \times 62$ : streamlines at different values of the blockage ratio. . . . .	92
3.12	Flow past a circular cylinder in a channel, IRBFE-CVM, $Re = 0$ , grid = $367 \times 62$ : iso-vorticity lines at different values of the blockage ratio. . . . .	93

- 
- 3.13 Flow past a circular cylinder in a channel, IRBFE-CVM,  $\gamma = 0.5$ ,  
 $Re = 60$ , grid =  $367 \times 62$ : streamlines and iso-vorticity lines. . . . . 94
- 3.14 Flow past a circular cylinder in a channel, IRBFE-CVM,  $\gamma = 0.5$ ,  
 $Re = 60$ , grid =  $367 \times 62$ : velocity vector field. . . . . 94
- 3.15 Flow past a circular cylinder in a channel, IRBFE-CVM,  $\gamma = 0.5$ :  
velocity profiles on the centreline behind the cylinder at different  
Reynold numbers. . . . . 95
- 4.1 A grid point  $P$  and its neighbouring points on a Cartesian grid. 101
- 4.2 Square cavity flow,  $Re = 1000$ ,  $51 \times 51$ : convergence behaviour.  
IRBFE-ADI method using a time step of  $6 \times 10^{-5}$  converges  
faster than the CD-ADI method using a time step of  $3 \times 10^{-5}$ .  
It is noted that the latter diverges for time steps greater than  
 $3 \times 10^{-5}$ .  $CM$  denotes the relative norm of the difference of the  
streamfunction fields between two successive time levels. . . . . 110
- 4.3 Square cavity flow,  $Re = 3200$ ,  $91 \times 91$ , solution at  $Re = 1000$   
used as initial guess: convergence behaviour. IRBFE-ADI method  
using a time step of  $7 \times 10^{-6}$  converges faster than the CD-ADI  
method using a time step of  $2 \times 10^{-6}$ . It is noted that the lat-  
ter diverges for time steps greater than  $2 \times 10^{-6}$ .  $CM$  denotes  
the relative norm of the difference of the streamfunction fields  
between two successive time levels. . . . . 111
- 4.4 Square cavity flow,  $Re = 7500$ ,  $131 \times 131$ , solution at  $Re = 5000$   
used as initial guess: convergence behaviour. CD-ADI method  
uses a time step of  $5 \times 10^{-7}$  and IRBFE-ADI method uses a time  
step of  $1 \times 10^{-6}$ .  $CM$  denotes the relative norm of the difference  
of the streamfunction fields between two successive time levels. . . 114

- 
- 4.5 Square cavity flow,  $Re = 100$ , grid =  $11 \times 11$ : streamlines. The contour values for CD-ADI and IRBFE-ADI plots are the same. 116
- 4.6 Square cavity flow,  $Re = 1000$ , grid =  $51 \times 51$ : stream and iso-vorticity lines. The contour values are taken to be the same as those in Ghia et al. (1982) and Sahin and Owens (2003) respectively. Note the oscillatory behaviour near the top right corner in the case of CD-ADI method. . . . . 116
- 4.7 Square cavity flow,  $Re = 3200$ , grid =  $91 \times 91$ : stream and iso-vorticity lines. The contour values are taken to be the same as those in Ghia et al. (1982) and Sahin and Owens (2003) respectively. Note the oscillatory behaviour near the top right corner in the case of CD-ADI method. . . . . 117
- 4.8 Square cavity flow,  $Re = 5000$ , grid =  $111 \times 111$ : stream and iso-vorticity lines. The contour values are taken to be the same as those in Ghia et al. (1982) and Sahin and Owens (2003) respectively. Note the oscillatory behaviour near the top right corner in the case of CD-ADI method. . . . . 118
- 4.9 Square cavity flow, IRBFE-ADI,  $Re = 7500$ , grid =  $131 \times 131$ : stream and iso-vorticity lines. The contour values are taken to be the same as those in Ghia et al. (1982) and Sahin and Owens (2003) respectively. . . . . 118
- 4.10 Square cavity flow: velocity profiles along the vertical and horizontal centrelines of the cavity. [\*] is Botella and Peyret (1998) and [\*\*] is Ghia et al. (1982). . . . . 119

4.11	Triangular cavity flow: schematic outline of the computational domain and boundary conditions. Note that the characteristic length is chosen to be $AD/3$ to facilitate comparison with other published results (Ribbens et al. 1994, Kohno and Bathe 2006).	121
4.12	Triangular cavity flow: the computational domain is discretised by four Cartesian grids. . . . .	122
4.13	Triangular cavity flow: streamlines which are drawn using 21 equi-spaced levels between the minimum and zero values, and 11 equi-spaced levels between the zero and maximum values. . . . .	123
4.14	Triangular cavity flow: iso-vorticity lines which are drawn at intervals of $\Delta\omega = 0.5$ for a range of $-5 \leq \omega \leq 0.5$ . . . . .	124
4.15	Triangular cavity flow: velocity profiles by the present method and the flow condition-based interpolation FEM (Kohno and Bathe 2006). . . . .	127
5.1	Schematic outline of a three-point stencil. . . . .	133
5.2	Schematic outline of a five-point stencil. . . . .	139
5.3	One-dimensional problem, Dirichlet boundary conditions only, $\Delta t = 0.001$ : Relative $L_2$ errors of the approximation solution $\phi$ at $t = 1$ against the RBF width ( $\beta$ ) for three different grids. . . . .	149
5.4	One-dimensional problem, Dirichlet boundary conditions only, $N = 63$ , $\Delta t = 0.001$ : Comparison of the accuracy of the field variable at each time level between the classical Crank-Nicolson method and the present Crank-Nicolson method. For the latter, three values of $\beta$ , i.e. 210, 231 and 243, are employed. . . . .	149

- 
- 5.5 One-dimensional problem, Dirichlet boundary conditions only,  $N = 63$ ,  $\Delta t = 0.001$ : Comparison of the accuracy of the first derivative at each time level between the classical Crank-Nicolson method and the present Crank-Nicolson method. For the latter, three values of  $\beta$ , i.e. 210, 231 and 243, are employed. . . . . 150
- 5.6 One-dimensional problem, Dirichlet boundary conditions only,  $N = 11$ ,  $\beta = 15$ ,  $\Delta t = 0.001$ : Error distribution on the problem domain of the present method and the direct IRBFE method (An-Vo et al. 2011b, 2013) for the first derivative at  $t = 1$ . . . . 150
- 5.7 One-dimensional problem, Dirichlet and Neumann boundary conditions,  $N = 63$ ,  $\Delta t = 0.001$ : Comparison of the accuracy of the field variable at each time level between the classical Crank-Nicolson method and the present Crank-Nicolson method. For the latter, three values of  $\beta$ , i.e. 210, 231 and 243, are employed. 152
- 5.8 One-dimensional problem, Dirichlet and Neumann boundary conditions,  $N = 63$ ,  $\Delta t = 0.001$ : Comparison of the accuracy of the first derivative at each time level between the classical Crank-Nicolson method and the present Crank-Nicolson method. For the latter, three values of  $\beta$ , i.e. 210, 231 and 243, are employed. 153
- 5.9 Rectangular domain problem, Dirichlet boundary conditions only,  $N_x \times N_y = 22 \times 22$ ,  $\Delta t = 0.001$ : Relative  $L_2$  errors of the approximate solution  $\phi$  at  $t = 0.6$  against the RBF width ( $\beta$ ). . . . 156
- 5.10 Rectangular domain problem, Dirichlet boundary conditions only,  $N_x \times N_y = 22 \times 22$ ,  $\Delta t = 0.001$ : Comparison of the accuracy of the field variable at each time level between the classical ADI method and the present ADI method. For the latter, three values of  $\beta$ , i.e. 170, 180 and 190, are employed. . . . . 156

- 
- 5.11 Rectangular domain problem, Dirichlet boundary conditions only,  $N_x \times N_y = 22 \times 22$ ,  $\Delta t = 0.001$ : Comparison of the accuracy of the first derivatives at each time level between the classical ADI method and the present ADI method. For the latter, three values of  $\beta$ , i.e. 170, 180 and 190, are employed. . . . . 157
- 5.12 Rectangular domain problem, Dirichlet and Neumann boundary conditions,  $N_x \times N_y = 22 \times 22$ ,  $\Delta t = 0.001$ : Comparison of the accuracy of the field variable at each time level between the classical ADI method and the present ADI method. For the latter, three values of  $\beta$ , i.e. 170, 180 and 190, are employed. . . 157
- 5.13 Rectangular domain problem, Dirichlet and Neumann boundary conditions,  $N_x \times N_y = 22 \times 22$ ,  $\Delta t = 0.001$ : Comparison of the accuracy of the first derivatives at each time level between the classical ADI method and the present ADI method. For the latter, three values of  $\beta$ , i.e. 170, 180 and 190, are employed. . . 158
- 5.14 Circular domain problem: Geometry and discretisation. Boundary nodes denoted by  $\circ$  are generated by the intersection of the grid lines and the boundary. . . . . 159
- 5.15 Circular domain problem: Exact solution over an extended domain. 160
- 5.16 Circular domain problem,  $\Delta t = 0.001$ ,  $\beta = 330$ : The accuracy at each time level by the present ADI method using three grids. 162
- 5.17 Circular domain problem,  $N_x \times N_y = 141 \times 141$ ,  $\Delta t = 0.001$ ,  $\beta = 25$ : Contour plot of the present ADI method solution at  $t = 1$ . 162

- 5.18 Lid-driven cavity flow,  $Re = 1000$ , grid =  $61 \times 61$ , solution at  $Re = 400$  used as initial guess: Convergence behaviour. Present method using a time step of  $1 \times 10^{-4}$  converges faster than the IRBFE-ADI method using a time step of  $5 \times 10^{-5}$  and the explicit treatment of convection method (ETCM) using a time step of  $1 \times 10^{-5}$ . It is noted that the IRBFE-ADI and the ETCM diverge for the time steps greater than  $5 \times 10^{-5}$  and  $1 \times 10^{-5}$  respectively. 170
- 5.19 Lid-driven cavity flow,  $Re = 3200$ , grid =  $91 \times 91$ , solution at  $Re = 1000$  used as initial guess: Convergence behaviour. Present method using a time step of  $1 \times 10^{-5}$  converges faster than the explicit treatment of convection method (ETCM) using a time step of  $1 \times 10^{-6}$ . It is noted that the ETCM diverges for the time steps greater than  $1 \times 10^{-6}$ . . . . . 171
- 5.20 Lid-driven cavity flow,  $Re = 1000$ , grid =  $71 \times 71$ : velocity profiles along the vertical and horizontal centrelines. [\*] is Botella and Peyret (1998). . . . . 173
- 5.21 Lid-driven cavity flow: contour plots of streamfunction (left) and vorticity (right) for several values of  $Re$ . The iso-vorticity lines are taken as  $0, \pm 0.5, \pm 1, \pm 2, \pm 3, \pm 4, \pm 5$ . . . . . 174
- 5.22 Lid-driven cavity flow,  $Re = 3200$ , grid=  $91 \times 91$ : overall stream lines (upper figures) and a magnified view of those in the upper right corner. The contour values for CD-ADI method and the present method plots are the same. . . . . 175
- 5.23 Lid-driven cavity flow,  $Re = 3200$ , grid=  $91 \times 91$ : overall iso-vorticity lines (upper figures) and a magnified view of those in the upper right corner. The contour values are taken as  $0, \pm 0.5, \pm 1, \pm 2, \pm 3, \pm 4, \pm 5$ . . . . . 176

5.24	Lid-driven cavity flow: stream and iso-vorticity lines by the present method for $Re = 5000$ and $Re = 7500$ . The iso-vorticity lines are taken as $0, \pm 0.5, \pm 1, \pm 2, \pm 3, \pm 4, \pm 5$ . . . . .	177
6.1	A computational domain $\Omega$ with the coarse grid (black dashed lines) and dual coarse grid (black solid lines); dashed and solid red lines indicate a selected control volume $\bar{\Omega}_k$ and a selected dual coarse cell $\tilde{\Omega}^l$ , respectively. Shown underneath is an enlarged control volume, on which is imposed a $n \times n = 11 \times 11$ local fine grid. It can be seen that the size of global fine grid (dashed green lines) is $41 \times 41$ . . . . .	187
6.2	Local indices of dual cells and nodal points associated with a coarse grid node $\mathbf{x}_k$ and $\mathbf{x}_k \equiv \mathbf{x}_1$ . . . . .	189
6.3	A CV discretisation scheme in 1D: node $i$ and its associated control volume. The circles represent the nodes, and the vertical dash lines represent the faces of the control volume. . . . .	194
6.4	Schematic outline for a 2D control volume on the fine scale grid.	203
6.5	One-dimensional example 1, $\varepsilon = 0.01$ , $N = 11$ , $n = 101$ : basis functions (a) and correction function (b) associated with the first coarse cell ( $l = 1$ ). It is noted that the coarse cell is mapped to a unit length. . . . .	212
6.6	One-dimensional example 1: mesh convergence of a basis function.	214
6.7	One-dimensional example 1, $\varepsilon = 0.01$ , $N = 11$ , $n = 101$ : field variable and its first derivatives obtained by the present method in comparison with those obtained by MFEM and the exact solution. . . . .	218

- 
- 6.8 One-dimensional example 1,  $\varepsilon = 0.01$ ,  $N = 11$ ,  $n = 101$ : second derivatives obtained by the present method in comparison with that obtained by the exact solution. . . . . 219
- 6.9 One-dimensional example 2,  $\varepsilon = 0.01$ ,  $N = 51$ ,  $n = 101$ : field variable, its first and second derivatives obtained by the present method in comparison with the exact solution. . . . . 223
- 6.10 Two-dimensional example 1: collection of all correction functions on the problem domain obtained with a grid system of  $N \times N = 5 \times 5$ ,  $n \times n = 21 \times 21$ . . . . . 225
- 6.11 Two-dimensional example 1,  $N \times N = 5 \times 5$ ,  $n \times n = 81 \times 81$  (left) and  $N \times N = 33 \times 33$ ,  $n \times n = 11 \times 11$  (right): effect of the number of smoothing steps  $n_s$  on the convergence behaviour. . . 226
- 6.12 Two-dimensional example 2: typical basis and correction functions for the cases of  $\varepsilon = 0.1$  using a grid system of  $N \times N = 5 \times 5$ ,  $n \times n = 21 \times 21$  and  $\varepsilon = 0.01$  using a grid system of  $N \times N = 11 \times 11$ ,  $n \times n = 21 \times 21$ . . . . . 229
- 6.13 Two-dimensional example 2: contour plots of correction functions on the problem domain for the cases of  $\varepsilon = 0.1$  using a grid system of  $N \times N = 5 \times 5$ ,  $n \times n = 21 \times 21$  and  $\varepsilon = 0.01$  using a grid system of  $N \times N = 11 \times 11$ ,  $n \times n = 21 \times 21$ . . . . . 230
- 6.14 Two-dimensional example 2,  $\varepsilon = 0.1$ ,  $N \times N = 5 \times 5$ ,  $n \times n = 61 \times 61$  (left) and  $N \times N = 25 \times 25$ ,  $n \times n = 11 \times 11$  (right): effect of the number of smoothing steps  $n_s$  on the convergence behaviour. 234
- 6.15 Two-dimensional example 2,  $\varepsilon = 0.01$ ,  $N \times N = 11 \times 11$ ,  $n \times n = 71 \times 71$  (a) and  $N \times N = 71 \times 71$ ,  $n \times n = 11 \times 11$  (b): effect of the number of smoothing steps  $n_s$  on the convergence behaviour. 237

- 
- 6.16 Two-dimensional example 2,  $\varepsilon = 0.1$ ,  $n_s = 1$ : convergence of the present method and the fine scale solver with increasing sizes of the global fine grid; grid 1 =  $241 \times 241$  ( $N \times N = 5 \times 5, n \times n = 61 \times 61$ ), grid 2 =  $281 \times 281$  ( $N \times N = 5 \times 5, n \times n = 71 \times 71$ ), grid 3 =  $321 \times 321$  ( $N \times N = 5 \times 5, n \times n = 81 \times 81$ ). . . . . 238
- 6.17 Two-dimensional example 2: contour plots of solutions for the cases of  $\varepsilon = 0.1$  and  $\varepsilon = 0.01$ , the former is obtained with  $N \times N = 5 \times 5, n \times n = 31 \times 31$  while the latter is obtained with  $N \times N = 11 \times 11, n \times n = 31 \times 31$ . . . . . 239

# Chapter 1

## Introduction

This chapter starts with the motivation for the present research. Then model problems are defined, followed by a review and discussion on multiscale methods. A brief review of radial basis function serve to introduce new ideas and objectives of the present research. Finally, the outline of the dissertation is described.

### 1.1 Motivation

Multiphase materials such as particulate fluids and fibre reinforced composites have been used in many engineering applications. The inclusion of particles and fibres into a fluid/elastic medium results in a new material that can have certain desired properties. The dispersed phase (i.e. particles or fibres) can be randomly distributed in the resin, giving rise to multiscale fluctuations in the thermal or electrical conductivity. A numerical prediction of the behaviour of such problems is thus extremely difficult since a wide range of length scales (multiscale) is involved, i.e. the scale of the constituents can be of much lower order than the scale of the resultant material and structure. For many prac-

tical problems, because of overwhelming costs, a direct representation of the full fine-scale solution is simply impossible on today's computer resources. This research project is concerned with the development of a high-order computational procedure which is capable of solving multiscale elliptic equations arising from the modelling of multiphase materials on the present computing facilities. The proposed procedure makes use of several recent advances in computational mechanics, including the non-polynomial multiscale space approach (heterogeneous media) and spectral universal interpolants based on integrated radial basis functions (high-order approximations).

## 1.2 Problem definition

The prediction of deformation or thermal behaviour of composites presents significant challenges. One must take into consideration the behaviour of individual constituents (i.e. reinforcements - particles, fibres, whiskers and platelets - and resin/matrix), the interaction between these components and the involvement of multiple length scales and also possibly multiphysics. Fortunately, certain phenomena/problems can be modeled by multiscale elliptic equations. To capture the solution at a fine scale, the use of traditional direct approaches, e.g. multigrid methods, domain decomposition methods and adaptive mesh refinement techniques, leads to discrete systems that have very large degrees of freedom from both spatial and temporal discretisations. For a brief illustration, we consider the following elliptic equation which arises from the modelling of composite materials and subsurface flows

$$-\nabla \cdot (a^\epsilon(\mathbf{x})\nabla u) = f(\mathbf{x}) \quad \text{in } \Omega, \quad (1.1)$$

where  $a^\epsilon(\mathbf{x})$  is the material property tensor involving a small scale parameter  $\epsilon$ ,  $u$  the field variable,  $f$  a given function and  $\Omega$  the problem domain. It was pointed out in Hou and Wu (1997) that applying conventional direct methods

to (1.1) gives an overly pessimistic estimate of error  $O(h/\epsilon)$  in the  $H^1$  norm, where  $h$  is the mesh size. Direct methods clearly cannot converge when  $h > \epsilon$  and it thus requires a mesh size to be much smaller than the small length scale ( $h \ll \epsilon$ ). It can be seen that tremendous amounts of computer memory and CPU time required by these methods can easily exceed the limit of today's computing resources. Consequently, several classes of numerical methods have been developed to deal with the multiscale nature of the solution. Examples include homogenisation methods (Kalamkarov et al. 2009), heterogeneous multiscale methods (E and Engquist 2003b) and multiscale shape function methods (Hou and Wu 1997). These methods seek to capture the fine scale effect on the coarse scales via a multi-stage resolution of the fine scale features. As a result, they make the solution of a multiscale problem possible, from which the coarse scale/bulk properties of multiphase materials such as the effective conductivity, elastic moduli and permeability can be predicted. However, dense meshes are still typically required in commonly employed low order approximations.

### 1.3 Review of multiscale methods

Consider the model problem (1.1). We assume that (i) the tensor  $a(\mathbf{y})$ ,  $\mathbf{y} = \mathbf{x}/\epsilon$ , is smooth and periodic in the domain of the variable  $\mathbf{y}$ , namely  $Y$ , and (ii) boundary conditions for  $u$  are homogeneous on the whole boundary, i.e.  $u = 0$  on  $\partial\Omega$ . We use  $\langle \dagger \rangle = \int_Y \dagger d\mathbf{y}/|Y|$  to denote the volume average of the physical quantity  $\dagger$  over  $Y$ .

Multiscale methods for solving (1.1) are in contrast with conventional direct methods, e.g. refined FEMs and multigrid methods (Fish and Belsky 1995a,b). Examples of these multiscale methods include mathematical homogenisation method (MHM) (Kalamkarov et al. 2009), heterogeneous multiscale method (HMM) (E and Engquist 2003b), and multiscale finite element method (MFEM) (Hou and Wu 1997). They have been designed to overcome the prohibitively

large system associated with the fine mesh resolution in order to achieve

$$\frac{\text{cost of multiscale method}}{\text{cost of direct method}} \ll 1. \quad (1.2)$$

For HMM and MFEM, fine-scale information is derived from the solution of the following auxiliary fine scale problem

$$-\nabla \cdot (a^\epsilon(\mathbf{x})\nabla\phi(\mathbf{x})) = 0 \quad \text{in } D \subset \Omega, \quad (1.3)$$

where  $D$  represents a local domain that is named a unit cell for HMM or an element for MFEM, and  $\phi(\mathbf{x})$ s are local adaptive functions used to calculate coarse element stiffness matrices for HMM and shape functions for MFEM.

For MHM, fine-scale information is derived from the following cell problem

$$\nabla_{\mathbf{y}} \cdot (a(\mathbf{y})\nabla_{\mathbf{y}}\chi_j(\mathbf{y})) = \frac{\partial a_{ij}(\mathbf{y})}{\partial y_i}, \quad (1.4)$$

where  $\chi_j(\mathbf{y})$ s, which are named influence functions, are chosen to be periodic with zero mean, i.e.  $\langle \chi_j \rangle = 0$ .

### 1.3.1 Mathematical homogenisation method

The mathematical homogenisation method (MHM) has been traditionally used as a primary tool for analysing heterogeneous medium and its details were explained in, for example, Babuška (1976), Benssousan et al. (1978), Oleinik et al. (1992), Guedes and Kikuchi (1990), Hassani and Hinton (1998), Takano et al. (2000), Fish and Yuan (2005). Based on the assumptions of microstructure periodicity and uniformity of a unit cell domain, the homogenisation theory decomposes the boundary value problem into a unit cell (fine scale) problem and a global (coarse scale) problem.

Suppose that a composite structure is globally heterogeneous and its con-

stituents are linearly elastic. In the following, for brevity, we present MHM for one component of the displacement vector. The actual displacement component, denoted by  $u^\epsilon$ , may be periodically oscillating due to the fine scale heterogeneity. The homogenised model can provide the homogenised displacement, denoted by  $u_0$ . The differences between the actual displacement  $u^\epsilon$  and the homogenised displacement  $u_0$  are determined as the perturbed displacement, denoted by  $u_1$ , multiplied by the small parameter  $\epsilon$ , and so on. Then, a double-scale asymptotic expansion of the actual displacement is

$$u^\epsilon(\mathbf{x}) = u_0(\mathbf{x}) + \epsilon u_1(\mathbf{x}, \mathbf{y}) + \epsilon^2 u_2(\mathbf{x}, \mathbf{y}) + \dots, \quad (1.5)$$

where  $u_i(\mathbf{x}, \mathbf{y})$ ,  $i = (1, 2, \dots)$ , are functions of both scales and  $\mathbf{y}$ -periodic in  $Y$ . The actual displacement  $u^\epsilon$  is also a function of both scales, whereas the homogenised displacement  $u_0$  is only a function of the coarse scale. The latter is the solution of the homogenised equation

$$-\nabla \cdot a^* \nabla u_0 = f \text{ in } \Omega, \quad (1.6)$$

$$u_0 = 0 \text{ on } \partial\Omega, \quad (1.7)$$

where  $a^*$  is the effective material coefficient tensor, given by

$$a_{ij}^* = \left\langle a_{ik}(\mathbf{y}) \left( \delta_{kj} - \frac{\partial \chi_j}{\partial y_k} \right) \right\rangle. \quad (1.8)$$

It was proved in Benssousan et al. (1978) that  $a^*$  is symmetric and positive definite. The leading perturbed displacement  $u_1$  in equation (1.5) can be expressed in terms of the homogenised displacement  $u_0$  as

$$u_1(\mathbf{x}, \mathbf{y}) = -\chi_j \frac{\partial u_0}{\partial x_j}, \quad (1.9)$$

where the influence functions  $\chi_j$  (Fish and Yuan 2005), which are the solution of

equation (1.4), are also referred to as the characteristic displacements (Takano et al. 2000). The proof of the existence and uniqueness of the solution of equation (1.4) in weak-form sense and the validity of equation (1.9) were detailed in several works (Babuška 1976, Benssousan et al. 1978, Oleinik et al. 1992, Guedes and Kikuchi 1990, Hassani and Hinton 1998). Since there is no assumption on the geometrical configuration of the constituents, the homogenisation theory can tackle arbitrary complex microstructures. The fine scale stress tensor  $\sigma_{ij}$  is given in Xing et al. (2010). The coarse scale stresses are defined as the volume average of the fine scale stresses within a unit cell

$$\sigma_{ij}^H = \langle \sigma_{ij} \rangle. \quad (1.10)$$

A salient feature of MHM is that the fine scale solution is completely described on the coarse scale, see equations (1.9). Nevertheless, the influence functions are computed at a material point from equation (1.4) prior to the fine scale solution.

It is apparent that meshes of a unit cell need to be fine enough for accurately computing derivatives of the influence functions and homogenised displacements. Moreover, the second order perturbation  $u_2(\mathbf{x}, \mathbf{y})$  in equation (1.5) may be required when the constituents have highly contrast properties. The error source also comes from the boundary condition since in general  $u_1 \neq 0$  on  $\partial\Omega$ . Therefore, the boundary condition  $u|_{\partial\Omega} = 0$  should be enforced through the first-order corrector term  $\theta_\epsilon$  (Benssousan et al. 1978), which is given by

$$\nabla \cdot (a^\epsilon(\mathbf{x}/\epsilon)\nabla\theta_\epsilon) = 0 \text{ in } \Omega, \quad (1.11)$$

$$\theta_\epsilon = u_1(\mathbf{x}, \mathbf{x}/\epsilon) \text{ on } \partial\Omega. \quad (1.12)$$

Reliability of computations using MHM for a heterogeneous medium depends strongly on the validity of the periodicity and uniformity, introduced by the

classical homogenisation theory. Recently, Kalamkarov et al. (2009) reviewed the state-of-the-art of asymptotic homogenisation techniques in the analysis of composite materials and thin-walled composite structures.

The implementation of MHM consists of three steps as follows.

- Solving the influence functions from equation (1.4) through FEM and evaluating the homogenised (effective) material properties from equation (1.8);
- Solving the homogenised displacement from equations; (1.6)-(1.7) with the effective material properties through FEM;
- Post-processing on the micro and macro levels.

### 1.3.2 Heterogeneous multiscale method

The heterogeneous multiscale method (HMM) (E and Engquist 2003b, 2005; Ming and Yue 2006; Ming and Zhang 2007; E and Engquist 2003a; Abdulle 2007; E et al. 2007) can be viewed as a general method for the computation of multiscale problems. HMM involves two main calculations. The first one is to select an overall macroscopic scheme such as FEM for the coarse scale variables on a coarse mesh, and the second one is employed to estimate the missing coarse scale data by solving locally the fine scale problem. To solve for the coarse scale features of the problem (1.1), one can employ the strain energy  $U$  of the global structure, which generally has the following form

$$U = \frac{1}{2} \int_{\Omega} a^{\epsilon}(\mathbf{x})(\nabla u_0)^2 d\Omega. \quad (1.13)$$

Assuming that the strain energy is calculated by means of the numerical quadrature rule as

$$U = \frac{1}{2} \sum_{D \in H} |D| \sum_{\mathbf{x}_l \in D} \alpha_l a^*(\mathbf{x}_l) (\nabla u_0(\mathbf{x}_l))^2, \quad (1.14)$$

where  $H$  is the coarse mesh,  $\mathbf{x}_l$  and  $\alpha_l$  are respectively the quadrature points and the weights in element  $D$ , and  $a^*(\mathbf{x}_l)$  is the effective material coefficient at those quadrature points and calculated by (1.8). Expression (1.14) must be approximated by solving the problem in the small domain  $I_\delta(\mathbf{x}_l)$  near the quadrature point  $\mathbf{x}_l$ , which is governed by

$$\nabla \cdot (a^\epsilon(\mathbf{x}) \nabla v(\mathbf{x})) = 0, \quad \mathbf{x} \in I_\delta(\mathbf{x}_l), \quad (1.15)$$

where  $I_\delta(\mathbf{x}_l)$  is a square of size  $\delta$  centered at  $\mathbf{x}_l$ . Different boundary conditions on  $\partial I_\delta(\mathbf{x}_l)$  and their effects were discussed in Yue and E (2007). Equation (1.15) can be typically solved by FEM in just several small domains of a unit cell rather than solving a whole cell problem. Then equation (1.14) is evaluated in the following way

$$U = \frac{1}{2} \sum_{D \in H} |D| \sum_{\mathbf{x}_l \in D} \alpha_l \int_{I_\delta(\mathbf{x}_l)} \frac{a^*(\mathbf{x}_l)}{\delta^2} (\nabla v(\mathbf{x}_l))^2 dI. \quad (1.16)$$

Finally, the HMM solution  $u_0(\mathbf{x})$  is obtained by solving

$$\min \sum_{D \in H} \left\{ U - \int_D f(\mathbf{x}) u_0(\mathbf{x}) dD \right\}, \quad (1.17)$$

which can be understood as the weak form of equation (1.1). It is noteworthy that the cost of HMM depends on the size of  $\delta$ . HMM can take advantages of the possible scale separation in the problem, but becomes similar to the fine scale solvers when there is a lack of scale separation.

All demonstrations of HMM assume that  $a^*(\mathbf{x})$  are smooth, symmetric and uniformly elliptic (E and Engquist 2003b, 2005; Ming and Zhang 2007). How-

ever, this assumption cannot be applicable for multiphase materials. If there are two or more kinds of materials in  $I_\delta(\mathbf{x}_l)$ , the accuracy will be deteriorated when solving equation (1.15) with the homogenised boundary conditions which cannot model the material jumps on the boundaries of  $I_\delta(\mathbf{x}_l)$ . Therefore, the application of HMM in composite structures needs to be studied in depth.

It is well known that the microstructure information in  $u^\epsilon$  is used for the local stress analysis. This information can be recovered using a simple postprocessing technique based on  $u_0$  (E and Engquist 2003a, Oden and Vemaganti 2000). Assume that we are interested in recovering  $u^\epsilon$  and  $\nabla u^\epsilon$  only in a local domain or a unit cell  $D$ . One of the recovering approaches is the local model refinement (Oden and Vemaganti 2000), in which the following auxiliary problem,

$$\begin{aligned} -\nabla \cdot (a^\epsilon(\mathbf{x})\nabla u(\mathbf{x})) &= f(\mathbf{x}) \text{ in } D \subset \Omega, \\ u(\mathbf{x}) &= u_0(\mathbf{x}) \text{ on } \partial D, \end{aligned} \tag{1.18}$$

is solved, and the approximation  $u^\epsilon$  with micro information, whose error is finite, is then obtained (E and Engquist 2005). Another recovering approach is similar to the asymptotic expansion as in MHM. Define the first order approximation of  $u^\epsilon(\mathbf{x})$  as

$$u^\epsilon(\mathbf{x}) = u_0(\mathbf{x}) + \epsilon\chi_j \frac{\partial u_0}{\partial x_j}, \tag{1.19}$$

where the influence function  $\chi_j$  is the solution of equation (1.4).

HMM generally gives a framework that allows us to maximally take advantage of the special features of the problem such as scale separation; for problems without any special features, HMM becomes a fine scale solver. The savings in HMM, compared with the cost of solving the full fine scale problem, comes from the fact that  $I_\delta(\mathbf{x}_l)$  can be chosen to be smaller than  $D$ , and the small domain  $I_\delta(\mathbf{x}_l)$  is determined by many factors, including the accuracy and cost requirement, the degree of scale separation, and the microstructure in  $a^\epsilon(\mathbf{x})$ .

HMM has been applied to a large variety of homogenisation problems either linear or nonlinear, periodic or non-periodic, stationary or dynamic (E and Engquist 2006), and can be naturally extended to higher order by using higher order finite elements as the macroscopic solver. Recently, E et al. (2007) presented a state-of-the-art review of HMM, including the fundamental philosophy, and the main process for complex fluids, micro-fluidics, solids, interface problems, stochastic problems and statistically self-similar problems. Chen (2009) has incorporated various macroscopic solvers, including finite differences, finite elements, discontinuous Galerkin, mixed finite elements, control volume finite elements, and nonconforming finite elements, into HMM and pointed out their advantages, shortcomings and adaptabilities.

The computational sequence of HMM includes four steps:

- Solving the sub-local problems governed by equation (1.15) around the quadrature points of a coarse element to capture the effects of microstructure;
- Evaluating the strain energy through equation (1.16);
- Solving the homogenised displacement  $u_0$  from equation (1.17) using FEM;
- Recovering the micro information in  $u^\epsilon$  by solving equation (1.18) or using equation (1.19).

### 1.3.3 Multiscale finite element method

The multiscale finite element method (MFEM) (Hou and Wu 1997) was proposed to solve a class of elliptic problems (1.1) with multiple spatial scales arising from modelling of composite materials. Its main idea is to capture the coarse scale behaviour of the solution through a multi-stage resolution of the fine scale features. This can be achieved by constructing the multiscale finite

element shape functions reflecting the local property of the differential operator. The MFEM is applicable to general multiscale problems without restrictive assumptions, and the construction of the shape functions for a coarse scale element is independent from each other.

In contrast with some empirical numerical upscaling methods (Sangalli 2003), MFEM is systematic and self-consistent. The idea of constructing finite element shape functions based on local differential operator in MFEM is an extension of the work of Babuška and Osborn (1983), which incorporates the fine scale information into the basis functions by solving the original fine scale differential equations on each element with proper boundary conditions.

The over-sampling MFEM reduces the effect of the boundary layers occurring at the inter-element boundaries by an indirect approach in constructing the base functions. Instead of directly working on an element  $D$ , a domain  $S$  larger than  $D$  is used with  $\text{diam}(S) = H > h + \epsilon$ . Any reasonable boundary condition can be imposed on the boundary of domain  $S$  in solving equation (1.3) to obtain temporary base functions denoted as  $\psi_i$  with  $i = (1, \dots, d)$  in which  $d$  is the number of element nodes. One then constructs the actual base functions from the linear combination of  $\psi_j$ s

$$\phi_i = \sum_{j=1}^d c_{ij} \psi_j, \quad i = (1, \dots, d), \quad (1.20)$$

where  $c_{ij}$  are the constants determined by the condition  $\phi_i(\mathbf{x}_j) = \delta_{ij}$ .

It has been shown that MFEM converges to the homogenised solution as  $\epsilon \rightarrow 0$  (Hou and Wu 1997, Efendiev et al. 2000, Hou et al. 1999). This property is not shared by the conventional FEM with polynomial bases, since fine scale information is averaged out incorrectly. Recently, the multiscale finite element methodology has been modified and successfully applied to two-phase flow simulations (Efendiev and Hou 2007), and the consolidation analysis of heterogeneous saturated porous media (Zhang et al. 2009). The steps of implementing

the over-sampling MFEM are as follows.

- Solving equation (1.3) on a domain  $S$  for the auxiliary shape functions  $\psi_j$ ;
- Evaluating the over-sampling multiscale finite element shape functions  $\phi_i$ s over a coarse element using equation (1.20);
- Solving the coarse mesh problem by using FEM.

## 1.4 Discussion

A brief review on multiscale computational methods (MHM, HMM, MFEM) for multiphase materials in Section 1.3 provides an understanding of their philosophy and main features. As discussed, MHM is based on the homogenisation theory and hence its range of applications is usually limited by restrictive assumptions on the media, such as scale separation and periodicity (Benssousan et al. 1978). It is also expensive to be used for solving problems with many separate scales since the cost of computation grows exponentially with the number of scales (Hou and Wu 1997). HMM is more general and can be applied to problems with random coefficients. However, its effectiveness is strongly dependent on the material structure assumptions such as scale separation. Without this assumption, HMM is equivalent to a direct solver. In the last case, MFEM is applicable to general multiple-scale problems without restrictive assumptions. In contrast to MHM, the number of scales are irrelevant to the computational cost in MFEM (Hou and Wu 1997). MFEM is systematic and self-consistent, which makes it easier to analyse especially large scale problems. Nevertheless, the accuracy of MFEM is low in the order of  $O(\epsilon/h)$  (Hou and Wu 1997) and its convergence for continuous scale problems needs to be further studied.

Another concern in current multiscale computational methods in the literature

is the error source coming from the cell problem (MHM, HMM) or element problem (MFEM). It was pointed out by Babuška and Osborn (1983) in the FEM context and recently by Yuan and Shu (2008) and Wang et al. (2011) in the context of discontinuous Galerkin method (DGM) that an approximation space  $S^r$  should be constructed as

$$S^r = \{\phi : \nabla \cdot (a^\epsilon(\mathbf{x})\nabla\phi) |_I \in P^{r-2}(I)\} \quad \text{for } r = 1, 2, \dots, \quad (1.21)$$

where  $I$  denotes the cell or element in the spatial discretisation,  $P^r(I)$  denotes the space of polynomials of degree less than or equal to  $r$  on  $I$  and  $P^{-1}(I) = \{0\}$ . It can be seen that the approximation spaces of current multiscale methods in the literature correspond to  $S^1$  except for the DGM case (e.g. Yuan and Shu 2008, Wang et al. 2011), in which high convergence rates are obtained for  $r > 1$ .

Generally, conventional numerical methods such as finite element methods (FEMs), finite difference methods (FDMs) and finite volume methods (FVMs) are utilised to numerically solve both the fine scale and coarse scale problems in a theoretical framework (MHM, HMM, MFEM). These methods are typically of low order of accuracy and provide a  $C^0$  solution. It is noted that there are high-order formulations, those using Hermite interpolation for instance, e.g. (Zienkiewicz 1971, Watkins 1976, Holdeman 2009) for FEM and e.g. (Qiu and Shu 2003, 2005) for FVM, that can afford higher continuity. To the best of our knowledge, such high-order methods currently are not yet applied to multiscale model problems of interest in this thesis. The field variables and their derivatives are highly oscillating in multiscale problems, posing a great challenge for conventional low-order methods.

A 1D example below, having an exact solution, can clearly display this challenge

$$-\frac{d}{dx} \left( a^\epsilon(x) \frac{du}{dx} \right) = x, \quad 0 \leq x \leq 1 \quad (1.22)$$

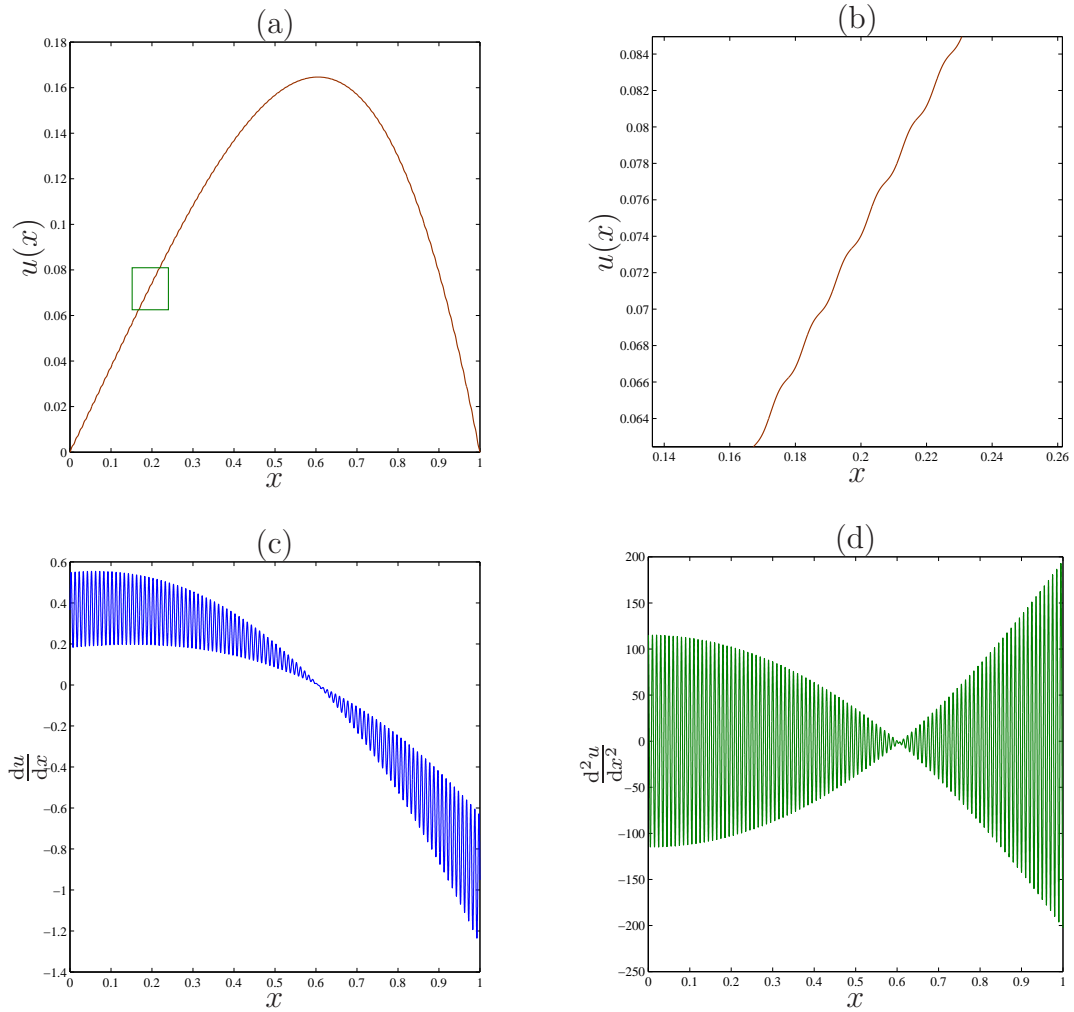


Figure 1.1: Exact solution of problem (1.22)-(1.24) for  $\epsilon = 0.01$ : (a) field variable, (b) its zoomed part, (c) its first-order derivative, (d) its second-order derivative.

with boundary conditions

$$u(0) = u(1) = 0 \quad (1.23)$$

where

$$a^\epsilon(x) = \frac{1}{2 + x + \sin(2\pi x/\epsilon)}. \quad (1.24)$$

The exact solution is depicted in Figure 1.1 for  $\epsilon = 0.01$  where we can see remarkable oscillations of first and second-order derivatives. One of the most

important issues in solving problem (1.1) is to recover the details of  $\nabla u^\epsilon$  (first-order derivative) since they contain information of great practical interest, such as the stress distribution and heat flux in composite materials or the velocity field in a porous medium (Ming and Yue 2006). In addition, even in the theoretical framework such as MHM, accurate approximations of derivatives of influence functions are necessary for evaluating the homogenised material coefficient in equation (1.8) and coarse scale displacement  $u_0$  in equations (1.6)-(1.7). It is also noteworthy that the first perturbation displacement  $u_1$  is also estimated from the first-order derivative of  $u_0$  in equation (1.9). In the case of MFEM, if the basis functions  $\phi$ s are obtained by a conventional linear FEM, they are only  $C^0$  functions, causing significant error in first-order derivative approximation and, as a result, it is impossible to approximate second-order derivatives. The discontinuity of derivatives is usually mitigated by using fine meshes, which can make conventional methods inefficient or even impracticable. Therefore, it is desirable to develop a method that has a higher order continuity of the solution across elements and also has a higher level of accuracy and efficiency. Incorporation of radial basis functions into the discretisation frameworks as trial functions can be a potential way to achieve these objectives.

## 1.5 Radial basis functions (RBFs)

Radial basis functions (RBFs) have successfully been used for the approximation of scattered data over the last several decades. They have also emerged as an attractive scheme for the numerical solution of ODEs and PDEs (e.g. Fasshauer (2007) and references therein). Theoretically, some RBF-based methods can be as competitive as spectral methods; the two types of method can exhibit spectral accuracy. Unlike pseudo-spectral techniques, RBF-based methods do not require the use of tensor products in constructing the approximations in two or more dimensions. The RBF approximations usually rely on a set of distinct points rather than a set of small elements. When this characteristic is combined

with the point-collocation formulation, the resultant discretisation methods are truly meshless (e.g. Kansa (1990)). RBF-based collocation methods can be applied to differential problems defined on irregular domains without added difficulties. Apart from point-collocation, RBFs have also been employed as trial functions in other formulations such as the Galerkin, subregion collocation and inverse statements, resulting in enhanced rates of convergence (error of  $O(h^\alpha)$  with  $\alpha > 2$ ) of these approaches. Works in this research trend include Atluri et al. (2004), Sellountos and Sequeira (2008), Orsini et al. (2008), Mohammadi (2008).

In a conventional RBF scheme (Kansa 1990), the original function is decomposed into RBFs and its derivatives are then obtained through differentiation. Some RBF schemes such as those based on multiquadric (MQ) function are known to possess spectral accuracy with error in the  $O(\lambda^\chi)$ , where  $0 < \lambda < 1$ . Through numerical experiment, for a certain range of the RBF-width  $a$ , Cheng et al. (2003) established the error estimate as  $O(\lambda^{\sqrt{a}/h})$ . In the approximation of  $k$ th derivative, Madych (1992) showed that the convergence rate is reduced to  $O(\lambda^{\chi-k})$ . To avoid such reduction of convergence rate caused by differentiation in a conventional scheme, Mai-Duy and Tran-Cong (2001, 2003) proposed an indirect approach. RBFs were used to represent highest order derivatives and such RBF-based approximants are then integrated to yield expressions for lower-order derivatives and eventually the function itself. This approach is less sensitive to noise than the usual differential approach and appears to be more suitable for applications involving derivatives such as the numerical solution of ODEs and PDEs. Recently, towards the analysis of large-scale problems, a numerical scheme, based on one-dimensional integrated RBFs (1D-IRBFs), point collocation and Cartesian grids, was reported in Mai-Duy and Tran-Cong (2007). In this scheme, the 1D-IRBF approximations at a grid point  $\mathbf{x}$  only involve nodal points that lie on grid lines crossing at  $\mathbf{x}$  rather than the whole set of nodal points, leading to a considerable saving of computing time and memory space over the original IRBF schemes (Mai-Duy et al. 2008, Le-Cao

et al. 2009, Ho-Minh et al. 2009).

Although 1D-IRBF schemes can yield a high level of accuracy using a relatively coarse grid, their system matrices are not as sparse as those produced by conventional FDMs. In addition, for a stable calculation, these schemes are limited to small values of the RBF width.

## 1.6 Objectives of the present research

In this research project, we further localise the 1D-IRBFs to construct a new type of element for the discretisation of ODEs/PDEs in point/subregion collocation formulations on Cartesian grids. The proposed element involves two nodes, called 2-node IRBFE, wherein the 1D-IRBFs are implemented with two RBF centres only and the approximations are nonoverlapping. It can be seen that the use of two RBFs (a smallest RBF set) allows a wide range of the RBF width to be used and leads to very sparse system matrices. Moreover, the approximate solution is guaranteed to be  $C^2$ -continuous across the interface of IRBFEs. We then verify the novel formulations through the solution of benchmark nonlinear flows of an incompressible Newtonian fluid (e.g. flows in lid-driven cavities and flows past a circular cylinder in a channel). We optimise the efficiency of the present approaches with the alternating direction implicit (ADI) procedure (Peaceman and Rachford 1955, Douglas and Gunn 1964) via different strategies. Finally, we introduce these proposed IRBFEs and subregion collocation into the non-polynomial multiscale space framework for solving the multiscale elliptic problems.

Accuracy will be enhanced by the following key features.

- High order RBFs rather than low order polynomials are employed to represent the solution over elements.

- Integration rather than differentiation is employed to construct the RBF approximations.
- The computed solution is a  $C^2$  function rather than the usual  $C^0$ .

Efficiency will be enhanced by the following key features.

- The IRBFE involves only two RBF centres, leading to a sparse system matrix.
- Cartesian grids are used to represent the problem domain. It is clear that generating a Cartesian grid is much simpler and easier than generating a finite-element mesh. Moreover, ADI procedure (Peaceman and Rachford 1955, Douglas and Gunn 1964) can be straightforwardly applied to accelerate computational processes.
- Point collocation formulation and control volume formulation employed with the middle point rule are utilised to discretise the governing equation. These discretisation approaches are integration free.
- Meaningful solutions can be obtained on a relatively coarse grid as mass and momentum conservations are preserved over control volumes associated with the grid nodes.

The central goal of the present research is to obtain multiscale solutions accurately and effectively.

## 1.7 Outline of the Dissertation

The dissertation has seven chapters including this chapter (Introduction); each chapter is presented in a self-explanatory way. The outline of the remaining chapters is as follows.

- Chapter 2 presents a new  $C^2$ -continuous control volume discretisation method, based on Cartesian grids and 2-node IRBFEs, for the solution of second-order elliptic problems in one and two dimensions. The proposed 2-node IRBFEs are then utilised by the following chapters.
- Chapter 3 develops 2-node IRBFEs for the simulation of incompressible viscous flows in two dimensions. Emphasis is placed on (i) the incorporation of  $C^2$ -continuous 2-node IRBFEs into the subregion and point collocation frameworks for the discretisation of the streamfunction-vorticity formulation on Cartesian grids; and (ii) the development of high order upwind schemes based on 2-node IRBFEs for the case of convection-dominant flows.
- Chapter 4 presents a  $C^2$ -continuous alternating direction implicit (ADI) method based on 2-node IRBFEs for the solution of the streamfunction-vorticity equations governing steady 2D incompressible viscous fluid flows. Unlike in Chapters 2 & 3 the solution strategy in this chapter consists of multiple use of a one-dimensional sparse matrix (associated with grid lines) algorithm that helps save the computational cost.
- Chapter 5 presents a novel  $C^2$ -continuous compact scheme based on 2-node IRBFEs. The proposed  $C^2$ -continuous compact scheme is applied to the discretisation of second-order parabolic equations in one- (1D) and two-space dimensions (2D) in an implicit manner. As in Chapter 4 the ADI procedure (Peaceman and Rachford 1955, Douglas and Gunn 1964) is applied for the time integration in 2D. However, the one-dimensional matrices associated with grid lines are optimised to be in standard tridiagonal form which can be solved efficiently by the Thomas algorithm. Moreover, the typical matrix size is half of that obtained in Chapter 4 and equal to the number of nodal unknowns of the dependent variable only.
- Chapter 6 presents a high order multiscale conservative method, based on

multiscale basis function approach and IRBFEs, for the solution of multiscale elliptic problems with reduced computational cost. Unlike other methods based on multiscale basis function approach, sets of basis and correction functions here are obtained through  $C^2$ -continuous IRBFE-CV formulation.

- Chapter 7 gives some concluding remarks and suggestion of possible future research developments.

## Chapter 2

# Two-node IRBF elements and a $C^2$ -continuous control-volume technique

This chapter presents a new control-volume discretisation method, based on Cartesian grids and integrated-radial-basis-function elements (IRBFEs), for the solution of second-order elliptic problems in one and two dimensions. The governing equation is discretised by means of the control-volume formulation and the division of the problem domain into non-overlapping control volumes is based on a Cartesian grid. Salient features of the present method include (i) an element is defined by two adjacent nodes on a grid line, (ii) the IRBF approximations on each element are constructed using only two RBF centres (a smallest RBF set) associated with the two nodes of the element and (iii) the IRBFE solution is  $C^2$ -continuous across the interface between two adjacent elements. The first feature guarantees consistency of the flux at control-volume faces. The second feature helps represent curved profiles between 2 adjacent nodes and leads to a sparse and banded system matrix, facilitating the employment of a large number of nodes. The third feature enhances the smoothness of

element-based solutions, allowing a better estimate for the physical quantities involving derivatives. Numerical results indicate that (i) the proposed method can work with a wide range of the shape-parameter/RBF-width and (ii) the proposed technique yields more accurate results and faster convergence, especially for the approximation of derivatives, than the standard control-volume technique.

## 2.1 Introduction

Traditional techniques used for solving second-order elliptic differential equations include overlapping finite difference methods (FDMs), non-overlapping finite element methods (FEMs), boundary element methods (BEMs) and control volume methods (CVMs). These methods typically utilise polynomials as an interpolator. To avoid notorious polynomial snaking phenomena, low-order polynomials such as linear variations are widely used, usually leading to errors of order  $h^2$ , where  $h$  is the mesh spacing. For element-based solutions, only the approximating function (not its partial derivatives) is continuous across elements (i.e.  $C^0$  continuity). The overall error can be reduced by using progressively denser meshes. A mesh needs be sufficiently fine to mitigate the effects of discontinuity of partial derivatives. It is thus desirable to have discretisation methods that can produce a solution of higher-order continuity across elements. There are high-order formulations in the literature, for instance those using Hermite interpolation e.g. (Zienkiewicz 1971, Watkins 1976, Holdeman 2009) for FEM and e.g. (Qiu and Shu 2003, 2005) for FVM that can provide such high-order continuity. Here, we develop a high-order continuity method based on IRBF interpolation and control-volume formulation.

Radial basis functions (RBFs) have successfully been used for the approximation of scattered data over the last several decades. They have also emerged as an attractive scheme for the numerical solution of ordinary and partial dif-

ferential equations (ODEs and PDEs) e.g. (Fasshauer 2007, and references therein). Theoretically, some RBF-based methods can be as competitive as spectral methods; the two types of methods can exhibit spectral accuracy. Unlike pseudo-spectral techniques, RBF-based methods do not require the use of tensor products in constructing the approximations in two or more dimensions. The RBF approximations usually rely on a set of distinct points rather than a set of small elements. When this characteristic is combined with the point-collocation formulation, the resultant discretisation methods are truly meshless e.g. (Kansa 1990). RBF-based collocation methods can be applied to differential problems defined on irregular domains without added difficulties. Apart from point-collocation, RBFs have also been employed as trial functions in other formulations such as the Galerkin, subregion collocation and inverse statements, resulting in enhanced rates of convergence ( $O(h^\alpha)$  with  $\alpha > 2$ ) of these approaches. Works in this research trend include Atluri et al. (2004), Sellountos and Sequeira (2008), Orsini et al. (2008), Mohammadi (2008).

In a pivotal paper on function approximation by Franke (1982), it was pointed out that the multiquadric (MQ) RBF scheme yields the most accurate results. The present work employs the MQ whose form is defined by

$$g_i(\mathbf{x}) = \sqrt{(\mathbf{x} - \mathbf{c}_i)^2 + a_i^2}, \quad (2.1)$$

where  $\mathbf{c}_i$  and  $a_i$  are the centre and the shape parameter of the  $i$ th MQ, respectively. A set of interpolation points is taken to be a set of RBF centres. In Mai-Duy and Tran-Cong (2001, 2003), the value of the shape parameter was simply chosen as  $a_i = \beta h_i$  with  $\beta$  being a given positive number and  $h_i$  the distance between  $\mathbf{c}_i$  and its nearest neighbour. When the direct way of computing the interpolants is used, RBF-based methods such as those using MQs are known to suffer from the so-called uncertainty principle. As the value of  $\beta$  increases, the error reduces while the matrix condition number increases undesirably. In practice, one desires to use large  $\beta$ s up to a value at which the system

matrix is still in good condition. RBF-based methods can be classified into two categories: global and local. Global methods use every RBF on the whole domain to construct the approximations at a point, resulting in a fully populated system matrix c.f. (Kansa 1990, Sarler 2005, Zerroukat et al. 1998, Mai-Duy and Tran-Cong 2001). When the number of RBF centres and/or the value of  $\beta$  increase, the condition of RBF matrices deteriorates rapidly. Such drawbacks typically render global methods unsuitable for complex problems, where many points are required for a proper simulation. In addition,  $\beta$  to be used is confined to small values. For local methods e.g. (Tolstykh and Shirobokov 2003, Shu et al. 2003, Lee et al. 2003, Šarler and Vertnik 2006, Divo and Kassab 2007, Sanyasiraju and Chandhini 2008, Mai-Duy and Tran-Cong 2009a), only a few RBFs are activated for the approximations at a point. The resultant system matrix is sparse and banded, which is suitable for handling large-scale problems. However, trade-offs include the loss of spectral accuracy and high-order continuity of the approximate solution. Various schemes have been proposed to enhance the performance of local methods. Using large values of  $\beta$  appears to be an economical and effective way (Cheng et al. 2003). In the case of non-overlapping domain-decompositions, where a large problem is replaced with a set of sub-problems of much smaller sizes, the computed solution is only a  $C^1$  function across the subdomain interfaces (Li and Hon 2004). It is noted that errors of RBF solutions are larger near interfaces/boundaries (Fedoseyev et al. 2002) and with Neumann boundary conditions than with Dirichlet boundary conditions (Libre et al. 2008).

In a conventional RBF scheme (Kansa 1990), the original function is decomposed into RBFs and its derivatives are then obtained through differentiation. Some RBF schemes such as those based on MQs are known to possess spectral accuracy with errors in the  $O(\lambda^\chi)$ , where  $0 < \lambda < 1$ . Through numerical experiment, for a certain range of  $a$ , Cheng et al. (2003) established the error estimate as  $O(\lambda^{\sqrt{a}/h})$ . In the approximation of  $k$ th derivative, Madych (1992) showed that the convergence rate is reduced to  $O(\lambda^{\chi-k})$ . To avoid such reduction of

convergence rate caused by differentiation in a conventional scheme, Mai-Duy and Tran-Cong (2001, 2003) proposed an indirect or integral approach. RBFs were used to represent highest order derivatives and such RBF-based approximants are then integrated to yield expressions for lower-order derivatives and eventually the function itself. This approach is less sensitive to noise than the usual differential approach and appears to be more suitable for applications involving derivatives such as the numerical solution of ODEs and PDEs. Recently, towards the analysis of large-scale problems, a numerical scheme, based on one-dimensional integrated RBFs (1D-IRBFs), point collocation and Cartesian grids, was reported in Mai-Duy and Tran-Cong (2007). In this scheme, the 1D-IRBF approximations at a grid point  $\mathbf{x}$  only involve nodal points that lie on grid lines crossing at  $\mathbf{x}$  rather than the whole set of nodal points, leading to a considerable saving of computing time and memory space over the original IRBF schemes (e.g. Mai-Duy et al. 2008, Le-Cao et al. 2009, Ho-Minh et al. 2009, Ngo-Cong et al. 2011).

In the present work, the problem domain, which can be rectangular or non-rectangular, is represented by a Cartesian grid. Each grid node is associated with a control volume (CV) of rectangular shape. To estimate the values of the flux at the middle points on the interfaces, the approximations for the field variable and its derivatives are constructed using IRBFs over elements defined by two adjacent grid nodes. Unlike a previous work by Mai-Duy and Tran-Cong (2010a), 1D-IRBFs are implemented here with two RBF centres only and the approximations are non-overlapping. Furthermore, the constants of integration are exploited to impose continuity of second-order derivatives across two adjacent elements. It can be seen that the use of two RBFs (a smallest RBF set) allows a wide range of  $\beta$  to be used and leads to sparse system matrices. To enhance accuracy, one can thus increase the value of  $\beta$  and/or the number of RBFs. Continuity of the approximate solution, its first and second-order derivatives across two adjacent IRBF elements (or simply across elements for brevity in the remaining discussion) is guaranteed in the proposed technique.

An outline of the chapter is as follows. In Section 2.2, a brief review of IRBFs including 1D-IRBFs is given. In Section 2.3, the proposed  $C^2$ -CV technique based on 2-node IRBFEs for second-order elliptic differential problems is presented. In Section 2.4, the proposed technique is verified through function approximation and solution of ODEs and PDEs. Section 2.5 concludes the chapter.

## 2.2 Brief review of integrated RBFs

The indirect/integral RBF approach consists in decomposing highest-order derivatives under consideration into RBFs and then integrating these RBFs to yield expressions for lower-order derivatives and finally the original function itself (Mai-Duy and Tran-Cong 2003). In the case of second-order PDEs in two dimensions, integrated MQ expressions are given by

$$\frac{\partial^2 \phi}{\partial \eta^2}(\mathbf{x}) = \sum_{i=1}^n w_i \sqrt{(\mathbf{x} - \mathbf{c}_i)^2 + a_i^2} = \sum_{i=1}^n w_i I_i^{(2)}(\mathbf{x}), \quad \mathbf{x} \in \Omega, \quad (2.2)$$

$$\frac{\partial \phi}{\partial \eta}(\mathbf{x}) = \sum_{i=1}^n w_i I_i^{(1)}(\mathbf{x}) + C_1(\theta), \quad (2.3)$$

$$\phi(\mathbf{x}) = \sum_{i=1}^n w_i I_i^{(0)}(\mathbf{x}) + C_1(\theta)\eta + C_2(\theta), \quad (2.4)$$

where  $\Omega$  is the domain of interest,  $\phi$  a function,  $\eta$  a component of  $\mathbf{x}$ ,  $n$  the number of RBFs,  $\{w_i\}_{i=1}^n$  the set of RBF weights,  $C_1(\theta)$  and  $C_2(\theta)$  the constants of integration which are functions of  $\theta$  ( $\theta \neq \eta$ ),  $I_i^{(2)}(\mathbf{x})$  conveniently denotes the MQ,  $I_i^{(1)}(\mathbf{x}) = \int I_i^{(2)}(\mathbf{x}) d\eta$ , and  $I_i^{(0)}(\mathbf{x}) = \int I_i^{(1)}(\mathbf{x}) d\eta$ . Explicit forms of  $I_i^{(1)}(\mathbf{x})$  and  $I_i^{(0)}(\mathbf{x})$  can be found in appendix A.

When the analysis domain  $\Omega$  is a line segment, expressions (2.2)-(2.4) reduce to

$$\frac{d^2\phi}{d\eta^2}(\eta) = \sum_{i=1}^n w_i \sqrt{(\eta - c_i)^2 + a_i^2} = \sum_{i=1}^n w_i I_i^{(2)}(\eta), \quad (2.5)$$

$$\frac{d\phi}{d\eta}(\eta) = \sum_{i=1}^n w_i I_i^{(1)}(\eta) + C_1, \quad (2.6)$$

$$\phi(\eta) = \sum_{i=1}^n w_i I_i^{(0)}(\eta) + C_1\eta + C_2, \quad (2.7)$$

where  $C_1$  and  $C_2$  are simply constant values.

Expressions (2.5), (2.6) and (2.7), called 1D-IRBFs, can also be used in conjunction with Cartesian grids for solving 2D problems. Advantages of 1D-IRBFs over 2D-IRBFs are that they possess some “local” properties and are constructed with a much lower cost. However, numerical experiments show that 1D-IRBFs still cannot work with large values of  $\beta$ . In the present work, 1D-IRBF-based schemes are further localised.

## 2.3 Proposed $C^2$ -continuous control-volume technique

The problem domain is embedded in a Cartesian grid. In the case of non-rectangular domains, we remove grid points outside the problem domain. Grid points inside the problem domain are taken to be interior nodes, while boundary nodes are defined as the intersection of the grid lines and the boundaries. Generally, each nodal point is associated with a control volume, over which the differential equation is directly integrated. For illustrative purposes, the proposed technique is presented for the following 2D PDE

$$\frac{\partial^2\phi}{\partial x^2} + \frac{\partial^2\phi}{\partial y^2} = b(x, y), \quad (2.8)$$

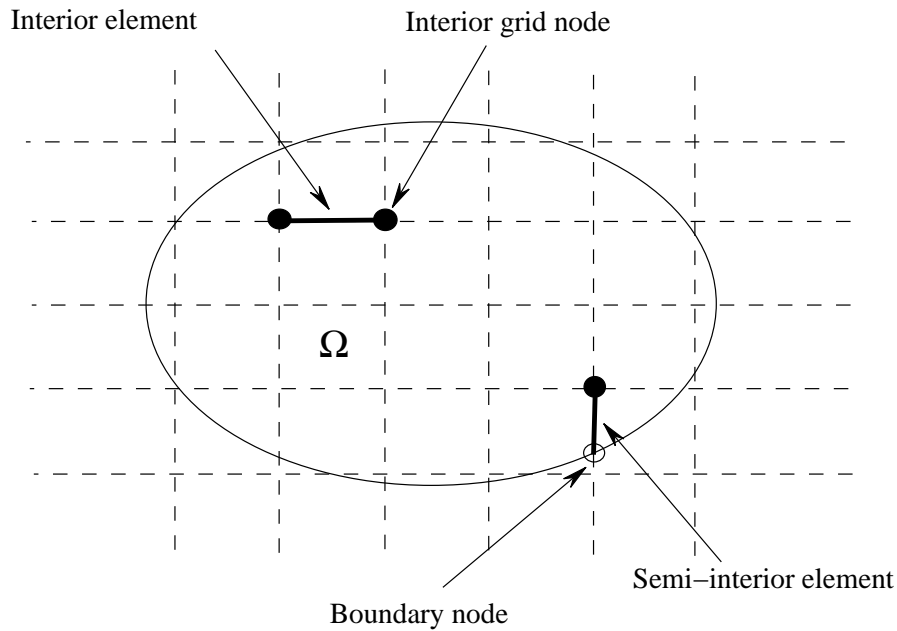


Figure 2.1: A domain is embedded in a Cartesian grid with interior and semi-interior elements.

where  $b(x, y)$  is some prescribed function. Following the work of Patankar (1980), (2.8) is transformed into a set of discretised equations. A distinguishing feature of the proposed technique is that the approximations used for the flux estimation at the interfaces are based on 1D-IRBFs rather than linear polynomials. In Mai-Duy and Tran-Cong (2010a), 1D-IRBFs were implemented using every node on a grid line. In contrast, the present 1D-IRBFs are constructed locally over straight-line segments between two adjacent nodal points only, called 2-node IRBF elements (IRBFEs). There are two types of elements, namely interior and semi-interior IRBFEs. An interior element is formed using two adjacent interior nodes while a semi-interior element is generated by an interior node and a boundary node (Figure 2.1). In the remainder of this section, 1D-IRBFs are first utilised to represent the variation of the field variable and its derivatives on interior and semi-interior elements, and IRBFEs are then incorporated into the CV formulation. It will be shown that the approximate solution is a  $C^2$  function across IRBFEs.

### 2.3.1 Interior elements

1D-IRBF expressions for interior elements are of similar forms. Consider an interior element,  $\eta \in [\eta_1, \eta_2]$ , and its two nodes are locally named as 1 and 2. Let  $\phi(\eta)$  be a function and  $\phi_1$ ,  $\partial\phi_1/\partial\eta$ ,  $\phi_2$  and  $\partial\phi_2/\partial\eta$  be the values of  $\phi$  and  $d\phi/d\eta$  at the two nodes, respectively (Figure 2.2). The 2-node IRBFE

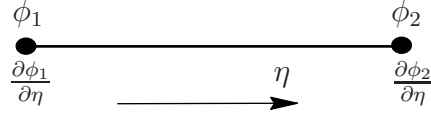


Figure 2.2: Schematic outline for 2-node IRBFE.

scheme approximates  $\phi(\eta)$  using two MQs whose centres are located at  $\eta_1$  and  $\eta_2$ . Expressions (2.5), (2.6) and (2.7) become

$$\frac{\partial^2 \phi}{\partial \eta^2}(\eta) = w_1 \sqrt{(\eta - c_1)^2 + a_1^2} + w_2 \sqrt{(\eta - c_2)^2 + a_2^2} = w_1 I_1^{(2)}(\eta) + w_2 I_2^{(2)}(\eta), \quad (2.9)$$

$$\frac{\partial \phi}{\partial \eta}(\eta) = w_1 I_1^{(1)}(\eta) + w_2 I_2^{(1)}(\eta) + C_1, \quad (2.10)$$

$$\phi(\eta) = w_1 I_1^{(0)}(\eta) + w_2 I_2^{(0)}(\eta) + C_1 \eta + C_2, \quad (2.11)$$

where  $I_i^{(1)}(\eta) = \int I_i^{(2)}(\eta) d\eta$ ,  $I_i^{(0)}(\eta) = \int I_i^{(1)}(\eta) d\eta$  with  $i = (1, 2)$ , and  $C_1$  and  $C_2$  are the constants of integration. By collocating (2.11) and (2.10) at  $\eta_1$  and  $\eta_2$ , the relation between the physical space and the RBF coefficient space is obtained

$$\underbrace{\begin{pmatrix} \phi_1 \\ \phi_2 \\ \frac{\partial \phi_1}{\partial \eta} \\ \frac{\partial \phi_2}{\partial \eta} \end{pmatrix}}_{\hat{\psi}} = \underbrace{\begin{pmatrix} I_1^{(0)}(\eta_1) & I_2^{(0)}(\eta_1) & \eta_1 & 1 \\ I_1^{(0)}(\eta_2) & I_2^{(0)}(\eta_2) & \eta_2 & 1 \\ I_1^{(1)}(\eta_1) & I_2^{(1)}(\eta_1) & 1 & 0 \\ I_1^{(1)}(\eta_2) & I_2^{(1)}(\eta_2) & 1 & 0 \end{pmatrix}}_{\mathcal{I}} \underbrace{\begin{pmatrix} w_1 \\ w_2 \\ C_1 \\ C_2 \end{pmatrix}}_{\hat{w}}, \quad (2.12)$$

where  $\widehat{\psi}$  is the nodal-value vector,  $\mathcal{I}$  the conversion matrix, and  $\widehat{w}$  the coefficient vector. It is noted that not only the nodal values of  $\phi$  but also of  $\partial\phi/\partial\eta$  are incorporated into the conversion system and this imposition is done in an exact manner owing to the presence of integration constants. Solving (2.12) yields

$$\widehat{w} = \mathcal{I}^{-1}\widehat{\psi}. \quad (2.13)$$

Substitution of (2.13) into (2.11), (2.10) and (2.9) leads to

$$\phi(\eta) = \left[ I_1^{(0)}(\eta), I_2^{(0)}(\eta), \eta, 1 \right] \mathcal{I}^{-1}\widehat{\psi}, \quad (2.14)$$

$$\frac{\partial\phi}{\partial\eta}(\eta) = \left[ I_1^{(1)}(\eta), I_2^{(1)}(\eta), 1, 0 \right] \mathcal{I}^{-1}\widehat{\psi}, \quad (2.15)$$

$$\frac{\partial^2\phi}{\partial\eta^2}(\eta) = \left[ I_1^{(2)}(\eta), I_2^{(2)}(\eta), 0, 0 \right] \mathcal{I}^{-1}\widehat{\psi}, \quad (2.16)$$

which allows one to express the values of  $\phi$  and  $\partial\phi/\partial\eta$  at any point  $\eta$  in  $[\eta_1, \eta_2]$  in terms of four nodal unknowns, i.e. the values of the field variable and its first-order derivatives at the two extremes (also grid points) of the element.

### 2.3.2 Semi-interior elements

As mentioned earlier, a semi-interior element is defined by two nodes: an interior node and a boundary node. The subscripts 1 and 2 are now replaced with  $b$  ( $b$  represents a boundary node) and  $g$  ( $g$  an interior grid node), respectively. Experience shows that boundary treatments strongly affect the overall accuracy of a numerical solution. Thus several semi-interior elements for the Dirichlet-type and Neumann-type boundary conditions are proposed and investigated. Their construction processes are similar to that for interior elements, and therefore only the main differences are presented in the following sections.

### Dirichlet boundary conditions

At  $\eta_b$ , the value of  $\phi$  is given. We propose three types of semi-interior elements. The first one can work with problems with irregular geometries while the last two are limited to the case of 1D problems and 2D problems defined on rectangular domains. For 1D and rectangular domain cases, a boundary node is also a grid node and one can express the governing equation at that node in terms of one independent variable only, i.e. either  $\eta \equiv x$  or  $\eta \equiv y$ . The last two types of semi-interior elements will take into account information on the governing equation at  $\eta_b$ .

*Element IRBFE-D1:* At  $\eta = \eta_b$ , this element uses information on  $\phi$  only. The conversion system (2.12) reduces to

$$\begin{pmatrix} \phi_b \\ \phi_g \\ \frac{\partial \phi_g}{\partial \eta} \end{pmatrix} = \begin{pmatrix} I_b^{(0)}(\eta_b) & I_g^{(0)}(\eta_b) & \eta_b & 1 \\ I_b^{(0)}(\eta_g) & I_g^{(0)}(\eta_g) & \eta_g & 1 \\ I_b^{(1)}(\eta_g) & I_g^{(1)}(\eta_g) & 1 & 0 \end{pmatrix} \begin{pmatrix} w_b \\ w_g \\ C_1 \\ C_2 \end{pmatrix}. \quad (2.17)$$

It can be seen that the interpolation matrix for element *IRBFE-D1* is under-determined and its inverse can be obtained using the SVD technique (pseudo-inversion).

*Element IRBFE-D2:* At  $\eta = \eta_b$ , this element uses information on  $\phi$  and the governing equation, which leads to the conversion system

$$\begin{pmatrix} \phi_b \\ \phi_g \\ \frac{\partial^2 \phi_b}{\partial \eta^2} \\ \frac{\partial \phi_g}{\partial \eta} \end{pmatrix} = \begin{pmatrix} I_b^{(0)}(\eta_b) & I_g^{(0)}(\eta_b) & \eta_b & 1 \\ I_b^{(0)}(\eta_g) & I_g^{(0)}(\eta_g) & \eta_g & 1 \\ I_b^{(2)}(\eta_b) & I_g^{(2)}(\eta_b) & 0 & 0 \\ I_b^{(1)}(\eta_g) & I_g^{(1)}(\eta_g) & 1 & 0 \end{pmatrix} \begin{pmatrix} w_b \\ w_g \\ C_1 \\ C_2 \end{pmatrix}. \quad (2.18)$$

In (2.18),  $\partial^2 \phi_b / \partial \eta^2$  is a known value, obtained from the governing equation (2.8). For example, if  $\eta$  represents  $x$ , one has  $\partial^2 \phi_b / \partial x^2 = b(x, y) - \partial^2 \phi_b / \partial y^2$  in

which  $\partial^2 \phi_b / \partial y^2$  is easily calculated from the given boundary condition  $\phi$  on the vertical line  $x = x_b$ .

*Element IRBFE-D3:* At  $\eta = \eta_b$ , this element uses information on  $\phi$  and  $\partial\phi/\partial\eta$ , resulting in the following system

$$\begin{pmatrix} \phi_b \\ \phi_g \\ \frac{\partial\phi_b}{\partial\eta} \\ \frac{\partial\phi_g}{\partial\eta} \end{pmatrix} = \begin{pmatrix} I_b^{(0)}(\eta_b) & I_g^{(0)}(\eta_b) & \eta_b & 1 \\ I_b^{(0)}(\eta_g) & I_g^{(0)}(\eta_g) & \eta_g & 1 \\ I_b^{(1)}(\eta_b) & I_g^{(1)}(\eta_b) & 1 & 0 \\ I_b^{(1)}(\eta_g) & I_g^{(1)}(\eta_g) & 1 & 0 \end{pmatrix} \begin{pmatrix} w_b \\ w_g \\ C_1 \\ C_2 \end{pmatrix}, \quad (2.19)$$

which has the same form as the interior element.

### Neumann boundary conditions

In the context of Cartesian-grid-based methods, the implementation of a Neumann boundary condition still presents a great challenge. Special treatments, e.g. a boundary node does lie on a grid point, are required. Here, we restrict our attention to rectangular domains. At  $\eta_b$ , the value of  $\partial\phi/\partial\eta$  is given. In the following, we propose two types of semi-interior elements.

*Element IRBFE-N1:* At  $\eta = \eta_b$ , this element uses information on  $\partial\phi/\partial\eta$  and  $\partial^2\phi/\partial\eta^2$ . The resultant conversion system is

$$\begin{pmatrix} \frac{\partial\phi_b}{\partial\eta} \\ \phi_g \\ \frac{\partial^2\phi_b}{\partial\eta^2} \\ \frac{\partial\phi_g}{\partial\eta} \end{pmatrix} = \begin{pmatrix} I_b^{(1)}(\eta_b) & I_g^{(1)}(\eta_b) & 1 & 0 \\ I_b^{(0)}(\eta_g) & I_g^{(0)}(\eta_g) & \eta_g & 1 \\ I_b^{(2)}(\eta_b) & I_g^{(2)}(\eta_b) & 0 & 0 \\ I_b^{(1)}(\eta_g) & I_g^{(1)}(\eta_g) & 1 & 0 \end{pmatrix} \begin{pmatrix} w_b \\ w_g \\ C_1 \\ C_2 \end{pmatrix}, \quad (2.20)$$

*Element IRBFE-N2:* At  $\eta = \eta_b$ , this element uses information on  $\phi$  and  $\partial\phi/\partial\eta$ . The corresponding conversion system is exactly the same as that of *IRBFE-D3*.

It should be pointed out that all nodal values at  $\eta = \eta_b$  in *IRBFE-D1* and

*IRBFE-D2* are given, while there is one nodal unknown at  $\eta = \eta_b$  in *IRBFE-D3*, *IRBFE-N1* and *IRBFE-N2*. For the latter cases, one extra equation is needed and how to generate this equation will be discussed later. Table 2.1 provides a list of semi-interior elements and their characteristics. Owing to the facts that point collocation is used and the RBF conversion matrix is not over-determined, all boundary values here are imposed in an exact manner in the sense that the error is due to the numerical inversion only and there is no intrinsic approximation errors such as those associated with “unconstrained” boundary conditions imposed by certain finite element methods (Burnett 1987).

Table 2.1: List of semi-interior elements and their characteristics.

Boundary condition	Element	Nodal values at a boundary point	Unknowns
Dirichlet	<i>IRBFE-D1</i>	$\phi_b$	None
	<i>IRBFE-D2</i>	$\phi_b$ and $\partial^2 \phi_b / \partial \eta^2$	None
	<i>IRBFE-D3</i>	$\phi_b$ and $\partial \phi_b / \partial \eta$	$\partial \phi_b / \partial \eta$
Neumann	<i>IRBFE-N1</i>	$\partial \phi_b / \partial \eta$ and $\partial^2 \phi_b / \partial \eta^2$	$\partial^2 \phi_b / \partial \eta^2$
	<i>IRBFE-N2</i>	$\phi_b$ and $\partial \phi_b / \partial \eta$	$\phi_b$

### 2.3.3 Incorporation of IRBFES into the control-volume formulation

Assuming that a Cartesian-grid represents the problem domain  $\Omega$ . In a control-volume approach, the domain is subdivided into a set of control volumes in such a way that there is one control volume surrounding each grid point without gaps or overlapped volumes between adjacent elements. A typical control volume associated with a grid point  $P$ , denoted by  $\Omega_P$ , is shown in Figure 2.3, where  $E, W, N$  and  $S$  are the neighbouring points of  $P$  on the horizontal and vertical grid lines. The governing equation (2.8) is discretised by means of subregion

collocation and this process is conducted in a similar fashion for all interior grid points of the problem domain. By directly integrating (2.8) over  $\Omega_P$ , the

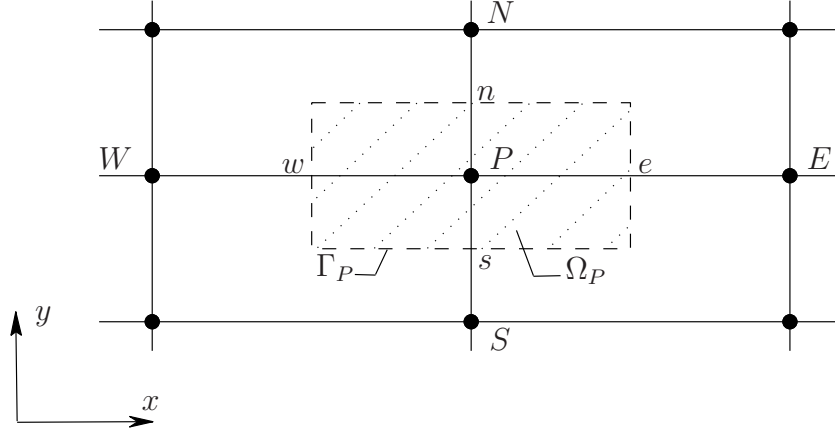


Figure 2.3: Schematic outline for a control volume in 2D.

subregion-collocation equation is obtained

$$\int_{\Omega_P} \left( \frac{\partial^2 \phi}{\partial x^2} + \frac{\partial^2 \phi}{\partial y^2} - b(x, y) \right) d\Omega_P = 0. \quad (2.21)$$

Applying the Gauss divergence theorem to (2.21) results in

$$\int_{\Gamma_P} \left( \frac{\partial \phi}{\partial x} dy - \frac{\partial \phi}{\partial y} dx \right) - \int_{\Omega_P} b(x, y) d\Omega_P = 0, \quad (2.22)$$

where  $\Gamma_P$  denotes the faces of  $\Omega_P$ . It is noted that partial derivatives of  $\phi$  in (2.22) are of first order only and no approximation is made at this stage.

Following the work of Patankar (1980), (2.22) reduces to

$$\left[ \left( \frac{\partial \phi}{\partial x} \right)_e - \left( \frac{\partial \phi}{\partial x} \right)_w \right] \Delta y + \left[ \left( \frac{\partial \phi}{\partial y} \right)_n - \left( \frac{\partial \phi}{\partial y} \right)_s \right] \Delta x - b(x_P, y_P) A_P = 0, \quad (2.23)$$

where  $A_P$  is the area of  $\Omega_P$  and the subscripts  $e, w, n$  and  $s$  are used to indicate that the flux is estimated at the intersections of the grid lines with the east, west, north and south faces of the control volume, respectively (Figure 2.3).

In the presently proposed technique, 2-node IRBFEs, which are defined over line segments between  $P$  and its neighbouring grid points ( $E, W, N$  and  $S$ ), are incorporated into (2.23) to represent the field variable  $\phi$  and its derivatives. There are 4 IRBFEs associated with a control volume. Assuming that  $PE$  and  $WP$  are interior elements and making use of (2.15), the values of the flux at the faces  $x = x_e$  and  $x = x_w$  are computed as

$$\left(\frac{\partial\phi}{\partial x}\right)_e = \left[ I_1^{(1)}(x_e), I_2^{(1)}(x_e), 1, 0 \right] \mathcal{I}^{-1} \hat{\psi} = \left[ I_1^{(1)}(x_e), I_2^{(1)}(x_e), 1, 0 \right] \mathcal{I}^{-1} \begin{pmatrix} \phi_P \\ \phi_E \\ \frac{\partial\phi_P}{\partial x} \\ \frac{\partial\phi_E}{\partial x} \end{pmatrix}$$

with  $\eta_1 \equiv x_P$  and  $\eta_2 \equiv x_E$ ,

(2.24)

$$\left(\frac{\partial\phi}{\partial x}\right)_w = \left[ I_1^{(1)}(x_w), I_2^{(1)}(x_w), 1, 0 \right] \mathcal{I}^{-1} \hat{\psi} = \left[ I_1^{(1)}(x_w), I_2^{(1)}(x_w), 1, 0 \right] \mathcal{I}^{-1} \begin{pmatrix} \phi_W \\ \phi_P \\ \frac{\partial\phi_W}{\partial x} \\ \frac{\partial\phi_P}{\partial x} \end{pmatrix}$$

with  $\eta_1 \equiv x_W$  and  $\eta_2 \equiv x_P$ ,

(2.25)

where  $I_1^{(1)}(x)$ ,  $I_2^{(1)}(x)$  and  $\mathcal{I}^{-1}$  are defined in (2.9)-(2.13). Vector  $\hat{\psi}$  may change if  $PE$  and  $WP$  are semi-interior elements. For example, one has

$$\begin{aligned} \hat{\psi} &= (\phi_W, \phi_P, \partial\phi_P/\partial x)^T && \text{if } WP \text{ is a } D1 \text{ element,} \\ \hat{\psi} &= (\phi_W, \partial^2\phi_W/\partial x^2, \phi_P, \partial\phi_P/\partial x)^T && \text{if } WP \text{ is a } D2 \text{ element,} \\ \hat{\psi} &= (\phi_W, \partial\phi_W/\partial x, \phi_P, \partial\phi_P/\partial x)^T && \text{if } WP \text{ is a } D3 \text{ element,} \\ \hat{\psi} &= (\partial\phi_W/\partial x, \partial^2\phi_W/\partial x^2, \phi_P, \partial\phi_P/\partial x)^T && \text{if } WP \text{ is a } N1 \text{ element,} \\ \hat{\psi} &= (\phi_W, \partial\phi_W/\partial x, \phi_P, \partial\phi_P/\partial x)^T && \text{if } WP \text{ is a } N2 \text{ element.} \end{aligned}$$

Expressions for the flux at the faces  $y = y_n$  and  $y = y_s$  are of similar forms.

### 2.3.4 Inter-element $C^2$ continuity

It can be seen from IRBFE expressions for computing the flux at the faces (e.g. (2.24) and (2.25)), there are three unknowns, namely  $\phi$ ,  $\partial\phi/\partial x$  and  $\partial\phi/\partial y$ , at a grid node  $P$ . Unlike conventional CVMs, the nodal values of  $\partial\phi/\partial x$  and  $\partial\phi/\partial y$  at  $P$  here constitute part of the nodal unknown vector. One thus needs to generate three independent equations. The first equation is obtained by conducting subregion-collocation of (2.8) at  $P$ , i.e. (2.23). The other two equations can be formed by enforcing the local continuity of  $\partial^2\phi/\partial x^2$  and  $\partial^2\phi/\partial y^2$  across the elements at  $P$

$$\left(\frac{\partial^2\phi_P}{\partial x^2}\right)_L = \left(\frac{\partial^2\phi_P}{\partial x^2}\right)_R, \quad (2.26)$$

$$\left(\frac{\partial^2\phi_P}{\partial y^2}\right)_B = \left(\frac{\partial^2\phi_P}{\partial y^2}\right)_T, \quad (2.27)$$

where  $(.)_L$  indicates that the computation of  $(.)$  is based on the element to the left of  $P$ , i.e. element  $WP$ , and similarly subscripts  $R, B, T$  denote the right ( $PE$ ), bottom ( $SP$ ) and top ( $PN$ ) elements.

Substitution of (2.16) into (2.26) and (2.27) yields

$$\left(\left[I_1^{(2)}(\eta_2), I_2^{(2)}(\eta_2), 0, 0\right] \mathcal{I}^{-1}\hat{\psi}\right)_L = \left(\left[I_1^{(2)}(\eta_1), I_2^{(2)}(\eta_1), 0, 0\right] \mathcal{I}^{-1}\hat{\psi}\right)_R, \quad (2.28)$$

where  $\eta$  represents  $x$  and  $\eta_2 \equiv \eta_1 \equiv x_P$ , and

$$\left(\left[I_1^{(2)}(\eta_2), I_2^{(2)}(\eta_2), 0, 0\right] \mathcal{I}^{-1}\hat{\psi}\right)_B = \left(\left[I_1^{(2)}(\eta_1), I_2^{(2)}(\eta_1), 0, 0\right] \mathcal{I}^{-1}\hat{\psi}\right)_T, \quad (2.29)$$

where  $\eta$  represents  $y$  and  $\eta_2 \equiv \eta_1 \equiv y_P$ . The conditions (2.26)-(2.27) or (2.28)-(2.29) guarantee that the solution  $\phi$  across IRBFEs is a  $C^2$  function.

As discussed earlier, for *IRBFE-D3*, *IRBFE-N1* and *IRBFE-N2* elements, there is one unknown at a boundary node and one more extra equation needs be formed. This equation can be generated by integrating (2.8) over a half control

volume associated with that boundary node (Patankar 1980).

Collection of the discretised equations at the appropriate nodal points and the continuity equations at the interior grid points leads to a square system of algebraic equations that is sparse and banded. Two-point line elements are well suited to discretisation methods based on Cartesian grids.

## 2.4 Numerical results

IRBFEs are now validated through function approximation and solution of boundary-value problems governed by ODEs and PDEs. For all numerical examples presented in this study, the MQ width  $a$  is simply chosen proportionally to the element length  $h$  by a factor  $\beta$ . The value of  $\beta$  is considered in a wide range from 1 to 85 to study its influence on the accuracy. In the case of non-rectangular domains, there may be some nodes that are too close to the boundary. If an interior node falls within a distance of  $h/2$  to the boundary, such a node is removed from the set of nodal points.

The solution accuracy of an approximation scheme is measured by means of the discrete relative  $L_2$  errors for the field variable and its first-order partial

derivatives

$$N_e(\phi) = \frac{\sqrt{\sum_{i=1}^M (\phi_i^{(e)} - \phi_i)^2}}{\sqrt{\sum_{i=1}^M (\phi_i^{(e)})^2}}, \quad (2.30)$$

$$N_e\left(\frac{\partial\phi}{\partial x}\right) = \frac{\sqrt{\sum_{i=1}^M \left(\frac{\partial\phi_i^{(e)}}{\partial x} - \frac{\partial\phi_i}{\partial x}\right)^2}}{\sqrt{\sum_{i=1}^M \left(\frac{\partial\phi_i^{(e)}}{\partial x}\right)^2}}, \quad (2.31)$$

$$N_e\left(\frac{\partial\phi}{\partial y}\right) = \frac{\sqrt{\sum_{i=1}^M \left(\frac{\partial\phi_i^{(e)}}{\partial y} - \frac{\partial\phi_i}{\partial y}\right)^2}}{\sqrt{\sum_{i=1}^M \left(\frac{\partial\phi_i^{(e)}}{\partial y}\right)^2}}, \quad (2.32)$$

where the superscript ( $e$ ) refers to the exact solution and  $M$  is the length of a test set that is comprised of groups of 500 uniformly distributed points on grid lines. Another important measure is the convergence rate of the solution with respect to the refinement of spatial discretisation

$$N_e(h) \approx \gamma h^\alpha = O(h^\alpha), \quad (2.33)$$

in which  $\alpha$  and  $\gamma$  are exponential model's parameters. Given a set of observations, these parameters can be found by the general linear least squares technique. To assess the performance of the proposed technique, the standard CVM (Patankar 1980) is also implemented here.

### 2.4.1 Function approximation

The present 2-node IRBFE scheme is first applied to the representation of functions. Consider four different test functions, namely straight line  $y = x$ , quadratic curve  $y = x^2$ , cubic curve  $y = x^3$  and trigonometric function  $y = \sin(2\pi x)$ . The domain of interest is  $[0, 1]$  that is represented by one element

only. Values of  $y$  and  $dy/dx$  are given at  $x = 0$  and  $x = 1$ . Figure 2.4 shows the plots of the approximate and exact functions for the first three cases where good agreement is achieved with only one element. It should be pointed out that, for the second and third functions, curved lines are reproduced even only two nodes (i.e. only one element) are employed. The fourth function  $y = \sin(2\pi x)$  is infinitely smooth and it is clear that one can construct several other approximate functions that would satisfy the four given input data. The present scheme picks up one of them, probably the simplest one (Figure 2.5(a)). As more elements are used, a closer approximation to the exact function is obtained as shown in Figure 2.5(b). Numerical results for the last three functions show that the present two-node IRBFE has the ability to produce curved lines between its two extremes. This can be seen as a strength of IRBFEs over linear elements used in conventional techniques.

## 2.4.2 Solution of ODEs

### Problem 1

Consider a 1D problem governed by

$$\frac{d}{dx} \left( \frac{d\phi}{dx} \right) + \phi + x = 0, \quad 0 \leq x \leq 1, \quad (2.34)$$

and subject to two cases of boundary conditions

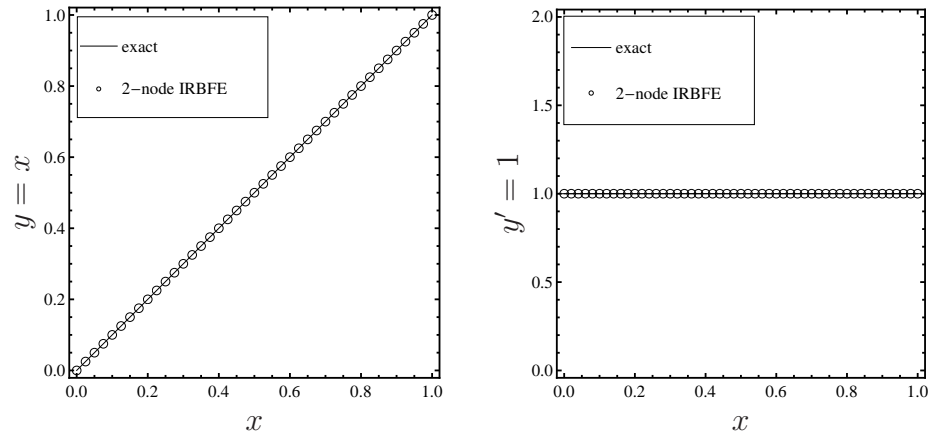
Case 1:  $\phi(0) = 0$  and  $\phi(1) = 0$  (Dirichlet boundary conditions only)

Case 2:  $\phi(0) = 0$  and  $d\phi(1)/dx = \cot(1) - 1$  (Dirichlet and Neumann boundary conditions).

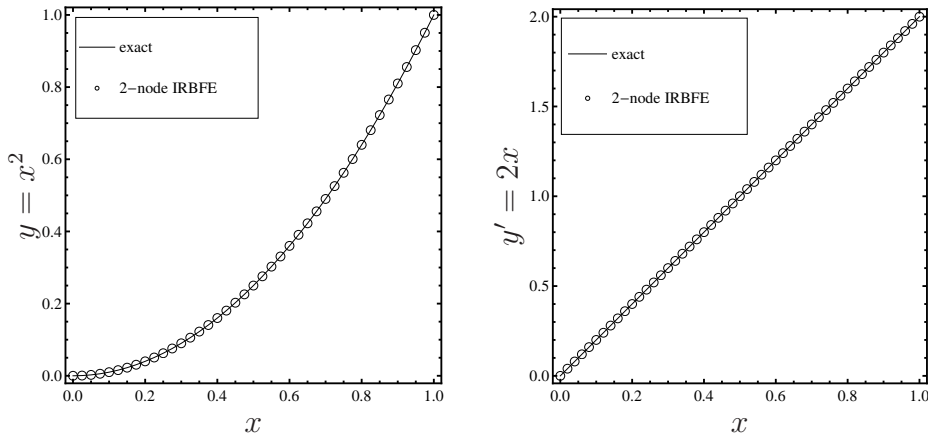
The exact solution of this problem can be verified to be

$$\phi^{(e)}(x) = \frac{\sin(x)}{\sin(1)} - x. \quad (2.35)$$

(a) Straight line &amp; first-order derivative



(b) Quadratic curve &amp; first-order derivative



(c) Cubic curve &amp; first-order derivative

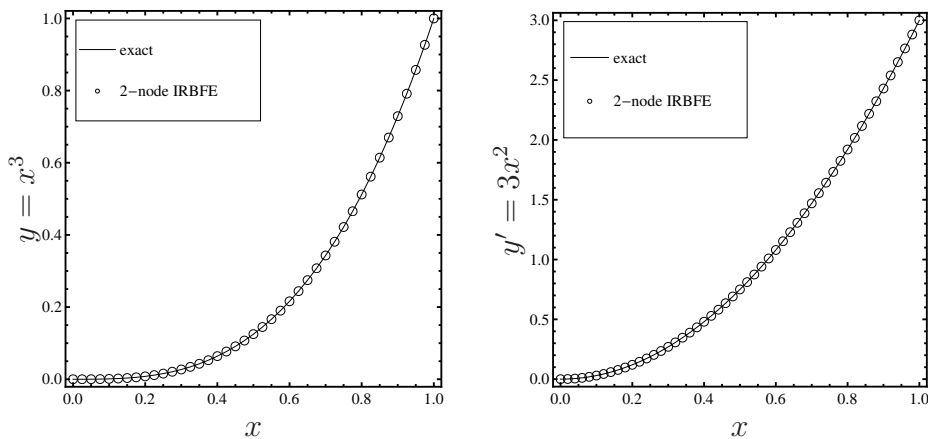
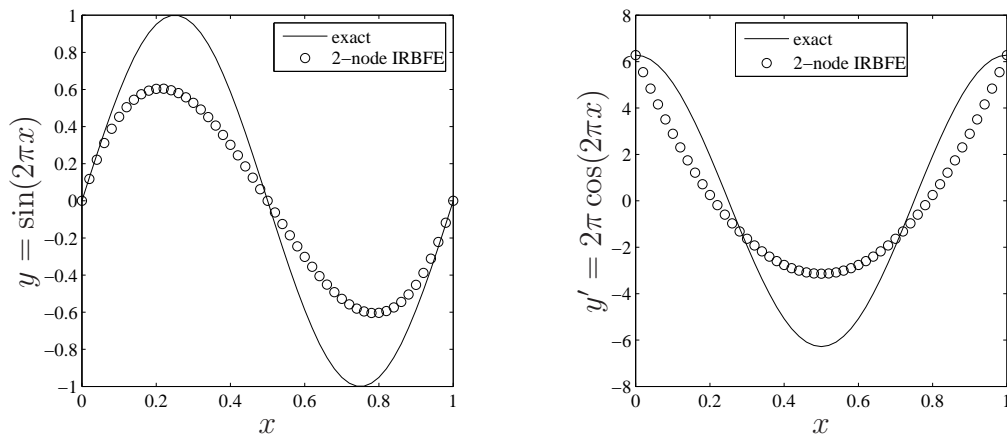


Figure 2.4: Function approximation: Approximation for functions (left) and their first-order derivative (right) by using one IRBFE only. It can be seen that the present two-node IRBFE is able to produce non-linear behaviours (i.e. curved lines) between the two extremes.

(a) 1 IRBFE



(b) 3 and 4 IRBFEs

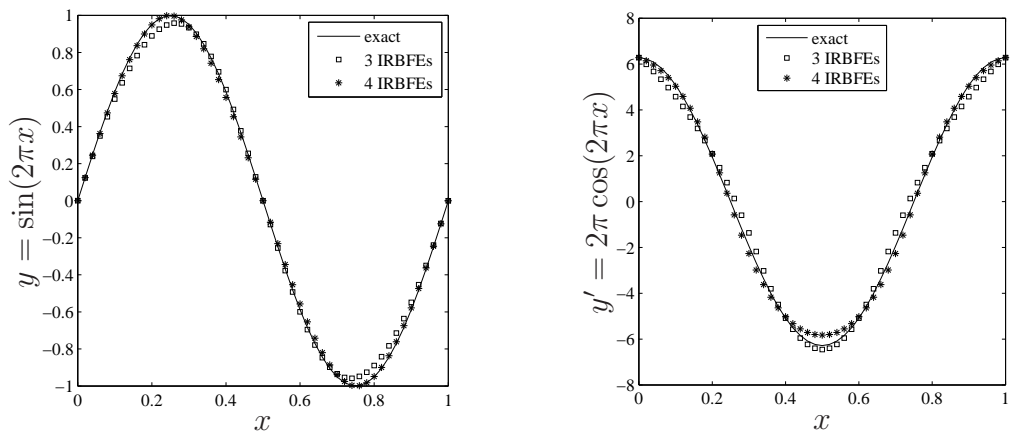


Figure 2.5: Function approximation (*continued*), trigonometric function: Approximations for the function (left) and its first-order derivative (right).

The problem domain is discretised by  $n$  uniformly-distributed points. Each node  $x_i$  is associated with a control volume denoted by  $\Omega_i$ . For  $2 \leq i \leq n-1$ ,  $\Omega_i$  is defined as  $[x_{i-1/2}, x_{i+1/2}]$  (full CV). For  $i=1$  and  $i=n$ ,  $\Omega_i$  is taken to be  $[x_1, x_{1+1/2}]$  and  $[x_{n-1/2}, x_n]$  (half CV), respectively. A schematic outline of a full CV and a half CV is presented in Figure 2.6. Generally speaking, to form a set of algebraic equations, (2.34) is integrated over full CVs at  $x_i$  with  $i = (2, 3, \dots, n-1)$  for Case 1, and over full CVs at  $x_i$  with  $i = (2, 3, \dots, n-1)$  and a half CV at  $x_n$  for Case 2. The resultant system is thus of dimensions  $(n-2) \times (n-2)$  for Case 1 and  $(n-1) \times (n-1)$  for Case 2. Hereafter,  $Di-Dj$  is used to denote the boundary treatment strategy in which the boundary region

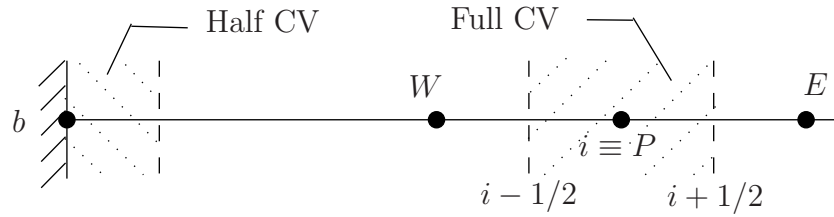


Figure 2.6: Control volumes associated with interior and boundary nodes in 1D.

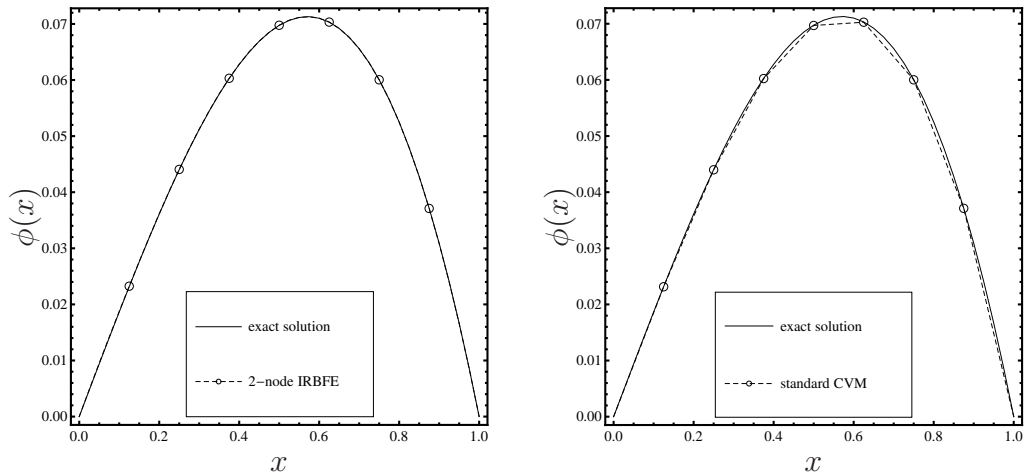
$[x_1, x_2]$  is represented by element  $IRBFE-Di$  and  $[x_{n-1}, x_n]$  by  $IRBFE-Dj$ , while  $Di-Nj$  represents the strategy in which  $[x_1, x_2]$  and  $[x_{n-1}, x_n]$  are modelled by elements  $IRBFE-Di$  and  $IRBFE-Nj$ , respectively. We employ the values of  $n$  ranging from 7 to 151 for  $h$ -adaptivity studies and the values of  $\beta$  from 1 to 85 for  $\beta$ -adaptivity studies.

**Case 1:** Figure 2.7 shows the plots of  $\phi$  and  $d\phi/dx$  by the proposed technique using the  $D1-D1$  strategy and by the standard CVM. It can be seen that the present solution is smooth for both  $\phi$  and  $d\phi/dx$  even with only a few interior nodes used. On the other hand, using linear interpolations, the standard CV solution for  $d\phi/dx$  has a stair-case shape. To alleviate this zigzag variation, much more grid points are needed. Grid convergence studies for the proposed method employed with various values of  $\beta$  and for the standard CVM are depicted in Figure 2.8. It can be seen that the former outperforms the latter. At dense grids, in terms of the error  $N_e$ , the results for  $d\phi/dx$  show a remarkable four orders of magnitude improvement (Figure 2.8(b)).

Figure 2.9 and Table 2.2 compare the performance of the proposed method among three types of semi-interior element strategies, namely  $D1-D1$ ,  $D2-D2$  and  $D3-D3$ . Results obtained by the standard CVM are also included and they are taken here as the reference. With more information incorporated into the IRBFE approximations, the  $D2-D2$  and  $D3-D3$  strategies yield much more accurate results than  $D1-D1$ , and  $D3-D3$  works better than  $D2-D2$  as shown in

Figure 2.9(a)-(b). Table 2.2 indicates that rates obtained by the three strategies are generally higher than those by the standard CVM. For example,  $D1-D1$  yields  $O(h^{2.99})$  for  $\phi$  and  $O(h^{2.61})$  for  $d\phi/dx$ , while the standard CVM gives  $O(h^{2.00})$  for  $\phi$  and  $O(h^{1.03})$  for  $d\phi/dx$ . An improvement in the approximation quality for  $d\phi/dx$  is thus much bigger than that for  $\phi$ . It should be noted that  $D1-D1$  exhibits higher rates of grid convergence but produces less accurate results than  $D2-D2$  and  $D3-D3$ .

(a) Field variable



(b) First-order derivative

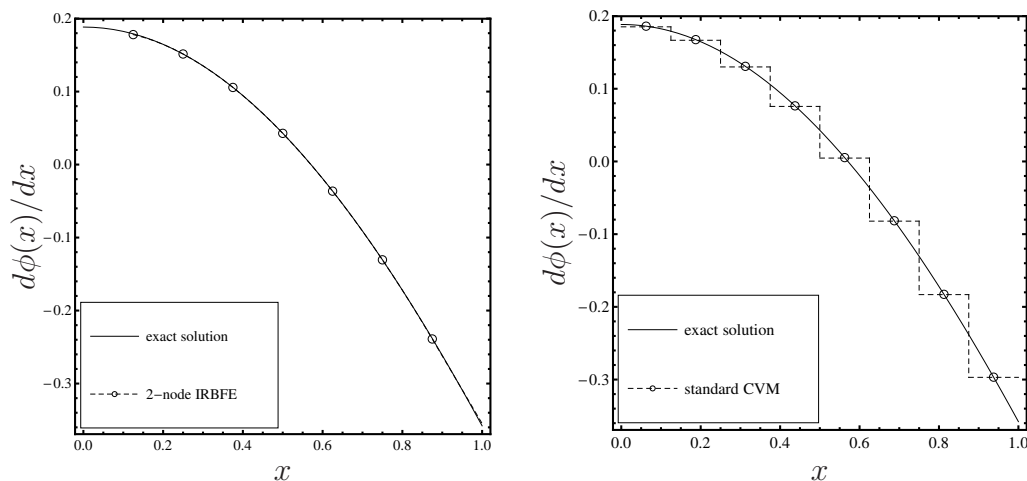


Figure 2.7: ODE, Problem 1, Dirichlet boundary conditions,  $n = 9$ : Comparison of the exact and approximate solutions for  $\phi$  and  $d\phi/dx$  by the present  $D1-D1$  strategy (left) and the standard CV method (right).

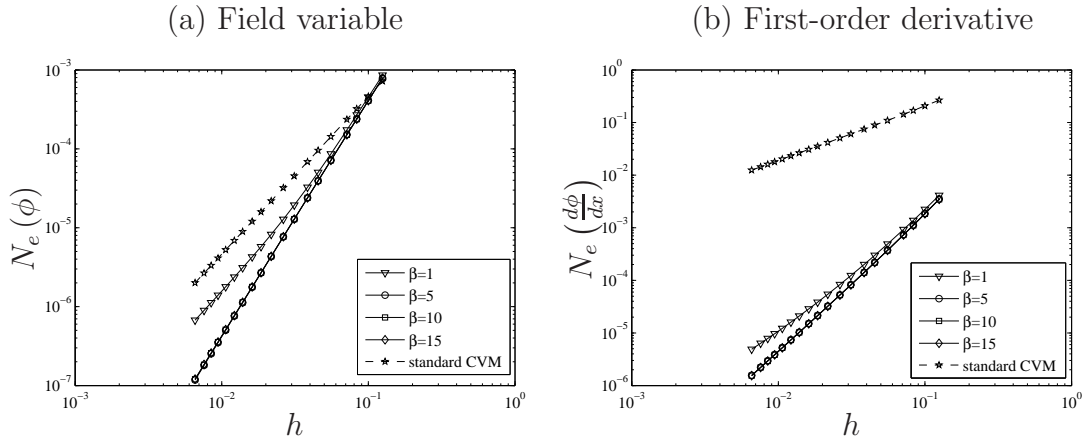


Figure 2.8: ODE, Problem 1, Dirichlet boundary conditions:  $h$ -adaptivity studies conducted with several values of  $\beta$  for the  $D1$ - $D1$  strategy. It is noted that results with  $\beta = (5, 10, 15)$  are undistinguishable.

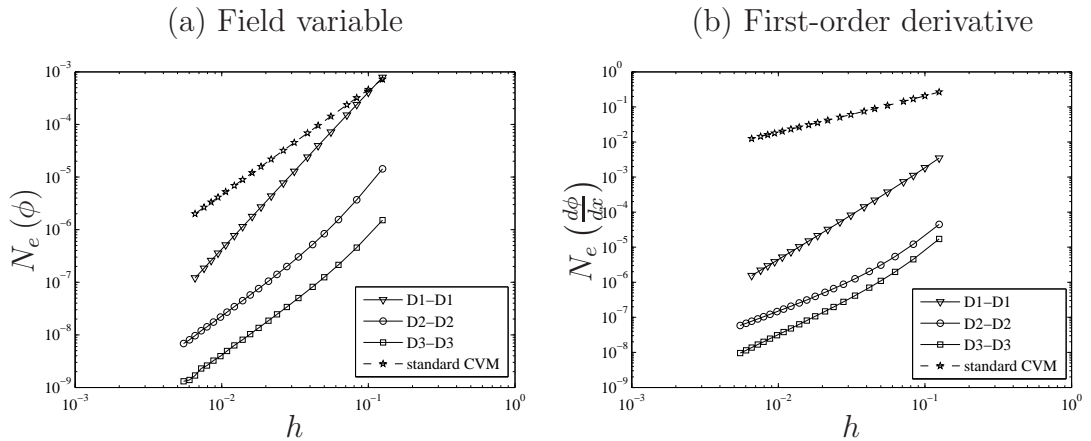


Figure 2.9: ODE, Problem 1, Dirichlet boundary conditions: Effects of types of semi-interior elements on the solution accuracy for  $\beta = 15$ .

In Figure 2.10, the effects of  $\beta$  on the solution accuracy for coarse ( $n = 9$ ) and dense ( $n = 153$ ) grids are studied. As  $\beta$  increases, the overall error of the IRBFE solution is first reduced and then becomes flat/fluctuated. There are dramatic reductions (i.e. exponential convergence) in  $N_e(\phi)$  and  $N_e(d\phi/dx)$  for the  $D2$ - $D2$  and  $D3$ - $D3$  strategies. In the case of large  $n$  and using  $D2$ - $D2$  and  $D3$ - $D3$ , it appears that there exists an optimal value for  $\beta$ , e.g.  $\beta = 42$  for  $D2$ - $D2$  and  $\beta = 32$  for  $D3$ - $D3$ . Nevertheless, the present method can work with a wide range of  $\beta$ . This ability is also clearly seen in Figure 2.8.

Table 2.2: ODE, Problem 1, Dirichlet boundary conditions: rates of convergence  $O(h^\alpha)$  for  $\phi$  and  $\partial\phi/\partial x$  for several large  $\beta$  values and semi-interior element types.

$\beta$	$\alpha$					
	$\phi$			$\partial\phi/\partial x$		
	<i>D1-D1</i>	<i>D2-D2</i>	<i>D3-D3</i>	<i>D1-D1</i>	<i>D2-D2</i>	<i>D3-D3</i>
5	2.995	2.057	2.009	2.604	1.719	2.096
10	2.987	2.188	2.086	2.606	1.842	2.180
15	2.985	2.332	2.185	2.606	1.983	2.283
20	2.984	2.475	2.332	2.606	2.119	2.391
Standard CVM		2.000			1.034	

Table 2.3: ODE, Problem 1, Dirichlet-Neumann boundary conditions: rates of convergence  $O(h^\alpha)$  for  $\phi$  and  $\partial\phi/\partial x$  for two semi-interior element types.

$\beta$	$\alpha$			
	$\phi$		$\partial\phi/\partial x$	
	<i>D1-N1</i>	<i>D1-N2</i>	<i>D1-N1</i>	<i>D1-N2</i>
1	1.722	1.722	2.183	2.183
15	3.016	3.016	2.529	2.529
Standard CVM		1.971		1.029

**Case 2:** Results obtained by the *D1-N1* and *D1-N2* strategies using  $\beta = 1$  and  $\beta = 15$  and by the standard CVM are depicted in Figure 2.11. The two strategies have similar performances which are far superior to that by the standard CVM. At dense grids, an improvement is up to one order of magnitude for  $\phi$  and four orders of magnitude for  $d\phi/dx$ . It is also observed that  $\beta$  can be used as an effective tool to enhance the solution accuracy. Table 2.3 shows that the present two schemes converge faster than the standard CVM. For example, the rates are  $O(h^{3.02})$  for  $\phi$  and  $O(h^{2.53})$  for  $d\phi/dx$  by the present two strategies ( $\beta = 15$ ), and  $O(h^{1.97})$  for  $\phi$  and  $O(h^{1.03})$  for  $d\phi/dx$  by the standard CVM.

Table 2.4: ODE, Problem 2, Dirichlet boundary conditions: rates of convergence  $O(h^\alpha)$  for  $\phi$  and  $\partial\phi/\partial x$  for several  $\beta$  values and semi-interior element types.

Boundary treatment	$\alpha$			
	$\phi$		$\partial\phi/\partial x$	
	$\beta = 1$	$\beta = 15$	$\beta = 1$	$\beta = 15$
<i>D1-D1</i>	2.540	2.582	2.554	2.670
<i>D2-D2</i>	2.679	3.965	2.713	3.932
<i>D3-D3</i>	2.971	4.229	2.588	3.801
Standard CVM	2.194		0.971	

Table 2.5: ODE, Problem 2, Dirichlet and Neumann boundary conditions, *D3-N2* treatment: rates of convergence  $O(h^\alpha)$  for  $\phi$  and  $\partial\phi/\partial x$  for several  $\beta$  values.

$\beta$	$\alpha$	
	$\phi$	$\partial\phi/\partial x$
1	3.240	2.706
15	4.380	3.919
Standard CVM	2.268	0.970

## Problem 2

In this example, the ODE involves more terms and its solution is highly oscillatory. The equation takes the form

$$\frac{d^2\phi}{dx^2} + \frac{d\phi}{dx} + \phi = -e^{-5x} (9979 \sin(100x) + 900 \cos(100x)), \quad 0 \leq x \leq 1. \quad (2.36)$$

We consider two cases of boundary conditions: Dirichlet-Dirichlet (Case 1) and Dirichlet-Neumann (Case 2). The plots of the exact solution  $\phi^{(e)} = \sin(100x)e^{-5x}$  and its first-order derivative are shown in Figure 2.12. Computations are conducted with the values of  $n$  varying from 23 to 403 and the values of  $\beta$  from 1 to 80. Results concerning  $h$  adaptivity and  $\beta$  adaptivity are presented in Figure 2.13, Figure 2.14 and Table 2.4 for Case 1, and in Figure 2.15 and Table 2.5 for Case 2. Remarks here are similar to those in Problem 1. It should be pointed

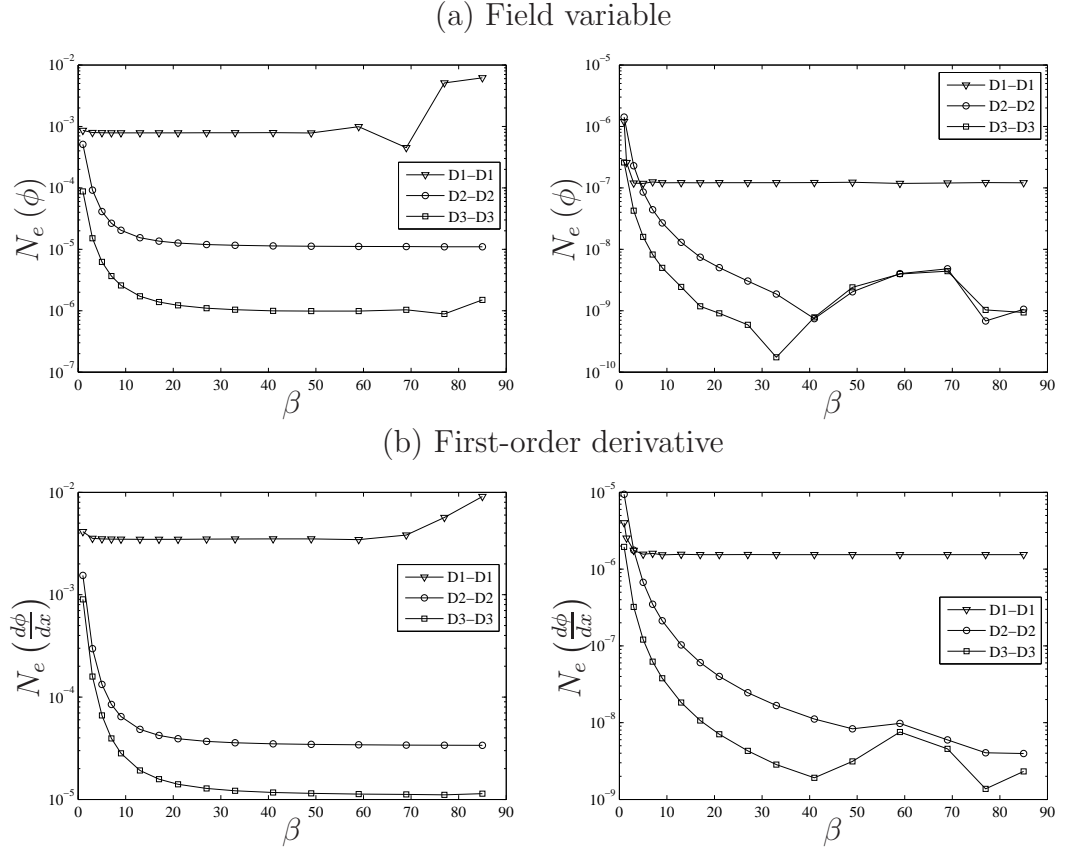


Figure 2.10: ODE, Problem 1, Dirichlet boundary conditions:  $\beta$ -adaptivity studies conducted with  $n = 9$  (left) and  $n = 153$  (right) for three boundary treatment strategies.

out that

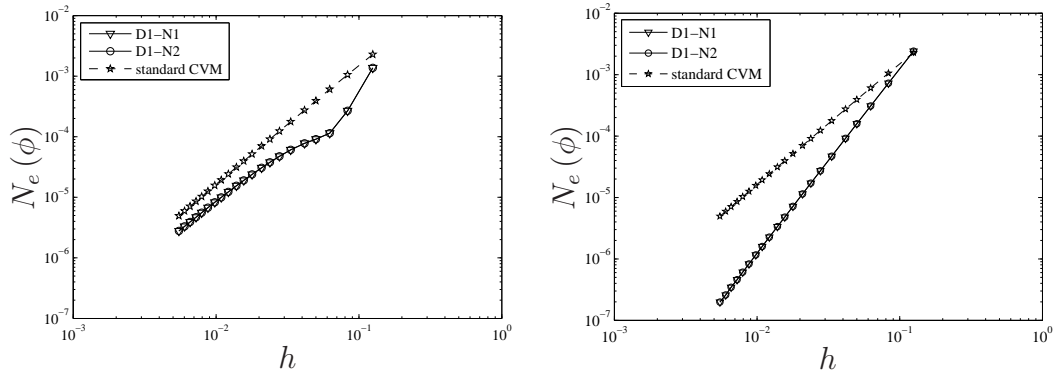
- (i) very high rates of grid convergence, i.e. up to  $O(h^{4.23})$  for  $\phi$  and  $O(h^{3.80})$  for  $d\phi/dx$  (Case 1), and  $O(h^{4.38})$  for  $\phi$  and  $O(h^{3.92})$  for  $d\phi/dx$  (Case 2), are achieved here,
- (ii) the IRBFE solution is very stable (i.e. no fluctuation) at large values of  $\beta$ ,
- (iii) given a grid size  $h$  and a value of  $\beta$ , the overall errors for Case 2 are as low as those for Case 1,

- (iv) the accuracy improvement is more significant for  $d\phi/dx$  than for  $\phi$ .

This problem (Case 1) was also solved in (Mai-Duy and Tran-Cong 2008) using the multidomain (MD) RBF collocation method. Two versions, namely differentiated-RBF (MD-DRBF) and integrated-RBF (MD-IRBF) schemes, were implemented. Using two non-overlapping subdomains,  $\beta = 1$  and 201 nodes per subdomain (i.e. 401 nodes for the whole domain), the obtained  $N_e$  errors for  $\phi$

were 0.2 for MD-DRBF and  $2.72 \times 10^{-4}$  for MD-IRBF. Using the same set of nodes (i.e. 401 points or 400 IRBFs),  $\beta = 15$  and  $D3-D3$ , the present method yields  $N_e = 1.28 \times 10^{-5}$ , which is much lower than those by the MD-RBF collocation method. It is noted that conventional/global RBF methods are able to work with low values of  $\beta$  such as  $\beta = 1$ .

(a) Field variable



(b) First-order derivative

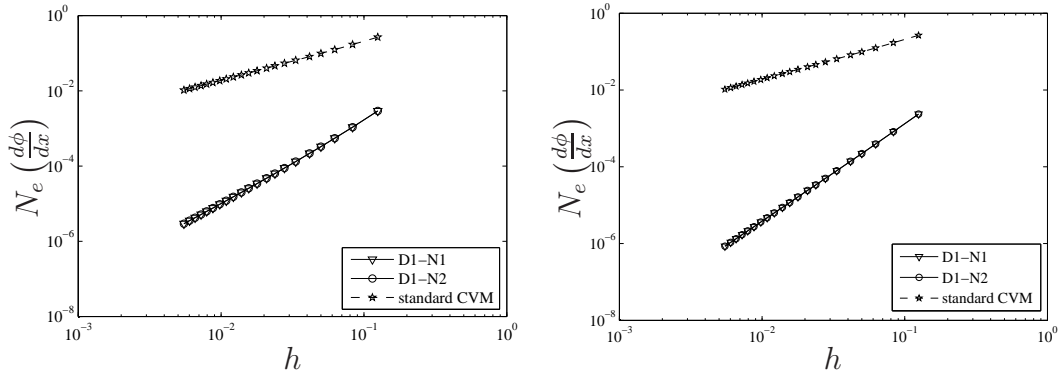


Figure 2.11: ODE, Problem 1, Dirichlet and Neumann boundary conditions: Effects of types of semi-interior elements on the solution accuracy for  $\beta = 1$  (left) and  $\beta = 15$  (right). It is noted that plots have the same scaling and results by the two boundary treatment strategies are undistinguishable.

### 2.4.3 Solution of PDEs

The proposed CV method is further validated through the solution of PDEs on both rectangular and non-rectangular domains. Elements *IRBFE-D1* and *IRBFE-D2* are employed to deal with Dirichlet boundary conditions, while

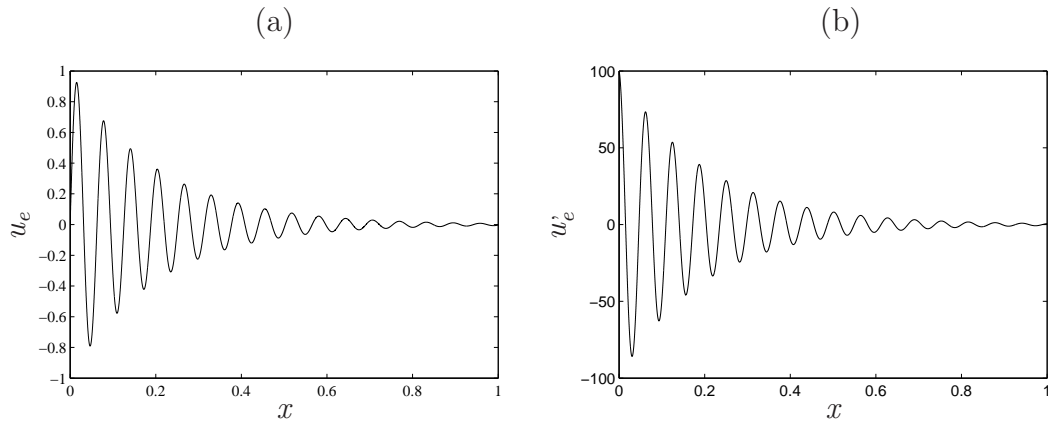


Figure 2.12: ODE, Problem 2: Exact solution (a) and its first-order derivative (b).

*IRBFE-N2* is used for Neumann boundary conditions. It is noted that *IRBFE-D1* can be applicable to problems with regular as well as irregular geometries. All IRBFE calculations here are carried out with two values of  $\beta$ , namely 1 and 15.

### Problem 1: rectangular domain

Consider the following Poisson equation

$$\frac{\partial^2 \phi}{\partial x^2} + \frac{\partial^2 \phi}{\partial y^2} = -2\pi^2 \cos(\pi x) \cos(\pi y), \quad (2.37)$$

on a square domain  $0 \leq x, y \leq 1$  with two different cases of boundary conditions

Case 1:

$$\begin{aligned} \phi &= \cos(\pi y) & \text{for } x = 0, 0 \leq y \leq 1 \\ \phi &= -\cos(\pi y) & \text{for } x = 1, 0 \leq y \leq 1 \\ \phi &= \cos(\pi x) & \text{for } y = 0, 0 \leq x \leq 1 \\ \phi &= -\cos(\pi x) & \text{for } y = 1, 0 \leq x \leq 1 \end{aligned}$$

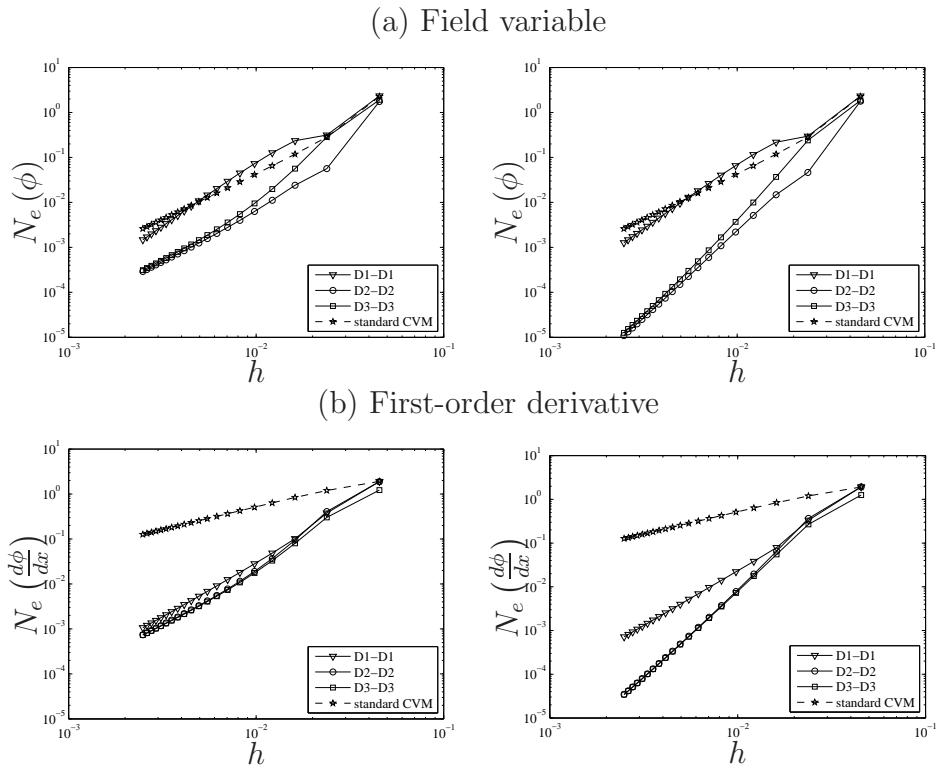


Figure 2.13: ODE, Problem 2, Dirichlet boundary conditions:  $h$ -adaptivity studies conducted with  $\beta = 1$  (left) and  $\beta = 15$  (right).

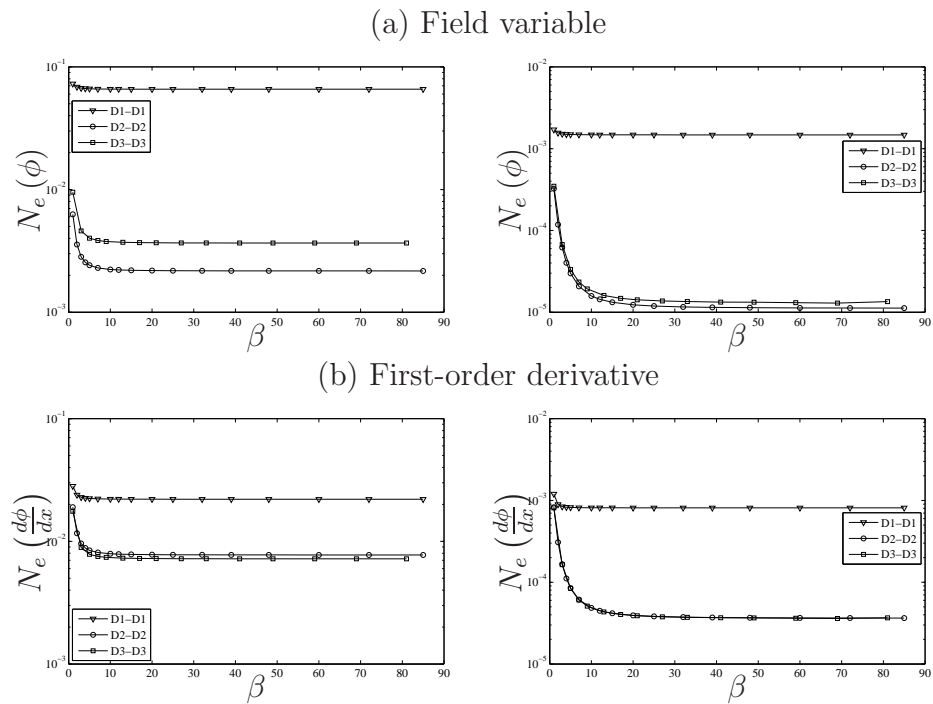
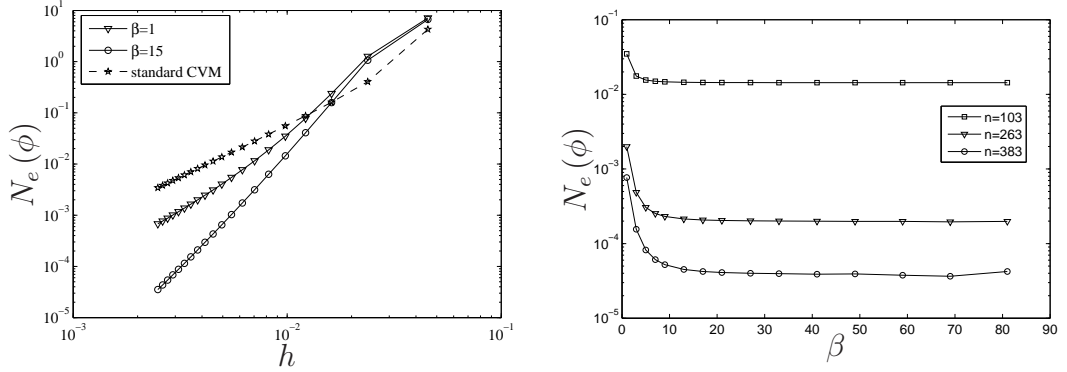


Figure 2.14: ODE, Problem 2:  $\beta$ -adaptivity studies conducted with  $n = 103$  (left) and  $n = 383$  (right) for three different semi-interior element strategies.

(a) Field variable



(b) First-order derivative

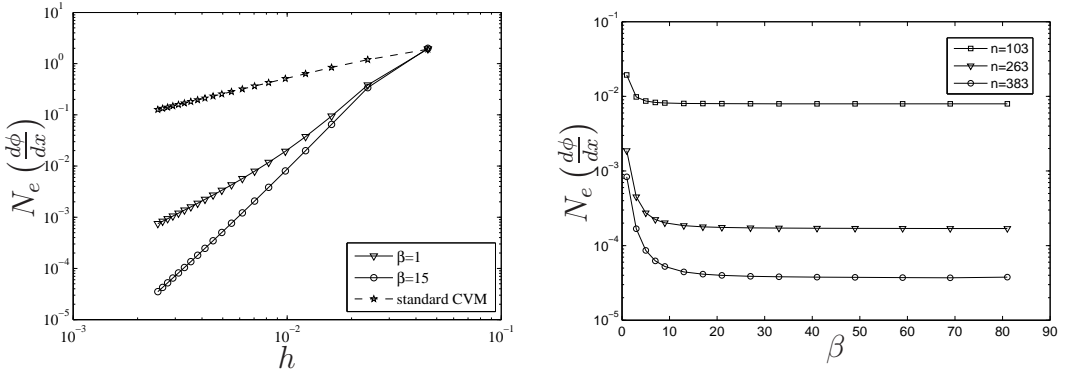


Figure 2.15: ODE, Problem 2, Dirichlet and Neumann boundary conditions:  $h$ -adaptivity (left) and  $\beta$ -adaptivity (right) studies for the  $D3-N2$  strategy.

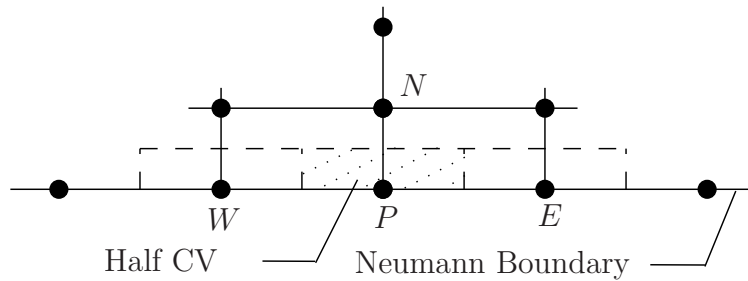
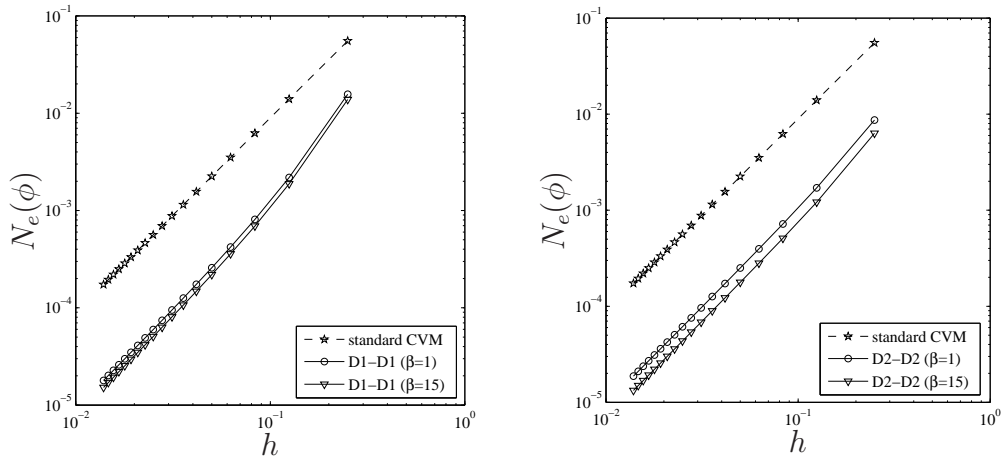
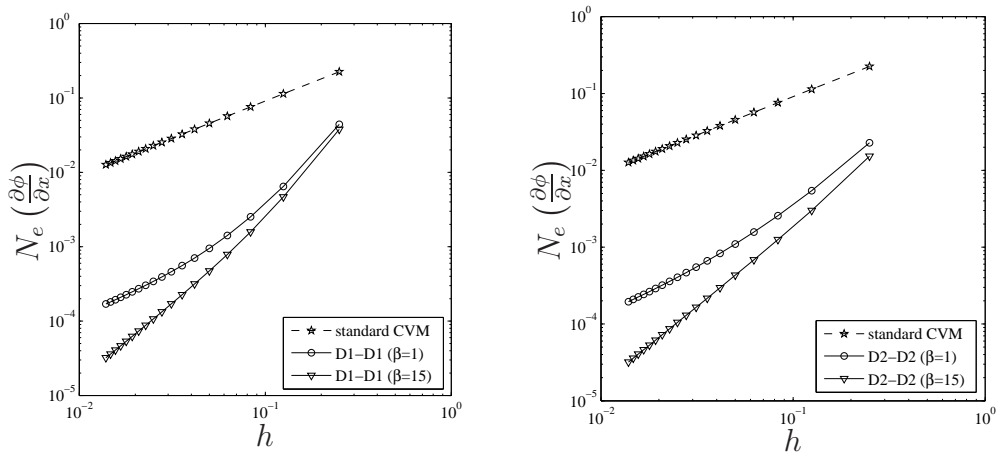


Figure 2.16: Half control volume associated with a boundary node in 2D.

(a) Field variable



(b) First-order derivative with respect to  $x$



(c) First-order derivative with respect to  $y$

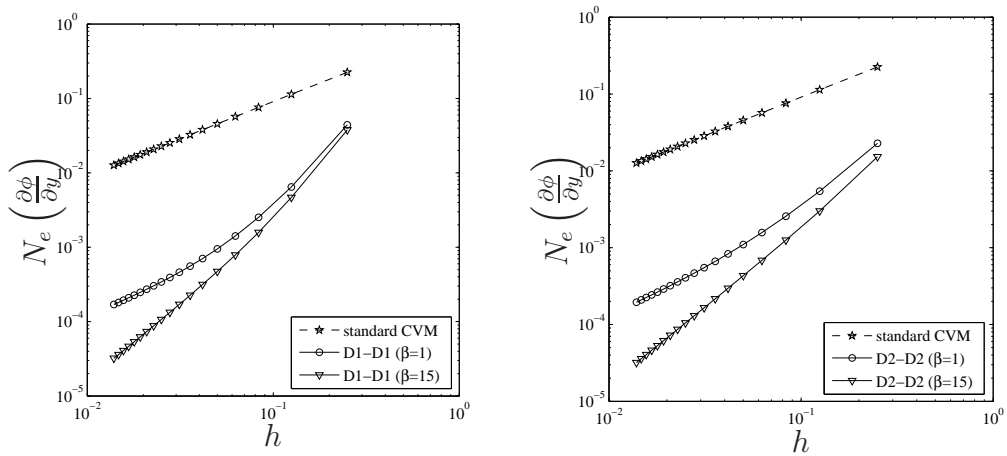


Figure 2.17: PDE, Problem 1, rectangular domain, Dirichlet boundary conditions:  $h$ -adaptivity studies for the  $D1-D1$  (left) and  $D2-D2$  (right) strategies.

(a) Field variable

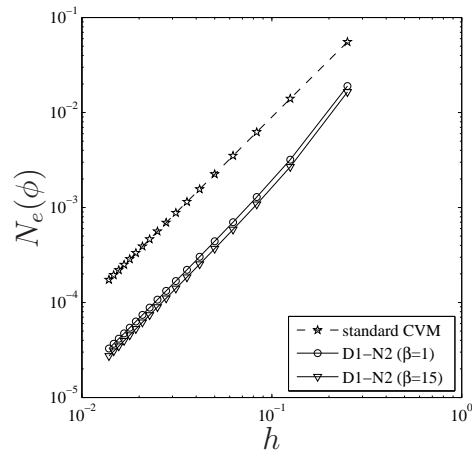
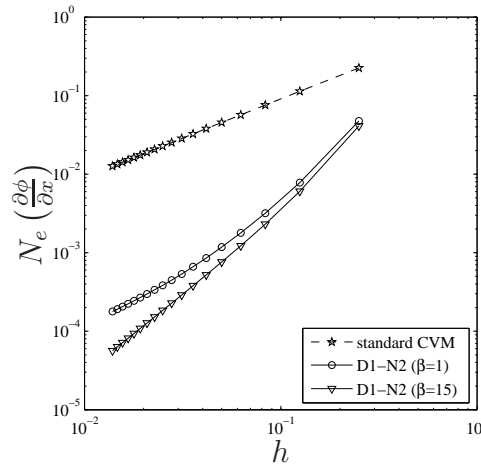
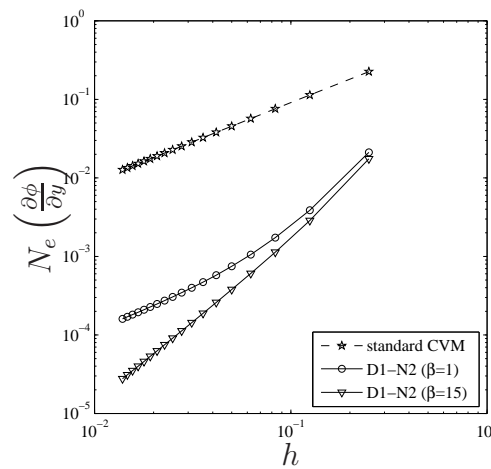
(b) First-order derivative with respect to  $x$ (c) First-order derivative with respect to  $y$ 

Figure 2.18: PDE, Problem 1, rectangular domain, Dirichlet and Neumann boundary conditions:  $h$ -adaptivity studies conducted with  $\beta = 1$  and  $\beta = 15$  for the  $D1-N2$  strategy.

Case 2:

$$\begin{aligned}
 \phi &= \cos(\pi y) && \text{for } x = 0, 0 \leq y \leq 1 \\
 \phi &= -\cos(\pi y) && \text{for } x = 1, 0 \leq y \leq 1 \\
 \frac{\partial \phi}{\partial y} &= 0 && \text{for } y = 0, 0 \leq x \leq 1 \\
 \frac{\partial \phi}{\partial y} &= 0 && \text{for } y = 1, 0 \leq x \leq 1.
 \end{aligned}$$

The exact solution to this problem can be verified to be

$$\phi^{(e)}(x, y) = \cos(\pi x) \cos(\pi y). \quad (2.38)$$

In Case 1 (i.e. Dirichlet boundary conditions only), the system of algebraic equations is generated by integrating (6.85) over full CVs associated with the interior nodes. In Case 2 (i.e. Dirichlet and Neumann boundary conditions), apart from the interior nodal variable values, there are additional unknown values of  $\phi$  at the boundary nodes on  $y = 0$  and  $y = 1$ . As a result, one needs to generate not only full-CV equations associated with the interior nodes but also half-CV equations associated with the boundary nodes on  $y = 0$  and  $y = 1$ . For the latter (Figure 2.16), the IRBFE approximations on  $y = 0$  and  $y = 1$  are constructed as in the case of a grid line and hence the approximate solution  $\phi$  is also  $C^2$ -continuous on these lines. It can be seen that the size of the discretised system in Case 2 is slightly larger than that in Case 1.

To study the convergent behaviour of the proposed technique, various grids, namely  $(5 \times 5, 9 \times 9, \dots, 73 \times 73)$ , are employed. Results concerning the relative  $L_2$  error and the rate of convergence with grid refinement by the present and standard CV methods are shown in Figure 2.17 for Case 1, Figure 2.18 for Case 2, and Table 2.6 for Case 1 and Case 2.

It can be seen from Figure 2.17 and Figure 2.18, the present  $D1-D1$ ,  $D2-D2$  and  $D1-N2$  strategies employed with a wide range of  $\beta$  produce much more

Table 2.6: PDE, Problem 1 and Problem 2: Rates of grid convergence  $O(h^\alpha)$  for the field variable and its first-order partial derivatives, (1): standard CVM.

	$\alpha$									
	Problem 1					Problem 2				
	(Rectangular domain)					(Circular domain)				
	Dirichlet				Dirichlet & Neumann			Dirichlet		
	<i>D1-D1</i>		<i>D2-D2</i>			<i>D1-N2</i>			<i>D1-D1</i>	
(1)	$\beta = 1$	$\beta = 15$	$\beta = 1$	$\beta = 15$	(1)	$\beta = 1$	$\beta = 15$	$\beta = 15$		
$\phi$	1.997	2.262	2.273	2.089	2.094	1.997	2.141	2.149	2.223	
$\partial\phi/\partial x$	0.997	1.787	2.350	1.583	2.101	0.997	1.833	2.200	2.140	
$\partial\phi/\partial y$	0.997	1.787	2.350	1.583	2.101	0.997	1.566	2.171	2.144	

accurate results especially for  $\partial\phi/\partial x$  and  $\partial\phi/\partial y$  than the standard CV method. For instance, at a grid of  $73 \times 73$  and  $\beta = 15$ , the improvement is about one order of magnitude for the field variable and about three orders of magnitude for its first-order partial derivatives. For Case 1 (Figure 2.17), results at coarse grids by the  $D2-D2$  strategy are a bit more accurate than those by  $D1-D1$ , probably owing to the fact that the former uses information about (6.85) on the boundary.

It can be seen from Table 2.6, the present method yields a faster convergence, especially for  $\partial\phi/\partial x$  and  $\partial\phi/\partial y$ , than the standard CV method for both Case 1 and Case 2. For example, in Case 1, the solutions  $\partial\phi/\partial x$  and  $\partial\phi/\partial y$  converge at the rate  $O(h^{2.35})$  using the  $D1-D1$  strategy,  $O(h^{2.10})$  using  $D2-D2$ , and  $O(h^{1.00})$  using the standard CV method.

Like in 1D problems, the use of  $\beta = 15$  (i.e. large values) here also leads to better accuracy and faster convergence especially for first-order partial derivatives than the use of  $\beta = 1$  (i.e. small values), and the IRBFE solutions for Case 1 and Case 2 have similar degrees of accuracy.

### Problem 2: circular domain

Find  $\phi$  such that

$$\frac{\partial^2 \phi}{\partial x^2} + \frac{\partial^2 \phi}{\partial y^2} = 0, \quad (2.39)$$

on a circular domain of radius  $\pi/2$  centred at  $(\pi/2, \pi/2)$  with Dirichlet boundary conditions. The exact solution to this problem is chosen to be

$$\phi^{(e)}(x, y) = \frac{1}{\sinh(\pi)} \sin(x) \sinh(y), \quad (2.40)$$

from which one can easily derive the boundary values of  $\phi$ .

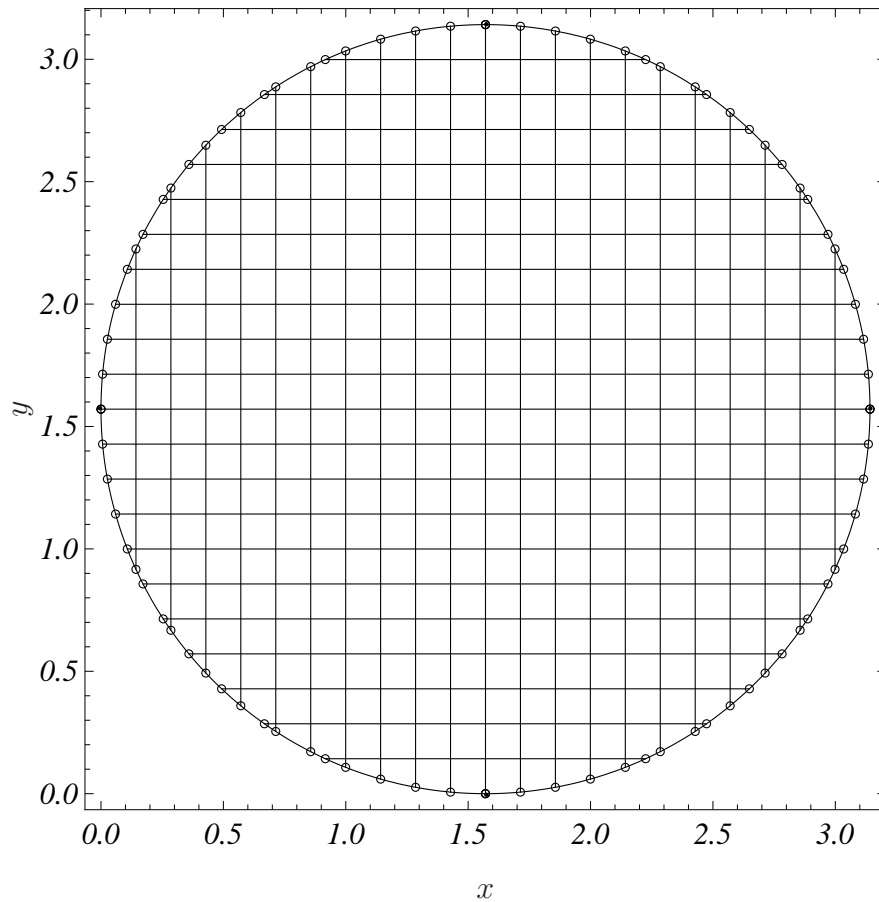


Figure 2.19: PDE, Problem 2: Geometry and discretisation. Boundary nodes denoted by  $\circ$  are generated by the intersection of the grid lines and the boundary.

The problem domain is discretised by a Cartesian grid as shown in Figure 2.19. Calculations are carried out with grids of  $(5 \times 5, 11 \times 11, \dots, 151 \times 151)$  and  $\beta = 15$ . We employ semi-interior elements *IRBFE-D1* for the handling of boundary conditions. Results obtained are presented in Figure 2.20, which plots the solution accuracy  $N_e$  against the grid size  $h$ . It can be seen that the error is consistently reduced as a grid is refined. Table 2.6 also compares the rate of convergence by the proposed technique between Problem 1 (rectangular domain) and Problem 2 (circular domain). Using the same *D1-D1* strategy and  $\beta = 15$ , the orders of accuracy of the solutions  $\phi$ ,  $\partial\phi/\partial x$  and  $\partial\phi/\partial y$  for the two types of domains are all greater than 2. It can be seen that the proposed technique is able to work well not only for rectangular domains but also for

non-rectangular domains.

## 2.5 Concluding remarks

In this chapter, a new Cartesian-grid-based control volume technique is proposed for the solution of second-order elliptic problems in one and two dimensions. Integrated RBFs are utilised to construct the approximations for the field variable and its derivatives, which are based on two-node elements and expressed in terms of nodal values of the field variable and its first-order partial derivatives. Various strategies for the imposition of boundary conditions are presented. The proposed control volume method leads to a system matrix that is sparse and produces a solution that is  $C^2$ -continuous on the grid lines. Its solution accuracy can be effectively controlled by means of the shape parameter ( $\beta$  up to 85) and/or grid size. A series of test problems including those defined on non-rectangular domains are employed to verify the present method. Numerical results show that the method is much more accurate and faster convergent, especially for the approximation of derivatives, than the standard control volume method.

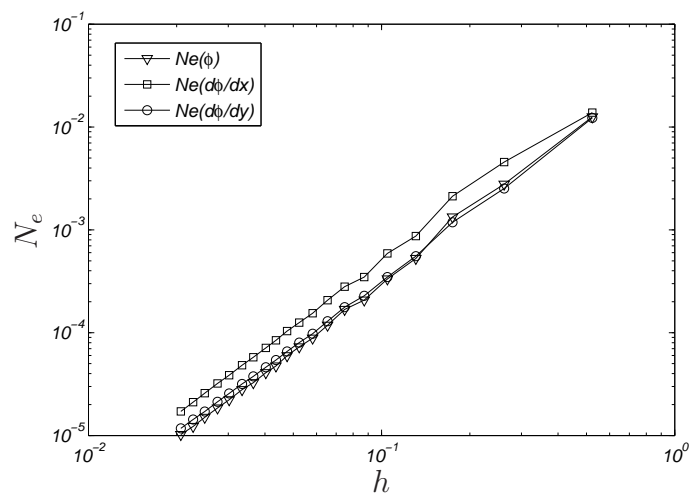


Figure 2.20: PDE, Problem 2, circular domain, Dirichlet boundary conditions: the solution accuracy using the  $D1$ - $D1$  strategy and  $\beta = 15$ .

# Chapter 3

## High-order upwind methods based on $C^2$ -continuous two-node IRBFEs for viscous flows

In this chapter, the proposed 2-node IRBFEs in Chapter 2 are further developed for the simulation of incompressible viscous flows in two dimensions. Emphasis is placed on (i) the incorporation of  $C^2$ -continuous 2-node IRBFEs into the subregion and point collocation frameworks for the discretisation of the streamfunction-vorticity formulation on Cartesian grids; and (ii) the development of high order upwind schemes based on 2-node IRBFEs for the case of convection-dominant flows. High levels of accuracy and efficiency of the present methods are demonstrated by solutions of several benchmark problems defined on rectangular and non-rectangular domains.

## 3.1 Introduction

Cartesian-grid-based subregion/point collocation methods can be very economical owing to the facts that (i) generating a grid and integrating the governing equations in these methods are low-cost; and (ii) FFT can be applied to accelerate computational processes (e.g. Huang and Greengard 2000). The approximations for the dependent variables and their spatial derivatives can be constructed globally on the whole grid or locally on small segments of the grid. Examples of local approximation schemes include standard control-volume (CV) methods and finite-difference methods. For the former, the fluxes are estimated by a linear variation between two grid points (e.g. Patankar 1980, Huilgol and Phan-Thien 1997). The use of two grid points allows for the consistency of the fluxes at CV faces - one of the four basic rules to guarantee a physically realistic solution (Patankar 1980). For the latter, local approximations can be constructed in each direction independently using two nodes (first-order accuracy) and three nodes (second-order accuracy). With two-node-based local approximations, Cartesian grid based methods typically produce solutions which are continuous for the fields but not for their partial derivatives, i.e.  $C^0$  continuity. The grid thus needs to be sufficiently fine to mitigate the effects of discontinuity of partial derivatives.

The Navier-Stokes (N-S) equations involve two main terms, namely convection and diffusion. At high values of the Reynolds number, the convection term is dominant and the numerical simulation of the N-S equations becomes challenging. Various treatments for the convection term have been proposed in the literature. Those which take the influence of the upstream information of the flow into account, e.g. the upwind differencing (Courant et al. 1952, Gentry et al. 1966), hybrid (Spalding 1972), power-law (Patankar 1981) and QUICK (Leonard 1979) schemes are known to provide a very stable solution. To maintain a high level of accuracy, an effective way is to employ high-order upwind schemes with the deferred-correction strategy (e.g. Khosla and Rubin 1974,

Ghia et al. 1982).

Radial basis functions (RBFs) have been successfully used for the approximation of scattered data. They have recently emerged as an attractive tool for the solution of ordinary and partial differential equations (ODEs and PDEs), e.g. Fasshauer (2007), Atluri and Shen (2002), Chen et al. (2008). RBF-based approximants are able to produce fast convergence especially for regular node arrangements such as those based on Cartesian grids. They can be constructed through a conventional differentiation process (e.g. Kansa 1990), or an integration process (e.g. Mai-Duy and Tran-Cong 2001, Mai-Duy and Tanner 2005, Mai-Duy and Tran-Cong 2005). The latter helps avoid the reduction of convergence rate caused by differentiation and provide effective ways of imposing the derivative boundary values. RBF-based approximants can be constructed globally or locally. Global RBF-based methods are very accurate (e.g. Cheng et al. 2003, Huang et al. 2007). However, they result in a system matrix that is dense and usually highly ill-conditioned. The use of RBF-approximants in local forms has the ability to circumvent these difficulties (e.g. Shu et al. 2003, Šarler and Vertnik 2006, Divo and Kassab 2007). Recently, a local high order approximant based on 2-node elements and integrated RBFs (IRBFs) for solving second-order elliptic problems in the CV framework has been proposed by An-Vo et al. (2011a). In such 2-node elements (IRBFEs), the integration constants are exploited to include the first derivatives at the element extremes in the approximations. It was shown that such elements lead to a  $C^2$ -continuous solution rather than the usual  $C^0$ -continuous solution.

In this study,  $C^2$ -continuous 2-node IRBFEs are incorporated into the sub-region and point collocation frameworks for solving the N-S equations in the streamfunction-vorticity formulation on Cartesian grids. Unlike conventional finite-element-based methods, the proposed methods can guarantee inter-element continuity of derivatives of the streamfunction and vorticity of orders up to 2. At high values of the Reynolds number, to achieve both good accuracy and stabil-

ity properties, several high-order upwind schemes are proposed. The resultant system of algebraic equations is sparse and banded; the solution accuracy can be controlled by means of the number of RBFs and/or the shape parameter. Several viscous flows defined on rectangular and non-rectangular domains are considered to verify the proposed methods.

The remainder of the chapter is organised as follows. Brief reviews of the governing equations and integrated RBF elements are given in Section 3.2 and 3.3, respectively. Section 3.4 describes the proposed  $C^2$ -continuous subregion/point collocation techniques for the streamfunction-vorticity formulation. In Section 3.5, two benchmark problems, namely the lid-driven cavity flow and the flow past a circular cylinder in a channel, are presented to demonstrate the attractiveness of the present techniques. Section 3.6 concludes the chapter.

## 3.2 Governing equations

The dimensionless N-S equations for steady incompressible planar viscous flows, subject to negligible body forces, can be expressed in terms of the streamfunction  $\psi$  and the vorticity  $\omega$  as follows

$$\frac{\partial^2 \psi}{\partial x^2} + \frac{\partial^2 \psi}{\partial y^2} + \omega = 0, \quad (3.1)$$

$$\frac{\partial^2 \omega}{\partial x^2} + \frac{\partial^2 \omega}{\partial y^2} = Re \left( \frac{\partial \psi}{\partial y} \frac{\partial \omega}{\partial x} - \frac{\partial \psi}{\partial x} \frac{\partial \omega}{\partial y} \right), \quad (x, y)^T \in \Omega, \quad (3.2)$$

where  $Re = UL/\nu$  is the Reynolds number, in which  $L$  is the characteristic length,  $U$  the characteristic speed of the flow and  $\nu$  the kinematic viscosity.

The vorticity and streamfunction variables are defined by

$$\omega = \frac{\partial v}{\partial x} - \frac{\partial u}{\partial y}, \quad (3.3)$$

$$\frac{\partial \psi}{\partial y} = u, \quad \frac{\partial \psi}{\partial x} = -v, \quad (3.4)$$

where  $u$  and  $v$  are the  $x$  and  $y$  components of the velocity vector. In this study, the method of modified dynamics or false transients (e.g. Mallinson and Davis 1973, Pozrikidis 1997) is applied to obtain the structure of a steady flow. The governing equations (3.1) and (3.2) are modified as

$$\frac{\partial^2 \psi}{\partial x^2} + \frac{\partial^2 \psi}{\partial y^2} + \omega = \frac{\partial \psi}{\partial t}, \quad (3.5)$$

$$\frac{\partial^2 \omega}{\partial x^2} + \frac{\partial^2 \omega}{\partial y^2} - Re \left( \frac{\partial \psi}{\partial y} \frac{\partial \omega}{\partial x} - \frac{\partial \psi}{\partial x} \frac{\partial \omega}{\partial y} \right) = \frac{\partial \omega}{\partial t}. \quad (3.6)$$

Solutions to (3.5) and (3.6), which are obtained from integrating the equations from a given initial condition up to the steady state, are also solutions to (3.1) and (3.2) respectively.

In the case of subregion collocation, one needs to define control volumes for grid nodes. Integrating (3.5) and (3.6) over a CV of a grid point  $P$ ,  $\Omega_P$ , leads to the following equations

$$\int_{\Omega_P} \left( \frac{\partial^2 \psi}{\partial x^2} + \frac{\partial^2 \psi}{\partial y^2} \right) d\Omega_P + \int_{\Omega_P} \omega d\Omega_P = \int_{\Omega_P} \frac{\partial \psi}{\partial t} d\Omega_P, \quad (3.7)$$

$$\int_{\Omega_P} \left( \frac{\partial^2 \omega}{\partial x^2} + \frac{\partial^2 \omega}{\partial y^2} \right) d\Omega_P - \int_{\Omega_P} Re \left( \frac{\partial \psi}{\partial y} \frac{\partial \omega}{\partial x} - \frac{\partial \psi}{\partial x} \frac{\partial \omega}{\partial y} \right) d\Omega_P = \int_{\Omega_P} \frac{\partial \omega}{\partial t} d\Omega_P, \quad (3.8)$$

which ensure that the flow field is conservative for a finite CV.

Applying the Green theorem to (3.7) and (3.8), one has

$$\oint_{\Gamma_P} \left( \frac{\partial \psi}{\partial x} dy - \frac{\partial \psi}{\partial y} dx \right) + \int_{\Omega_P} \omega d\Omega_P = \int_{\Omega_P} \frac{\partial \psi}{\partial t} d\Omega_P, \quad (3.9)$$

$$\oint_{\Gamma_P} \left[ \left( \frac{\partial \omega}{\partial x} - Re \omega \frac{\partial \psi}{\partial y} \right) dy - \left( \frac{\partial \omega}{\partial y} + Re \omega \frac{\partial \psi}{\partial x} \right) dx \right] = \int_{\Omega_P} \frac{\partial \omega}{\partial t} d\Omega_P, \quad (3.10)$$

where  $\Gamma_P$  is the CV boundary. The governing differential equations (3.5) and (3.6) are thus transformed into a CV form (3.7)-(3.8) or (3.9)-(3.10). It is noted

that no approximation is made at this stage.

### 3.3 Two-node IRBFEs

These elements are applicable to problems defined on rectangular and non-rectangular domains. The problem domain is simply discretised by using a Cartesian grid. In the case of non-rectangular domain, grid points outside the problem domain are removed while grid points inside the problem domain are taken to be interior nodes. Boundary nodes are defined as the intersection of the grid lines and the boundaries. Over straight-line segments between two adjacent nodal points, 1D-IRBFs are utilised to represent the variation of the field variable and its derivatives, which are called 2-node IRBFEs. It can be seen that there are two types of elements, namely interior and semi-interior elements. An interior element is formed using two adjacent interior nodes while a semi-interior element is generated by an interior node and a boundary node (Figure 2.1).

#### 3.3.1 Interior elements

Consider an interior element,  $\eta \in [\eta_1, \eta_2]$ , and its two nodes are locally named as 1 and 2. Let  $\phi(\eta)$  be a function and  $\phi_1, \partial\phi_1/\partial\eta, \phi_2$  and  $\partial\phi_2/\partial\eta$  be the values of  $\phi$  and  $\partial\phi/\partial\eta$  at the two nodes, respectively (Figure 2.2). Expressions (2.14), (2.15) and (2.16) can be rewritten in the form

$$\phi(\eta) = \varphi_1(\eta)\phi_1 + \varphi_2(\eta)\phi_2 + \varphi_3(\eta)\frac{\partial\phi_1}{\partial\eta} + \varphi_4(\eta)\frac{\partial\phi_2}{\partial\eta}, \quad (3.11)$$

$$\frac{\partial\phi}{\partial\eta}(\eta) = \frac{d\varphi_1(\eta)}{d\eta}\phi_1 + \frac{d\varphi_2(\eta)}{d\eta}\phi_2 + \frac{d\varphi_3(\eta)}{d\eta}\frac{\partial\phi_1}{\partial\eta} + \frac{d\varphi_4(\eta)}{d\eta}\frac{\partial\phi_2}{\partial\eta}, \quad (3.12)$$

$$\frac{\partial^2\phi}{\partial\eta^2}(\eta) = \frac{d^2\varphi_1(\eta)}{d\eta^2}\phi_1 + \frac{d^2\varphi_2(\eta)}{d\eta^2}\phi_2 + \frac{d^2\varphi_3(\eta)}{d\eta^2}\frac{\partial\phi_1}{\partial\eta} + \frac{d^2\varphi_4(\eta)}{d\eta^2}\frac{\partial\phi_2}{\partial\eta}, \quad (3.13)$$

where  $\{\varphi_i(\eta)\}_{i=1}^4$  is the set of basis functions in the physical space. These expressions allow one to compute the values of  $\phi$ ,  $\partial\phi/\partial\eta$ , and  $\partial^2\phi/\partial\eta^2$  at any point  $\eta$  in  $[\eta_1, \eta_2]$  in terms of four nodal unknowns, i.e. the values of the field variable and its first-order derivatives at the two extremes (also grid points) of the element.

### 3.3.2 Semi-interior elements

As mentioned earlier, a semi-interior element is defined by two nodes: an interior node and a boundary node. The subscripts 1 and 2 are now replaced with  $b$  ( $b$  represents a boundary node) and  $g$  ( $g$  an interior grid node), respectively. Assume that the value of  $\phi$  is given at  $\eta_b$ . The element *IRBFE-D1* is employed here. The conversion system (2.17) leads to

$$\phi(\eta) = \varphi_1(\eta)\phi_b + \varphi_2(\eta)\phi_g + \varphi_3(\eta)\frac{\partial\phi_g}{\partial\eta}, \quad (3.14)$$

$$\frac{\partial\phi}{\partial\eta}(\eta) = \frac{d\varphi_1(\eta)}{d\eta}\phi_b + \frac{d\varphi_2(\eta)}{d\eta}\phi_g + \frac{d\varphi_3(\eta)}{d\eta}\frac{\partial\phi_g}{\partial\eta}, \quad (3.15)$$

$$\frac{\partial^2\phi}{\partial\eta^2}(\eta) = \frac{d^2\varphi_1(\eta)}{d\eta^2}\phi_b + \frac{d^2\varphi_2(\eta)}{d\eta^2}\phi_g + \frac{d^2\varphi_3(\eta)}{d\eta^2}\frac{\partial\phi_g}{\partial\eta}. \quad (3.16)$$

For other types of semi-interior elements, the reader is referred to Chapter 2 for details.

## 3.4 Proposed $C^2$ -continuous subregion/point collocation methods

In this study, 2-node IRBFEs are extended to the solution of the streamfunction-vorticity formulation. In addition, several high-order upwind schemes are incorporated into the 2-node IRBFE methods to enhance their performance for the case of convection-dominant flows. The proposed methods lead to a sparse

system and their solution is a  $C^2$  function across IRBFEs.

### 3.4.1 Discretisation of governing equations

Two formulations, namely subregion collocation and point collocation, are employed to discretise the governing differential equations. As mentioned earlier, the structure of a steady flow is found through the method of false transients. Time derivative terms in (3.5) and (3.6) are simply approximated here with a first-order backward difference.

#### Subregion collocation

Consider a grid point  $P$  surrounded by a rectangular control volume  $\Omega_P$  (Figure 2.3). There are no gaps and overlapping regions between control volumes. For integrals involving the rate of change and generation, the value of the quantity at  $P$  is assumed to prevail over  $\Omega_P$ . Using the middle-point rule to evaluate the integrals of the convection and diffusion terms over  $\Omega_P$ , equations (3.9) and (3.10) become

$$-\frac{A_P}{\Delta t}\psi_P + \left[ \left( \frac{\partial \psi}{\partial x} \right)_e \Delta y - \left( \frac{\partial \psi}{\partial x} \right)_w \Delta y + \left( \frac{\partial \psi}{\partial y} \right)_n \Delta x - \left( \frac{\partial \psi}{\partial y} \right)_s \Delta x \right] = -A_P \left( \omega_P^0 + \frac{\psi_P^0}{\Delta t} \right), \quad (3.17)$$

$$-\frac{A_P}{\Delta t}\omega_P + \left[ \left( \frac{\partial \omega}{\partial x} \right)_e \Delta y - \left( \frac{\partial \omega}{\partial x} \right)_w \Delta y + \left( \frac{\partial \omega}{\partial y} \right)_n \Delta x - \left( \frac{\partial \omega}{\partial y} \right)_s \Delta x \right] + Re \left[ - \left( \omega \frac{\partial \psi}{\partial y} \right)_e \Delta y + \left( \omega \frac{\partial \psi}{\partial y} \right)_w \Delta y + \left( \omega \frac{\partial \psi}{\partial x} \right)_n \Delta x - \left( \omega \frac{\partial \psi}{\partial x} \right)_s \Delta x \right] = -\frac{A_P}{\Delta t}\omega_P^0, \quad (3.18)$$

where the superscript 0 represents the value obtained from the previous time level; the subscripts  $e, w, n$  and  $s$  denote the values of the property at the intersections of grid lines and the east, west, north and south faces of a CV; and  $A_P$  the volume of  $\Omega_P$ . It can be seen that equations (3.17) and (3.18) require the estimation of first derivative values of  $\psi$  and  $\omega$  at the interface points  $e, w, n$  and  $s$ .

### Point collocation

Consider a grid point  $P$ . Collocating (3.5) and (3.6) at  $P$ , one obtains

$$-\frac{\psi_P}{\Delta t} + \frac{\partial^2 \psi_P}{\partial x^2} + \frac{\partial^2 \psi_P}{\partial y^2} = -\left(\omega_P^0 + \frac{\psi_P^0}{\Delta t}\right), \quad (3.19)$$

$$-\frac{\omega_P}{\Delta t} + \frac{\partial^2 \omega_P}{\partial x^2} + \frac{\partial^2 \omega_P}{\partial y^2} - Re \left( \frac{\partial \psi_P}{\partial y} \frac{\partial \omega_P}{\partial x} - \frac{\partial \psi_P}{\partial x} \frac{\partial \omega_P}{\partial y} \right) = -\frac{\omega_P^0}{\Delta t}. \quad (3.20)$$

It can be seen that equations (3.19) and (3.20) require the estimation of both first and second derivative values of  $\psi$  and  $\omega$  at the collocation point  $P$ .

### 3.4.2 Approximations of diffusion term

The diffusion term is treated implicitly. Its role is important at regions where the strength of the convection term is small. 2-node IRBFs are employed here for the approximation of the second terms on the LHSs of (3.17) and (3.18) in the subregion collocation framework and (3.19) and (3.20) in the point collocation framework. Let  $E, W, N$  and  $S$  denote the east, west, north and south neighbouring nodes of  $P$ , respectively. One can form 4 two-node IRBFs, namely  $WP, PE, SP$  and  $PN$ .

### Subregion collocation

In the case that  $WP$  and  $PE$  are interior elements, the values of the flux at  $x = x_e$  and  $x = x_w$  are computed by using (3.12)

$$\left(\frac{\partial\phi}{\partial x}\right)_e = \frac{d\varphi_1(x_e)}{dx}\phi_P + \frac{d\varphi_2(x_e)}{dx}\phi_E + \frac{d\varphi_3(x_e)}{dx}\frac{\partial\phi_P}{\partial x} + \frac{d\varphi_4(x_e)}{dx}\frac{\partial\phi_E}{\partial x}, \quad (3.21)$$

$$\left(\frac{\partial\phi}{\partial x}\right)_w = \frac{d\varphi_1(x_w)}{dx}\phi_W + \frac{d\varphi_2(x_w)}{dx}\phi_P + \frac{d\varphi_3(x_w)}{dx}\frac{\partial\phi_W}{\partial x} + \frac{d\varphi_4(x_w)}{dx}\frac{\partial\phi_P}{\partial x}, \quad (3.22)$$

where  $\phi$  represents  $\psi$  and  $\omega$ .

In the case that  $WP$  is a semi-interior element, the value of the flux at  $x = x_w$  is computed by using (3.15)

$$\left(\frac{\partial\phi}{\partial x}\right)_w = \frac{d\varphi_1(x_w)}{dx}\phi_W + \frac{d\varphi_2(x_w)}{dx}\phi_P + \frac{d\varphi_3(x_w)}{dx}\frac{\partial\phi_P}{\partial x}. \quad (3.23)$$

Expressions for the flux at  $y = y_n$  and  $y = y_s$  are of similar forms.

### Point collocation

The values of  $\partial^2\psi/\partial x^2$  and  $\partial^2\omega/\partial x^2$  at  $P$  can be derived from 2-node IRBFEs in the  $x$  direction, i.e.  $WP$  and  $PE$ . It will be shown later that these two elements give the same results, and one can thus choose one of them for calculation, e.g.  $WP$ . Through (3.13) if  $WP$  is an interior element and (3.16) if  $WP$  is a semi-interior element, the required values are, respectively, estimated as

$$\frac{\partial^2\phi_P}{\partial x^2} = \frac{d^2\varphi_1(x_P)}{dx^2}\phi_W + \frac{d^2\varphi_2(x_P)}{dx^2}\phi_P + \frac{d^2\varphi_3(x_P)}{dx^2}\frac{\partial\phi_W}{\partial x} + \frac{d^2\varphi_4(x_P)}{dx^2}\frac{\partial\phi_P}{\partial x} \quad (3.24)$$

and

$$\frac{\partial^2 \phi_P}{\partial x^2} = \frac{d^2 \varphi_1(x_P)}{dx^2} \phi_W + \frac{d^2 \varphi_2(x_P)}{dx^2} \phi_P + \frac{d^2 \varphi_3(x_P)}{dx^2} \frac{\partial \phi_P}{\partial x}, \quad (3.25)$$

where  $\phi$  represents  $\psi$  and  $\omega$ .

The values of  $\partial^2 \psi / \partial y^2$  and  $\partial^2 \omega / \partial y^2$  at  $P$  can be computed in a similar fashion.

### 3.4.3 Approximations of convection term

At high values of the  $Re$  number, the third term (i.e. convection term) on the LHS of (3.18) or (3.20) is dominant and strongly affects the stability of a numerical solution. From a physical point of view, convection is directed by the velocity field from the upstream to the downstream of the flow. Three high-order upwind schemes, namely Scheme 1, Scheme 2 and Scheme 3, are proposed here for the discretisation of the convection term.

#### Scheme 1 for subregion collocation

This scheme is concerned with an upwind treatment with the deferred correction strategy. Let  $f$  be the intersection of the CV face and the grid line. The value of  $\omega$  at point  $f$  is computed as

$$\omega_f = \omega_U + \Delta\omega_f, \quad (3.26)$$

where  $\omega_U$  is the upstream value and  $\Delta\omega_f$  the correction term that is a known value. It is noted that  $f$  represents  $w, e, s$  and  $n$ .  $\Delta\omega_f$  is presently derived from the 2-node IRBFE approximation, i.e. (3.11) and (3.14). As an example, when

$f \equiv w$  and  $u_w > 0$ , one has

$$\omega_U = \omega_W, \quad (3.27)$$

$$\Delta\omega_f = (\varphi_1(x_w) - 1)\omega_W^0 + \varphi_2(x_w)\omega_P^0 + \varphi_3(x_w)\frac{\partial\omega_W^0}{\partial x} + \varphi_4(x_w)\frac{\partial\omega_P^0}{\partial x}, \quad (3.28)$$

where the superscript 0 is used to denote the values obtained from the previous time level. For a special case, where  $W$  is a boundary point, expression (3.28) reduces to

$$\Delta\omega_f = (\varphi_1(x_w) - 1)\omega_W^0 + \varphi_2(x_w)\omega_P^0 + \varphi_3(x_w)\frac{\partial\omega_P^0}{\partial x}. \quad (3.29)$$

When the solution reaches a steady state,  $\omega_f$ s are purely predicted by 2-node IRBFEs and their accuracy is thus recovered. Velocity values in the convection term are simply estimated by a linear profile

$$\left(\frac{\partial\psi}{\partial y}\right)_e = \frac{1}{2} \left(\frac{\partial\psi_P^0}{\partial y} + \frac{\partial\psi_E^0}{\partial y}\right), \quad (3.30)$$

$$\left(\frac{\partial\psi}{\partial y}\right)_w = \frac{1}{2} \left(\frac{\partial\psi_W^0}{\partial y} + \frac{\partial\psi_P^0}{\partial y}\right), \quad (3.31)$$

$$\left(\frac{\partial\psi}{\partial x}\right)_n = \frac{1}{2} \left(\frac{\partial\psi_P^0}{\partial x} + \frac{\partial\psi_N^0}{\partial x}\right), \quad (3.32)$$

$$\left(\frac{\partial\psi}{\partial x}\right)_s = \frac{1}{2} \left(\frac{\partial\psi_S^0}{\partial x} + \frac{\partial\psi_P^0}{\partial x}\right). \quad (3.33)$$

### Scheme 2 for point collocation

Without loss of generality, assuming that  $u_P > 0$ .  $W$  thus becomes an upstream node. A special approximation is constructed over  $WP$  for the purpose of computing  $\partial\omega_P/\partial x$ ; not only  $\omega_W$  and  $\partial\omega_W/\partial x$  but also  $\partial^2\omega_W/\partial x^2$  are employed

in the conversion process

$$\begin{pmatrix} \omega_P \\ \omega_W \\ \frac{\partial \omega_W}{\partial \eta} \\ \frac{\partial^2 \omega_W}{\partial \eta^2} \end{pmatrix} = \begin{pmatrix} I_1^{(0)}(x_P) & I_2^{(0)}(x_P) & x_P & 1 \\ I_1^{(0)}(x_W) & I_2^{(0)}(x_W) & x_W & 1 \\ I_1^{(1)}(x_W) & I_2^{(1)}(x_W) & 1 & 0 \\ I_1^{(2)}(x_W) & I_2^{(2)}(x_W) & 0 & 0 \end{pmatrix} \begin{pmatrix} w_1 \\ w_2 \\ C_1 \\ C_2 \end{pmatrix}. \quad (3.34)$$

This leads to

$$\frac{\partial \omega_P}{\partial x} = \frac{d\varphi_1(x_P)}{dx} \omega_P + \frac{d\varphi_2(x_P)}{dx} \omega_W + \frac{d\varphi_3(x_P)}{dx} \frac{\partial \omega_W}{\partial x} + \frac{d\varphi_4(x_P)}{dx} \frac{\partial^2 \omega_W}{\partial x^2}. \quad (3.35)$$

### Scheme 3 for point collocation

Assuming that  $u_P > 0$ .  $W$  becomes an upstream point. The value of  $\partial \omega / \partial x$  at  $P$  is estimated over  $WP$  with the deferred correction strategy

$$\frac{\partial \omega_P}{\partial x} = \left( \frac{\omega_P - \omega_W}{h} \right) + \Delta \left( \frac{\partial \omega_P}{\partial x} \right), \quad (3.36)$$

where  $h$  is the length of  $WP$ , the first term on the RHS is simply a standard linear estimation; and the second term is a correction amount defined as

$$\Delta \left( \frac{\partial \omega_P}{\partial x} \right) = - \left( \frac{\omega_P^0 - \omega_W^0}{h} \right) + \left( \frac{\partial \omega_P}{\partial x} \right)^0, \quad (3.37)$$

The value  $(\partial \omega_P / \partial x)^0$  in (3.37) is obtained using (3.12) if  $WP$  is an interior element and using (3.15) if  $WP$  is a semi-interior element. When the flow is steady, the first term on the RHS of (3.36) and the first term on the RHS of (3.37) will cancel out each other.

### 3.4.4 $C^2$ continuity solution

It can be seen from IRBFE expressions for computing the flux ( $\partial\phi/\partial x$  or  $\partial\phi/\partial y$ ) at the CV faces (e.g. (3.21), (3.22)) and  $\partial^2\phi/\partial x^2$  and  $\partial^2\phi/\partial y^2$  at a nodal point  $P$ , e.g. (3.24), there are three unknowns, namely  $\phi$ ,  $\partial\phi/\partial x$  and  $\partial\phi/\partial y$ , at a nodal point  $P$ . It is noted that  $\phi$  represents  $\psi$  and  $\omega$ . Unlike conventional subregion/point collocation methods, the nodal values of  $\partial\phi/\partial x$  and  $\partial\phi/\partial y$  at  $P$  here constitute part of the nodal unknown vector. One thus needs to generate three independent equations. The first equation is obtained by conducting subregion/point collocation at  $P$ , i.e. (3.17)-(3.18) or (3.19)-(3.20), respectively. The other two equations can be formed by enforcing the local continuity of  $\partial^2\phi/\partial x^2$  and  $\partial^2\phi/\partial y^2$  across the elements at  $P$  similar to (2.26)-(2.27) or (2.28)-(2.29).

Collection of the governing equations and the continuity equations at the interior grid points leads to a square system of algebraic equations. Since local approximations are presently based on two RBFs only, the resultant system matrix is sparse and a wide range of  $\beta$  can be used. One can thus control the solution accuracy by means of the number of RBFs and/or the shape parameter. It can be seen that two-point line elements are well suited to discretisation methods based on Cartesian grids.

## 3.5 Numerical examples

The performance of the proposed  $C^2$  discretisation methods with three upwind schemes, i.e. Scheme 1, Scheme 2 and Scheme 3, is studied through the simulation of lid-driven cavity flows and flows past a circular cylinder in a channel. The subregion collocation version is from now on denoted by IRBFE-CVM while IRBFE-CM is used to represent the point collocation version. For all numerical examples presented in this study, the MQ shape parameter  $a$  is simply chosen

proportionally to the element length  $h$  by a factor  $\beta$ . The effects of the shape parameter on the solution accuracy is thus investigated through the parameter  $\beta$ . In the case of non-rectangular domains, there may be some nodes that are too close to the boundary. If an interior node falls within a distance of  $h/2$  to the boundary, such a node is removed from the set of nodal points. A steady solution is obtained with a time marching approach starting from a computed solution at a lower Reynolds number. For the special case of Stokes equation, the starting condition is the rest state.

The solution procedure involves the following steps

- (1) Guess the initial distributions of the streamfunction and vorticity in the case of Stokes flow. Otherwise, take the solution of a lower Reynolds number as an initial guess.
- (2) Solve the streamfunction equation (3.17)/(3.19) subject to Dirichlet boundary conditions, and calculate the nonlinear terms in the vorticity equation (3.18)/(3.20) by the upwind schemes.
- (3) Estimate Dirichlet boundary conditions for the vorticity equation (3.18)/(3.20) from the Neumann boundary conditions of the streamfunction.
- (4) Solve the vorticity equation (3.18)/(3.20).
- (5) Check to see whether the solution has reached a steady state through a condition on convergence measure

$$CM(\psi) = \frac{\sqrt{\sum_{i=1}^N (\psi_i - \psi_i^0)^2}}{\sqrt{\sum_{i=1}^N \psi_i^2}} < 10^{-9}, \quad (3.38)$$

where  $N$  is the total number of grid nodes.

- (6) If  $CM$  is not satisfactorily small, advance pseudo-time and repeat from step (2). Otherwise, stop the computation and output the results.

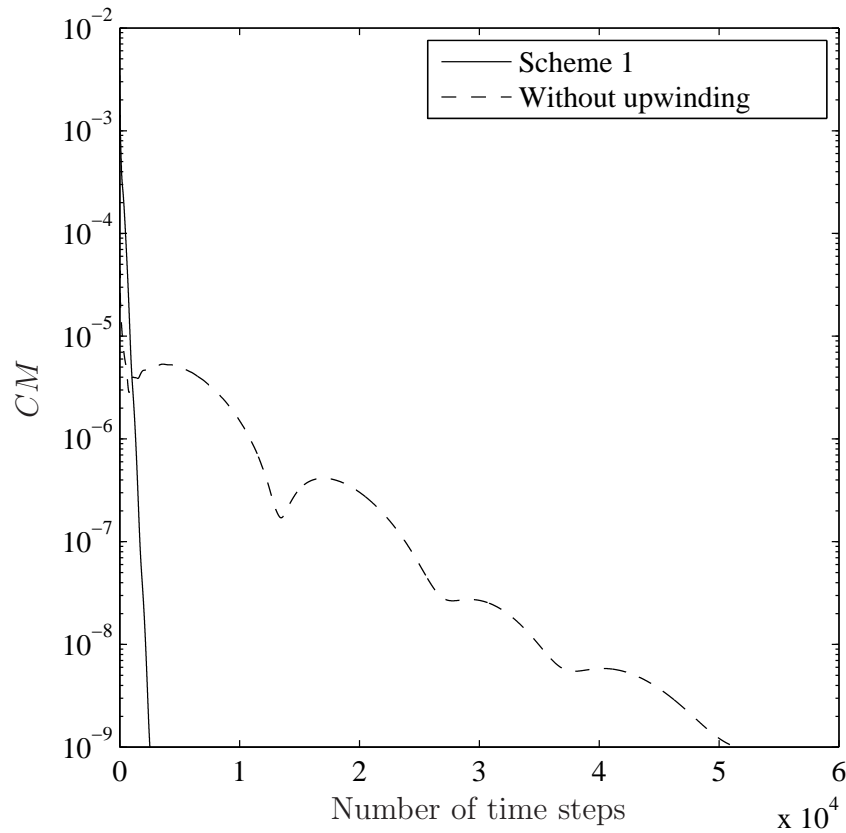


Figure 3.1: Lid-driven cavity flow, IRBFE-CVM,  $Re = 1000$ , grid =  $81 \times 81$ , solution at  $Re = 400$  used as initial guess: convergence behaviour. Scheme 1 using a time step of  $3 \times 10^{-4}$  converges remarkably faster than the no-upwind version using a time step of  $7 \times 10^{-6}$ . It is noted that the latter diverges for time steps greater than  $7 \times 10^{-6}$ .  $CM$  denotes the convergence measure as defined by (3.38).

### 3.5.1 Lid-driven cavity flow

Lid-driven cavity flow is a very useful benchmark problem for the validation of new numerical methods in CFD because of its simple geometry and rich flow physics at different Reynolds numbers. The cavity is taken to be a unit square, with the lid sliding from left to right at a unit velocity. The boundary conditions for  $u$  and  $v$  become

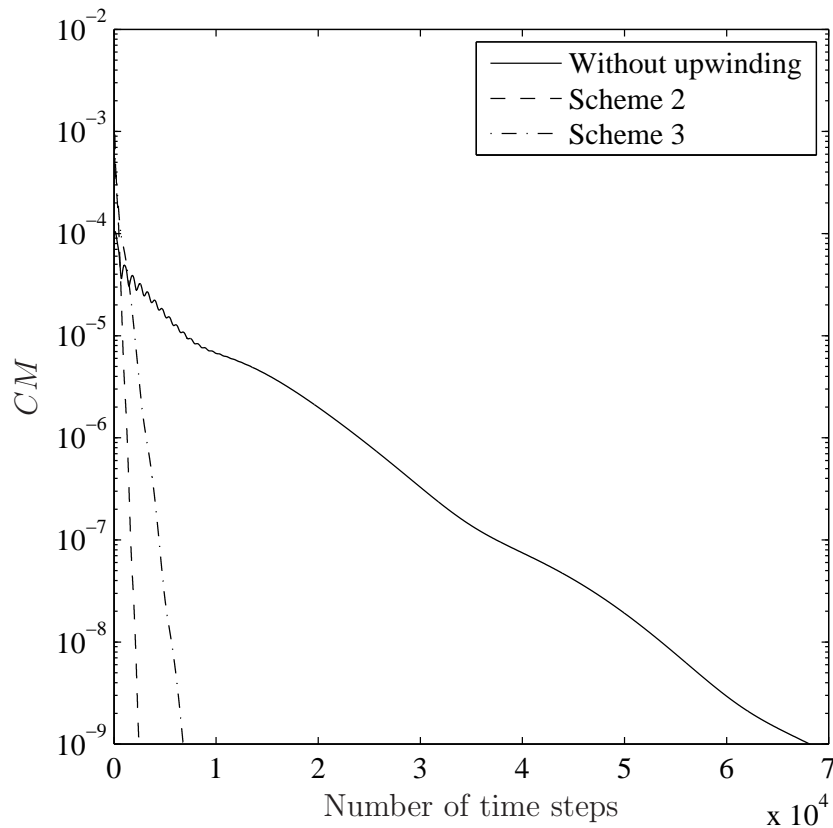


Figure 3.2: Lid-driven cavity flow, IRBFE-CM,  $Re = 1000$ , grid =  $81 \times 81$ , solution at  $Re = 400$  used as initial guess: convergence behaviour. Scheme 2 and Scheme 3, using a time step of  $3 \times 10^{-4}$  and  $10^{-4}$ , respectively, converge remarkably faster than the no-upwind version using a time step of  $8 \times 10^{-6}$ . It is noted that the latter diverges for time steps greater than  $8 \times 10^{-6}$ .  $CM$  denotes the convergence measure as defined by (3.38).

$$\begin{aligned}
 \psi = 0, \quad \partial\psi/\partial x = 0, \quad x = 0, \quad x = 1, \\
 \psi = 0, \quad \partial\psi/\partial y = 0, \quad y = 0, \\
 \psi = 0, \quad \partial\psi/\partial y = 1, \quad y = 1.
 \end{aligned}$$

Both IRBFE-CVM and IRBFE-CM are considered here. We take Dirichlet boundary conditions,  $\psi = 0$ , on all walls for solving (3.17) and (3.19). The Neumann boundary conditions,  $\partial\psi/\partial n$  (i.e.  $\partial\psi/\partial n = \nabla\psi \cdot \hat{n}$ , where  $\hat{n}$  is the outward unit normal vector at a point on the boundary), are used to derive computational boundary conditions for  $\omega$  in solving (3.18) and (3.20). Making

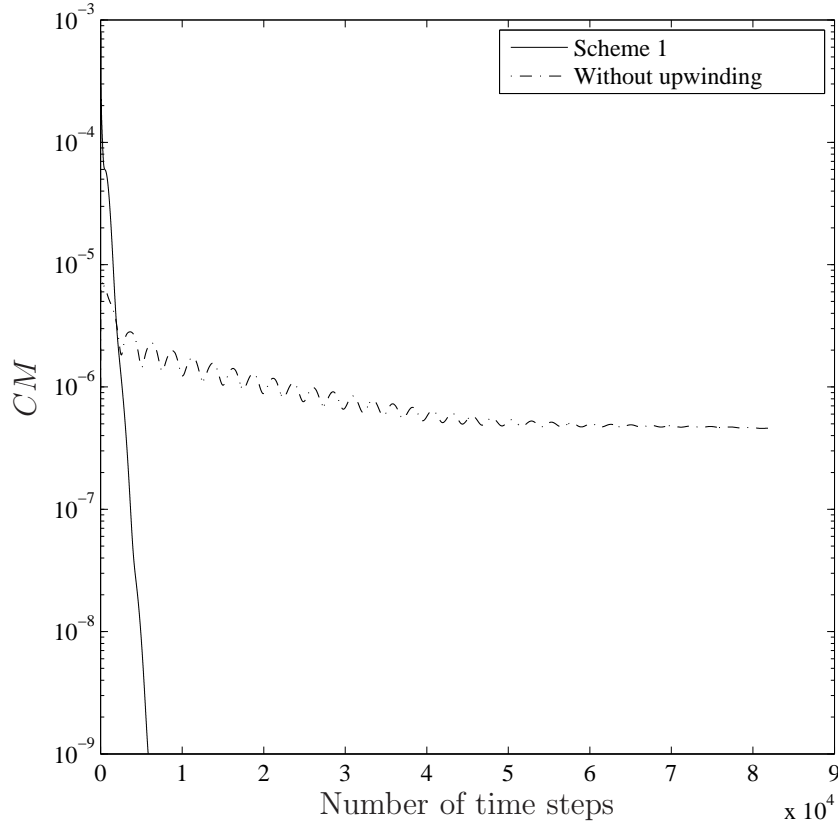


Figure 3.3: Lid-driven cavity flow, IRBFE-CVM,  $Re = 3200$ , grid =  $91 \times 91$ , solution at  $Re = 2000$  used as initial guess: convergence behaviour. Scheme 1 using a time step of  $10^{-4}$  converges remarkably faster than the no-upwind version using a time step of  $8 \times 10^{-7}$ . It is noted that the latter diverges for time steps greater than  $8 \times 10^{-7}$ .  $CM$  denotes the convergence measure as defined by (3.38).

use of (3.1), the values of  $\omega$  on the boundaries are computed by

$$\omega_b = -\frac{\partial^2 \psi_b}{\partial x^2}, \quad x = 0 \text{ and } x = 1, \quad (3.39)$$

$$\omega_b = -\frac{\partial^2 \psi_b}{\partial y^2}, \quad y = 0 \text{ and } y = 1. \quad (3.40)$$

In computing (3.39) and (3.40), one needs to incorporate  $\partial \psi_b / \partial x$  into  $\partial^2 \psi_b / \partial x^2$ , and  $\partial \psi_b / \partial y$  into  $\partial^2 \psi_b / \partial y^2$ , respectively. We present a simple technique to derive boundary values for  $\omega$  in the context of 2-node IRBFs. Assuming that node 1 and 2 of an IRBFE are a boundary node and an interior grid node respectively

(i.e.  $1 \equiv b$  and  $2 \equiv g$ ). Boundary values of the vorticity are obtained by applying (3.13) as

$$\omega_b = -\frac{\partial^2 \psi_b}{\partial \eta^2} = -\left( \frac{d^2 \varphi_1(\eta_b)}{d\eta^2} \psi_b + \frac{d^2 \varphi_2(\eta_b)}{d\eta^2} \psi_g + \frac{d^2 \varphi_3(\eta_b)}{d\eta^2} \frac{\partial \psi_b}{\partial \eta} + \frac{d^2 \varphi_4(\eta_b)}{d\eta^2} \frac{\partial \psi_g}{\partial \eta} \right), \quad (3.41)$$

where  $\eta$  represents  $x$  and  $y$ ;  $\psi_b$  and  $\partial \psi_b / \partial \eta$  are the Dirichlet and Neumann boundary conditions for  $\psi$ , and  $\psi_g$  and  $\partial \psi_g / \partial \eta$  are known values taken from the solution of the streamfunction equation (3.17)/(3.19). It is noted that (i) all given boundary conditions are imposed in an exact manner; and (ii) this technique only requires the local values of  $\psi$  and  $\partial \psi / \partial \eta$  at the boundary node and its adjacent grid node to estimate the Dirichlet boundary conditions for the vorticity equation (3.18)/(3.20).

It can be seen that the set of 2-node IRBFEs is generated here from grid lines that pass through interior grid nodes. As a result, the set of interpolation points does not include the four corners of the cavity and hence corner singularities do not explicitly enter the discrete system.

Simulation is carried out for a wide range of  $Re$ , namely (100, 400, 1000, 3200). Grid convergence is studied using 12 uniform grids, i.e. ( $11 \times 11$ ,  $21 \times 21$ ,  $\dots$ ,  $121 \times 121$ ). Results obtained are compared with the benchmark solutions taken from Ghia et al. (1982) and Botella and Peyret (1998) to assess the performance of the present methods. The former was obtained using a multi-grid based finite-difference method with fine grids. For the latter, spectral scheme and analytical method were employed to calculate the regular and singular parts of the solution and the benchmark results were given for  $Re = 100$  and  $Re = 1000$ . In addition, global 1D-IRBF subregion/point collocation (1D-IRBF-CVM/CM) results and also standard CV results, recently given in Mai-Duy and Tran-Cong (2009b, 2011a), are also included. It is noted that, in Mai-Duy and Tran-Cong (2011a), CD-CD means that both the convection and diffusion terms were approximated with a central difference, while UW-CD means that the convection term is

treated with a first-order upwind.

**Time-step convergence:** The convergence behaviours of IRBFE-CVM and IRBFE-CM with respect to time are shown in Figures 3.1, 3.2 and 3.3. Results without an upwind treatment are also presented. It can be seen that solutions converge remarkably faster for those with upwind than those without upwind. Much larger time steps can be used for the former. Consider the case of  $Re = 1000$  and a grid of  $81 \times 81$  (Figures 3.1 and 3.2). IRBFE-CVM reaches  $CM < 10^{-9}$  after about  $5 \times 10^4$  iterations for its no-upwind version and after about  $2.5 \times 10^3$  iterations for Scheme 1, while IRBFE-CM requires about  $6.9 \times 10^4$  for its no-upwind version and about  $2.5 \times 10^3$  for Scheme 2,  $6.8 \times 10^3$  for Scheme 3. It was reported in Mai-Duy and Tran-Cong (2011a) that the global 1D-IRBF-CVM takes about  $8.5 \times 10^4$  and  $1.2 \times 10^4$  iterations to have  $CM < 10^{-8}$  for its no-upwind and upwind versions, respectively. It appears that local IRBF versions help make the convergence faster. In the case of  $Re = 3200$  and a grid of  $91 \times 91$ , in contrast to the upwind version, the no-upwind version is not able to reach  $CM = 10^{-9}$  as shown in Figure 3.3.

**Grid-size convergence:** The convergence of velocity profiles on the vertical and horizontal centrelines at  $Re = (0, 100, 400, 1000, 3200)$  with respect to grid refinement is presented in Figures 3.4 and 3.5 and Tables 3.1-3.4. Benchmark results by Ghia et al. (1982) and Botella and Peyret (1998) are also included for comparison purposes. It can be seen that (i) errors relative to the benchmark results are consistency reduced as the grid is refined; and (ii) converged profiles are obtained with relatively coarse grids (e.g.  $21 \times 21$  for  $Re = 100$  and  $61 \times 61$  for  $Re = 1000$ ).

Table 3.1: Lid-driven cavity flow, IRBFE-CVM,  $Re = 100$ : extrema of velocity profiles on the vertical and horizontal centrelines of the cavity. [ $\star$ ] is Ghia et al. (1982) and [ $\star\star$ ] is Botella and Peyret (1998).

Method	Grid	$u_{min}$	Error %	$y$	$v_{max}$	Error %	$x$	$v_{min}$	Error %	$x$
IRBFE-CVM	11x11	-0.20604	3.74	0.505	0.15971	11.06	0.225	-0.21745	14.32	0.804
	21x21	-0.21190	1.00	0.466	0.17609	1.94	0.235	-0.24673	2.79	0.809
	31x31	-0.21288	0.55	0.462	0.17798	0.89	0.236	-0.25077	1.20	0.810
	41x41	-0.21327	0.36	0.460	0.17857	0.56	0.237	-0.25203	0.70	0.810
FDM ( $\psi - \omega$ ) [ $\star$ ]	129x129	-0.21090	1.47	0.453	0.17527	2.40	0.234	-0.24533	3.34	0.805
Benchmark [ $\star\star$ ]		-0.21404		0.458	0.17957		0.237	-0.25380		0.810

Table 3.2: Lid-driven cavity flow, IRBFE-CVM,  $Re = 1000$ : extrema of the vertical and horizontal velocity profiles through the centrelines of the cavity. [ $\star$ ] is Ghia et al. (1982) and [ $\star\star$ ] is Botella and Peyret (1998).

Method	Grid	$u_{min}$	$y$	$v_{max}$	$x$	$v_{min}$	$x$
IRBFE-CVM	31x31	-0.36093	0.195	0.35084	0.167	-0.48074	0.899
	41x41	-0.37140	0.182	0.36144	0.162	-0.50172	0.905
	51x51	-0.37720	0.177	0.36673	0.160	-0.51083	0.907
	61x61	-0.38057	0.176	0.36980	0.160	-0.51588	0.908
	71x71	-0.38266	0.174	0.37166	0.159	-0.51897	0.908
	81x81	-0.38407	0.174	0.37293	0.159	-0.52097	0.909
	91x91	-0.38502	0.173	0.37377	0.159	-0.52233	0.909
	101x101	-0.38569	0.173	0.37437	0.158	-0.52330	0.909
	111x111	-0.38619	0.173	0.37482	0.158	-0.52402	0.909
	121x121	-0.38657	0.172	0.37515	0.158	-0.52454	0.909
FDM ( $\psi - \omega$ ) [ $\star$ ]	129x129	-0.38289	0.172	0.37095	0.156	-0.51550	0.906
Benchmark [ $\star\star$ ]		-0.38857	0.172	0.37694	0.158	-0.52708	0.909

Table 3.3: Lid-driven cavity flow, IRBFE-CVM,  $Re = 1000$ : percentage errors relative to the spectral benchmark results for the extreme values of the velocity profiles on the centrelines. Results of upwind central difference (UW-CD), central difference (CD-CD) and global 1D-IRBF-CVM are taken from Mai-Duy and Tran-Cong (2011a).

Grid	Error (%)			
	UW-CD	CD-CD	1D-IRBF-CVM	IRBFE-CVM
$u_{min}$				
31x31	46.10	29.19	11.86	7.11
41x41	38.17	18.13	6.50	4.42
51x51	32.92	12.11	4.09	2.93
61x61	29.12	8.63	2.80	2.06
71x71	26.21	6.46	2.03	1.52
81x81	23.88	5.02	1.54	1.16
91x91	21.95	4.01	1.19	0.91
101x101	20.33	3.28	0.96	0.74
111x111	18.94	2.73	0.78	0.61
121x121	17.74	2.31	0.65	0.51
$v_{max}$				
31x31	48.01	29.98	11.91	6.92
41x41	39.71	18.45	6.55	4.11
51x51	34.43	12.32	4.13	2.71
61x61	30.62	8.79	2.83	1.90
71x71	27.68	6.58	2.05	1.40
81x81	25.31	5.12	1.56	1.06
91x91	23.34	4.09	1.21	0.84
101x101	21.67	3.35	0.97	0.68
111x111	20.23	2.79	0.79	0.56
121x121	18.98	2.36	0.66	0.48
$v_{min}$				
31x31	40.12	29.83	11.53	8.79
41x41	30.42	18.08	6.25	4.81
51x51	24.70	11.90	3.87	3.08
61x61	20.94	8.40	2.58	2.12
71x71	18.24	6.25	1.85	1.54
81x81	16.19	4.83	1.39	1.16
91x91	14.56	3.85	1.07	0.90
101x101	13.24	3.14	0.85	0.72
111x111	12.14	2.61	0.70	0.58
121x121	11.22	2.20	0.58	0.48

Table 3.4: Lid-driven cavity flow, IRBFE-CM,  $Re = 1000$ : effects of  $\beta$  on the solution accuracy. The present results at the “optimal” value (i.e. about 3) with a grid of  $51 \times 51$  are in better agreement with the benchmark spectral results than those by 1D-IRBF-CM using the same grid and by FDM using a much denser grid. [ $\star$ ] is Mai-Duy and Tran-Cong (2009b), [ $\star\star$ ] is Ghia et al. (1982), and [ $\star\star\star$ ] is Botella and Peyret (1998).

Method	Grid	$\beta$	$u_{min}$	Error %	$y$	$v_{max}$	Error %	$x$	$v_{min}$	Error %	$x$
IRBFE-CM	51x51	1	-0.36134	7.00	0.188	0.35048	7.02	0.168	-0.48532	7.92	0.898
	51x51	3	-0.38803	0.14	0.174	0.37677	0.05	0.161	-0.52184	0.99	0.906
	51x51	5	-0.38948	0.23	0.174	0.37832	0.37	0.161	-0.52357	0.67	0.906
1D-IRBF-CM [ $\star$ ]	51x51		-0.37985	2.25	0.174	0.36781	2.42	0.160	-0.51469	2.35	0.908
FDM ( $\psi - \omega$ ) [ $\star\star$ ]	129x129		-0.38289	1.46	0.172	0.37095	1.59	0.156	-0.51550	2.20	0.906
Benchmark [ $\star\star\star$ ]			-0.38857		0.172	0.37694		0.158	-0.52708		0.909

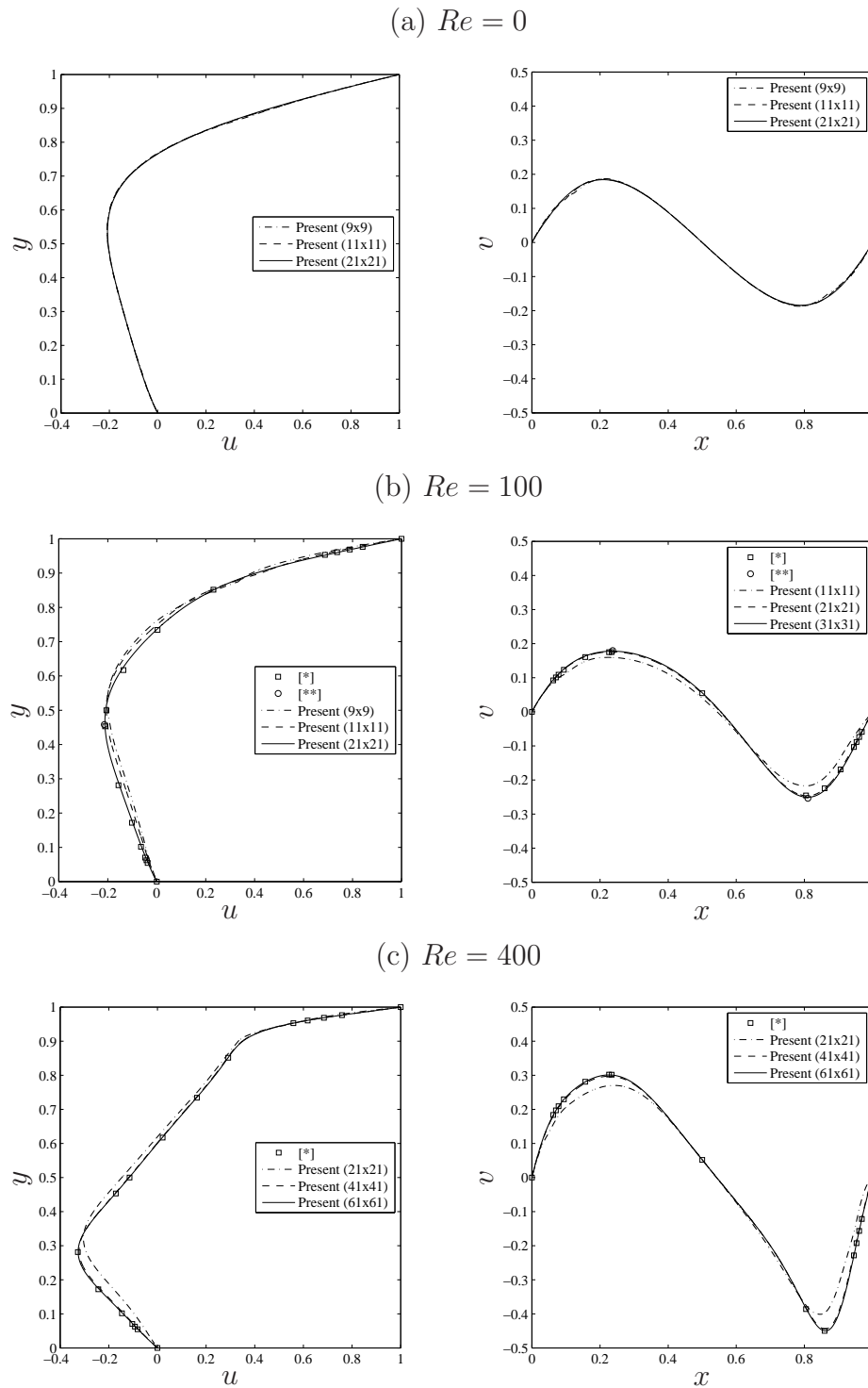


Figure 3.4: Lid-driven cavity flow, IRBFE-CVM: velocity profiles on the vertical (left) and horizontal (right) centrelines at different grids, results by Ghia et al. (1982) were obtained at a grid of  $129 \times 129$ . [\*] is Ghia et al. (1982) and [\*\*] is Botella and Peyret (1998).

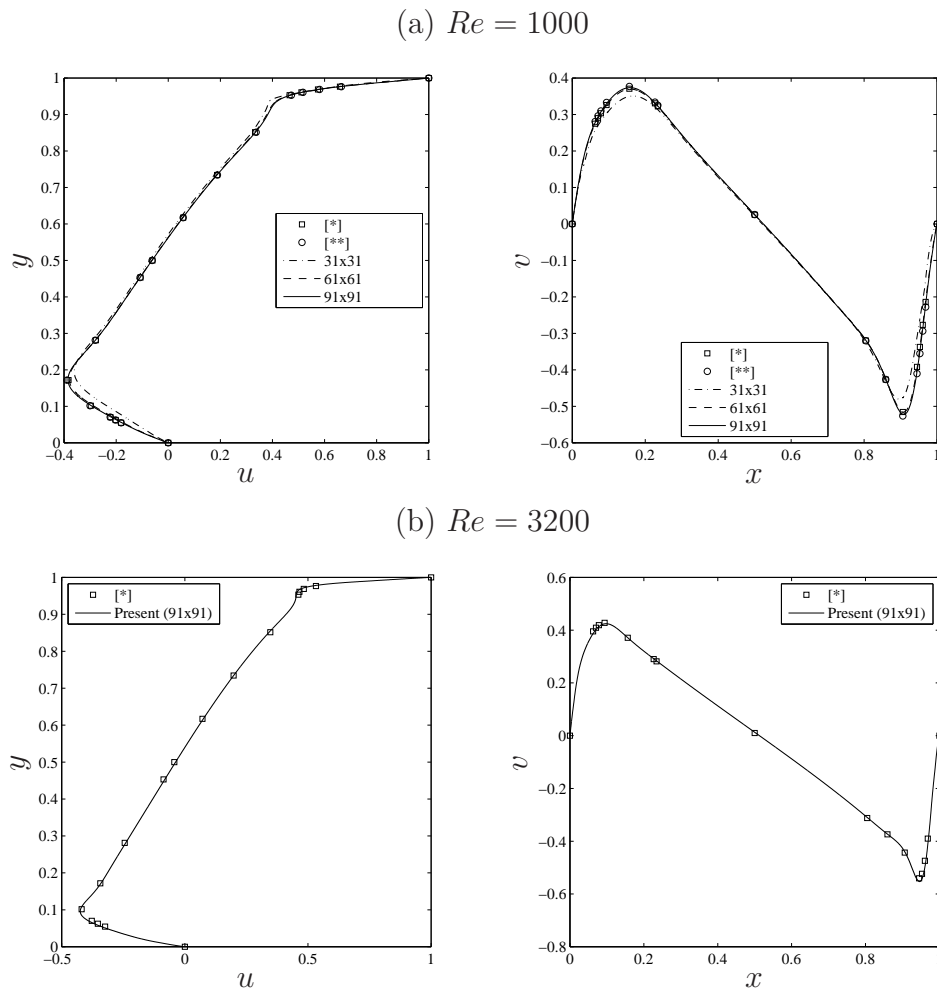


Figure 3.5: Lid-driven cavity flow, IRBFE-CVM: velocity profiles on the vertical (left) and horizontal (right) centerlines at different grids, results by Ghia et al. (1982) were obtained at a grid of  $129 \times 129$ . [\*] is Ghia et al. (1982) and [\*\*] is Botella and Peyret (1998).

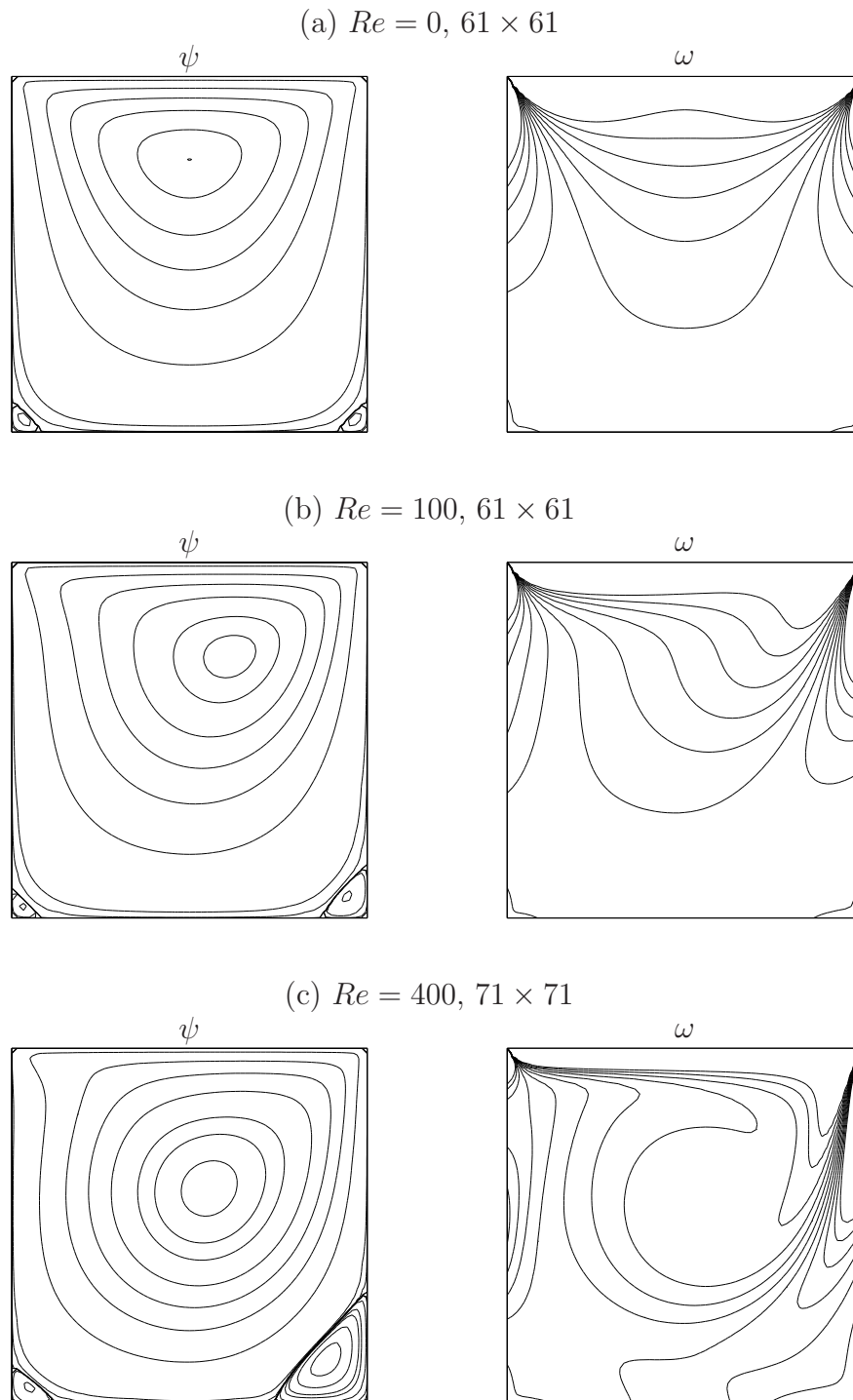


Figure 3.6: Lid-driven cavity flow, IRBFE-CVM: stream and iso-vorticity lines for several  $Re$  numbers and grid sizes. The contour values are taken to be the same as those in Ghia et al. (1982) and Sahin and Owens (2003) respectively.

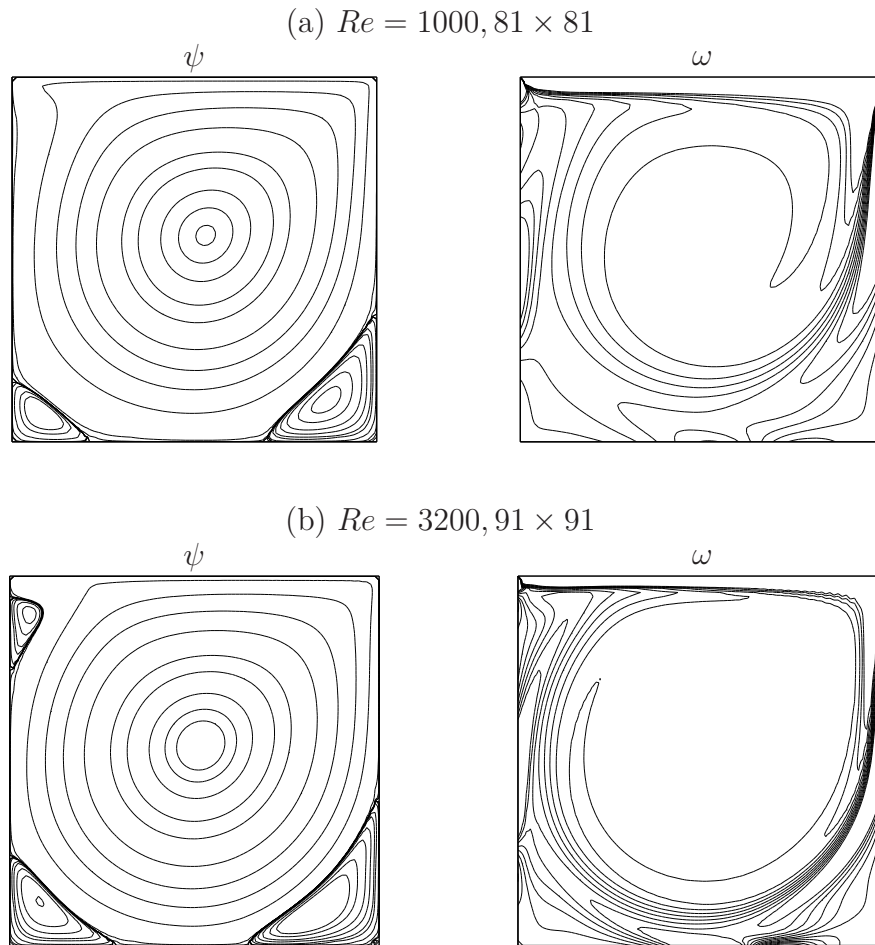


Figure 3.7: Lid-driven cavity flow, IRBFE-CVM: stream and iso-vorticity lines for several  $Re$  numbers and grid sizes. The contour values are taken to be the same as those in Ghia et al. (1982) and Sahin and Owens (2003) respectively.

**Solution quality:** The solution qualities of IRBFE-CVM and IRBFE-CM are shown in Tables 3.1-3.4 and Figures 3.6-3.7. Tables 3.1-3.4 reveal that the present results are closer to the benchmark spectral solutions than the benchmark finite-difference results and also those of the global 1D-IRBF-CVM. Errors relative to the benchmark spectral results are less than 1% for  $Re = 100$  using a grid of  $41 \times 41$  (Table 3.1) and for  $Re = 1000$  using a grid of  $91 \times 91$  (Table 3.3). These IRBFE results correspond to  $\beta = 15$ . Table 3.4 indicates that the solution accuracy can be controlled by means of  $\beta$ . The quality of the solution can be significantly improved at the optimal value of  $\beta$ . It can

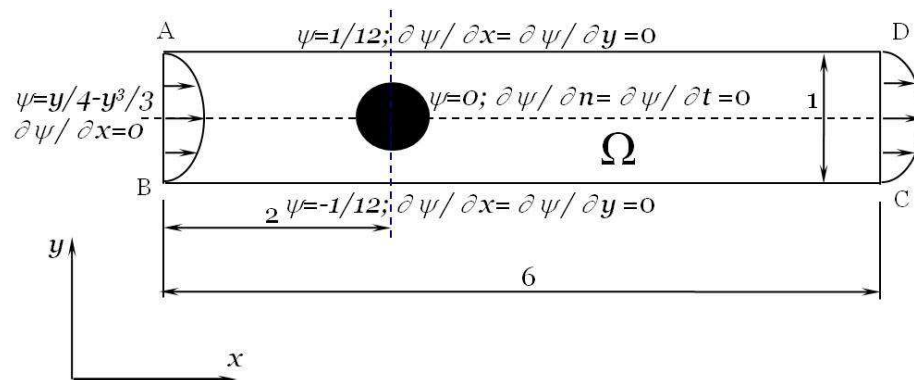


Figure 3.8: Flow past a circular cylinder in a channel: schematic representation of the computational domain.

be seen from Figures 3.6-3.7 that smooth contours are obtained for both the streamfunction and vorticity fields and the corner eddies are clearly captured at relatively coarse grids.

### 3.5.2 Flow past a circular cylinder in a channel

We further verify IRFBE-CVM and IRBFE-CM through the simulation of flow past a circular cylinder in a channel (Figure 3.8). Works involving simulation of such a flow are reported in, for example, Chen et al. (1995), Sahin and Owens (2004) and Singha and Sinhamahapatra (2010). Let  $D$  be the cylinder diameter and  $H$  the channel height. One important geometric parameter to characterise the flow is the blockage ratio defined as  $\gamma = D/H$ . Chen et al. (1995) did a numerical linear stability analysis and identified the curve of neutral stability for Hopf bifurcation at values of  $\gamma$  up to 0.7. Sahin and Owens (2004) extended the linear stability analysis to a wider range of  $\gamma$  from 0.1 to 0.9 and uncovered the complex dynamics of the flow at sufficiently high values of the Reynolds number and the blockage ratio. The paper by Anagnostopoulos and Iliadis (1996) provided the flow patterns for  $\gamma = (0.05, 0.15, 0.25)$  and  $Re = 106$  using the finite element technique. Recently, Singha and Sinhamahapatra (2010) reported the flow patterns for  $Re = (45, 100, 150)$  and  $\gamma = (0.5, 0.25, 0.333, 0.125)$  using the

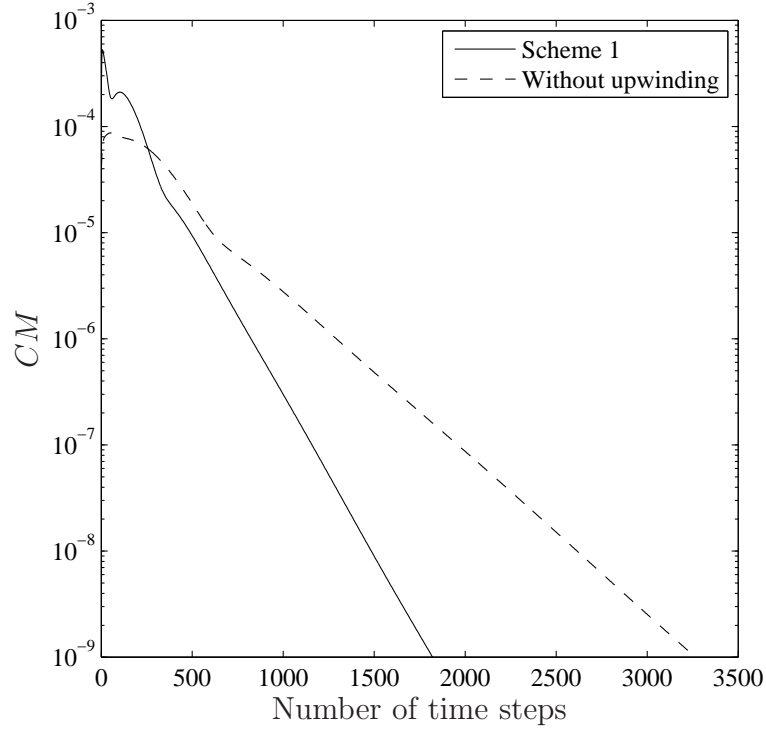


Figure 3.9: Flow past a circular cylinder in a channel, IRBFE-CVM,  $\gamma = 0.5$ ,  $Re = 60$ , grid =  $367 \times 62$ , solution at  $Re = 35$  used as initial guess: convergence behaviour. Scheme 1 using a time step of  $2 \times 10^{-4}$  converges faster than the no-upwind version using a time step of  $10^{-4}$ . It is noted that the latter diverges for time steps greater than  $10^{-4}$ .  $CM$  denotes the convergence measure as defined by (3.38).

finite volume technique. The problem domain is multiply-connected as shown in Figure 3.8. We choose the geometry and boundary conditions here as those in Chen et al. (1995). The ratio between the upstream and downstream lengths is taken to be  $1/3$  and the length of the channel is chosen to be  $6H$  to assure the fully developed conditions of the flow at upstream and downstream boundaries (Chen et al. 1995). All lengths are scaled by the channel height  $H$  (Figure 3.8). Parabolic velocity profiles can thus be imposed at the inlet and outlet as

$$u_{in} = u_{out} = u_0 \left( \frac{1}{4} - y^2 \right), \quad (3.42)$$

$$v_{in} = v_{out} = 0. \quad (3.43)$$

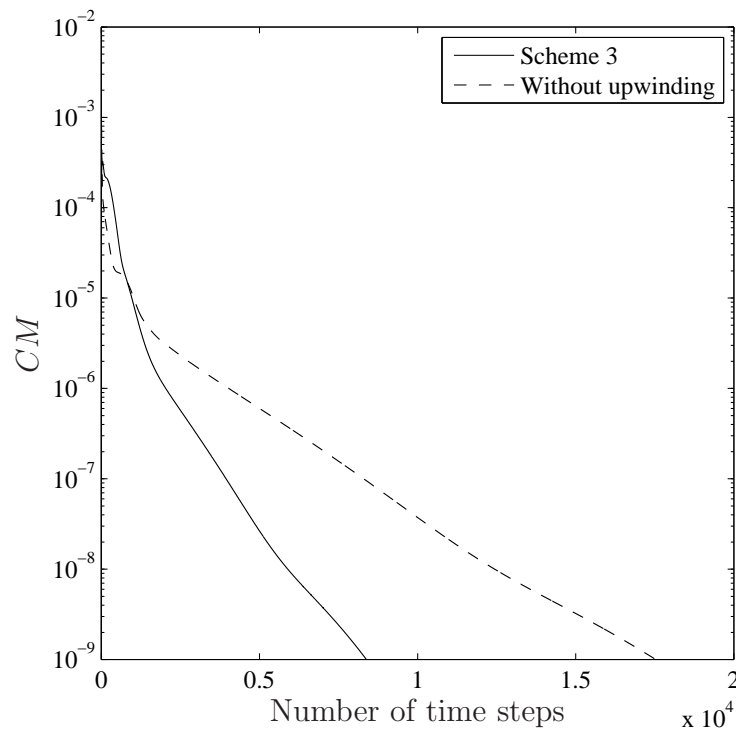


Figure 3.10: Flow past a circular cylinder in a channel, IRBFE-CM,  $\gamma = 0.5$ ,  $Re = 60$ , grid =  $367 \times 62$ , solution at  $Re = 0$  used as initial guess: convergence behaviour. Scheme 3 using a time step of  $10^{-4}$  converges faster than the no-upwind version using a time step of  $5 \times 10^{-5}$ . It is noted that the latter diverges for time steps greater than  $5 \times 10^{-5}$ .  $CM$  denotes the convergence measure as defined by (3.38).

Using  $u_0 = 1$ , the flow rate takes the value

$$Q = \int_{-1/2}^{1/2} \left( \frac{1}{4} - y^2 \right) dy = \frac{1}{6}, \quad (3.44)$$

and we define the Reynolds number as  $Re = 1/(6\nu)$ . Figure 3.8 displays boundary conditions for the streamfunction variable, which are derived from (3.42)-(3.43) at the inlet and outlet, and non-slip conditions at the remaining boundaries. The imposition of boundary conditions for  $\omega$  on the walls, inlet and outlet are similar to that used in the lid driven-cavity flow, i.e. (3.41). On the cylinder surface, analytic formulae for computing the vorticity boundary condition on a

non-rectangular boundary (Le-Cao et al. 2009) are utilised here

$$\omega_b = - \left[ 1 + \left( \frac{t_x}{t_y} \right)^2 \right] \frac{\partial^2 \psi_b}{\partial x^2}, \quad (3.45)$$

for an  $x$ -grid line, and

$$\omega_b = - \left[ 1 + \left( \frac{t_y}{t_x} \right)^2 \right] \frac{\partial^2 \psi_b}{\partial y^2}, \quad (3.46)$$

for a  $y$ -grid line. In (3.45) and (3.46),  $t_x$  and  $t_y$  are the  $x$ - and  $y$ -components of the unit vector tangential to the boundary. The approximations in (3.45) and (3.46) require information about  $\psi$  in one direction only and they are conducted here by means of 2-node IRBFEs, i.e. (3.13).

We implement Scheme 1 of IRBFE-CVM and Scheme 3 of IRBFE-CM with three different grids,  $(127 \times 22, 247 \times 42, 367 \times 62)$ , to study the flow at  $Re = (0, 25, 35, 60)$  and  $\gamma = (0.3, 0.5, 0.7)$ .

The convergence behaviours of IRBFE-CVM and IRBFE-CM with respect to time in the case of  $\gamma = 0.5$ ,  $Re = 60$  and a grid of  $367 \times 62$  are shown in Figures 3.9 and 3.10. Results without an upwind treatment are also included. It can be seen that solutions converge faster for those with upwind than those without upwind. Larger time steps can be used for the former. In the case of IRBFE-CVM (Figure 3.9),  $CM = 10^{-9}$  is obtained after about  $3.3 \times 10^3$  iterations for the no-upwind version and after about  $1.8 \times 10^3$  iterations for Scheme 1. In Figure 3.10, IRBFE-CM reaches  $CM = 10^{-9}$  after about  $1.7 \times 10^4$  iterations for the no-upwind version and after about  $8.3 \times 10^3$  iterations for Scheme 3.

Results concerning the critical  $Re$  number and the length of recirculation zones behind the cylinder are shown in Tables 3.5 and 3.6, respectively. For all three grids and different values of  $\beta$  used, the obtained values are in satisfactory agreement with those reported in Chen et al. (1995) and Singha and Sinhamahapatra (2010).

Table 3.5: Flow past a circular cylinder in a channel, IRBFE-CVM,  $\gamma = 0.5$ : The critical Reynolds number  $Re_{crit}$  for the formation of the steady recirculation zone behind the cylinder.

Method	Grid	$Re_{crit}$
IRBFE-CVM	127x22	27.498
	247x42	26.133
	367x62	25.078
Chen et al. (1995)		24.3

Table 3.6: Flow past a circular cylinder in a channel,  $\gamma = 0.5$ ,  $Re = 60$ : minimum velocity  $u_{min}$  and its position on the centreline, and the length of recirculation zones behind the cylinder ( $L_w$ ). It is noted that the case of  $Re = 60$  and  $\gamma = 0.5$  here is equivalent to the case of  $Re = 45$  and  $\gamma = 0.5$  in Singha and Sinhamahapatra (2010).

Method	Grid	$\beta$	$u_{min}$	$x$	$L_w$
IRBFE-CVM	127x22	15	-0.067	0.141	0.269
	247x42	15	-0.074	0.140	0.270
	367x62	15	-0.076	0.139	0.270
IRBFE-CM	367x62	1	-0.076	0.141	0.271
	367x62	3	-0.076	0.141	0.270
	367x62	5	-0.075	0.140	0.269
Singha and Sinhamahapatra (2010)					0.284
( $Re = 45$ )					

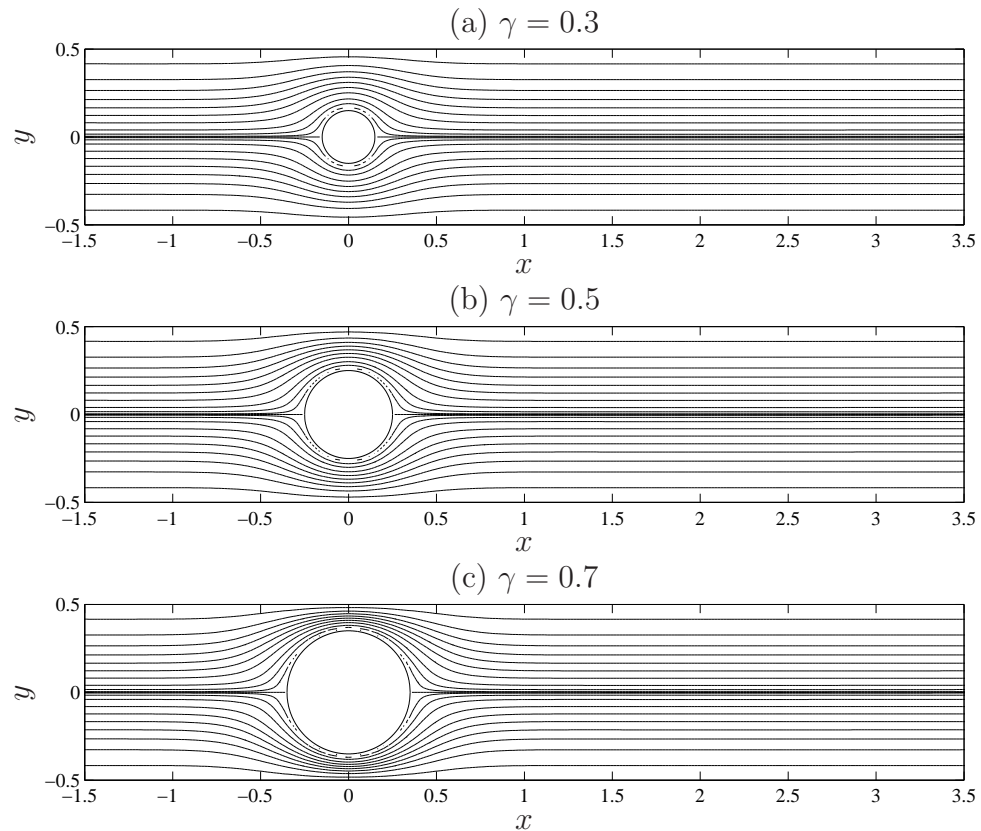


Figure 3.11: Flow past a circular cylinder in a channel, IRBFE-CVM,  $Re = 0$ , grid =  $367 \times 62$ : streamlines at different values of the blockage ratio.

Contour plots for the streamfunction and vorticity fields are presented in Figures 3.11, 3.12 and 3.13, while the velocity vector field is displayed in Figure 3.14. Stronger interaction in regions between the cylinder and the walls is observed at higher values of the blockage ratio (Figures 3.11 and 3.12). At  $Re = 60$  and  $\gamma = 0.5$ , symmetrical recirculation zones appear behind the cylinder in the streamfunction field (Figure 3.13(a)). The flow features are similar to those obtained by Singha and Sinhamahapatra (2010) at  $Re = 45$  (i.e.  $Re = 60$  according to the present definition of  $Re$ ) and  $\gamma = 0.5$ . Figure 3.15 shows velocity profiles on the centreline behind the cylinder for the case of  $\gamma = 0.5$ . It can be seen that the incipience of recirculation zones appears around  $Re = 25$ .

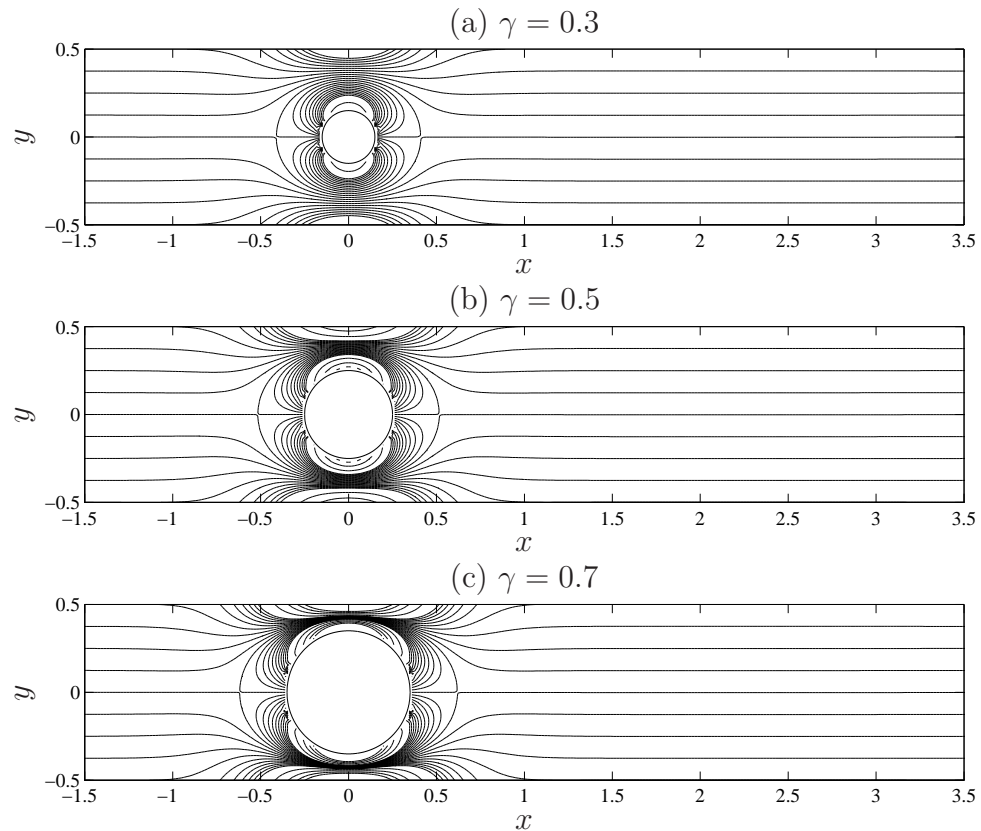


Figure 3.12: Flow past a circular cylinder in a channel, IRBFE-CVM,  $Re = 0$ , grid =  $367 \times 62$ : iso-vorticity lines at different values of the blockage ratio.

### 3.6 Concluding remarks

In this chapter, we have extended our 2-node IRBFEs to the solution of the streamfunction-vorticity formulation governing fluid flows in rectangular and non-rectangular domains. Several high-order upwind schemes based on 2-node IRBFEs were also proposed and investigated. Attractive features of the proposed point/subregion collocation methods include (i) a simple preprocessing (Cartesian grids); (ii) a sparse system matrix (2-node approximations); and a higher order of continuity across grid nodes ( $C^2$ -continuous elements). Numerical results show that (i) much larger time steps can be used with the upwind versions; and (ii) a high level of accuracy is achieved using relatively coarse grids.

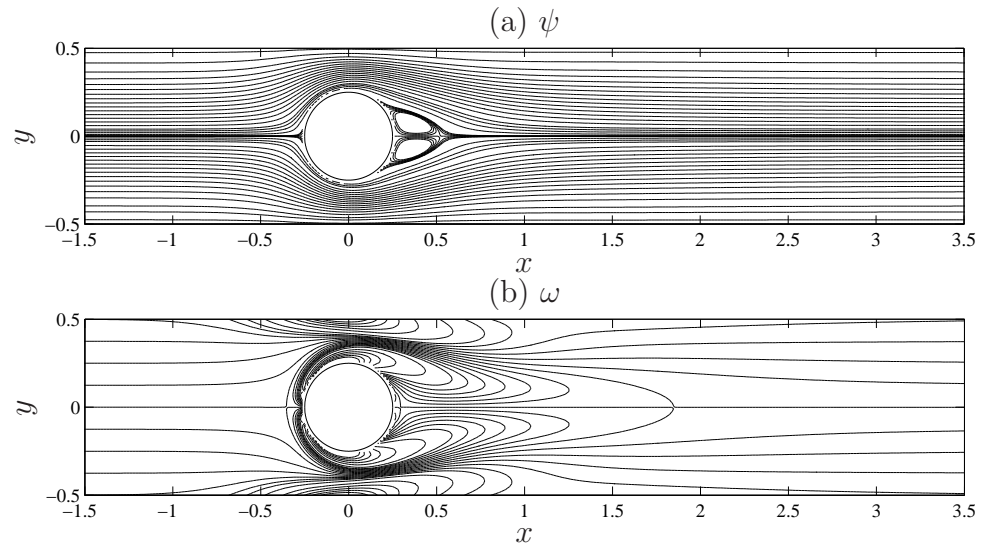


Figure 3.13: Flow past a circular cylinder in a channel, IRBFE-CVM,  $\gamma = 0.5$ ,  $Re = 60$ , grid =  $367 \times 62$ : streamlines and iso-vorticity lines.

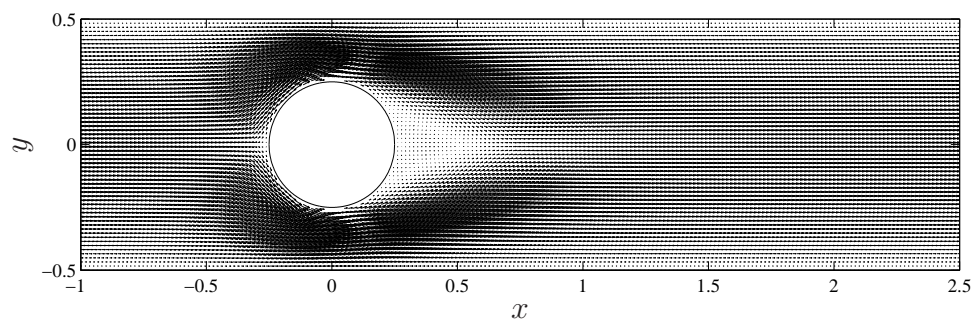


Figure 3.14: Flow past a circular cylinder in a channel, IRBFE-CVM,  $\gamma = 0.5$ ,  $Re = 60$ , grid =  $367 \times 62$ : velocity vector field.

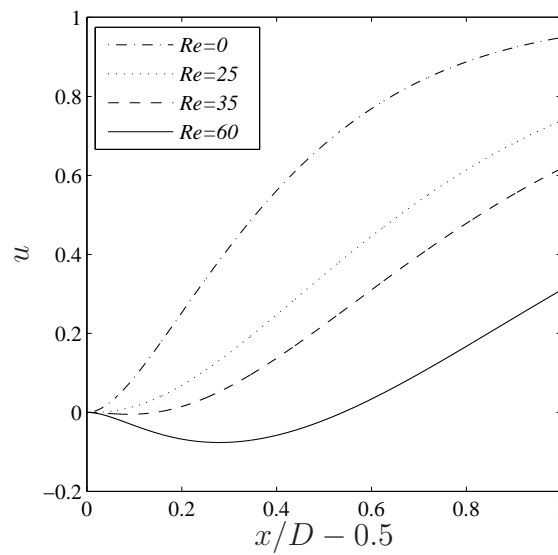


Figure 3.15: Flow past a circular cylinder in a channel, IRBFE-CVM,  $\gamma = 0.5$ : velocity profiles on the centreline behind the cylinder at different Reynold numbers.

# Chapter 4

## ADI method based on $C^2$ -continuous two-node IRBFEs for viscous flows

In the present chapter, we propose a  $C^2$ -continuous alternating direction implicit (ADI) method for the solution of the streamfunction-vorticity equations governing steady 2D incompressible viscous fluid flows. Discretisation is simply achieved with Cartesian grids. Local two-node IRBFEs are used for the discretisation of the diffusion terms, and then the convection terms are incorporated into system matrices by treating nodal derivatives as unknowns. ADI procedure is applied for the time integration. Following ADI factorisation, the two-dimensional problem becomes a sequence of one-dimensional problems. The solution strategy consists of multiple use of a one-dimensional sparse matrix algorithm that helps save the computational cost. High levels of accuracy and efficiency of the present method are demonstrated with solutions of several benchmark problems defined on rectangular and non-rectangular domains.

## 4.1 Introduction

The dimensionless Navier-Stokes (N-S) equations for steady incompressible planar viscous flows, subject to negligible body forces, can be expressed in terms of the streamfunction  $\psi$  and the vorticity  $\omega$  as in (3.1) and (3.2). The vorticity and streamfunction variables are defined by (3.3) and (3.4) respectively. In this study, the method of modified dynamics or false transients (e.g. Mallinson and Davis 1973, Pozrikidis 1997) is applied to obtain the structure of a steady flow. The governing equations (3.1) and (3.2) are modified as

$$\frac{\partial^2 \psi}{\partial x^2} + \frac{\partial^2 \psi}{\partial y^2} + \omega = 0, \quad (4.1)$$

$$\frac{\partial \omega}{\partial t} + \frac{\partial^2 \omega}{\partial x^2} + \frac{\partial^2 \omega}{\partial y^2} = Re \left( \frac{\partial \psi}{\partial y} \frac{\partial \omega}{\partial x} - \frac{\partial \psi}{\partial x} \frac{\partial \omega}{\partial y} \right). \quad (4.2)$$

A steady state solution to (4.1) and (4.2), which is obtained by integrating the equations from a given initial condition up to the steady state, is also solution to (3.1) and (3.2).

Cartesian-grid-based methods for solving (3.1) and (3.2) can be very economical owing to the facts that (i) generating a grid is low-cost; and (ii) ADI procedure (Peaceman and Rachford 1955, Douglas and Gunn 1964) can be straightforwardly applied to accelerate computational processes. The approximations for the dependent variables and their spatial derivatives can be constructed globally on the whole grid or locally on small segments of the grid. A very prominent local approximation scheme is the finite-difference (FD) which can be based on two nodes (first-order accuracy) and three nodes. The three-node approximations can take the second-order central difference (CD) form, e.g. Benjamin and Denny (1979), or high-order compact (HOC) implicit forms, e.g. Collatz (1960), Hirsh (1975), Lele (1992), where nodal values of the field variables and their derivatives are considered as unknowns. The three-node HOC implicit schemes can achieve higher order numerical accuracy and yield greater computational efficiency compared with CD schemes for the same level of the accuracy

(e.g. Hirsh 1975). However, the computational cost of these implicit schemes was quite high because of time consumption for solving (i) less-than-optimal banded matrices (block diagonal structure where each block corresponds to a grid line) (Karaa and Zhang 2004, Karaa 2007, Ma et al. 2012); or (ii) a larger number of equations per grid point (Hirsh 1975), i.e.  $3N$  equations for  $N$  grid points in 1D problems and  $5N$  equations for  $N$  grid points in 2D problems. In addition, these finite difference schemes (i.e. the two-node and the three-node schemes) typically produce solutions which are continuous for the fields but not for their partial derivatives, i.e.  $C^0$ -continuity. The grid thus needs to be sufficiently fine to mitigate the effects of discontinuity of partial derivatives.

On the other hand, the well-known alternating direction implicit (ADI) method proposed by Peaceman and Rachford (PR-ADI) was much more computationally cost-effective than the HOC implicit schemes. In the PR-ADI method, the solution is obtained by solving sets of equations defined on grid lines in  $x$ - and then  $y$ -direction sequentially. Each set includes  $N_\eta$  equations (matrix dimensions are  $N_\eta \times N_\eta$ ) for  $N_\eta$  grid points on a particular  $\eta$ -grid line where  $\eta$  represents  $x$  and  $y$ . These relatively small sets of equation (in tridiagonal matrix form) are solved separately and effectively by the Thomas algorithm that helps save the computational cost. However, the numerical accuracy of PR-ADI is only second-order in space (Peaceman and Rachford 1955). The combination of the ADI approach and the HOC schemes has been proposed by e.g. Hirsh (1975) and Karaa (2007) for solving fluid mechanics problems, by e.g. Adam (1976) for parabolic partial differential equations, and by e.g. Karaa and Zhang (2004) and Ma et al. (2012) for convection-diffusion problems. Hirsh (1975) applied the ADI procedure to HOC implicit schemes for simulating a model square cavity flow through solving sets of  $3N_\eta$  equations for  $N_\eta$  grid points on  $\eta$ -grid lines. Adam (1976) further reduced the number of equations on each grid line to sets of  $2N_\eta$  equations by means of the so-called implicit elimination. Recently, Karaa and Zhang (2004) and Karaa (2007) solve sets of  $N_\eta$  equations on  $\eta$ -grid lines through block matrices. However, as shown in You (2006), the

solution quality of this ADI method is degraded for convection-diffusion equations with high Peclet numbers. Ma et al. (2012) proposed to use fourth-order schemes for convection terms and second-order schemes for diffusion terms for convection-dominated diffusion problems and achieved very efficient sets of  $N_\eta$  equations in tridiagonal matrix form on  $\eta$ -grid lines. This ADI method hence becomes second-order accurate when diffusion terms are dominant.

Radial basis functions (RBFs) have recently emerged as an attractive tool for the solution of ordinary and partial differential equations (ODEs and PDEs) (e.g. Fasshauer 2007, Atluri and Shen 2002, Chen et al. 2008). RBF-based approximants can be constructed through a conventional differentiation process (e.g. Kansa 1990), or an integration process (e.g. Mai-Duy and Tran-Cong 2001, Mai-Duy and Tanner 2005, Mai-Duy and Tran-Cong 2005). RBF-based approximants can be global or local. Global RBF-based methods are very accurate (e.g. Cheng et al. 2003, Huang et al. 2007). However, they result in a system matrix that is dense and usually highly ill-conditioned for large problems. The use of RBF-approximants in local forms can help circumvent these difficulties (e.g. Shu et al. 2003, Šarler and Vertnik 2006, Divo and Kassab 2007). Recently, a local high order approximant based on 2-node elements and integrated RBFs (IRBFs) has been proposed by An-Vo et al. (2011a). It was shown that such elements lead to a  $C^2$ -continuous solution rather than the usual  $C^0$ -continuous solution.

In this chapter, we develop a high-order ADI method based on  $C^2$ -continuous 2-node IRBFEs (An-Vo et al. 2011a) for solving the N-S equations in the form of streamfunction-vorticity formulation, discretised by Cartesian grids. Unlike finite difference methods, the proposed method can guarantee inter-element continuity of derivatives of the streamfunction and vorticity of orders up to 2. 2-node IRBFEs are used for the discretisation of the diffusion terms, and then the convection terms are incorporated into system matrices by treating nodal first-derivatives as unknowns. By treating the convection terms as unknowns,

we obtain matrices on grid lines that are always diagonally dominant. The matrix of each  $\eta$ -grid line includes  $2N_\eta$  equations for  $N_\eta$  grid points as in Adam (1976) without the need of implicit elimination. It is noted that in Adam (1976), one has 6 nonzero entries for the governing equation and 5 nonzero entries for the equation of first-derivatives at a grid point. It will be shown later that the proposed  $C^2$ -continuous ADI method yields 4 nonzero entries for the governing equation and 6 nonzero entries for the equation of first-derivatives (by imposing  $C^2$ -continuity condition) at a grid point. Several viscous flows defined on rectangular and non-rectangular domains are considered to verify the proposed method in terms of computational cost and numerical accuracy on a wide range of Reynolds number.

The remainder of the chapter is organised as follows. A brief review of integrated RBF elements is given in Section 4.2. Section 4.3 describes the proposed  $C^2$ -continuous ADI method for the streamfunction-vorticity formulation. In Section 4.4, viscous flows in square and triangular cavities are presented to demonstrate the attractiveness of the present method. Section 4.5 concludes the chapter.

## 4.2 Two-node IRBFEs

In the present chapter, expressions (3.11)-(3.13) are employed as the interior element approximations. For convenience, in the case of  $\eta \equiv x$ , we denote

$$\mu_i = \frac{\partial^2 \varphi_i(x_1)}{\partial x^2}, \quad (4.3)$$

$$\nu_i = \frac{\partial^2 \varphi_i(x_2)}{\partial x^2}, \quad (4.4)$$

and in the case of  $\eta \equiv y$ ,

$$\theta_i = \frac{\partial^2 \varphi_i(y_1)}{\partial y^2}, \quad (4.5)$$

$$\vartheta_i = \frac{\partial^2 \varphi_i(y_2)}{\partial y^2}, \quad (4.6)$$

where  $i \in \{1, 2, 3, 4\}$ .

The semi-interior element *IRBFE-D1* via expressions (3.14)-(3.16) is employed at Dirichlet boundary. For Neumann boundary conditions such as given surface traction or boundary pressure, other types of semi-interior elements have been proposed in Chapter 2 to which the reader is referred for details.

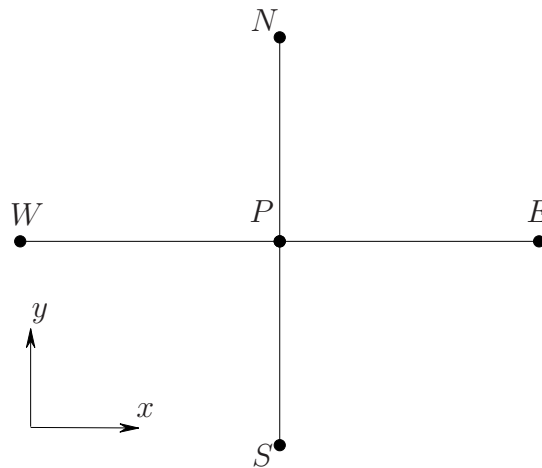


Figure 4.1: A grid point  $P$  and its neighbouring points on a Cartesian grid.

## 4.3 Derivation of $C^2$ -continuous ADI method

### 4.3.1 ADI scheme for N-S equations on a Cartesian grid

Consider a grid point  $P$  and its east, west, north and south neighbouring nodes denoted as  $E$ ,  $W$ ,  $N$  and  $S$ , respectively (Figure 4.1). Collocating (4.1) and

(4.2) at  $P$ , one obtains

$$\frac{\partial^2 \psi_P}{\partial x^2} + \frac{\partial^2 \psi_P}{\partial y^2} + \omega_P = 0, \quad (4.7)$$

$$\frac{\partial \omega_P}{\partial t} + \frac{\partial^2 \omega_P}{\partial x^2} + \frac{\partial^2 \omega_P}{\partial y^2} = \text{Re} \left( \frac{\partial \psi_P}{\partial y} \frac{\partial \omega_P}{\partial x} - \frac{\partial \psi_P}{\partial x} \frac{\partial \omega_P}{\partial y} \right). \quad (4.8)$$

We now employ the ADI (Alternating Direction Implicit) procedure (Peaceman and Rachford 1955, Douglas and Gunn 1964) to relax the time derivative term in (4.8) in two stages. At a time instant  $t^n$ , (4.22) and (4.8) become

$$\frac{\partial^2 \psi_P^n}{\partial x^2} + \frac{\partial^2 \psi_P^n}{\partial y^2} + \omega_P^{n-1} = 0, \quad (4.9)$$

$$\frac{\omega_P^{n-1/2} - \omega_P^{n-1}}{\Delta t/2} + \frac{\partial^2 \omega_P^{n-1/2}}{\partial x^2} + \frac{\partial^2 \omega_P^{n-1}}{\partial y^2} = \text{Re} \left( \frac{\partial \psi_P^n}{\partial y} \frac{\partial \omega_P^{n-1/2}}{\partial x} - \frac{\partial \psi_P^n}{\partial x} \frac{\partial \omega_P^{n-1}}{\partial y} \right), \quad (4.10)$$

$$\frac{\omega_P^n - \omega_P^{n-1/2}}{\Delta t/2} + \frac{\partial^2 \omega_P^{n-1/2}}{\partial x^2} + \frac{\partial^2 \omega_P^n}{\partial y^2} = \text{Re} \left( \frac{\partial \psi_P^n}{\partial y} \frac{\partial \omega_P^{n-1/2}}{\partial x} - \frac{\partial \psi_P^n}{\partial x} \frac{\partial \omega_P^n}{\partial y} \right). \quad (4.11)$$

It can be seen that in the first stage, i.e. (4.10),  $\partial^2 \omega_P^{n-1/2} / \partial x^2$  and  $\partial \omega_P^{n-1/2} / \partial x$  are treated implicitly and  $\partial^2 \omega_P^n / \partial y^2$  and  $\partial \omega_P^n / \partial y$  are treated implicitly in the second stage, i.e. (4.11). These derivatives and the second-order derivatives of streamfunction in (4.9) are typically approximated by a second-order CD scheme (e.g. Benjamin and Denny 1979), or HOC implicit schemes (e.g. Collatz 1960, Hirsh 1975, Adam 1976, Tian and Ge 2003). For instance in the  $x$ -direction, one has

$$\frac{\partial \omega_P^{n-1/2}}{\partial x} = \frac{\omega_E^{n-1/2} - \omega_W^{n-1/2}}{2h} + O(h^2), \quad (4.12)$$

$$\frac{\partial^2 \omega_P^{n-1/2}}{\partial x^2} = \frac{\omega_E^{n-1/2} - 2\omega_P^{n-1/2} + \omega_W^{n-1/2}}{h^2} + O(h^2), \quad (4.13)$$

$$\frac{\partial^2 \psi_P^n}{\partial x^2} = \frac{\psi_E^n - 2\psi_P^n + \psi_W^n}{h^2} + O(h^2), \quad (4.14)$$

or

$$\frac{1}{6} \frac{\partial \omega_W^{n-1/2}}{\partial x} + \frac{2}{3} \frac{\partial \omega_P^{n-1/2}}{\partial x} + \frac{1}{6} \frac{\partial \omega_E^{n-1/2}}{\partial x} = \frac{\omega_E^{n-1/2} - \omega_W^{n-1/2}}{2h} + O(h^4), \quad (4.15)$$

$$\frac{1}{12} \frac{\partial^2 \omega_W^{n-1/2}}{\partial x^2} + \frac{10}{12} \frac{\partial^2 \omega_P^{n-1/2}}{\partial x^2} + \frac{1}{12} \frac{\partial^2 \omega_E^{n-1/2}}{\partial x^2} = \frac{\omega_E^{n-1/2} - 2\omega_P^{n-1/2} + \omega_W^{n-1/2}}{h^2} + O(h^4), \quad (4.16)$$

$$\frac{1}{12} \frac{\partial^2 \psi_W^n}{\partial x^2} + \frac{10}{12} \frac{\partial^2 \psi_P^n}{\partial x^2} + \frac{1}{12} \frac{\partial^2 \psi_E^n}{\partial x^2} = \frac{\psi_E^n - 2\psi_P^n + \psi_W^n}{h^2} + O(h^4). \quad (4.17)$$

In (4.12), (4.13) and (4.14) the derivatives are explicitly given in term of nodal values of the field variable while one has to solve tridiagonal systems to obtain the derivative values in (4.15), (4.16) and (4.17). If one makes use of (4.12) or (4.15) to approximate the convection term of (4.10), the obtained system matrix might not be diagonally dominant at high values of the  $Re$ . As a result, they suffer from the so-called cell Reynolds number limitation (e.g. Khosla and Rubin 1974). Similar discussions can be made for equation (4.11) in the  $y$ -direction.

### 4.3.2 Proposed $C^2$ -continuous IRBFE-ADI method

As in Figure 4.1, one can form four two-node IRBFEs associated with  $P$ , namely  $WP$ ,  $PE$ ,  $SP$  and  $PN$ , assumed to be interior elements. To approximate  $\partial^2 \psi_P^n / \partial x^2$  and  $\partial^2 \omega_P^{n-1/2} / \partial x^2$ ,  $\partial^2 \psi_P^n / \partial y^2$  and  $\partial^2 \omega_P^n / \partial y^2$  via (3.13), we propose to use the elements  $WP$ ,  $SP$ , respectively, with abbreviations (4.4) and (4.6),

$$\frac{\partial^2 \psi_P^n}{\partial x^2} = \nu_1 \psi_W^n + \nu_2 \psi_P^n + \nu_3 \frac{\partial \psi_W^n}{\partial x} + \nu_4 \frac{\partial \psi_P^n}{\partial x}, \quad (4.18)$$

$$\frac{\partial^2 \omega_P^{n-1/2}}{\partial x^2} = \nu_1 \omega_W^{n-1/2} + \nu_2 \omega_P^{n-1/2} + \nu_3 \frac{\partial \omega_W^{n-1/2}}{\partial x} + \nu_4 \frac{\partial \omega_P^{n-1/2}}{\partial x}, \quad (4.19)$$

$$\frac{\partial^2 \psi_P^n}{\partial y^2} = \vartheta_1 \psi_S^n + \vartheta_2 \psi_P^n + \vartheta_3 \frac{\partial \psi_S^n}{\partial y} + \vartheta_4 \frac{\partial \psi_P^n}{\partial y}, \quad (4.20)$$

$$\frac{\partial^2 \omega_P^n}{\partial y^2} = \vartheta_1 \omega_S^n + \vartheta_2 \omega_P^n + \vartheta_3 \frac{\partial \omega_S^n}{\partial y} + \vartheta_4 \frac{\partial \omega_P^n}{\partial y}. \quad (4.21)$$

It will be shown later that  $C^2$ -continuous conditions are imposed at  $P$  in both  $x$ - and  $y$ -directions. As a result, either element  $WP$  or  $PE$  can be used to give approximations of  $\partial^2 \psi_P^n / \partial x^2$  and  $\partial^2 \omega_P^{n-1/2} / \partial x^2$ . Similarly, either element  $SP$  or  $PN$  can be used to give approximations of  $\partial^2 \psi_P^n / \partial y^2$  and  $\partial^2 \omega_P^n / \partial y^2$ . Substituting (4.18) and (4.20) into (4.9), (4.19) into (4.10), and (4.21) into (4.11), we have

$$\nu_1 \psi_W^n + \vartheta_1 \psi_S^n + (\nu_2 + \vartheta_2) \psi_P^n + \nu_3 \frac{\partial \psi_W^n}{\partial x} + \vartheta_3 \frac{\partial \psi_S^n}{\partial y} + \nu_4 \frac{\partial \psi_P^n}{\partial x} + \vartheta_4 \frac{\partial \psi_P^n}{\partial y} = \omega_P^{n-1}, \quad (4.22)$$

$$\nu_1 \omega_W^{n-1/2} + (\nu_2 + \frac{1}{\Delta t/2}) \omega_P^{n-1/2} + \nu_3 \frac{\partial \omega_W^{n-1/2}}{\partial x} + (\nu_4 - Re \frac{\partial \psi_P^n}{\partial y}) \frac{\partial \omega_P^{n-1/2}}{\partial x} = \frac{\omega_P^{n-1}}{\Delta t/2} - \frac{\partial^2 \omega_P^{n-1}}{\partial y^2} - Re \frac{\partial \psi_P^n}{\partial x} \frac{\partial \omega_P^{n-1}}{\partial y}, \quad (4.23)$$

$$\vartheta_1 \omega_S^n + (\vartheta_2 + \frac{1}{\Delta t/2}) \omega_P^n + \vartheta_3 \frac{\partial \omega_S^n}{\partial y} + (\vartheta_4 + Re \frac{\partial \psi_P^n}{\partial x}) \frac{\partial \omega_P^n}{\partial y} = \frac{\omega_P^{n-1/2}}{\Delta t/2} - \frac{\partial^2 \omega_P^{n-1/2}}{\partial x^2} + Re \frac{\partial \psi_P^n}{\partial y} \frac{\partial \omega_P^{n-1/2}}{\partial x}. \quad (4.24)$$

Thus, at a nodal point  $P$  in (4.22) there are three unknowns, namely  $\psi_P^n$ ,  $\partial \psi_P^n / \partial x$  and  $\partial \psi_P^n / \partial y$ . To solve (4.22), two additional equations are needed and devised here by imposing  $C^2$ -continuous conditions at  $P$  in both  $x$ - and

$y$ -directions, i.e.

$$\left(\frac{\partial^2 \psi_P^n}{\partial x^2}\right)_L = \left(\frac{\partial^2 \psi_P^n}{\partial x^2}\right)_R, \quad (4.25)$$

$$\left(\frac{\partial^2 \psi_P^n}{\partial y^2}\right)_B = \left(\frac{\partial^2 \psi_P^n}{\partial y^2}\right)_T, \quad (4.26)$$

where  $(\cdot)_L$  indicates that the computation of  $(\cdot)$  is based on the element to the left of  $P$ , i.e. element  $WP$ , and similarly subscript  $R, B, T$  denotes the right ( $PE$ ), bottom ( $SP$ ) and top ( $PN$ ) elements. The left of equations (4.25) and (4.26) are replaced by (4.18) and (4.20) and the right by similar expressions obtained via (3.13), noting (4.3) and (4.5) respectively, yielding

$$\nu_1 \psi_W^n + \nu_2 \psi_P^n + \nu_3 \frac{\partial \psi_W^n}{\partial x} + \nu_4 \frac{\partial \psi_P^n}{\partial x} = \mu_1 \psi_P^n + \mu_2 \psi_E^n + \mu_3 \frac{\partial \psi_P^n}{\partial x} + \mu_4 \frac{\partial \psi_E^n}{\partial x}, \quad (4.27)$$

$$\vartheta_1 \psi_S^n + \vartheta_2 \psi_P^n + \vartheta_3 \frac{\partial \psi_S^n}{\partial y} + \vartheta_4 \frac{\partial \psi_P^n}{\partial y} = \theta_1 \psi_P^n + \theta_2 \psi_N^n + \theta_3 \frac{\partial \psi_P^n}{\partial y} + \theta_4 \frac{\partial \psi_N^n}{\partial y}. \quad (4.28)$$

At the nodal point  $P$  and for the vorticity field, in the first relaxation stage in the  $x$ -direction, there are two unknowns in (4.23), namely  $\omega_P^{n-1/2}$  and  $\partial \omega_P^{n-1/2} / \partial x$  and in the second stage of relaxation in the  $y$ -direction, two unknowns in (4.24), namely  $\omega_P^n$  and  $\partial \omega_P^n / \partial y$ . To solve (4.23), one additional equation is needed and also devised by imposing  $C^2$ -continuity condition at  $P$  in  $x$ -direction, i.e.

$$\left(\frac{\partial^2 \omega_P^{n-1/2}}{\partial x^2}\right)_L = \left(\frac{\partial^2 \omega_P^{n-1/2}}{\partial x^2}\right)_R. \quad (4.29)$$

The left of equation (4.29) is replaced by (4.19) and the right by a similar expression obtained via (3.13), noting (4.3), yielding

$$\begin{aligned} \nu_1 \omega_W^{n-1/2} + \nu_2 \omega_P^{n-1/2} + \nu_3 \frac{\partial \omega_W^{n-1/2}}{\partial x} + \nu_4 \frac{\partial \omega_P^{n-1/2}}{\partial x} = \\ \mu_1 \omega_P^{n-1/2} + \mu_2 \omega_E^{n-1/2} + \mu_3 \frac{\partial \omega_P^{n-1/2}}{\partial x} + \mu_4 \frac{\partial \omega_E^{n-1/2}}{\partial x}. \end{aligned} \quad (4.30)$$

In a similar manner, to solve (4.24), one additional equation is created by imposing  $C^2$ -continuity condition at  $P$  in the  $y$ -direction, i.e.

$$\left(\frac{\partial^2 \omega_P^n}{\partial y^2}\right)_B = \left(\frac{\partial^2 \omega_P^n}{\partial y^2}\right)_T, \quad (4.31)$$

The left of equation (4.31) is replaced by (4.21) and the right by a similar expression obtained via (3.13), noting (4.5), yielding

$$\vartheta_1 \omega_S^n + \vartheta_2 \omega_P^n + \vartheta_3 \frac{\partial \omega_S^n}{\partial y} + \vartheta_4 \frac{\partial \omega_P^n}{\partial y} = \theta_1 \omega_P^n + \theta_2 \omega_N^n + \theta_3 \frac{\partial \omega_P^n}{\partial y} + \theta_4 \frac{\partial \omega_N^n}{\partial y}. \quad (4.32)$$

(4.22)-(4.24), (4.27), (4.28), (4.30) and (4.32) will be slightly different at the domain boundary where (3.16) for semi-interior elements is used instead of (3.13). To solve for the streamfunction field we collect equations (4.22), (4.27) and (4.28) at all nodal points which leads to a large system matrix of size  $3N \times 3N$  where  $N$  is the total number of grid points of the problem domain. Nonetheless, this system is sparse and banded. As a result, the LU technique is very efficient for factorisation. It is noted that the factorisation needs to be done only once.

For the vorticity field, it can be seen from (4.23), (4.24), (4.30) and (4.32) that there are 4 nonzero entries for the governing equations, i.e. (4.23) and (4.24), and 6 nonzero entries for the  $C^2$ -continuity conditions at the grid point  $P$ , i.e. (4.30) and (4.32). At the first relaxation stage, collection of equations (4.23) and (4.30) at nodal points on each and every  $x$ -grid line leads to  $N_y$  independent sets of equations. Each set contains  $2N_x$  equations for  $2N_x$  unknowns associated with an  $x$ -grid line with  $N_x$  nodes. At the second stage, collection of equations (4.24) and (4.32) at nodal points on each and every  $y$ -grid line leads to  $N_x$  independent sets of equations. Each set contains  $2N_y$  equations for  $2N_y$  unknowns associated with a  $y$ -grid line with  $N_y$  nodes. In contrast to the direct solution approaches in An-Vo et al. (2011a,b) where a system of  $3N$  equations for  $3N$  unknowns are required, the current approach results in considerable savings in terms of both storage and computational time. The latter is significantly reduced further when

parallelisation is implemented to independently solve these relatively small sets of  $2N_\eta$  equations.

At high values of the  $Re$ , the fourth terms on the LHS of (4.23) and (4.24) are dominant, which guarantees diagonally dominant system matrices. Owing to the fact that two-node IRBFs are used, the proposed method also leads to very sparse systems and its solution is a  $C^2$  function across IRBFs.

## 4.4 Numerical examples

The performance of the proposed  $C^2$ -continuous IRBFE-ADI method is studied through the simulation of flows in square and triangular cavities. For all numerical examples presented in this study, the MQ shape parameter  $a$  is simply chosen proportionally to the element length  $h$  by a factor  $\beta$ .  $\beta = 1$  is used throughout the computations. In the case of non-rectangular domains, there may be some nodes that are too close to the boundary. If an interior node falls within a distance of  $h/4$  to the boundary, such a node is removed from the set of nodal points. A steady solution is obtained with a time marching approach starting from a computed solution at a lower Reynolds number. For the special case of Stokes equation, the starting condition is the rest state.

The solution procedure involves the following steps

- (1) Guess the initial distributions of the streamfunction and vorticity in the case of Stokes flow. Otherwise, take the solution of a lower Reynolds number as an initial guess.
- (2) Discretise the streamfunction equation at a time instant  $t^n$  (4.9) by means of  $C^2$ -continuous IRBFs, i.e. (4.22), (4.27) and (4.28), and then apply the LU technique to factorise the system matrix into two triangular matrices. It is noted that the factorisation needs to be done only once.
- (3) Solve (4.9) subjects to boundary conditions for the new streamfunction field.

- (4) Derive a computational boundary condition for the vorticity from the updated streamfunction field.
- (5) Solve for the new vorticity field in two stages by using (4.23) and (4.30), (4.24) and (4.32) in the  $x$ - and  $y$ -direction respectively.
- (6) Check to see whether the solution has reached a steady state through a condition on convergence measure

$$CM(\psi) = \frac{\sqrt{\sum_{i=1}^N (\psi_i - \psi_i^0)^2}}{\sqrt{\sum_{i=1}^N \psi_i^2}} < 10^{-9}, \quad (4.33)$$

where  $N$  is the total number of grid nodes.

- (7) If  $CM$  is not satisfactorily small, advance pseudo-time and repeat from step (3). Otherwise, stop the computation and output the results.

#### 4.4.1 Square cavity

Square cavity flow is one of the most studied cases in the literature of internal flows. This type of flow is important firstly in its own right as a basic physical model. Then, owing to its simple geometry and rich flow physics at different Reynolds numbers, the problem also serves as a useful test for numerical algorithms in CFD. The cavity is taken to be a unit square, with the lid sliding from left to right at a unit velocity. The boundary conditions can be specified as

$$\begin{aligned} \psi = 0, \quad \partial\psi/\partial x = 0 \quad \text{on} \quad x = 0, \quad x = 1, \\ \psi = 0, \quad \partial\psi/\partial y = 0 \quad \text{on} \quad y = 0, \\ \psi = 0, \quad \partial\psi/\partial y = 1 \quad \text{on} \quad y = 1. \end{aligned}$$

We take Dirichlet boundary conditions,  $\psi = 0$ , on all walls for solving (4.1). The Neumann boundary conditions,  $\partial\psi/\partial n$  (i.e.  $\partial\psi/\partial n = \nabla\psi \cdot \hat{n}$ , where  $\hat{n}$  is the

outward unit vector normal to the boundary), are used to derive computational boundary conditions for  $\omega$  in solving (4.2). Making use of (4.1), the values of  $\omega$  on the boundaries are computed by

$$\omega_b = -\frac{\partial^2 \psi_b}{\partial x^2} \quad \text{on } x = 0, \quad x = 1, \quad (4.34)$$

$$\omega_b = -\frac{\partial^2 \psi_b}{\partial y^2} \quad \text{on } y = 0, \quad y = 1. \quad (4.35)$$

In computing (4.34) and (4.35), one needs to incorporate  $\partial\psi_b/\partial x$  into  $\partial^2\psi_b/\partial x^2$ , and  $\partial\psi_b/\partial y$  into  $\partial^2\psi_b/\partial y^2$ , respectively. A simple technique to derive  $\omega_b$  in the context of 2-node IRBFEs can be found in An-Vo et al. (2011b). It will be briefly reproduced here for the sake of completeness. Assuming that node 1 and 2 of an IRBFE are a boundary node and an interior grid node respectively (i.e.  $1 \equiv b$  and  $2 \equiv g$ ). Boundary values of the vorticity are obtained by applying (3.13) as

$$\omega_b = -\frac{\partial^2 \psi_b}{\partial \eta^2} = -\left( \frac{\partial^2 \varphi_1(\eta_b)}{\partial \eta^2} \psi_b + \frac{\partial^2 \varphi_2(\eta_b)}{\partial \eta^2} \psi_g + \frac{\partial^2 \varphi_3(\eta_b)}{\partial \eta^2} \frac{\partial \psi_b}{\partial \eta} + \frac{\partial^2 \varphi_4(\eta_b)}{\partial \eta^2} \frac{\partial \psi_g}{\partial \eta} \right), \quad (4.36)$$

where  $\eta$  represents  $x$  and  $y$ ;  $\psi_b$  and  $\partial\psi_b/\partial\eta$  are the Dirichlet and Neumann boundary conditions for  $\psi$ , and  $\psi_g$  and  $\partial\psi_g/\partial\eta$  are known values taken from the solution of the streamfunction equation (4.1). It is noted that (i) all given boundary conditions are imposed in an exact manner; and (ii) this technique only requires the local values of  $\psi$  and  $\partial\psi/\partial\eta$  at the boundary node and its adjacent grid node to estimate the Dirichlet boundary conditions for the vorticity equation (4.2). It can be seen that there are two values of  $u$  at each top corner of the cavity making the solution singular. In the well-known paper by Ghia et al. (1982), the flow was simulated by the finite-difference scheme and a multigrid method using very fine grids (i.e.  $129 \times 129$  and  $257 \times 257$ ). The obtained results are very accurate and they have been considered as a benchmark of finite-difference methods. In the later work by Botella and Peyret (1998),

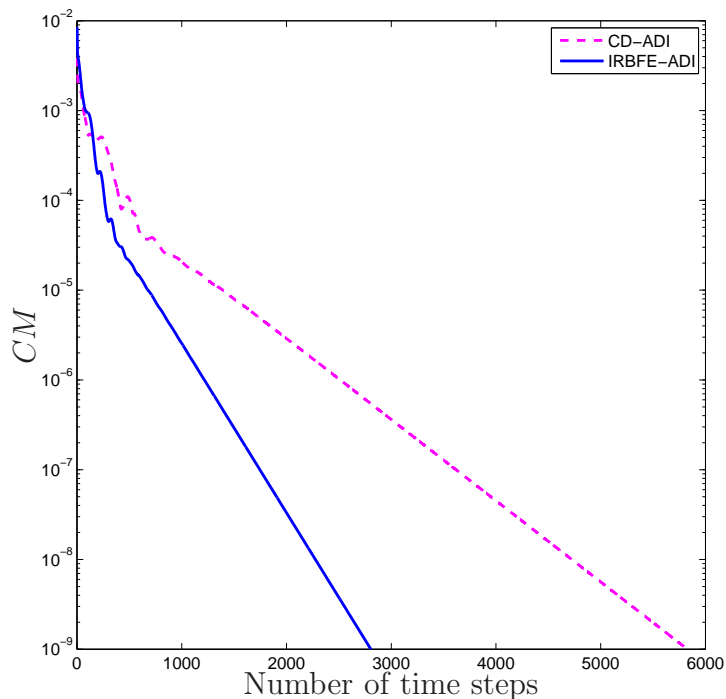


Figure 4.2: Square cavity flow,  $Re = 1000$ ,  $51 \times 51$ : convergence behaviour. IRBFE-ADI method using a time step of  $6 \times 10^{-5}$  converges faster than the CD-ADI method using a time step of  $3 \times 10^{-5}$ . It is noted that the latter diverges for time steps greater than  $3 \times 10^{-5}$ .  $CM$  denotes the relative norm of the difference of the streamfunction fields between two successive time levels.

the regular and singular parts of the solution are handled by a Chebyshev collocation and an analytic method respectively. Benchmark spectral results for the flow at  $Re = 100$  and  $Re = 1000$  were reported. In the present study, the set of 2-node IRBFEs is generated from grid lines that pass through interior grid nodes. As a result, the set of interpolation points does not include the top corners of the cavity and hence corner singularities do not explicitly enter the discrete system. Simulation is carried out for a wide range of  $Re$ , namely (100, 400, 1000, 3200, 5000, 7500). Grid convergence is also studied. Results obtained are compared with the benchmark solutions (Ghia et al. 1982 and Botella and Peyret 1998), and with the global 1D-IRBF collocation (1D-IRBF-C) results recently given in Mai-Duy and Tran-Cong (2011a). These comparisons aim to assess the accuracy of the present method. To assess the efficiency and stability, an ADI method where streamfunction and vorticity are discretised by a three-

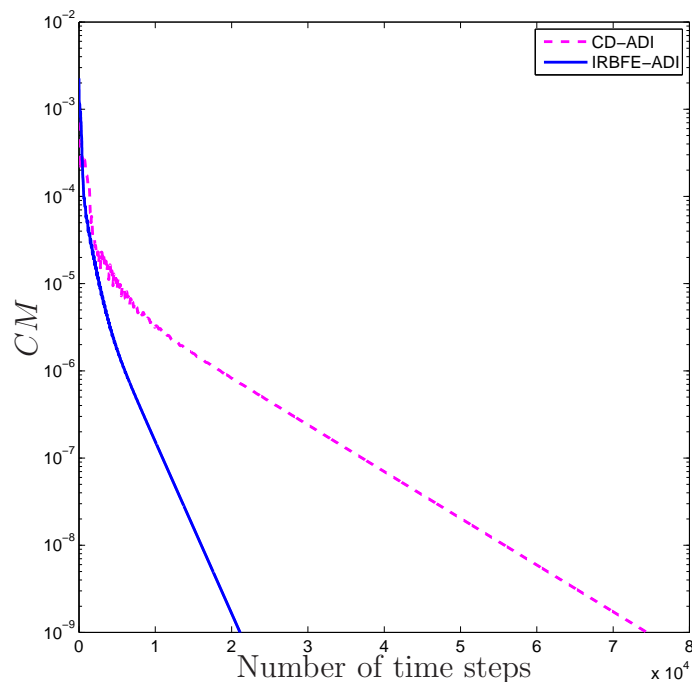


Figure 4.3: Square cavity flow,  $Re = 3200$ ,  $91 \times 91$ , solution at  $Re = 1000$  used as initial guess: convergence behaviour. IRBFE-ADI method using a time step of  $7 \times 10^{-6}$  converges faster than the CD-ADI method using a time step of  $2 \times 10^{-6}$ . It is noted that the latter diverges for time steps greater than  $2 \times 10^{-6}$ .  $CM$  denotes the relative norm of the difference of the streamfunction fields between two successive time levels.

node CD is also implemented. We denote this method as CD-ADI. It is noted that the same method of deriving computational vorticity boundary conditions is used in both IRBFE-ADI and CD-ADI methods.

**Time-stepping convergence:** The convergence behaviours of IRBFE-ADI and CD-ADI with respect to time are shown in Figures 4.2-4.4 and Table 4.1. It can be seen that solutions converge faster and larger time steps can be used for the present IRBFE-ADI method. The numbers of iterations are about  $2.8 \times 10^3$  and  $5.8 \times 10^3$  to reach  $CM < 10^{-9}$  for IRBFE-ADI and CD-ADI respectively in the case of  $Re = 1000$  and a grid of  $51 \times 51$  (Figure 4.2). In the case of  $Re = 3200$  and a grid of  $91 \times 91$  (Figure 4.3), IRBFE-ADI takes about  $2.1 \times 10^4$  to have  $CM < 10^{-9}$  while CD-ADI requires about  $7.4 \times 10^4$  to have the same  $CM$ . At  $Re = 7500$ , in contrast to the IRBFE-ADI method ( $\Delta t = 1 \times 10^{-6}$ ),

the CD-ADI method diverges even with a smaller time step of  $5 \times 10^{-7}$  as shown in Figure 4.4. The numbers of iterations in IRBFE-ADI method are generally lower than in CD-ADI method, yielding shorter computational time (Table 4.1). It is noted that the Thomas algorithm is used to solve tridiagonal systems in CD-ADI method and CPU seconds are associated with a computer which has 3.25 GB of RAM and one Intel(R) Core(TM)2 Duo CPU of 3.0 GHz. All codes are written in MATLAB<sup>®</sup> language.

**Grid-size convergence:** The convergence of extrema of the vertical and horizontal velocity profiles along the centrelines of the cavity with respect to grid refinement is presented in Table 4.2. Benchmark results by Ghia et al. (1982) and Botella and Peyret (1998) are also included for comparison purposes. It can be seen that errors relative to the benchmark results are consistency reduced as the grid is refined ( $Re = 100, 1000$ ); and (ii) extrema values very close to the benchmark values are obtained with relatively coarse grids (e.g.  $21 \times 21$  for  $Re = 100$ ,  $41 \times 41$  for  $Re = 400$  and  $61 \times 61$  for  $Re = 1000$ ).

**Solution quality:** The solution qualities of IRBFE-ADI are shown in Table 4.2 and Figures 4.5-4.10. Table 4.2 reveals that the IRBFE-ADI results are the closest to the benchmark spectral solutions in comparison with the CD-ADI, the benchmark finite-difference and the global 1D-IRBF-C results. Errors relative to the benchmark spectral results are less than 1% for  $Re = 100$  using a grid of  $21 \times 21$  and for  $Re = 1000$  using a grid of  $61 \times 61$ . It can be seen from Figures 4.5-4.9 that smooth contours are obtained in the present IRBFE-ADI method for both the streamfunction and vorticity fields at relatively coarse grids. In Figure 4.5, the IRBFE-ADI method captures the primary vortex and the bottom-right corner eddy better than the CD-ADI method at  $Re = 100$  and a grid of  $11 \times 11$ . With the same grids, CD-ADI method yields oscillatory contours especially for the vorticity field as shown in Figures 4.6-4.8. Converged velocity profiles at  $Re = 1000$  and  $Re = 3200$  are obtained by IRBFE-ADI method with grids of  $51 \times 51$  and  $91 \times 91$ , respectively, as shown in Figure 4.10.

Table 4.1: Square cavity flow: computational times.

$Re$	Method	Grid	$\Delta t$	Cycle seconds	Number of cycles	CPU seconds
100	CD-ADI	11x11	4.0E-3	2.7E-4	198	5.3E-2
	IRBFE-ADI	11x11	4.0E-3	1.7E-4	110	1.9E-2
	CD-ADI	21x21	1.0E-3	9.5E-4	413	0.393
	IRBFE-ADI	21x21	1.0E-3	8.9E-4	276	0.246
400	CD-ADI	21x21	2.0E-4	9.3E-4	1144	1.066
	IRBFE-ADI	21x21	4.0E-4	9.6E-4	452	0.432
	CD-ADI	31x31	2.0E-4	2.1E-3	922	1.945
	IRBFE-ADI	31x31	3.0E-4	2.8E-3	588	1.654
	CD-ADI	41x41	2.5E-4	4.1E-3	1568	6.378
	IRBFE-ADI	41x41	2.5E-4	5.8E-3	693	3.997
1000	CD-ADI	31x31	2.0E-5	2.2E-3	8884	19.853
	IRBFE-ADI	31x31	6.0E-5	2.7E-3	2851	7.785
	CD-ADI	41x41	2.0E-5	3.9E-3	8681	33.510
	IRBFE-ADI	41x41	6.0E-5	5.4E-3	2853	15.451
	CD-ADI	51x51	2.0E-5	6.6E-3	8447	55.910
	IRBFE-ADI	51x51	6.0E-5	1.2E-2	2807	33.880

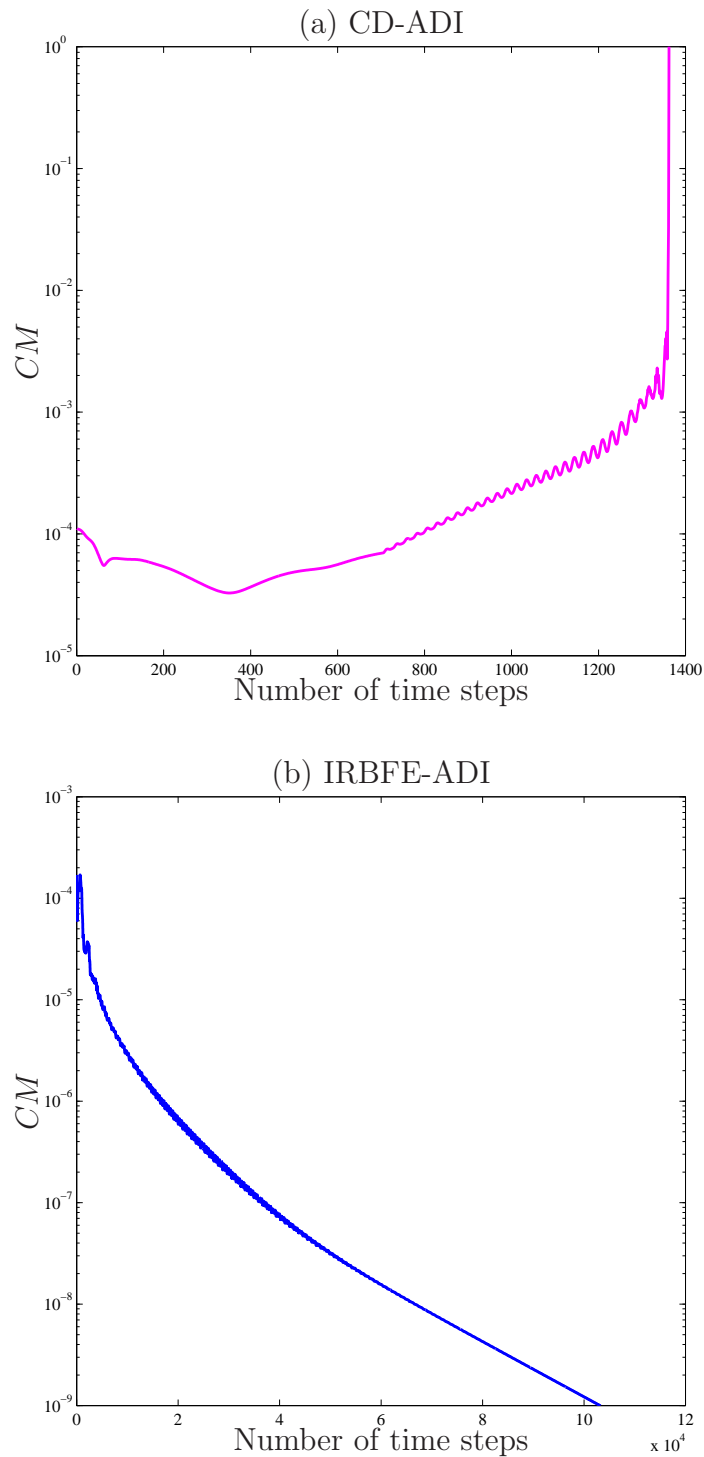


Figure 4.4: Square cavity flow,  $Re = 7500$ ,  $131 \times 131$ , solution at  $Re = 5000$  used as initial guess: convergence behaviour. CD-ADI method uses a time step of  $5 \times 10^{-7}$  and IRBFE-ADI method uses a time step of  $1 \times 10^{-6}$ .  $CM$  denotes the relative norm of the difference of the streamfunction fields between two successive time levels.

Table 4.2: Square cavity flow: extrema of the vertical and horizontal velocity profiles along the centrelines of the cavity. % denotes percentage errors relative to the benchmark spectral results (Botella and Peyret 1998). Results of the global 1D-IRBF-C, FDM and Benchmark are taken from Mai-Duy and Tran-Cong (2009b), Ghia et al. (1982) and Botella and Peyret (1998) respectively.

$Re$	Method	Grid	$u_{min}$	%	$v_{max}$	%	$v_{min}$	%
100	CD-ADI	11x11	-0.15242	28.79	0.10823	39.73	-0.14355	43.44
	IRBFE-ADI	11x11	-0.19916	6.95	0.14276	20.50	-0.18436	27.36
	CD-ADI	21x21	-0.19725	7.84	0.16069	10.51	-0.22401	11.74
	IRBFE-ADI	21x21	-0.21537	0.62	0.17932	0.14	-0.24960	0.78
	FDM ( $\psi - \omega$ )	129x129	-0.21090	1.47	0.17527	2.40	-0.24533	3.34
	Benchmark		-0.21404		0.17957		-0.25380	
400	CD-ADI	21x21	-0.20572		0.16693		-0.25885	
	IRBFE-ADI	21x21	-0.29015		0.24953		-0.36327	
	CD-ADI	31x31	-0.27258		0.24391		-0.37199	
	IRBFE-ADI	31x31	-0.32166		0.29581		-0.43622	
	CD-ADI	41x41	-0.29689		0.26978		-0.40808	
	IRBFE-ADI	41x41	-0.32780		0.30305		-0.44986	
FDM ( $\psi - \omega$ )	129x129	-0.32726		0.30203		-0.44993		
1000	CD-ADI	31x31	-0.26073	32.90	0.24723	34.41	-0.36708	30.36
	1D-IRBF-C	31x31	-0.34791	10.46	0.33580	10.91	-0.46765	11.27
	IRBFE-ADI	31x31	-0.33775	13.08	0.32592	13.54	-0.44434	15.70
	CD-ADI	41x41	-0.30741	20.89	0.29382	22.05	-0.42451	19.46
	1D-IRBF-C	41x41	-0.37122	4.47	0.35910	4.73	-0.50168	4.82
	IRBFE-ADI	41x41	-0.37334	3.92	0.36193	3.98	-0.49863	5.40
	CD-ADI	51x51	-0.33242	14.45	0.31932	15.29	-0.45556	13.57
	1D-IRBF-C	51x51	-0.37985	2.25	0.36781	2.42	-0.51469	2.35
	IRBFE-ADI	51x51	-0.38482	0.97	0.37336	0.95	-0.51831	1.66
	CD-ADI	61x61	-0.34772	10.51	0.33502	11.12	-0.47488	9.90
	1D-IRBF-C	61x61	-0.38366	1.26	0.37173	1.38	-0.52029	1.29
	IRBFE-ADI	61x61	-0.38886	0.08	0.37719	0.07	-0.52537	0.32
	FDM ( $\psi - \omega$ )	129x129	-0.38289	1.46	0.37095	1.59	-0.51550	2.20
Benchmark		-0.38857		0.37694		-0.52708		

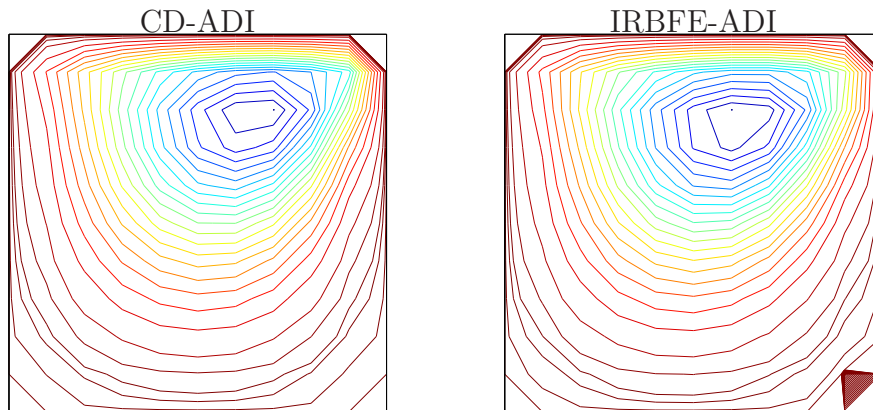


Figure 4.5: Square cavity flow,  $Re = 100$ , grid =  $11 \times 11$ : streamlines. The contour values for CD-ADI and IRBFE-ADI plots are the same.

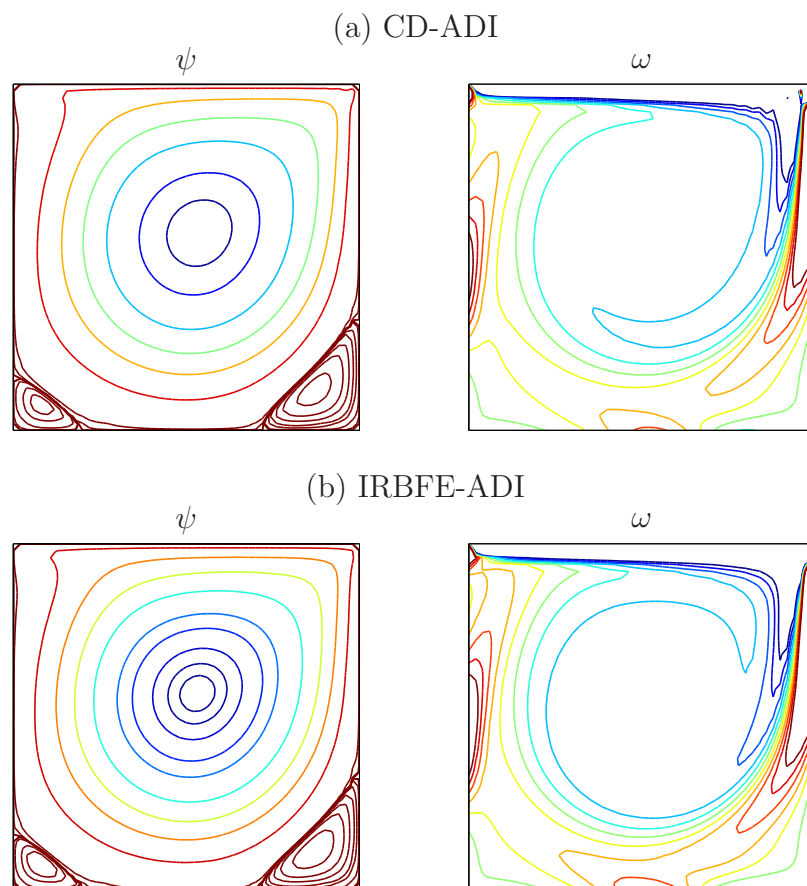


Figure 4.6: Square cavity flow,  $Re = 1000$ , grid =  $51 \times 51$ : stream and isovorticity lines. The contour values are taken to be the same as those in Ghia et al. (1982) and Sahin and Owens (2003) respectively. Note the oscillatory behaviour near the top right corner in the case of CD-ADI method.

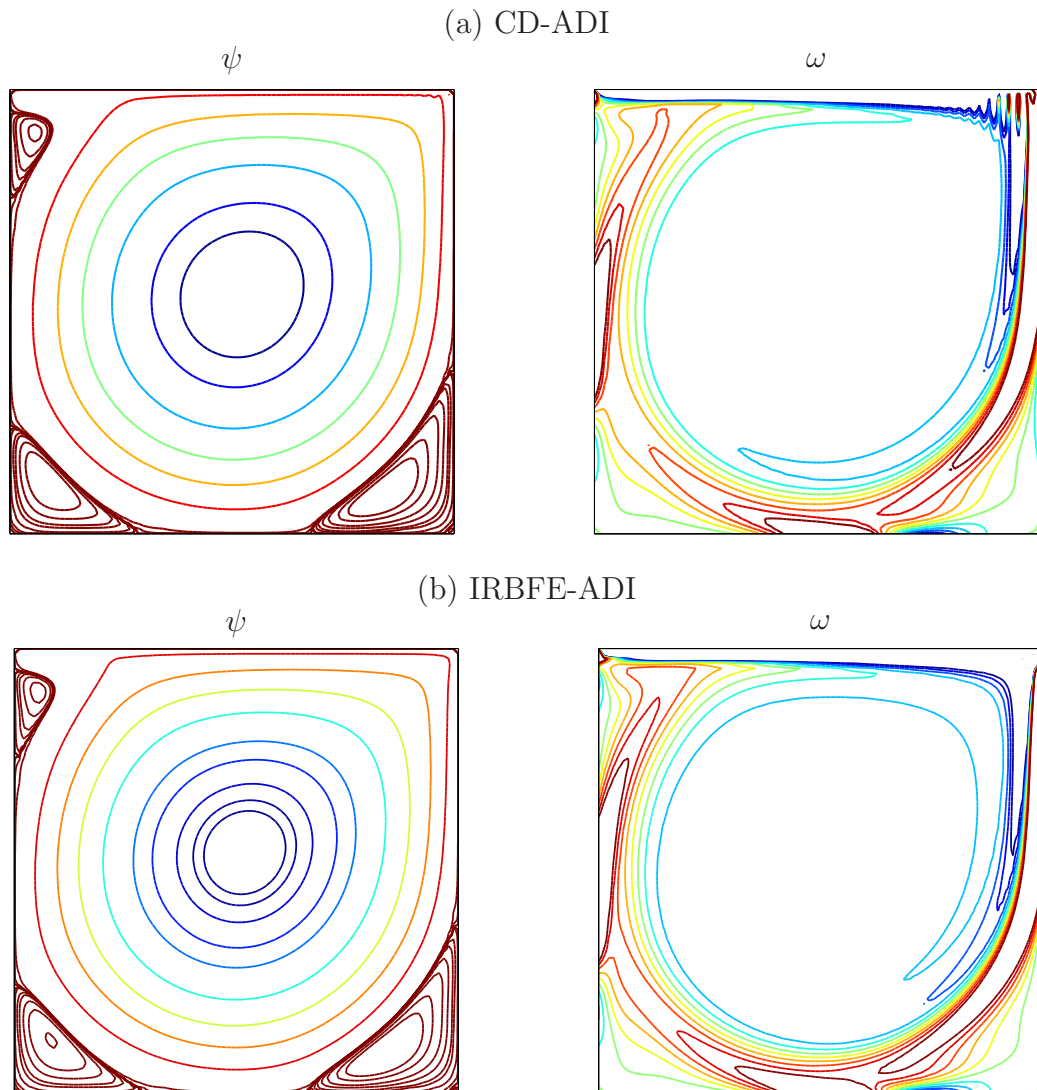


Figure 4.7: Square cavity flow,  $Re = 3200$ , grid =  $91 \times 91$ : stream and iso-vorticity lines. The contour values are taken to be the same as those in Ghia et al. (1982) and Sahin and Owens (2003) respectively. Note the oscillatory behaviour near the top right corner in the case of CD-ADI method.

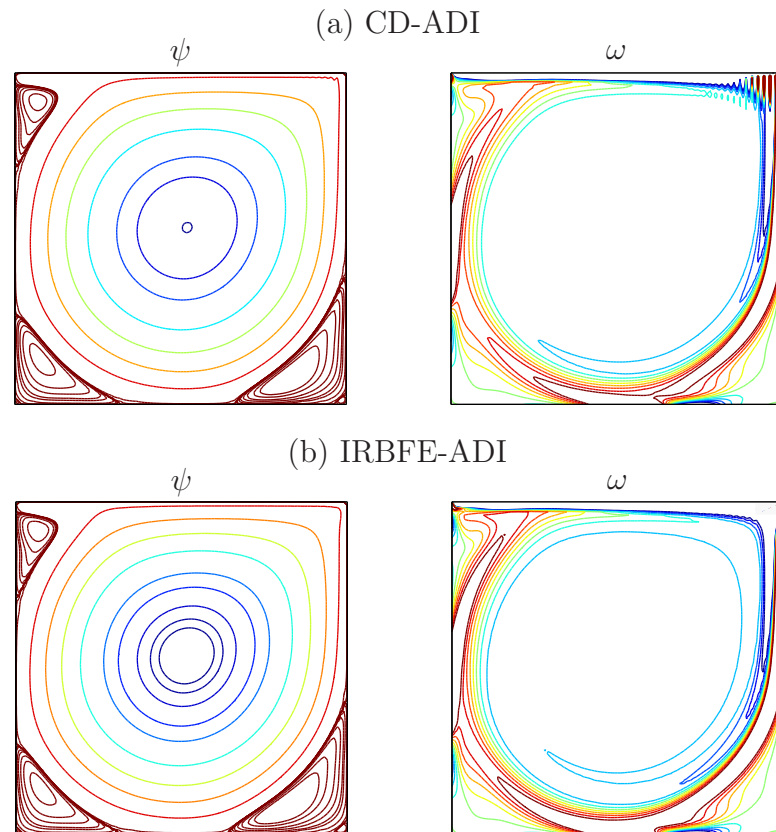


Figure 4.8: Square cavity flow,  $Re = 5000$ , grid =  $111 \times 111$ : stream and iso-vorticity lines. The contour values are taken to be the same as those in Ghia et al. (1982) and Sahin and Owens (2003) respectively. Note the oscillatory behaviour near the top right corner in the case of CD-ADI method.

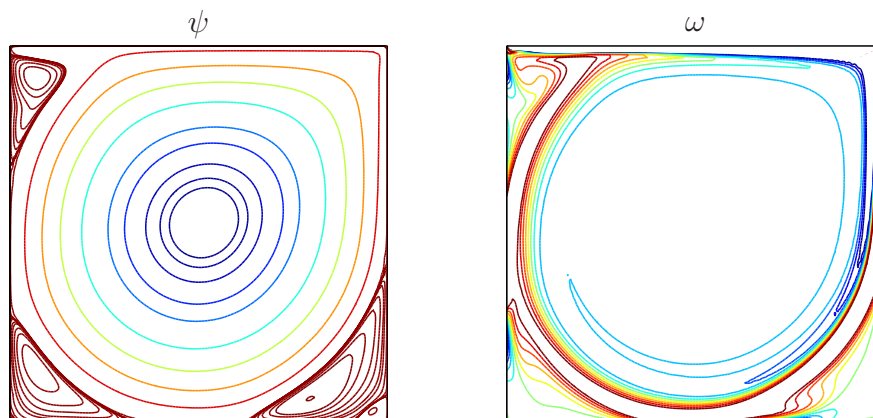


Figure 4.9: Square cavity flow, IRBFE-ADI,  $Re = 7500$ , grid =  $131 \times 131$ : stream and iso-vorticity lines. The contour values are taken to be the same as those in Ghia et al. (1982) and Sahin and Owens (2003) respectively.

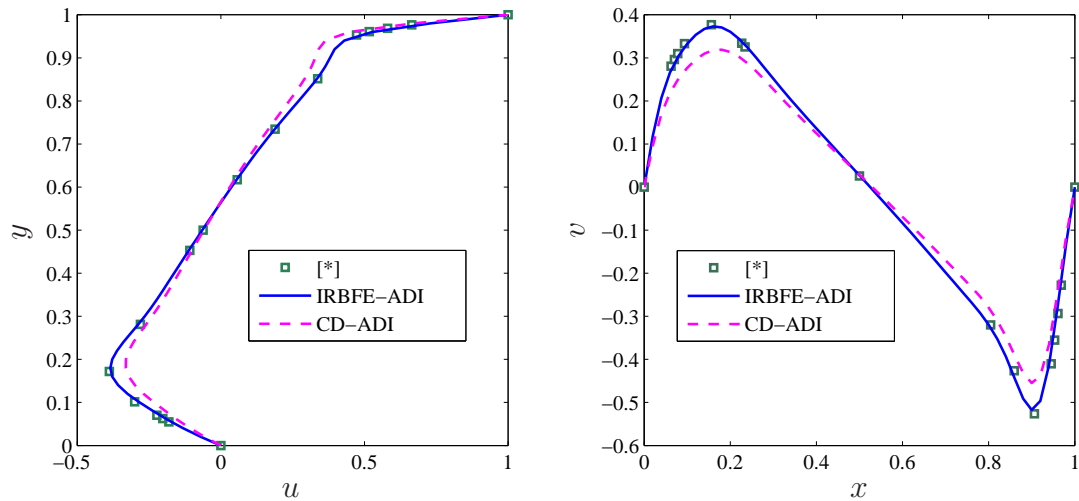
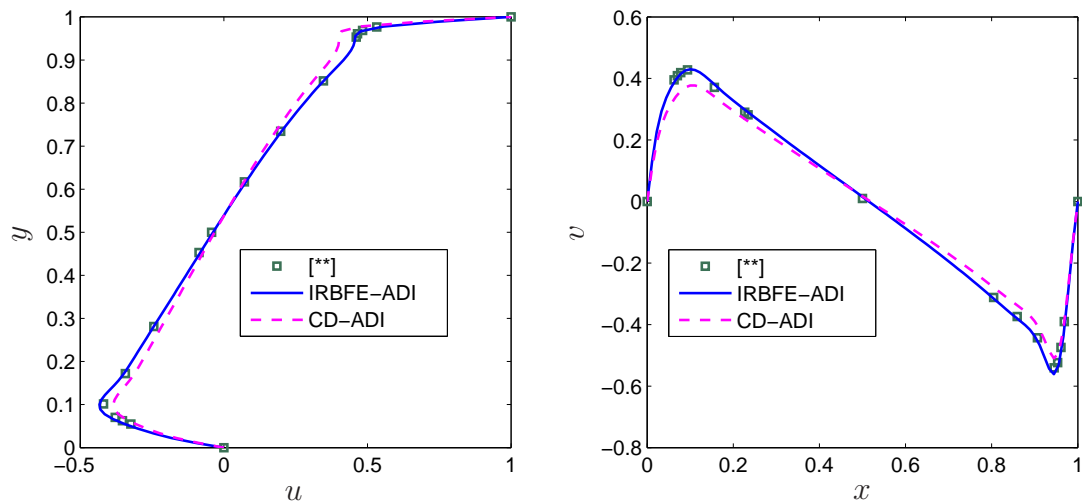
(a)  $Re = 1000$ , grid=  $51 \times 51$ (b)  $Re = 3200$ , grid=  $91 \times 91$ 

Figure 4.10: Square cavity flow: velocity profiles along the vertical and horizontal centrelines of the cavity. [\*] is Botella and Peyret (1998) and [\*\*] is Ghia et al. (1982).

### 4.4.2 Triangular cavity

The proposed method is further verified through the simulation of steady recirculating flow in an equilateral triangle cavity. This is an example that presents a severe test for structured grid-based numerical methods (Ribbens et al. 1994, Jyotsna and Vanka 1995). Figure 4.11 shows the geometry of the triangular cavity with the boundary conditions and the coordinate system. As in the square cavity flow problem, no-slip boundary condition is imposed on the left and right boundaries, while a unit horizontal velocity is prescribed on the top boundary. Numerical studies of this problem can be categorised into structured and unstructured grid/mesh-based methods. The former includes e.g. Ribbens et al. (1994), Li and Tang (1996), Erturk and Gokcol (2007) where a finite difference method (FDM) was employed and the equilateral triangle had to be transformed to a computational domain on an isosceles right triangle. In the latter, Jyotsna and Vanka (1995) used a multigrid procedure and a control volume formulation on triangular grids. They numerically verified interesting features of the flow in the Stokes regime. Kohno and Bathe (2006) presented a flow-condition-based interpolation finite element scheme on triangular meshes to achieve solutions for high Reynolds numbers.

The imposition of boundary conditions for  $\omega$  on the top is similar to that used in the square cavity flow, i.e. (4.36). On the left and right sides, analytic formulae for computing the vorticity boundary condition can be obtained from the general formulae developed in Le-Cao et al. (2009) for general curved boundary. For the present problem, such general formulae are reduced to

$$\omega_b = - \left[ 1 + \left( \frac{t_x}{t_y} \right)^2 \right] \frac{\partial^2 \psi_b}{\partial x^2}, \quad (4.37)$$

for a  $x$ -grid line, and

$$\omega_b = - \left[ 1 + \left( \frac{t_y}{t_x} \right)^2 \right] \frac{\partial^2 \psi_b}{\partial y^2}, \quad (4.38)$$

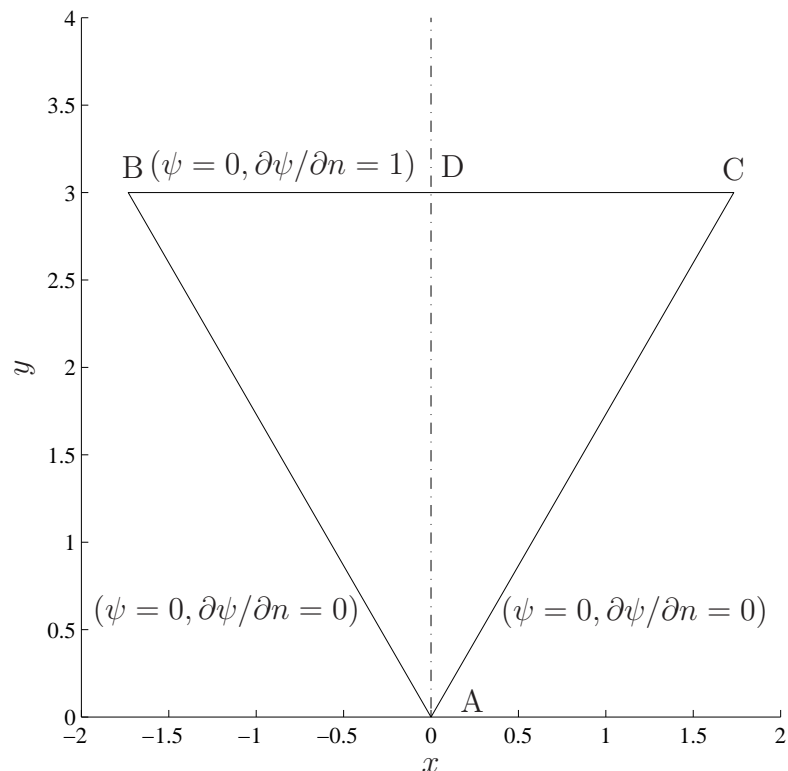


Figure 4.11: Triangular cavity flow: schematic outline of the computational domain and boundary conditions. Note that the characteristic length is chosen to be  $AD/3$  to facilitate comparison with other published results (Ribbens et al. 1994, Kohno and Bathe 2006).

for a  $y$ -grid line. In (4.37) and (4.38),  $t_x$  and  $t_y$  are the  $x$ - and  $y$ -components of the unit vector tangential to the boundary. The approximations in (4.37) and (4.38) require information about  $\psi$  in one direction only and they are constructed here by means of 2-node IRBFs, i.e. (3.13). No exterior/fictitious points as in Ribbens et al. (1994) are involved here.

Four Cartesian grids, namely Grid 1 (1952 interior points), Grid 2 (2680 points), Grid 3 (3526 points) and Grid 4 (4486 points) as shown in Figure 4.12, are employed to study the convergence of the solution. Unlike FDMs (Ribbens et al. 1994, Li and Tang 1996, Erturk and Gokcol 2007), the present method does not require any coordinate transformation, making modelling simple. The

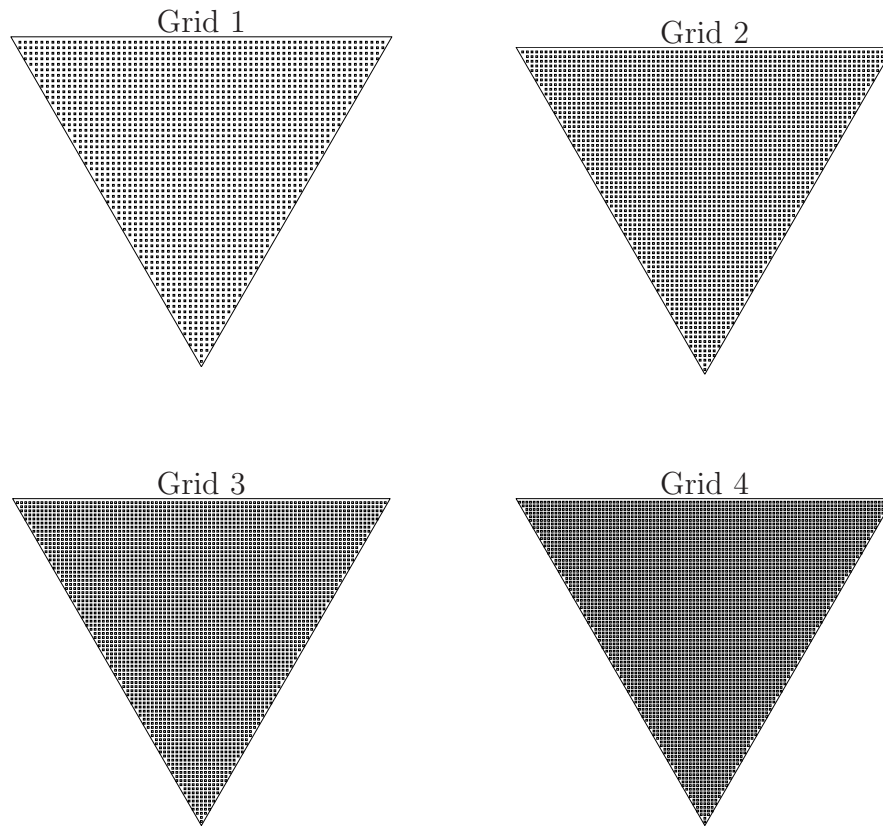


Figure 4.12: Triangular cavity flow: the computational domain is discretised by four Cartesian grids.

flow is simulated at  $Re = (0, 100, 200, 500)$  where  $Re = U(H/3)/\nu$ ,  $U$  the lid velocity and  $H$  the cavity height (i.e. length AD in Figure 4.11). An alternative definition of Reynolds number was  $Re_s = US/\nu$  where  $S$  is the cavity side length. We have  $Re_s = 2\sqrt{3}Re$ . For example,  $Re = 500$  here is equivalent to  $Re_s = 1732$ .

Figures 4.13 and 4.14 present contour plots of the streamfunction and vorticity fields, the stream and iso-vorticity lines look comparable to those available in the literature (e.g. Ribbens et al. 1994, Kohno and Bathe 2006).

Figure 4.15 shows the profiles of  $u$  along the vertical centreline  $x = 0$  and  $v$  along the horizontal line  $y = 2$ . Results obtained in Kohno and Bathe (2006)

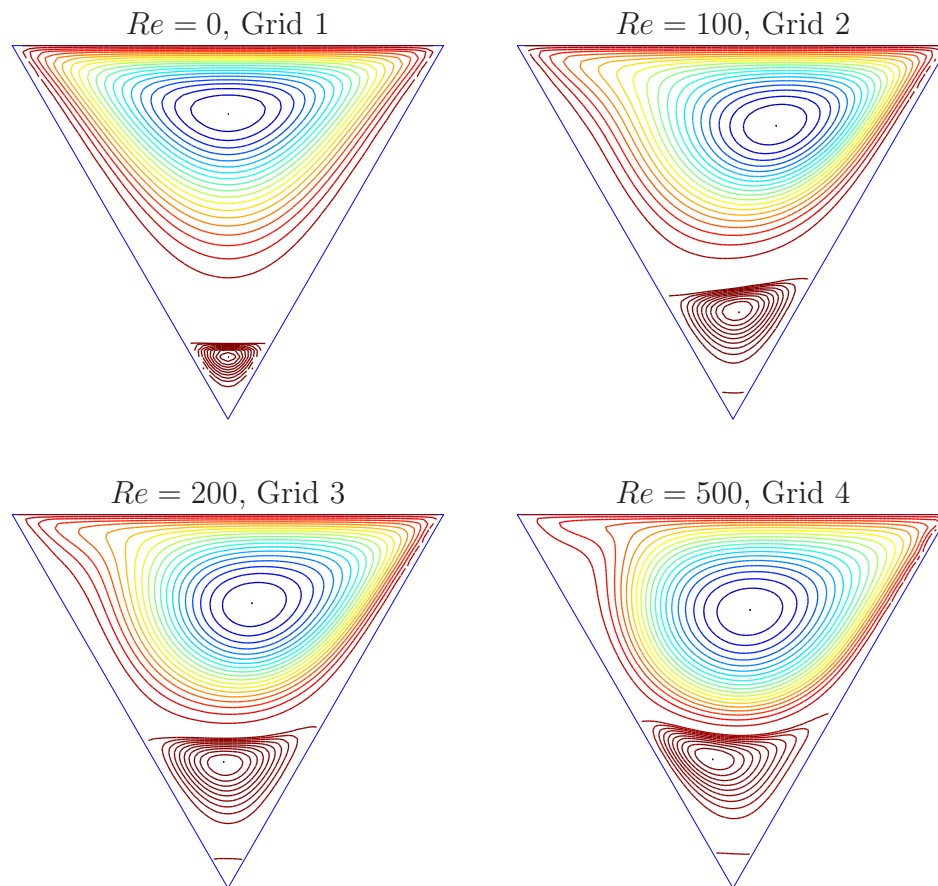


Figure 4.13: Triangular cavity flow: streamlines which are drawn using 21 equi-spaced levels between the minimum and zero values, and 11 equi-spaced levels between the zero and maximum values.

are also included for comparison purposes. It can be seen that the velocity profiles obtained by Grid 1 and Grid 2 at  $Re = 100$ , and by Grid 2 and Grid 3 at  $Re = 200$  are almost identical. The present results are in good agreement with those by the flow-conditioned-based interpolation FEM for all values of  $Re$ . The profiles of  $v$  near the the stagnant corner at different Reynolds numbers also confirm the Stokes flow assumption of the flow field in this region (Moffat 1963).

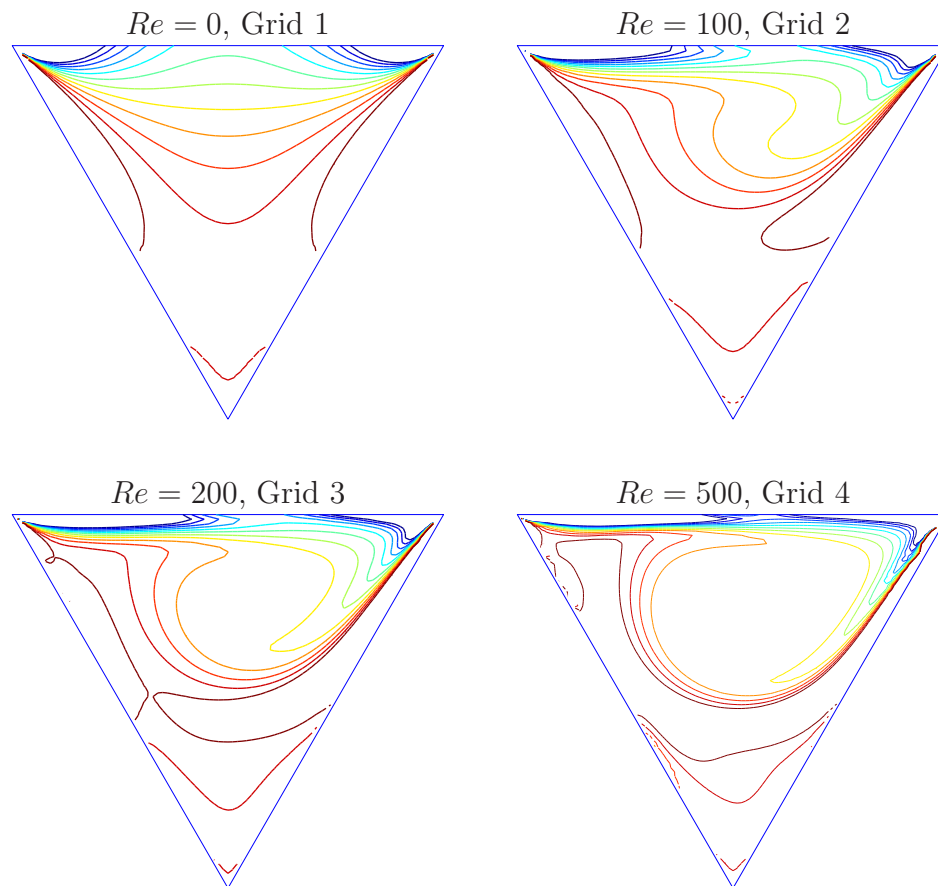


Figure 4.14: Triangular cavity flow: iso-vorticity lines which are drawn at intervals of  $\Delta\omega = 0.5$  for a range of  $-5 \leq \omega \leq 0.5$ .

### 4.4.3 Discussion

#### Comparison with other RBF techniques

To the best of our knowledge, the present two-node RBF scheme yields the smallest RBF set ever used for constructing approximation. When compared with other local RBF techniques, the present method results in remarkably sparse and banded system matrices and  $C^2$ -continuous solutions rather than the usual  $C^0$ -continuous solutions.  $C^2$ -continuous streamfunction field leads to smooth and highly accurate velocity field.

Unlike other conventional RBF techniques, the present technique considers both

the field variables and their partial derivatives in Cartesian directions in the formulation. As a result, the convection terms are naturally incorporated into the system matrices as unknowns and diagonally dominant systems are always guaranteed. Numerical results show that the present technique is very stable for high  $Re$  flows without recourse to up-winding schemes. Although the present system matrices are much larger, bigger time steps can be used and hence a smaller number of iterations are required to obtain a steady state solution. The computational time hence becomes competitive to those required by the conventional techniques as shown in Table 4.1.

### Comparison with other conventional discretisation techniques

In terms of geometric modelling, unlike pseudo-spectral and finite-difference methods, the present Cartesian-grid technique can handle irregular domains well. In contrast to finite element and finite volumes, the pre-processing here is much more economical. Non-boundary grid points are trivially generated and the intersections between grid lines and the domain boundary can be determined as in a typical FE mesh generation (Thompson et al. 1999). For example, the intersections of an  $x$ -grid line with the boundary can be found as follows. Either an  $xy$ -plane or an  $xz$ -plane passing through the  $x$ -grid line is used and the intersection between this plane and the boundary (a curve or curves) is determined by analytic geometric methods. The intersection between the grid line and the curve(s) can then be easily determined.

In terms of solution, the governing equations are collocated at nodal points without the need for numerical integration. ADI solution strategies are conveniently applied to accelerate the computational process. When compared with low-order techniques, the present technique can produce accurate results on a relatively coarse mesh, therefore has the ability to reduce computational effort for a given accuracy. On the other hand, with more information (first derivatives are also involved in the interpolation) the cost to construct the approximation

is quite higher than the standard CD scheme. In addition, the system matrix on each grid line of the present ADI method is not as sparse as and twice the size of those obtained by the PR-ADI method, requiring more than twice the memory storage. However, works on optimising the proposed ADI method are presented in Chapter 5. It is pointed out that we can approach tridiagonal system matrices with the same size as those in PR-ADI for diffusion-convection type equations.

## 4.5 Concluding remarks

We propose a  $C^2$ -continuous alternating direction implicit solution method for solving the streamfunction-vorticity formulation governing fluid flows. Numerical experiments are conducted with problems on rectangular and non-rectangular domains. The method successfully simulates the fluid flows considered in a wide range of Reynolds numbers. Attractive features of the proposed methods include (i) simple preprocessing (Cartesian grids); (ii) a sparse system matrix (2-node approximations); and a higher order of continuity across grid nodes ( $C^2$ -continuous elements). Numerical results show that (i) larger time steps can be used and smaller numbers of iterations are required in comparison with the classical CD-ADI method; and (ii) smooth solutions and high levels of accuracy are achieved using relatively coarse grids.

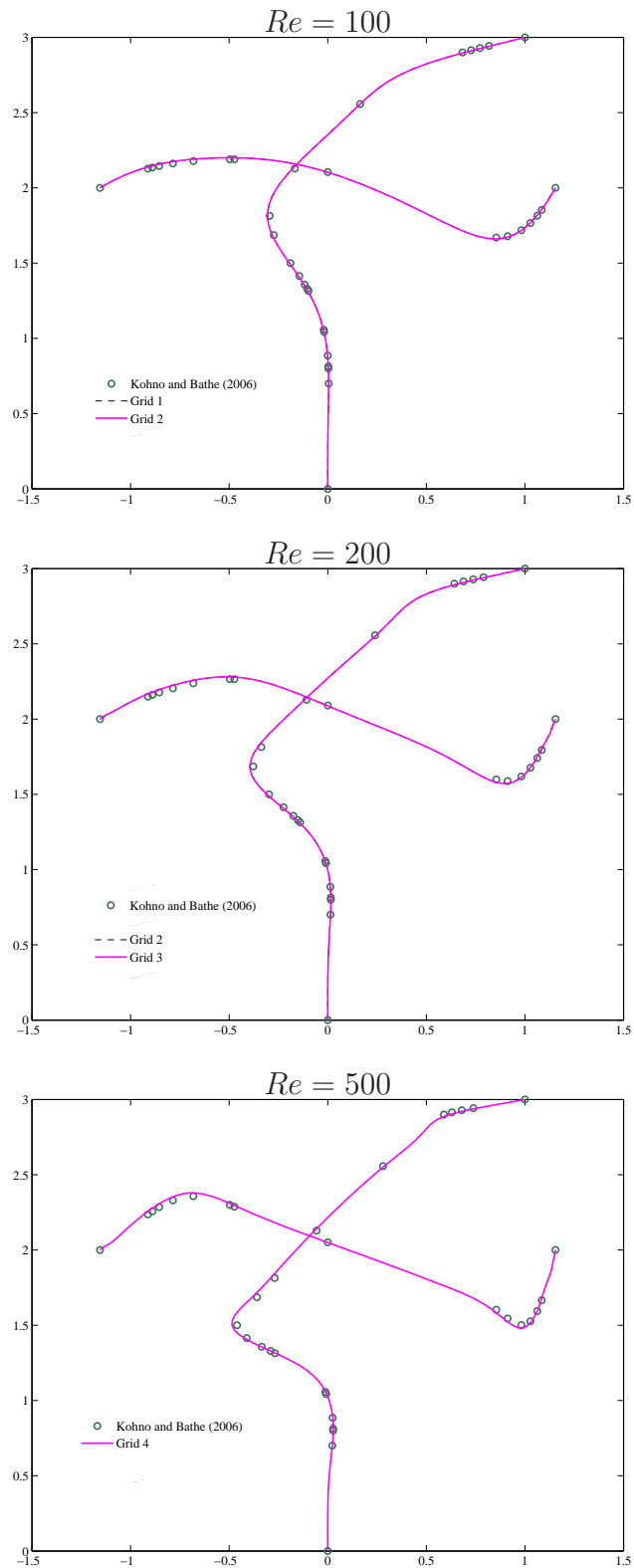


Figure 4.15: Triangular cavity flow: velocity profiles by the present method and the flow condition-based interpolation FEM (Kohno and Bathe 2006).

# Chapter 5

## A $C^2$ -continuous compact implicit method for parabolic equations

In this chapter, novel  $C^2$ -continuous compact schemes based on integrated radial basis function elements (IRBFEs) on uniform and nonuniform grids are proposed. Integrated radial basis functions are employed to construct approximations on a 2-node element. The approximations comprise nodal values and associated basis functions of the field variable and its first derivative at the two element extremes. Unlike previous IRBFE works, the basis functions are obtained in close forms in the present work which helps clarify the insight of  $C^2$ -continuity conditions across two adjacent elements. Such  $C^2$ -continuity conditions in fact create the novel compact schemes for derivatives, including consistent first and second derivative schemes on uniform grids and transformation-free schemes on nonuniform grids. The proposed  $C^2$ -continuous schemes are applied to the discretisation of second-order parabolic equations in one- (1D) and two-space dimensions (2D) in an implicit manner. Emphasis is placed on (i) combinations of the schemes with the implicit elimination approach to yield op-

timal tridiagonal system matrices on grid lines, especially for problems involving both first and second derivatives; and (ii) better choices of the RBF-width to yield better accuracy and rates of convergence. We verify the proposed method with solutions of several linear problems on rectangular and non-rectangular domains. We demonstrate the method with the solution of the 2D incompressible Navier-Stokes equation using the streamfunction-vorticity formulation for the non-linear lid-driven cavity flow problem where the obtained numerical results are compared with benchmark results available in the literature.

## 5.1 Introduction

Given the values of a function at nodes generated by a Cartesian grid, the finite difference approximations to the derivatives of the function can be expressed as linear combinations of the given function values. For simplicity, consider uniformly spaced nodes where the nodes are indexed by  $i$ . The independent variable at the node is  $\eta_i = h(i - 1)$  for  $1 \leq i \leq N$ , and the function values at the nodes  $i$ ,  $\phi_i$ , are given. The finite difference approximations to the first and second derivatives can be in conventional second-order forms (e.g. Pozrikidis 1997, Roache 1998), i.e.

$$\frac{\partial \phi_i}{\partial \eta} = \frac{\phi_{i+1} - \phi_{i-1}}{2h} + O(h^2), \quad (5.1)$$

$$\frac{\partial^2 \phi_i}{\partial \eta^2} = \frac{\phi_{i+1} - 2\phi_i + \phi_{i-1}}{h^2} + O(h^2), \quad (5.2)$$

or compact fourth-order forms (e.g. Collatz 1960, Hirsh 1975, Lele 1992), i.e.

$$\frac{1}{6} \frac{\partial \phi_{i-1}}{\partial \eta} + \frac{2}{3} \frac{\partial \phi_i}{\partial \eta} + \frac{1}{6} \frac{\partial \phi_{i+1}}{\partial \eta} = \frac{\phi_{i+1} - \phi_{i-1}}{2h} + O(h^4), \quad (5.3)$$

$$\frac{1}{12} \frac{\partial^2 \phi_{i-1}}{\partial \eta^2} + \frac{10}{12} \frac{\partial^2 \phi_i}{\partial \eta^2} + \frac{1}{12} \frac{\partial^2 \phi_{i+1}}{\partial \eta^2} = \frac{\phi_{i+1} - 2\phi_i + \phi_{i-1}}{h^2} + O(h^4). \quad (5.4)$$

It can be seen in (5.1) and (5.2) that the derivatives are explicitly obtained from the given function values while one has to solve tridiagonal systems to obtain the derivatives in (5.3) and (5.4). Compared to explicit finite difference schemes, the compact schemes are implicit and give a higher order of accuracy for the same number of grid nodes and also provide high resolution characteristics. In addition, compact schemes are more flexible in terms of application to complex geometries and boundary conditions when compared to spectral methods.

In terms of solution, compact schemes typically require solving a larger number of equations per grid node (Hirsh 1975). For problems involving only first or second derivatives (Type 1 problems), one has to solve  $2N$  equations for  $N$  grid nodes in 1D and  $3N$  equations for  $N$  grid nodes in 2D. The number of equations increases to  $3N$  and  $5N$  respectively for problems involving both first and second derivatives (Type 2 problems) such as the convection diffusion type equations. When Type 1 problems are time dependent and solved with a Crank-Nicolson scheme, one can easily reduce the system of equations to standard  $N$  equations for  $N$  grid nodes in 1D by means of the implicit elimination (Adam 1976). The resultant system matrix is in a tridiagonal form which can be solved effectively by the Thomas algorithms. In 2D, an operator-splitting technique can be applied to factorise a 2D problem into 1D problems in Cartesian directions whose systems are then transformed easily into standard tridiagonal forms. For Type 2 problems, to obtain the standard tridiagonal systems is not a trivial task since there is an inconsistency where the coefficients of the first and second derivative schemes are different as shown in the left hand sides of (5.3) and (5.4), respectively. As a result, one has to solve less-than-optimal banded matrices (e.g. Karaa and Zhang 2004, Karaa 2007) or use a second-order scheme for diffusion terms so that the coefficients match those of the fourth-order scheme for convection terms (Ma et al. 2012).

Recently, there is an emerging use of radial basis functions (RBFs) to construct approximations for the solution of partial differential equations (ODEs

and PDEs) (e.g. Fasshauer 2007, Kansa 1990, Mai-Duy and Tran-Cong 2001). Among RBFs, the Gaussian and multiquadric basis functions have potential for achieving a spectral accuracy (e.g. Madych 1992). RBF-based approximants can be constructed through differentiation (DRBFs) (Kansa 1990) or integration (IRBFs) (Mai-Duy and Tran-Cong 2001) using meshless scattered nodes or Cartesian grid. In the latter context, both classical and compact forms have been proposed. Given a stencil, compact forms have the ability to produce a higher order of accuracy than classical forms (Tolstykh and Shirobokov 2003, Wright and Fornberg 2006, Mai-Duy and Tran-Cong 2011b, An-Vo et al. 2011a,b, 2013, Mai-Duy and Tran-Cong 2013).

In An-Vo et al. (2011a), we developed local approximants based on 2-node IRBF elements (IRBFEs) for solving second-order elliptic PDEs defined on rectangular and non-rectangular domains in a conservative formulation. On such elements, IRBF approximations for the field variable and its derivatives involve not only nodal values of the field but also its first derivative at the two nodes of the element. In this chapter, we construct new compact schemes by imposing  $C^2$ -continuous conditions across the interface between two adjacent IRBFEs on uniform and nonuniform grids. The new compact schemes on uniform grids have consistent first and second derivative schemes and hence are very convenient for solving problems involving both first and second derivatives. We then apply the schemes to the discretisation of parabolic equations with a Crank-Nicholson time integration and the implicit elimination approach (Adam 1976) in 1D and 2D. Note that, in 2D, we adopt the ADI method (Peaceman and Rachford 1955, Douglas and Kim 2001) to split a 2D problems into 1D problems in Cartesian directions. The proposed method yields standard tridiagonal systems on each and every grid line in  $x$ - and then  $y$ -direction sequentially. We verify the proposed method through the solution of some linear problems and the lid-driven cavity flow in streamfunction-vorticity formulation where both first and second derivatives appear in the vorticity transport equation. It will be shown that the solutions are  $C^2$ -continuous.

The remainder of the chapter is organised as follows. In Section 5.2, we construct the new compact schemes on uniform and nonuniform grids. We then apply the schemes to parabolic equations in Section 5.3. Numerical results are given in Section 5.4 to demonstrate the attractiveness of the present method. Discussion is given in Section 5.5 and Section 5.6 concludes the chapter.

## 5.2 Proposed compact 2-node IRBF schemes

Mathematical expressions of the basis functions and their derivatives in physical space, i.e.  $\{\varphi_i(\eta), \partial\varphi_i(\eta)/\partial\eta, \partial^2\varphi_i(\eta)/\partial\eta^2\}_{i=1}^4$  in (3.11)-(3.13), can be obtained in closed form. We present here the analytic forms for  $\{\partial^2\varphi_i(\eta)/\partial\eta^2\}_{i=1}^4$  as follows.

$$\frac{\partial^2\varphi_1(\eta)}{\partial\eta^2} = \frac{-\left(\bar{I}_1^{(2)} + \bar{I}_2^{(2)}\right) B_2 + \bar{I}_1^{(2)} L_1 + \bar{I}_2^{(2)} L_2}{Dh^2}, \quad (5.5)$$

$$\frac{\partial^2\varphi_2(\eta)}{\partial\eta^2} = \frac{\left(\bar{I}_1^{(2)} + \bar{I}_2^{(2)}\right) B_2 - \bar{I}_1^{(2)} L_1 - \bar{I}_2^{(2)} L_2}{Dh^2}, \quad (5.6)$$

$$\frac{\partial^2\varphi_3(\eta)}{\partial\eta^2} = \frac{\left(\bar{I}_1^{(2)} + \bar{I}_2^{(2)}\right) B_1 - \bar{I}_1^{(2)} B_2 - \bar{I}_2^{(2)} R_2 - \bar{I}_1^{(2)} R_1 + \bar{I}_2^{(2)} L_2}{Dh}, \quad (5.7)$$

$$\frac{\partial^2\varphi_4(\eta)}{\partial\eta^2} = \frac{-\left(\bar{I}_1^{(2)} + \bar{I}_2^{(2)}\right) B_1 - \bar{I}_2^{(2)} B_2 + \bar{I}_2^{(2)} R_2 + \bar{I}_1^{(2)} R_1 + \bar{I}_1^{(2)} L_1}{Dh}, \quad (5.8)$$

where

$$\eta = \eta_1 + \bar{\eta}h, \quad 0 \leq \bar{\eta} \leq 1, \quad (5.9)$$

$$\bar{I}_1^{(2)} = \frac{I_1^{(2)}}{h} = \sqrt{\bar{\eta}^2 + \beta^2}, \quad (5.10)$$

$$\bar{I}_2^{(2)} = \frac{I_2^{(2)}}{h} = \sqrt{(\bar{\eta} - 1)^2 + \beta^2}, \quad (5.11)$$

$$R_1 = \frac{1}{6} \left[ (1 - 2\beta^2) \sqrt{1 + \beta^2} - 3\beta^2 \ln(-1 + \sqrt{1 + \beta^2}) \right], \quad (5.12)$$

$$R_2 = \frac{1}{6} \left[ (1 - 2\beta^2)\sqrt{1 + \beta^2} + 3\beta^2 \ln(1 + \sqrt{1 + \beta^2}) \right], \quad (5.13)$$

$$L_1 = \frac{1}{2} \left[ -\sqrt{1 + \beta^2} + \beta^2 \ln(-1 + \sqrt{1 + \beta^2}) \right], \quad (5.14)$$

$$L_2 = \frac{1}{2} \left[ \sqrt{1 + \beta^2} + \beta^2 \ln(1 + \sqrt{1 + \beta^2}) \right], \quad (5.15)$$

$$B_1 = -\frac{\beta^3}{3}, \quad (5.16)$$

$$B_2 = \frac{\beta^2 \ln \beta}{2}, \quad (5.17)$$

$$D = -B_2^2 + B_1(L_1 - L_2) + L_2 R_1 - L_1(R_2 - L_2) + B_2(R_2 - R_1). \quad (5.18)$$

The results for  $\{\varphi_i(\eta)\}_{i=1}^4$  and  $\{\partial\varphi_i(\eta)/\partial\eta\}_{i=1}^4$  can be found in the appendix B. It can be seen from (5.5)-(5.18) that the values of  $\{\partial^2\varphi_i(\eta)/\partial\eta^2\}_{i=1}^4$  depend only on  $\beta$ , the element length  $h$  and  $\bar{\eta}$ . In special cases of  $\eta = \eta_1$  ( $\bar{\eta} = 0$ ) and  $\eta = \eta_2$  ( $\bar{\eta} = 1$ ), we denote

$$\mu_i = \frac{\partial^2\varphi_i}{\partial\eta^2}(\eta_1) = \frac{\partial^2\varphi_i}{\partial\eta^2}(\bar{\eta} = 0), \quad (5.19)$$

$$\nu_i = \frac{\partial^2\varphi_i}{\partial\eta^2}(\eta_2) = \frac{\partial^2\varphi_i}{\partial\eta^2}(\bar{\eta} = 1), \quad i \in \{1, 2, 3, 4\}. \quad (5.20)$$

By using (5.5)-(5.8), we can verify that

$$\mu_1 = \nu_2 = -\mu_2 = -\nu_1, \quad (5.21)$$

$$\mu_3 = -\nu_4, \quad (5.22)$$

$$\mu_4 = -\nu_3. \quad (5.23)$$

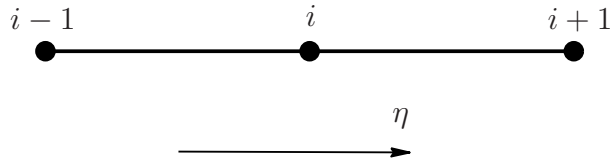


Figure 5.1: Schematic outline of a three-point stencil.

### 5.2.1 $C^2$ -continuous compact schemes on a uniform grid

Consider a three-point stencil as shown in Figure 5.1 where  $i = 2, 3, \dots, N_\eta - 1$ ,  $N_\eta$  is the total number of points on an  $\eta$ -grid line of a Cartesian grid. We can form two 2-node elements, i.e.  $[\eta_{i-1}, \eta_i]$  and  $[\eta_i, \eta_{i+1}]$  assumed as having the same element length  $h$ , to approximate the second derivatives at  $\eta_{i-1}$ ,  $\eta_i$ , and  $\eta_{i+1}$  via (3.13). Using element  $[\eta_{i-1}, \eta_i]$  with abbreviations (5.19) and (5.20) we obtain

$$\frac{\partial^2 \phi_{i-1}}{\partial \eta^2} = \mu_1 \phi_{i-1} + \mu_2 \phi_i + \mu_3 \frac{\partial \phi_{i-1}}{\partial \eta} + \mu_4 \frac{\partial \phi_i}{\partial \eta}, \quad (5.24)$$

$$\frac{\partial^2 \phi_i}{\partial \eta^2} = \nu_1 \phi_{i-1} + \nu_2 \phi_i + \nu_3 \frac{\partial \phi_{i-1}}{\partial \eta} + \nu_4 \frac{\partial \phi_i}{\partial \eta}. \quad (5.25)$$

Similarly using element  $[\eta_i, \eta_{i+1}]$  we have

$$\frac{\partial^2 \phi_i}{\partial \eta^2} = \mu_1 \phi_i + \mu_2 \phi_{i+1} + \mu_3 \frac{\partial \phi_i}{\partial \eta} + \mu_4 \frac{\partial \phi_{i+1}}{\partial \eta}, \quad (5.26)$$

$$\frac{\partial^2 \phi_{i+1}}{\partial \eta^2} = \nu_1 \phi_i + \nu_2 \phi_{i+1} + \nu_3 \frac{\partial \phi_i}{\partial \eta} + \nu_4 \frac{\partial \phi_{i+1}}{\partial \eta}. \quad (5.27)$$

#### First derivative scheme

From (5.25) and (5.26), the  $C^2$ -continuity condition at  $\eta_i$  gives us

$$\nu_1 \phi_{i-1} + \nu_2 \phi_i + \nu_3 \frac{\partial \phi_{i-1}}{\partial \eta} + \nu_4 \frac{\partial \phi_i}{\partial \eta} = \mu_1 \phi_i + \mu_2 \phi_{i+1} + \mu_3 \frac{\partial \phi_i}{\partial \eta} + \mu_4 \frac{\partial \phi_{i+1}}{\partial \eta}. \quad (5.28)$$

Making use of (5.21)-(5.23), equation (5.28) becomes

$$\frac{\partial \phi_{i-1}}{\partial \eta} + 2 \left( \frac{\mu_3}{\mu_4} \right) \frac{\partial \phi_i}{\partial \eta} + \frac{\partial \phi_{i+1}}{\partial \eta} = \frac{\mu_1}{\mu_4} (\phi_{i+1} - \phi_{i-1}) \quad (5.29)$$

or

$$\frac{\partial \phi_{i-1}}{\partial \eta} + 2 \left( \frac{\nu_4}{\nu_3} \right) \frac{\partial \phi_i}{\partial \eta} + \frac{\partial \phi_{i+1}}{\partial \eta} = \frac{\nu_1}{\nu_3} (\phi_{i+1} - \phi_{i-1}), \quad (5.30)$$

In matrix-vector notations, equations (5.29) or (5.30) can be rewritten as

$$L\Phi_\eta^{[\eta]} = A\Phi^{[\eta]}, \quad (5.31)$$

where  $\Phi^{[\eta]} = [\phi_1, \phi_2, \dots, \phi_{N_\eta}]^T$  which is the nodal value vector of an  $\eta$ -grid line,  $\Phi_\eta^{[\eta]}$  is the first derivative in  $\eta$ -direction.  $L$  and  $A$  are  $(N_\eta - 2) \times N_\eta$  tridiagonal matrices determined from equations (5.29) or (5.30). These equations are the compact implicit forms of first derivative approximation which guarantee that the approximation is  $C^2$ -continuous across the elements.

### Second derivative scheme

By adding (5.25) and (5.26) we get another form of  $C^2$ -continuity condition at  $\eta_i$ , i.e.

$$2\frac{\partial^2 \phi_i}{\partial \eta^2} = \left( \nu_1 \phi_{i-1} + \nu_2 \phi_i + \nu_3 \frac{\partial \phi_{i-1}}{\partial \eta} + \nu_4 \frac{\partial \phi_i}{\partial \eta} \right) + \left( \mu_1 \phi_i + \mu_2 \phi_{i+1} + \mu_3 \frac{\partial \phi_i}{\partial \eta} + \mu_4 \frac{\partial \phi_{i+1}}{\partial \eta} \right). \quad (5.32)$$

Making use of (5.21)-(5.23), equation (5.32) becomes

$$2\frac{\partial^2 \phi_i}{\partial \eta^2} = \mu_2 \phi_{i-1} + 2\mu_1 \phi_i + \mu_2 \phi_{i+1} + \mu_4 \left( \frac{\partial \phi_{i+1}}{\partial \eta} - \frac{\partial \phi_{i-1}}{\partial \eta} \right). \quad (5.33)$$

In a similar manner, adding (5.24) and (5.27) gives us

$$\frac{\partial^2 \phi_{i-1}}{\partial \eta^2} + \frac{\partial^2 \phi_{i+1}}{\partial \eta^2} = \mu_1 \phi_{i-1} + 2\mu_2 \phi_i + \mu_1 \phi_{i+1} + \mu_3 \left( \frac{\partial \phi_{i-1}}{\partial \eta} - \frac{\partial \phi_{i+1}}{\partial \eta} \right). \quad (5.34)$$

Multiply (5.33) by  $(\mu_3/\mu_4)$  and add the result to (5.34), one has

$$\frac{\partial^2 \phi_{i-1}}{\partial \eta^2} + 2 \left( \frac{\mu_3}{\mu_4} \right) \frac{\partial^2 \phi_i}{\partial \eta^2} + \frac{\partial^2 \phi_{i+1}}{\partial \eta^2} = \mu_1 \left( 1 - \frac{\mu_3}{\mu_4} \right) (\phi_{i-1} - 2\phi_i + \phi_{i+1}) \quad (5.35)$$

or

$$\frac{\partial^2 \phi_{i-1}}{\partial \eta^2} + 2 \left( \frac{\nu_4}{\nu_3} \right) \frac{\partial^2 \phi_i}{\partial \eta^2} + \frac{\partial^2 \phi_{i+1}}{\partial \eta^2} = \nu_2 \left( 1 - \frac{\nu_4}{\nu_3} \right) (\phi_{i-1} - 2\phi_i + \phi_{i+1}). \quad (5.36)$$

It can be seen that equations (5.35) or (5.36) can be written in matrix-vector notation as

$$L\Phi_{\eta\eta}^{[\eta]} = B\Phi^{[\eta]}, \quad (5.37)$$

where  $\Phi_{\eta\eta}^{[\eta]}$  is the second derivative vector in  $\eta$  direction of an  $\eta$ -grid line.  $B$  is a  $(N_\eta - 2) \times N_\eta$  tridiagonal matrix determined from the right hand sides of equations (5.35) or (5.36). These equations are the compact implicit forms of second derivative approximation which ensure the  $C^2$ -continuity condition across the elements.

### 5.2.2 $C^2$ -continuous compact schemes on a nonuniform grid

It is necessary to extend the above  $C^2$ -continuous compact schemes, i.e. (5.29)/(5.30) and (5.35)/(5.36), to a nonuniform distribution of grid nodes to adjust the numerical solution to complex boundaries and/or regions of high gradients or boundary layers. Consider a three-point stencil as shown in Figure 5.1 with a nonuniform distribution of points assumed as

$$\eta_i - \eta_{i-1} = \gamma_L h, \quad (5.38)$$

$$\eta_{i+1} - \eta_i = \gamma_R h, \quad (5.39)$$

where  $\gamma_L$  and  $\gamma_R$  denote length ratios of the elements to the left and right of  $\eta_i$  respectively. Applying (3.13) with similar abbreviations to (5.19) and (5.20) to

the left element, one gets

$$\frac{\partial^2 \phi_{i-1}}{\partial \eta^2} = (\mu_1)_L \phi_{i-1} + (\mu_2)_L \phi_i + (\mu_3)_L \frac{\partial \phi_{i-1}}{\partial \eta} + (\mu_4)_L \frac{\partial \phi_i}{\partial \eta}, \quad (5.40)$$

$$\frac{\partial^2 \phi_i}{\partial \eta^2} = (\nu_1)_L \phi_{i-1} + (\nu_2)_L \phi_i + (\nu_3)_L \frac{\partial \phi_{i-1}}{\partial \eta} + (\nu_4)_L \frac{\partial \phi_i}{\partial \eta}, \quad (5.41)$$

and to the right element, one gets

$$\frac{\partial^2 \phi_i}{\partial \eta^2} = (\mu_1)_R \phi_i + (\mu_2)_R \phi_{i+1} + (\mu_3)_R \frac{\partial \phi_i}{\partial \eta} + (\mu_4)_R \frac{\partial \phi_{i+1}}{\partial \eta}, \quad (5.42)$$

$$\frac{\partial^2 \phi_{i+1}}{\partial \eta^2} = (\nu_1)_R \phi_i + (\nu_2)_R \phi_{i+1} + (\nu_3)_R \frac{\partial \phi_i}{\partial \eta} + (\nu_4)_R \frac{\partial \phi_{i+1}}{\partial \eta}, \quad (5.43)$$

where  $(\cdot)_L$  and  $(\cdot)_R$  denotes values of the basis functions associated with the left and right elements, respectively. From (5.5)-(5.8) we have

$$(\mu_{1,2})_{L,R} = \frac{\mu_{1,2}}{\gamma_{L,R}^2}, \quad (\mu_{3,4})_{L,R} = \frac{\mu_{3,4}}{\gamma_{L,R}}, \quad (5.44)$$

$$(\nu_{1,2})_{L,R} = \frac{\nu_{1,2}}{\gamma_{L,R}^2}, \quad (\nu_{3,4})_{L,R} = \frac{\nu_{3,4}}{\gamma_{L,R}}. \quad (5.45)$$

### First derivative scheme

Making use of (5.41) and (5.42) with conditions (5.45) and (5.44), respectively, the  $C^2$ -continuous condition at  $\eta_i$  gives us

$$\frac{\nu_1}{\gamma_L^2} \phi_{i-1} + \frac{\nu_2}{\gamma_L^2} \phi_i + \frac{\nu_3}{\gamma_L} \frac{\partial \phi_{i-1}}{\partial \eta} + \frac{\nu_4}{\gamma_L} \frac{\partial \phi_i}{\partial \eta} = \frac{\mu_1}{\gamma_R^2} \phi_i + \frac{\mu_2}{\gamma_R^2} \phi_{i+1} + \frac{\mu_3}{\gamma_R} \frac{\partial \phi_i}{\partial \eta} + \frac{\mu_4}{\gamma_R} \frac{\partial \phi_{i+1}}{\partial \eta}. \quad (5.46)$$

By using (5.21)-(5.23) and rearranging (5.46), one obtains

$$\begin{aligned} \frac{\gamma_R}{\gamma_L} \frac{\partial \phi_{i-1}}{\partial \eta} + \frac{\mu_3}{\mu_4} \left( 1 + \frac{\gamma_R}{\gamma_L} \right) \frac{\partial \phi_i}{\partial \eta} + \frac{\partial \phi_{i+1}}{\partial \eta} = \\ \frac{1}{\gamma_L \mu_4} \left[ -\frac{\gamma_R}{\gamma_L} \phi_{i-1} + \left( \frac{\gamma_R}{\gamma_L} - \frac{\gamma_L}{\gamma_R} \right) \phi_i + \frac{\gamma_L}{\gamma_R} \phi_{i+1} \right]. \end{aligned} \quad (5.47)$$

It can be seen that (5.29) is a special case of (5.47) with  $\gamma_L = \gamma_R = 1$ .

### Second derivative scheme

Making use of (5.22) and (5.23), equations (5.40) and (5.43) give us

$$\frac{\partial^2 \phi_{i-1}}{\partial \eta^2} + \frac{\gamma_R}{\gamma_L} \frac{\partial^2 \phi_{i+1}}{\partial \eta^2} = \frac{\mu_1}{\gamma_L^2} \phi_{i-1} + \left( \frac{\mu_2}{\gamma_L^2} + \frac{\nu_1}{\gamma_L \gamma_R} \right) \phi_i + \frac{\nu_2}{\gamma_L \gamma_R} \phi_{i+1} + \frac{\mu_3}{\gamma_L} \left( \frac{\partial \phi_{i-1}}{\partial \eta} - \frac{\partial \phi_{i+1}}{\partial \eta} \right). \quad (5.48)$$

In a similar manner, (5.41) and (5.42) give us

$$\left( 1 + \frac{\gamma_R}{\gamma_L} \right) \frac{\partial^2 \phi_i}{\partial \eta^2} = \frac{\nu_1}{\gamma_L^2} \phi_{i-1} + \left( \frac{\nu_2}{\gamma_L^2} + \frac{\mu_1}{\gamma_L \gamma_R} \right) \phi_i + \frac{\mu_2}{\gamma_L \gamma_R} \phi_{i+1} - \frac{\mu_4}{\gamma_L} \left( \frac{\partial \phi_{i-1}}{\partial \eta} - \frac{\partial \phi_{i+1}}{\partial \eta} \right). \quad (5.49)$$

From (5.48) and (5.49) one obtains

$$\frac{1}{\mu_3} \left( \frac{\partial^2 \phi_{i-1}}{\partial \eta^2} + \frac{\gamma_R}{\gamma_L} \frac{\partial^2 \phi_{i+1}}{\partial \eta^2} \right) + \frac{1}{\mu_4} \left( 1 + \frac{\gamma_R}{\gamma_L} \right) \frac{\partial^2 \phi_i}{\partial \eta^2} = \frac{\mu_1}{\gamma_L^2} \left( \frac{1}{\mu_3} - \frac{1}{\mu_4} \right) \left[ \phi_{i-1} - \left( 1 + \frac{\gamma_L}{\gamma_R} \right) \phi_i + \frac{\gamma_L}{\gamma_R} \phi_{i+1} \right] \quad (5.50)$$

or

$$\frac{\partial^2 \phi_{i-1}}{\partial \eta^2} + \frac{\mu_3}{\mu_4} \left( 1 + \frac{\gamma_R}{\gamma_L} \right) \frac{\partial^2 \phi_i}{\partial \eta^2} + \frac{\gamma_R}{\gamma_L} \frac{\partial^2 \phi_{i+1}}{\partial \eta^2} = \frac{\mu_1}{\gamma_L^2} \left( 1 - \frac{\mu_3}{\mu_4} \right) \left[ \phi_{i-1} - \left( 1 + \frac{\gamma_L}{\gamma_R} \right) \phi_i + \frac{\gamma_L}{\gamma_R} \phi_{i+1} \right]. \quad (5.51)$$

When  $\gamma_L = \gamma_R = 1$  (5.51) reduces to (5.35).

(5.47) and (5.51) give us a transformation-free compact scheme on a nonuniform grid. Moreover, the approximations are  $C^2$ -continuous.

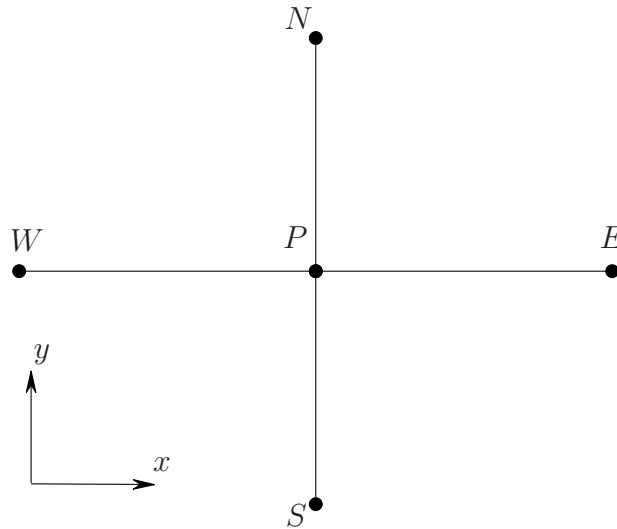


Figure 5.2: Schematic outline of a five-point stencil.

### 5.3 Application to parabolic equations

Consider the following form of parabolic equations

$$\frac{\partial \phi}{\partial t} = \frac{\partial^2 \phi}{\partial x^2} + \frac{\partial^2 \phi}{\partial y^2} + f, \quad (x, y)^T \in \Omega, \quad (5.52)$$

where  $f$  is some driving function.

The problem domain  $\Omega$  is embedded in a Cartesian grid. Grid points inside the problem domain are taken to be interior nodes, while boundary nodes are defined as the intersection of the grid lines and the boundaries. Let consider a grid point  $P$  and its neighbouring nodes as shown in Figure 5.2. Collocating equation (5.52) at  $P$  at the time instant  $t^n$  and approximating the time derivative by a finite difference, leading to

$$\frac{\phi_P^n - \phi_P^{n-1}}{\Delta t} = \gamma \left( \frac{\partial^2 \phi_P^n}{\partial x^2} + \frac{\partial^2 \phi_P^n}{\partial y^2} \right) + (1-\gamma) \left( \frac{\partial^2 \phi_P^{n-1}}{\partial x^2} + \frac{\partial^2 \phi_P^{n-1}}{\partial y^2} \right) + f_P^{n-1+\gamma}, \quad (5.53)$$

where  $\Delta t = t^n - t^{n-1}$  and  $0 \leq \gamma \leq 1$ . In the extreme cases, i.e.  $\gamma = 0$  and  $\gamma = 1$ , the first-order forward (fully explicit) and backward (fully implicit) Euler

methods are obtained, respectively. We are interested in the case  $\gamma = 0.5$  which is equivalent to the Crank-Nicolson method and second-order accurate in time. Equation (5.53) takes the form

$$\frac{\phi_P^n - \phi_P^{n-1}}{\Delta t} = \frac{1}{2} \left( \frac{\partial^2 \phi_P^n}{\partial x^2} + \frac{\partial^2 \phi_P^n}{\partial y^2} \right) + \frac{1}{2} \left( \frac{\partial^2 \phi_P^{n-1}}{\partial x^2} + \frac{\partial^2 \phi_P^{n-1}}{\partial y^2} \right) + f_P^{n-1/2}. \quad (5.54)$$

### 5.3.1 One-dimensional problems

Equation (5.54) reduces to

$$\frac{\phi_P^n - \phi_P^{n-1}}{\Delta t} = \frac{1}{2} \frac{\partial^2 \phi_P^n}{\partial x^2} + \frac{1}{2} \frac{\partial^2 \phi_P^{n-1}}{\partial x^2} + f_P^{n-1/2}. \quad (5.55)$$

Apply equation (5.55) at nodes  $W$  and  $E$  assumed as uniform distributions to the left and the right of  $P$  as shown in Figure 5.2, one has respectively

$$\frac{\phi_W^n - \phi_W^{n-1}}{\Delta t} = \frac{1}{2} \frac{\partial^2 \phi_W^n}{\partial x^2} + \frac{1}{2} \frac{\partial^2 \phi_W^{n-1}}{\partial x^2} + f_W^{n-1/2}, \quad (5.56)$$

$$\frac{\phi_E^n - \phi_E^{n-1}}{\Delta t} = \frac{1}{2} \frac{\partial^2 \phi_E^n}{\partial x^2} + \frac{1}{2} \frac{\partial^2 \phi_E^{n-1}}{\partial x^2} + f_E^{n-1/2}. \quad (5.57)$$

Multiply equation (5.55) by  $2(\mu_3/\mu_4)$  and then add the result, (5.56) and (5.57) together, we obtain

$$\begin{aligned} \frac{\phi_W^n - \phi_W^{n-1}}{\Delta t} + 2 \left( \frac{\mu_3}{\mu_4} \right) \frac{\phi_P^n - \phi_P^{n-1}}{\Delta t} + \frac{\phi_E^n - \phi_E^{n-1}}{\Delta t} = \\ \frac{1}{2} \left[ \frac{\partial^2 \phi_W^n}{\partial x^2} + 2 \left( \frac{\mu_3}{\mu_4} \right) \frac{\partial^2 \phi_P^n}{\partial x^2} + \frac{1}{2} \frac{\partial^2 \phi_E^n}{\partial x^2} \right] \\ + \frac{1}{2} \left[ \frac{\partial^2 \phi_W^{n-1}}{\partial x^2} + 2 \left( \frac{\mu_3}{\mu_4} \right) \frac{\partial^2 \phi_P^{n-1}}{\partial x^2} + \frac{1}{2} \frac{\partial^2 \phi_E^{n-1}}{\partial x^2} \right] \\ + f_W^{n-1/2} + 2 \left( \frac{\mu_3}{\mu_4} \right) f_P^{n-1/2} + f_E^{n-1/2}. \quad (5.58) \end{aligned}$$

Making use of (5.35) at steps  $n$  and  $n - 1$ , one obtains

$$\begin{aligned} \frac{\phi_W^n - \phi_W^{n-1}}{\Delta t} + 2 \left( \frac{\mu_3}{\mu_4} \right) \frac{\phi_P^n - \phi_P^{n-1}}{\Delta t} + \frac{\phi_E^n - \phi_E^{n-1}}{\Delta t} = \\ \frac{1}{2} \mu_1 \left( 1 - \frac{\mu_3}{\mu_4} \right) (\phi_W^n - 2\phi_P^n + \phi_E^n) + \frac{1}{2} \mu_1 \left( 1 - \frac{\mu_3}{\mu_4} \right) (\phi_W^{n-1} - 2\phi_P^{n-1} + \phi_E^{n-1}) \\ + f_W^{n-1/2} + 2 \left( \frac{\mu_3}{\mu_4} \right) f_P^{n-1/2} + f_E^{n-1/2}. \end{aligned} \quad (5.59)$$

A compact equation for  $\phi_P^n$  is obtained by rearranging (5.59) as

$$\begin{aligned} \left[ \frac{1}{\Delta t} - \frac{1}{2} \mu_1 \left( 1 - \frac{\mu_3}{\mu_4} \right) \right] \phi_W^n + \left[ \frac{2}{\Delta t} \frac{\mu_3}{\mu_4} + \mu_1 \left( 1 - \frac{\mu_3}{\mu_4} \right) \right] \phi_P^n + \\ \left[ \frac{1}{\Delta t} - \frac{1}{2} \mu_1 \left( 1 - \frac{\mu_3}{\mu_4} \right) \right] \phi_E^n = \left[ \frac{1}{\Delta t} + \frac{1}{2} \mu_1 \left( 1 - \frac{\mu_3}{\mu_4} \right) \right] \phi_W^{n-1} + \\ \left[ \frac{2}{\Delta t} \frac{\mu_3}{\mu_4} - \mu_1 \left( 1 - \frac{\mu_3}{\mu_4} \right) \right] \phi_P^{n-1} + \left[ \frac{1}{\Delta t} + \frac{1}{2} \mu_1 \left( 1 - \frac{\mu_3}{\mu_4} \right) \right] \phi_E^{n-1} \\ + f_W^{n-1/2} + 2 \left( \frac{\mu_3}{\mu_4} \right) f_P^{n-1/2} + f_E^{n-1/2}. \end{aligned} \quad (5.60)$$

Equation (5.60) leads to a tridiagonal system of algebraic equations for the problem, which can be solved efficiently with the Thomas algorithm (Fletcher 1991, Pozrikidis 1997). Equation (5.60) can be slightly different on a nonuniform grid where (5.51) is used instead of (5.35).

### Boundary treatment

It can be seen from (5.60) that Dirichlet boundary conditions are easily treated by the present solution strategy. The Neumann boundary conditions, however, require an additional treatment. Assuming that a Neumann condition is imposed at the right boundary and  $P$  is the adjacent node to the right boundary node  $b$ . The two nodes,  $P$  and  $b$ , form an element which helps to approximate  $\partial^2 \phi_P^n / \partial x^2$  in (5.55). Using (3.13) with abbreviation (5.19), one has

$$\frac{\phi_P^n - \phi_P^{n-1}}{\Delta t} = \frac{1}{2} \left( \mu_1 \phi_P^n + \mu_2 \phi_b^n + \mu_3 \frac{\partial \phi_P^n}{\partial x} + \mu_4 \frac{\partial \phi_b^n}{\partial x} \right) + \frac{1}{2} \frac{\partial^2 \phi_P^{n-1}}{\partial x^2} + f_P^{n-1/2}. \quad (5.61)$$

In a similar manner, apply equation (5.55) to the the boundary node  $b$  and

using (3.13) with abbreviation (5.20) to approximate  $\partial^2 \phi_b^n / \partial x^2$ , one obtains

$$\frac{\phi_b^n - \phi_b^{n-1}}{\Delta t} = \frac{1}{2} \left( \nu_1 \phi_P^n + \nu_2 \phi_b^n + \nu_3 \frac{\partial \phi_P^n}{\partial x} + \nu_4 \frac{\partial \phi_b^n}{\partial x} \right) + \frac{1}{2} \frac{\partial^2 \phi_b^{n-1}}{\partial x^2} + f_b^{n-1/2}. \quad (5.62)$$

Divide (5.61) by  $\mu_3$  and (5.62) by  $\mu_4$  then adding the results together and making use of (5.21)-(5.23), we obtain

$$\begin{aligned} \left[ \frac{1}{\mu_3 \Delta t} - \frac{1}{2} \left( \frac{\mu_1}{\mu_3} - \frac{\mu_1}{\mu_4} \right) \right] \phi_P^n + \left[ \frac{1}{\mu_4 \Delta t} + \frac{1}{2} \left( \frac{\mu_1}{\mu_3} - \frac{\mu_1}{\mu_4} \right) \right] \phi_b^n &= \frac{1}{\mu_3 \Delta t} \phi_P^{n-1} + \\ \frac{1}{\mu_4 \Delta t} \phi_b^{n-1} + \frac{1}{2} \left( \frac{\mu_4}{\mu_3} - \frac{\mu_3}{\mu_4} \right) \frac{\partial \phi_b^n}{\partial x} + \frac{1}{2\mu_3} \frac{\partial^2 \phi_P^{n-1}}{\partial x^2} + \frac{1}{2\mu_4} \frac{\partial^2 \phi_b^{n-1}}{\partial x^2} + \frac{1}{\mu_3} f_P^{n-1/2} & \\ + \frac{1}{\mu_4} f_b^{n-1/2}. & \quad (5.63) \end{aligned}$$

In a similar manner, if Neumann condition is at the left boundary and  $P$  is the adjacent grid node to the left boundary node  $b$ , we have

$$\begin{aligned} \left[ \frac{1}{\mu_4 \Delta t} + \frac{1}{2} \left( \frac{\mu_1}{\mu_3} - \frac{\mu_1}{\mu_4} \right) \right] \phi_b^n + \left[ \frac{1}{\mu_3 \Delta t} - \frac{1}{2} \left( \frac{\mu_1}{\mu_3} - \frac{\mu_1}{\mu_4} \right) \right] \phi_P^n &= \frac{1}{\mu_4 \Delta t} \phi_b^{n-1} + \\ \frac{1}{\mu_3 \Delta t} \phi_P^{n-1} + \frac{1}{2} \left( \frac{\mu_3}{\mu_4} - \frac{\mu_4}{\mu_3} \right) \frac{\partial \phi_b^n}{\partial x} + \frac{1}{2\mu_4} \frac{\partial^2 \phi_b^{n-1}}{\partial x^2} + \frac{1}{2\mu_3} \frac{\partial^2 \phi_P^{n-1}}{\partial x^2} + \frac{1}{\mu_4} f_b^{n-1/2} & \\ + \frac{1}{\mu_3} f_P^{n-1/2}. & \quad (5.64) \end{aligned}$$

$\partial^2 \phi_b^{n-1} / \partial x^2$  can be calculated by a global 1D-IRBF approximation (Mai-Duy and Tanner 2007). Equation (5.63) or (5.64) involves the Neumann boundary value  $\partial \phi_b^n / \partial x$  in the right hand side and together with  $N-2$  algebraic equations (5.60) associated with  $N-2$  interior nodes, leads to a tridiagonal system of  $N-1$  equations for  $N-1$  unknowns. Note that the solution is  $C^2$ -continuous.

### 5.3.2 Two-dimensional problems

We apply the ADI (Alternating-Direction Implicit) procedure (Peaceman and Rachford 1955, Douglas and Gunn 1964) to solve equation (5.54). This procedure treats the spatial derivatives in each Cartesian direction individually in a

cyclic fashion with two half steps, i.e.

$$\frac{\phi_P^{n-1/2} - \phi_P^{n-1}}{\Delta t/2} = \frac{\partial^2 \phi_P^{n-1/2}}{\partial x^2} + \frac{\partial^2 \phi_P^{n-1}}{\partial y^2} + f_P^{n-1/2}, \quad (5.65)$$

$$\frac{\phi_P^n - \phi_P^{n-1/2}}{\Delta t/2} = \frac{\partial^2 \phi_P^{n-1/2}}{\partial x^2} + \frac{\partial^2 \phi_P^n}{\partial y^2} + f_P^{n-1/2}, \quad (5.66)$$

where the splitting error term is given by

$$\frac{\Delta t}{4} \frac{\partial^2}{\partial x^2} \frac{\partial^2}{\partial y^2} (\phi_P^n - \phi_P^{n-1}). \quad (5.67)$$

It is noted that the above ADI procedure (5.65) and (5.66) can be interpreted as a perturbation of the Crank-Nicolson time difference equation (5.54).

We now write the same form of equation (5.65) at nodes  $W$  and  $E$  assumed as uniform distributions to  $P$ , i.e.

$$\frac{\phi_W^{n-1/2} - \phi_W^{n-1}}{\Delta t/2} = \frac{\partial^2 \phi_W^{n-1/2}}{\partial x^2} + \frac{\partial^2 \phi_W^{n-1}}{\partial y^2} + f_W^{n-1/2}, \quad (5.68)$$

$$\frac{\phi_E^{n-1/2} - \phi_E^{n-1}}{\Delta t/2} = \frac{\partial^2 \phi_E^{n-1/2}}{\partial x^2} + \frac{\partial^2 \phi_E^{n-1}}{\partial y^2} + f_E^{n-1/2}. \quad (5.69)$$

Multiply equation (5.65) by  $2(\mu_3/\mu_4)$  then add the result, (5.68) and (5.69) together one has

$$\begin{aligned} & \frac{\phi_W^{n-1/2} - \phi_W^{n-1}}{\Delta t/2} + 2 \left( \frac{\mu_3}{\mu_4} \right) \frac{\phi_P^{n-1/2} - \phi_P^{n-1}}{\Delta t/2} + \frac{\phi_E^{n-1/2} - \phi_E^{n-1}}{\Delta t/2} = \frac{\partial^2 \phi_W^{n-1/2}}{\partial x^2} + \\ & 2 \left( \frac{\mu_3}{\mu_4} \right) \frac{\partial^2 \phi_P^{n-1/2}}{\partial x^2} + \frac{\partial^2 \phi_E^{n-1/2}}{\partial x^2} + \frac{\partial^2 \phi_W^{n-1}}{\partial y^2} + 2 \left( \frac{\mu_3}{\mu_4} \right) \frac{\partial^2 \phi_P^{n-1}}{\partial y^2} + \frac{\partial^2 \phi_E^{n-1}}{\partial y^2} \\ & + f_W^{n-1/2} + 2 \left( \frac{\mu_3}{\mu_4} \right) f_P^{n-1/2} + f_E^{n-1/2}. \quad (5.70) \end{aligned}$$

Making use of (5.35), equation (5.70) becomes

$$\begin{aligned} & \frac{\phi_W^{n-1/2} - \phi_W^{n-1}}{\Delta t/2} + 2 \left( \frac{\mu_3}{\mu_4} \right) \frac{\phi_P^{n-1/2} - \phi_P^{n-1}}{\Delta t/2} + \frac{\phi_E^{n-1/2} - \phi_E^{n-1}}{\Delta t/2} = \\ & \mu_1 \left( 1 - \frac{\mu_3}{\mu_4} \right) (\phi_W^{n-1/2} - 2\phi_P^{n-1/2} + \phi_E^{n-1/2}) + \frac{\partial^2 \phi_W^{n-1}}{\partial y^2} + 2 \left( \frac{\mu_3}{\mu_4} \right) \frac{\partial^2 \phi_P^{n-1}}{\partial y^2} + \frac{\partial^2 \phi_E^{n-1}}{\partial y^2} \\ & \quad + f_W^{n-1/2} + 2 \left( \frac{\mu_3}{\mu_4} \right) f_P^{n-1/2} + f_E^{n-1/2}. \end{aligned} \quad (5.71)$$

Equation (5.71) can be rewritten as

$$\begin{aligned} & \left[ \frac{1}{\Delta t/2} - \mu_1 \left( 1 - \frac{\mu_3}{\mu_4} \right) \right] \phi_W^{n-1/2} + 2 \left[ \left( \frac{\mu_3}{\mu_4} \right) \frac{1}{\Delta t/2} + \mu_1 \left( 1 - \frac{\mu_3}{\mu_4} \right) \right] \phi_P^{n-1/2} + \\ & \left[ \frac{1}{\Delta t/2} - \mu_1 \left( 1 - \frac{\mu_3}{\mu_4} \right) \right] \phi_E^{n-1/2} = \frac{1}{\Delta t/2} \phi_W^{n-1} + 2 \left( \frac{\mu_3}{\mu_4} \right) \frac{1}{\Delta t/2} \phi_P^{n-1} + \frac{1}{\Delta t/2} \phi_E^{n-1} \\ & + \frac{\partial^2 \phi_W^{n-1}}{\partial y^2} + 2 \left( \frac{\mu_3}{\mu_4} \right) \frac{\partial^2 \phi_P^{n-1}}{\partial y^2} + \frac{\partial^2 \phi_E^{n-1}}{\partial y^2} + f_W^{n-1/2} + 2 \left( \frac{\mu_3}{\mu_4} \right) f_P^{n-1/2} + f_E^{n-1/2}. \end{aligned} \quad (5.72)$$

Equation (5.72) is an equation for  $\phi_P^{n-1/2}$  in the  $x$ -direction. In a similar manner, assume that  $S$  and  $N$  are uniformly distributed to the south and north of  $P$ , one can transform (5.66) into an equation for  $\phi_P^n$  in the  $y$ -direction, i.e.

$$\begin{aligned} & \left[ \frac{1}{\Delta t/2} - \mu_1 \left( 1 - \frac{\mu_3}{\mu_4} \right) \right] \phi_S^n + 2 \left[ \left( \frac{\mu_3}{\mu_4} \right) \frac{1}{\Delta t/2} + \mu_1 \left( 1 - \frac{\mu_3}{\mu_4} \right) \right] \phi_P^n + \\ & \left[ \frac{1}{\Delta t/2} - \mu_1 \left( 1 - \frac{\mu_3}{\mu_4} \right) \right] \phi_N^n = \frac{1}{\Delta t/2} \phi_S^{n-1/2} + 2 \left( \frac{\mu_3}{\mu_4} \right) \frac{1}{\Delta t/2} \phi_P^{n-1/2} + \frac{1}{\Delta t/2} \phi_E^{n-1/2} \\ & + \frac{\partial^2 \phi_S^{n-1/2}}{\partial x^2} + 2 \left( \frac{\mu_3}{\mu_4} \right) \frac{\partial^2 \phi_P^{n-1/2}}{\partial x^2} + \frac{\partial^2 \phi_N^{n-1/2}}{\partial x^2} + f_S^{n-1/2} + 2 \left( \frac{\mu_3}{\mu_4} \right) f_P^{n-1/2} + f_N^{n-1/2}. \end{aligned} \quad (5.73)$$

Equations (5.72) and (5.73) will be slightly different with nonuniform distributions of grid points where (5.51) is used instead of (5.35). Collection of equations (5.72) or (5.73) for all nodal points on an  $x$ - or a  $y$ -grid line, respectively, leads to a tridiagonal system which can be efficiently solved by the Thomas algorithm.

### Boundary treatment

From (5.72) and (5.73) we can see that the Dirichlet boundary conditions are easily imposed on the system of algebraic equations on each and every grid line. The imposition of Neumann conditions, however, need an additional treatment similar to those in the one-dimensional case. Since the treatment is similar between an  $x$ - and a  $y$ -grid line we present here the treatment for an  $x$ -grid line only. If the Neumann condition is on the left boundary we have

$$\begin{aligned} & \left[ \frac{1}{\mu_4 \Delta t / 2} + \left( \frac{\mu_1}{\mu_3} - \frac{\mu_1}{\mu_4} \right) \right] \phi_b^{n-1/2} + \left[ \frac{1}{\mu_3 \Delta t / 2} - \left( \frac{\mu_1}{\mu_3} - \frac{\mu_1}{\mu_4} \right) \right] \phi_P^{n-1/2} = \\ & \frac{1}{\mu_4 \Delta t / 2} \phi_b^{n-1} + \frac{1}{\mu_3 \Delta t / 2} \phi_P^{n-1} + \left( \frac{\mu_3}{\mu_4} - \frac{\mu_4}{\mu_3} \right) \frac{\partial \phi_b^{n-1/2}}{\partial x} + \frac{1}{\mu_4} \frac{\partial^2 \phi_b^{n-1}}{\partial y^2} + \frac{1}{\mu_3} \frac{\partial^2 \phi_P^{n-1}}{\partial y^2} \\ & \quad + \frac{1}{\mu_4} f_b^{n-1/2} + \frac{1}{\mu_3} f_P^{n-1/2}, \quad (5.74) \end{aligned}$$

where  $b$  is the Neumann boundary node and  $P$  is its adjacent grid node. For the Neumann condition on the right boundary we have

$$\begin{aligned} & \left[ \frac{1}{\mu_3 \Delta t / 2} - \left( \frac{\mu_1}{\mu_3} - \frac{\mu_1}{\mu_4} \right) \right] \phi_P^{n-1/2} + \left[ \frac{1}{\mu_4 \Delta t / 2} + \left( \frac{\mu_1}{\mu_3} - \frac{\mu_1}{\mu_4} \right) \right] \phi_b^{n-1/2} = \\ & \frac{1}{\mu_3 \Delta t / 2} \phi_P^{n-1} + \frac{1}{\mu_4 \Delta t / 2} \phi_b^{n-1} + \left( \frac{\mu_4}{\mu_3} - \frac{\mu_3}{\mu_4} \right) \frac{\partial \phi_b^{n-1/2}}{\partial x} + \frac{1}{\mu_3} \frac{\partial^2 \phi_P^{n-1}}{\partial y^2} + \frac{1}{\mu_4} \frac{\partial^2 \phi_b^{n-1}}{\partial y^2} \\ & \quad + \frac{1}{\mu_3} f_P^{n-1/2} + \frac{1}{\mu_4} f_b^{n-1/2}, \quad (5.75) \end{aligned}$$

Equations (5.74) and/or (5.75) and  $N_x - 2$  equations (5.72) associated with  $N_x - 2$  interior grid nodes of an  $x$ -grid line form a system of  $N_x$  or  $N_x - 1$  algebraic equations for  $N_x$  or  $N_x - 1$  unknowns. Similarly, we can form a system of  $N_y$  or  $N_y - 1$  equations on a  $y$ -grid line with Neumann boundary conditions.

## 5.4 Numerical examples

The proposed method is verified through the solution of linear and non-linear problems. For all numerical examples presented in this study, the MQ shape parameter  $a$  is simply chosen proportionally to the element length  $h$  by a factor  $\beta$ .

The effects of the shape parameter on the solution accuracy is thus investigated through the parameter  $\beta$ .

### 5.4.1 Example 1: one-dimensional problem

Consider the following one-dimensional problem

$$\frac{\partial \phi}{\partial t} = \frac{\partial^2 \phi}{\partial x^2} + \sin(2\pi x)(\cos t + 4\pi^2 \sin t), \quad 0 \leq x \leq 1, \quad (5.76)$$

with two possible sets of boundary conditions:

$$\phi = 0 \text{ at } x = 0 \text{ and } x = 1 \text{ or} \quad (5.77)$$

$$\phi = 0 \text{ at } x = 0 \text{ and } \frac{\partial \phi}{\partial x} = 2\pi \sin t \text{ at } x = 1. \quad (5.78)$$

The exact solution can be verified as  $\phi^{(e)}(x, t) = \sin(2\pi x) \sin t$ .

Calculations are conducted using several uniform grids, from 21 to 63 nodes with an increment of 2, to study the effects of the grid size  $h$ . The time step  $\Delta t$  is chosen to be 0.001.

*Dirichlet boundary conditions only (5.77):* Results concerning the solution accuracy at  $t = 1$ , the convergence rate and the matrix condition by the classical 3-point finite difference implicit method (FDM) and the present  $C^2$ -continuous compact 2-node IRBF implicit method (C2NIRBFM) are presented in Table 5.1. For the latter, the factor  $\beta$  is chosen to be 231. The condition numbers of the system matrix, denoted by  $\text{cond}(A)$ , indicate that the present method is better conditioned than the FDM. In terms of accuracy, the proposed method converges faster. The point (grid)-wise order of accuracy is about 2 for the FDM but can be up to 148.75 for the present method. In an average sense, the 3-point FD and the C2NIRBF solutions converge apparently as  $O(h^{2.00})$  and

$O(h^{4.90})$ , respectively. For the 63 point grid, the error  $Ne(u)$  is  $8.42 \times 10^{-4}$  for FDM and  $4.38 \times 10^{-7}$  for the C2NIRBFM. Note that the system matrices are tridiagonal in the two methods and hence the CPU times are fairly comparable for a given grid size. The proposed method is therefore much more efficient than the 3-point FD method for a given accuracy.

Figure 5.3 shows the error distributions in a wide range of  $\beta$  for three different grids at a fixed time  $t = 1$ . It can be seen that there are good ranges of  $\beta$  values where the solution accuracy is improved significantly and an optimal  $\beta$  for each grid. Figures 5.4 and 5.5 present the accuracy of the proposed method at each time level for the field variable and its first derivative respectively associated with the grid  $N = 63$ . FD results are also included for comparison purpose. It can be seen that the present method using good values of  $\beta$  yields much more accurate results than the classical FD ones. With  $\beta = 231$  (optimal  $\beta$ ), about 3 orders of magnitude improvements are obtained for both the field variable and its first derivative. The proposed  $C^2$ -continuous method thus results in high levels of accuracy for not only the field variable but also its first derivative. Moreover, the accuracy can be controlled effectively by means of the MQ width ( $\beta$ ). Note that the first derivative values on boundaries are estimated by a global 1D-IRBF approximation (Mai-Duy and Tanner 2007) in the present calculation and involved in the first derivative approximation in the interior domain via (5.29)/(5.30). In previous IRBFE works, i.e. An-Vo et al. (2011b, 2013), semi-interior elements are employed at the boundaries and we ignore the boundary derivative values which leads to a lower accuracy at the boundaries compared with the interior domain. Figure 5.6 presents the first derivative error distribution on the problem domain of the direct IRBFE method (An-Vo et al. 2011b, 2013) and the present method using a grid of  $N = 11$  at  $t = 1$ . It can be seen that the errors are equivalent at the boundaries and the interior domain for the latter while the errors are high at boundary for the former. The relative  $L_2$  errors are  $3.27 \times 10^{-2}$  and  $8.51 \times 10^{-2}$  for the present method and the direct IRBFE method respectively.

Table 5.1: One-dimensional problem, Dirichlet boundary conditions only,  $N = (21, 23, \dots, 63)$ ,  $\Delta t = 0.001$ : condition numbers of the system matrix and relative  $L_2$  errors of the approximate solution  $\phi$  at  $t = 1$  for various values of  $h$  by the 3-point FD method and the present compact 2-point IRBF method ( $\beta = 231$ ). LCR stands for local convergence rate.

$h$	3-point FD			Present compact 2-point IRBF		
	cond(A)	$Ne(\phi)$	LCR	cond(A)	$Ne(\phi)$	LCR
$5.00e-2$	1.80	$8.12e-3$		1.13	$7.21e-3$	
$4.55e-2$	1.97	$6.71e-3$	2.01	1.30	$5.82e-3$	2.25
$4.17e-2$	2.15	$5.63e-3$	2.01	1.48	$4.76e-3$	2.31
$3.85e-2$	2.35	$4.80e-3$	2.01	1.68	$3.93e-3$	2.38
$3.57e-2$	2.57	$4.14e-3$	2.01	1.90	$3.28e-3$	2.46
$3.33e-2$	2.80	$3.60e-3$	2.00	2.13	$2.75e-3$	2.56
$3.13e-2$	3.05	$3.16e-3$	2.00	2.38	$2.31e-3$	2.66
$2.94e-2$	3.31	$2.80e-3$	2.00	2.64	$1.95e-3$	2.79
$2.78e-2$	3.59	$2.50e-3$	2.00	2.92	$1.65e-3$	2.93
$2.63e-2$	3.89	$2.24e-3$	2.00	3.22	$1.40e-3$	3.10
$2.50e-2$	4.20	$2.02e-3$	2.00	3.53	$1.18e-3$	3.31
$2.38e-2$	4.53	$1.84e-3$	2.00	3.86	$9.92e-4$	3.55
$2.27e-2$	4.87	$1.67e-3$	2.00	4.20	$8.29e-4$	3.85
$2.17e-2$	5.23	$1.53e-3$	2.00	4.56	$6.87e-4$	4.22
$2.08e-2$	5.61	$1.41e-3$	2.00	4.94	$5.63e-4$	4.70
$2.00e-2$	6.00	$1.29e-3$	2.00	5.33	$4.53e-4$	5.33
$1.92e-2$	6.41	$1.20e-3$	2.00	5.74	$3.55e-4$	6.19
$1.85e-2$	6.83	$1.11e-3$	2.00	6.16	$2.68e-4$	7.44
$1.79e-2$	7.27	$1.03e-3$	2.00	6.60	$1.90e-4$	9.42
$1.72e-2$	7.73	$9.62e-4$	2.00	7.06	$1.20e-4$	13.04
$1.67e-2$	8.20	$8.99e-4$	2.00	7.53	$5.75e-5$	21.84
$1.61e-2$	8.69	$8.42e-4$	2.00	8.01	$4.38e-7$	148.75
		$O(h^{2.00})$			$O(h^{4.90})$	

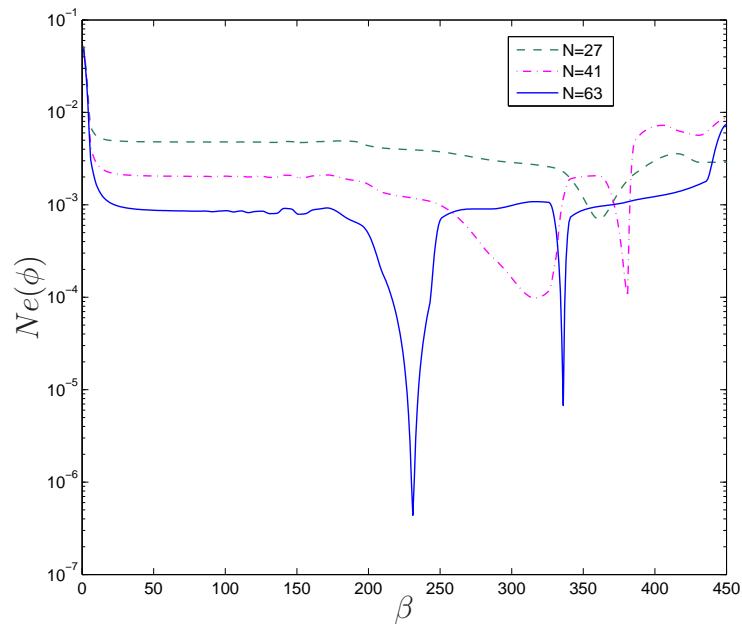


Figure 5.3: One-dimensional problem, Dirichlet boundary conditions only,  $\Delta t = 0.001$ : Relative  $L_2$  errors of the approximation solution  $\phi$  at  $t = 1$  against the RBF width ( $\beta$ ) for three different grids.

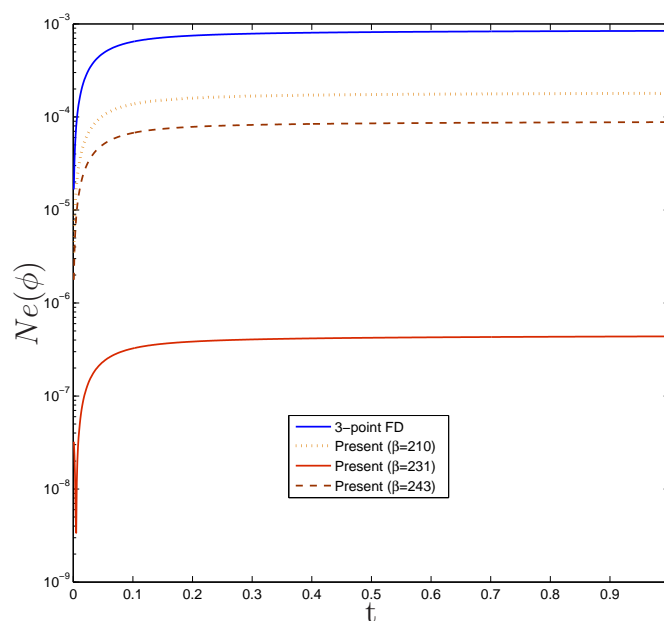


Figure 5.4: One-dimensional problem, Dirichlet boundary conditions only,  $N = 63$ ,  $\Delta t = 0.001$ : Comparison of the accuracy of the field variable at each time level between the classical Crank-Nicolson method and the present Crank-Nicolson method. For the latter, three values of  $\beta$ , i.e. 210, 231 and 243, are employed.

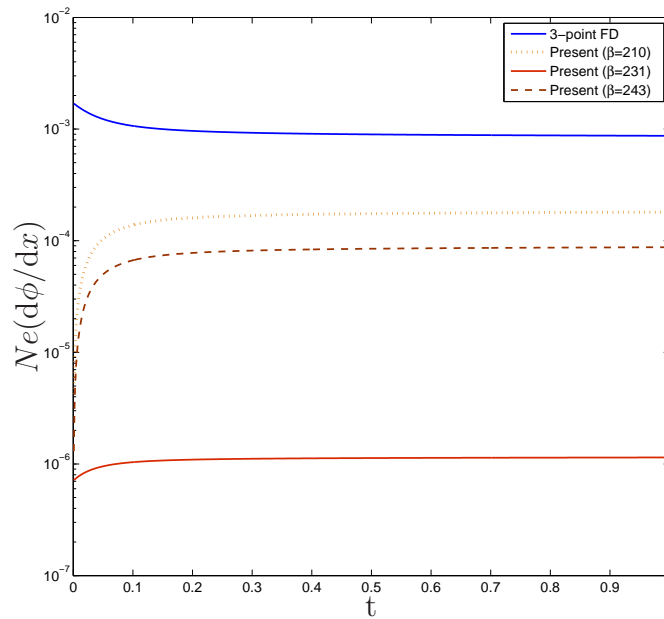


Figure 5.5: One-dimensional problem, Dirichlet boundary conditions only,  $N = 63$ ,  $\Delta t = 0.001$ : Comparison of the accuracy of the first derivative at each time level between the classical Crank-Nicolson method and the present Crank-Nicolson method. For the latter, three values of  $\beta$ , i.e. 210, 231 and 243, are employed.

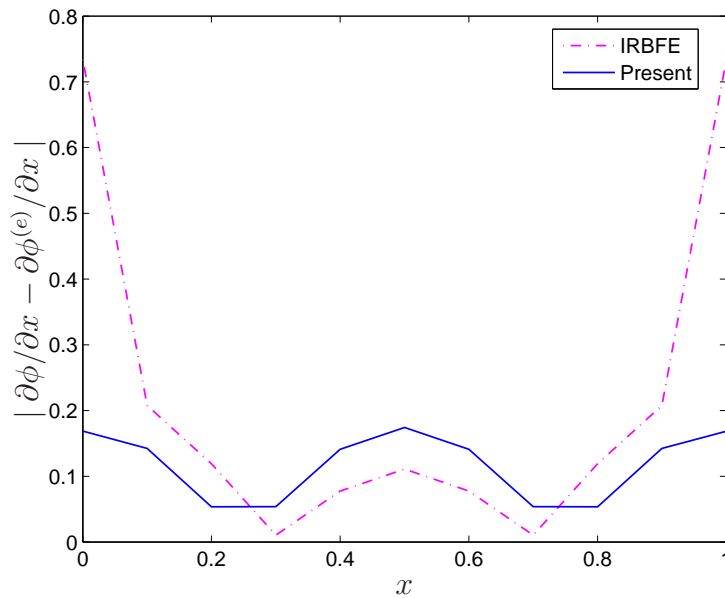


Figure 5.6: One-dimensional problem, Dirichlet boundary conditions only,  $N = 11$ ,  $\beta = 15$ ,  $\Delta t = 0.001$ : Error distribution on the problem domain of the present method and the direct IRBFE method (An-Vo et al. 2011b, 2013) for the first derivative at  $t = 1$ .

Table 5.2: One-dimensional problem, Dirichlet and Neumann boundary conditions,  $N = (21, 23, \dots, 63)$ ,  $\Delta t = 0.001$ : condition numbers of the system matrix and relative  $L_2$  errors of the approximate solution  $\phi$  at  $t = 1$  for various values of  $h$  by the 3-point FD method and the present compact 2-point IRBF method ( $\beta = 231$ ). LCR stands for local convergence rate.

$h$	3-point FD			Present compact 2-point IRBF		
	cond(A)	$Ne(\phi)$	LCR	cond(A)	$Ne(\phi)$	LCR
$5.00e-2$	2.22	$2.85e-2$		$3.51e+2$	$2.90e-2$	
$4.55e-2$	2.47	$2.35e-2$	2.05	$4.29e+2$	$2.34e-2$	2.24
$4.17e-2$	2.75	$1.97e-2$	2.05	$5.18e+2$	$1.91e-2$	2.34
$3.85e-2$	3.06	$1.67e-2$	2.04	$6.20e+2$	$1.57e-2$	2.40
$3.57e-2$	3.39	$1.44e-2$	2.04	$7.34e+2$	$1.31e-2$	2.46
$3.33e-2$	3.74	$1.25e-2$	2.04	$8.61e+2$	$1.10e-2$	2.58
$3.13e-2$	4.11	$1.09e-2$	2.03	$1.00e+3$	$9.26e-3$	2.63
$2.94e-2$	4.51	$9.67e-3$	2.03	$1.16e+3$	$7.81e-3$	2.82
$2.78e-2$	4.93	$8.61e-3$	2.03	$1.33e+3$	$6.60e-3$	2.95
$2.63e-2$	5.37	$7.72e-3$	2.03	$1.52e+3$	$5.58e-3$	3.09
$2.50e-2$	5.84	$6.95e-3$	2.03	$1.73e+3$	$4.71e-3$	3.33
$2.38e-2$	6.33	$6.30e-3$	2.03	$1.95e+3$	$3.95e-3$	3.57
$2.27e-2$	6.84	$5.73e-3$	2.02	$2.20e+3$	$3.30e-3$	3.88
$2.17e-2$	7.37	$5.24e-3$	2.02	$2.46e+3$	$2.74e-3$	4.19
$2.08e-2$	7.92	$4.81e-3$	2.02	$2.75e+3$	$2.24e-3$	4.69
$2.00e-2$	8.49	$4.43e-3$	2.02	$3.05e+3$	$1.80e-3$	5.34
$1.92e-2$	9.09	$4.09e-3$	2.02	$3.38e+3$	$1.41e-3$	6.20
$1.85e-2$	9.71	$3.79e-3$	2.02	$3.73e+3$	$1.07e-3$	7.40
$1.79e-2$	10.35	$3.52e-3$	2.02	$4.10e+3$	$7.61e-4$	9.37
$1.72e-2$	11.00	$3.28e-3$	2.02	$4.50e+3$	$4.82e-4$	12.99
$1.67e-2$	11.68	$3.06e-3$	2.02	$4.93e+3$	$2.32e-4$	21.55
$1.61e-2$	12.39	$2.87e-3$	2.02	$5.37e+3$	$5.98e-6$	111.62
		$O(h^{2.03})$			$O(h^{4.67})$	

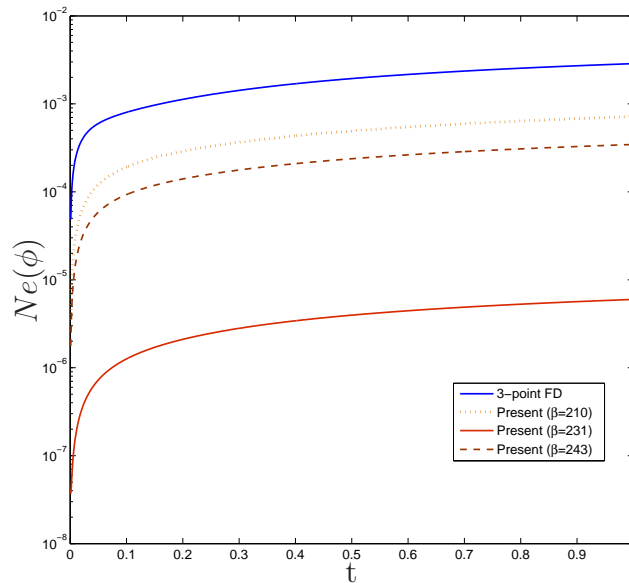


Figure 5.7: One-dimensional problem, Dirichlet and Neumann boundary conditions,  $N = 63$ ,  $\Delta t = 0.001$ : Comparison of the accuracy of the field variable at each time level between the classical Crank-Nicolson method and the present Crank-Nicolson method. For the latter, three values of  $\beta$ , i.e. 210, 231 and 243, are employed.

*Dirichlet and Neumann boundary conditions (5.78)*: Table 5.2 presents results regarding the solution accuracy at  $t = 1$ , the convergence rate and the matrix condition of the FDM and the present method (using  $\beta = 231$ ). It can be seen that the matrix condition numbers of the present method are quite higher than those of the classical FD method. In terms of accuracy, faster convergence is obtained. The point-wise order of accuracy can be up to 111.62 in the proposed method. The average order of accuracy is  $O(h^{4.67})$  which is much higher than  $O(h^{2.03})$  for the FDM. For the 63 point grid, the  $L_2$  error is  $2.87 \times 10^{-3}$  for FDM and  $5.98 \times 10^{-6}$  for the C2NIRBFM. Note that a ghost node has to be used to impose the Neumann boundary condition in the FDM.

Figures 5.7 and 5.8 present a comparison of the accuracy between the present method and the classical FD one for the field variable and its first derivative at each time level, respectively. Similar to the Dirichlet boundary conditions only case, much more accurate results (up to 3 orders of magnitude) are obtained

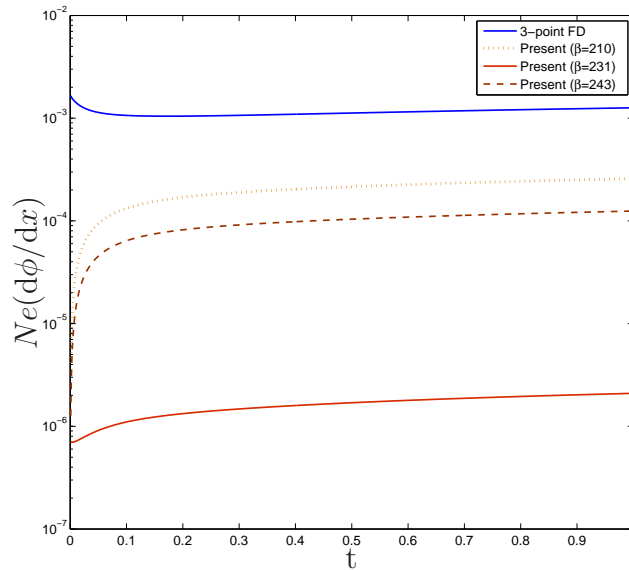


Figure 5.8: One-dimensional problem, Dirichlet and Neumann boundary conditions,  $N = 63$ ,  $\Delta t = 0.001$ : Comparison of the accuracy of the first derivative at each time level between the classical Crank-Nicolson method and the present Crank-Nicolson method. For the latter, three values of  $\beta$ , i.e. 210, 231 and 243, are employed.

with the present implicit method by using good values of  $\beta$ .

### 5.4.2 Example 2: rectangular domain problem

Consider equation (5.52) with  $0 \leq x, y \leq 1$  and  $f = \sin x \sin y (\cos t - 2 \sin t)$ , the exact solution to (5.52) is

$$\phi^{(e)}(x, y, t) = \sin x \sin y \sin t, \quad (5.79)$$

with two possible sets of boundary conditions: Dirichlet boundary conditions only and Dirichlet and Neumann boundary conditions as discussed below.

At each half time level one needs to compute the nodal values of derivatives at the previous half level appeared in equations (5.72) and (5.73). Boundary values of derivatives are required for this computation. It is straightforward to

obtain tangential and normal derivatives of  $\phi$  on the boundaries by means of the global 1D-IRBF approximation (Mai-Duy and Tanner 2007).

*Dirichlet boundary conditions only:* The boundary values of  $\phi$  are

$$\phi = 0 \text{ on } x = 0 \text{ and } y = 0,$$

$$\phi = \sin 1 \sin y \sin t \text{ on } x = 1,$$

$$\phi = \sin x \sin 1 \sin t \text{ on } y = 1.$$

Calculations are conducted using a series of grids, namely  $(21 \times 21, 23 \times 23, \dots, 63 \times 63)$ , to study the effects of the grid size  $h$ . Table 5.3 presents the results of convergence rates and grid-line matrix condition at  $t = 1$  using a time step of 0.001 by the classical ADI and the present ADI method ( $\beta = 124$ ). It can be seen that very low matrix condition numbers and higher convergence rates are obtained by the latter. The point-wise order of accuracy can be up to 45.70 and the average rate of convergence is 4.10 in the present method. For the grid of  $63 \times 63$ , the present method gives an error  $Ne(u)$  of  $2.70 \times 10^{-8}$  which is about 2 orders of magnitudes better compared with the error of the classical ADI.

Figure 5.9 shows the error distribution in a wide range of  $\beta$  for a grid of  $22 \times 22$  at a fixed time  $t = 0.6$ . It can be seen that there is a good range of  $\beta$  values and an optimal  $\beta$ . The accuracy at each time level using the grid of  $22 \times 22$  is presented in Figures 5.10 and 5.11 for the field variable and its first derivatives respectively. It can be seen that the present method yields much more accurate results than the classical one in most of the time levels by using good values of  $\beta$ . At  $\beta = 180$  (optimal  $\beta$ ), more than 2 and 3 orders of magnitude improvements are obtained for the field variable and its first derivatives respectively at  $t = 1$ . The proposed  $C^2$ -continuous ADI method thus results in high levels of accuracy especially for the first derivatives in  $x$ - (Figure 5.11(a)) and  $y$ - (Figure 5.11(b)) directions. We can effectively control the accuracy by means of  $\beta$ .

Table 5.3: Rectangular domain problem, Dirichlet boundary conditions only,  $N_x \times N_y = (21 \times 21, 23 \times 23, \dots, 63 \times 63)$ ,  $\Delta t = 0.001$ : condition numbers of the system matrix on a grid line and relative  $L_2$  errors of the approximate solution  $\phi$  at  $t = 1$  for various values of  $h$  by the 3-point FD method and the present compact 2-point IRBF method ( $\beta = 124$ ). LCR stands for local convergence rate.

$h$	Classical ADI			Present ADI		
	cond(A)	$Ne(\phi)$	LCR	cond(A)	$Ne(\phi)$	LCR
$5.00e - 2$	1.80	$1.29e - 5$		1.13	$1.16e - 5$	
$4.55e - 2$	1.97	$1.08e - 5$	1.94	1.30	$9.43e - 6$	2.19
$4.17e - 2$	2.15	$9.08e - 6$	1.95	1.49	$7.75e - 6$	2.25
$3.85e - 2$	2.35	$7.77e - 6$	1.95	1.69	$6.43e - 6$	2.33
$3.57e - 2$	2.57	$6.72e - 6$	1.96	1.90	$5.38e - 6$	2.41
$3.33e - 2$	2.80	$5.87e - 6$	1.96	2.13	$4.53e - 6$	2.50
$3.13e - 2$	3.05	$5.17e - 6$	1.96	2.38	$3.83e - 6$	2.61
$2.94e - 2$	3.31	$4.59e - 6$	1.97	2.65	$3.24e - 6$	2.73
$2.78e - 2$	3.59	$4.10e - 6$	1.97	2.93	$2.75e - 6$	2.87
$2.63e - 2$	3.89	$3.69e - 6$	1.97	3.22	$2.33e - 6$	3.04
$2.50e - 2$	4.20	$3.33e - 6$	1.97	3.53	$1.98e - 6$	3.24
$2.38e - 2$	4.53	$3.02e - 6$	1.98	3.86	$1.67e - 6$	3.47
$2.27e - 2$	4.87	$2.76e - 6$	1.98	4.21	$1.40e - 6$	3.76
$2.17e - 2$	5.23	$2.53e - 6$	1.98	4.57	$1.17e - 6$	4.12
$2.08e - 2$	5.61	$2.32e - 6$	1.98	4.94	$9.61e - 7$	4.57
$2.00e - 2$	6.00	$2.14e - 6$	1.99	5.33	$7.78e - 7$	5.15
$1.92e - 2$	6.41	$1.98e - 6$	1.99	5.74	$6.16e - 7$	5.95
$1.85e - 2$	6.83	$1.84e - 6$	1.99	6.17	$4.72e - 7$	7.08
$1.79e - 2$	7.27	$1.71e - 6$	1.99	6.61	$3.42e - 7$	8.82
$1.72e - 2$	7.73	$1.59e - 6$	1.99	7.06	$2.26e - 7$	11.85
$1.67e - 2$	8.20	$1.49e - 6$	2.00	7.53	$1.21e - 7$	18.46
$1.61e - 2$	8.69	$1.39e - 6$	2.00	8.02	$2.70e - 8$	45.70
		$O(h^{1.97})$			$O(h^{4.10})$	

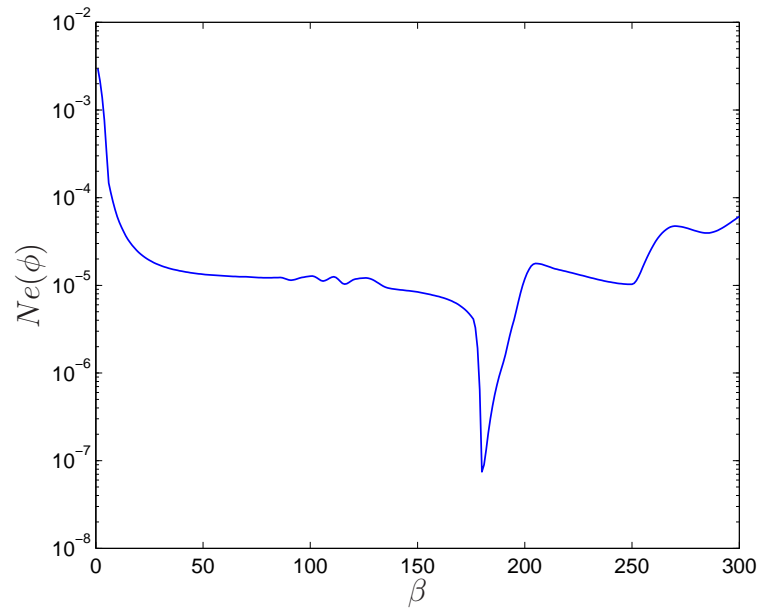


Figure 5.9: Rectangular domain problem, Dirichlet boundary conditions only,  $N_x \times N_y = 22 \times 22$ ,  $\Delta t = 0.001$ : Relative  $L_2$  errors of the approximate solution  $\phi$  at  $t = 0.6$  against the RBF width ( $\beta$ ).

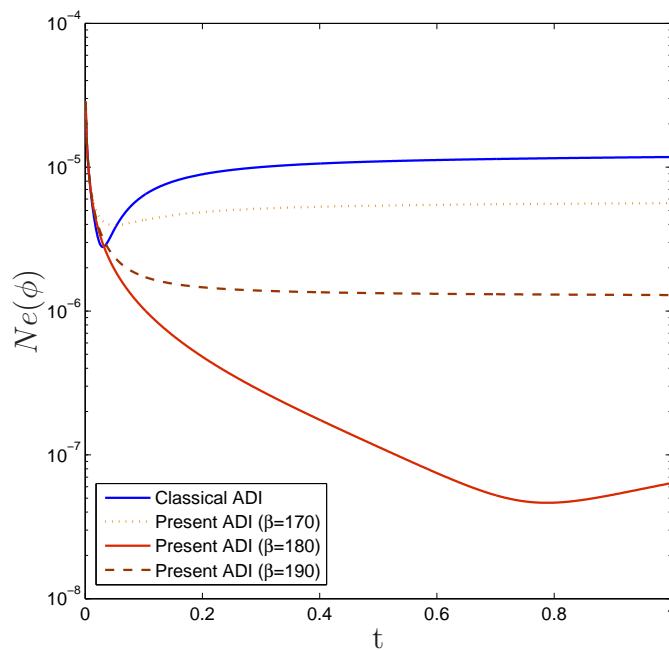


Figure 5.10: Rectangular domain problem, Dirichlet boundary conditions only,  $N_x \times N_y = 22 \times 22$ ,  $\Delta t = 0.001$ : Comparison of the accuracy of the field variable at each time level between the classical ADI method and the present ADI method. For the latter, three values of  $\beta$ , i.e. 170, 180 and 190, are employed.

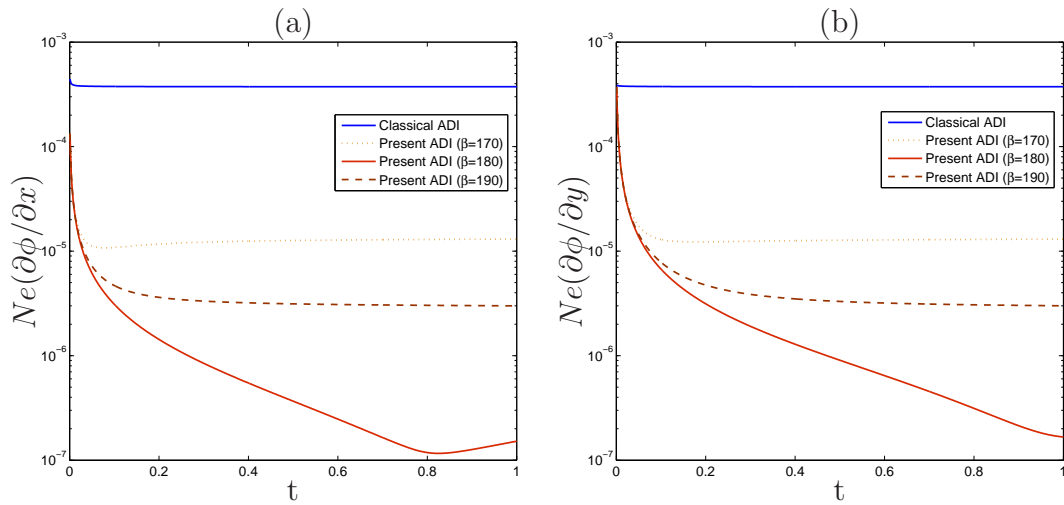


Figure 5.11: Rectangular domain problem, Dirichlet boundary conditions only,  $N_x \times N_y = 22 \times 22$ ,  $\Delta t = 0.001$ : Comparison of the accuracy of the first derivatives at each time level between the classical ADI method and the present ADI method. For the latter, three values of  $\beta$ , i.e. 170, 180 and 190, are employed.

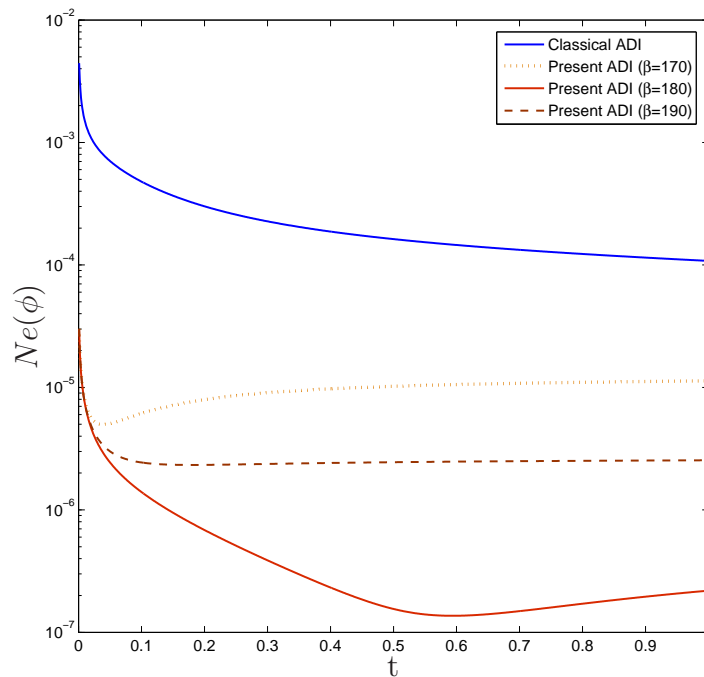


Figure 5.12: Rectangular domain problem, Dirichlet and Neumann boundary conditions,  $N_x \times N_y = 22 \times 22$ ,  $\Delta t = 0.001$ : Comparison of the accuracy of the field variable at each time level between the classical ADI method and the present ADI method. For the latter, three values of  $\beta$ , i.e. 170, 180 and 190, are employed.

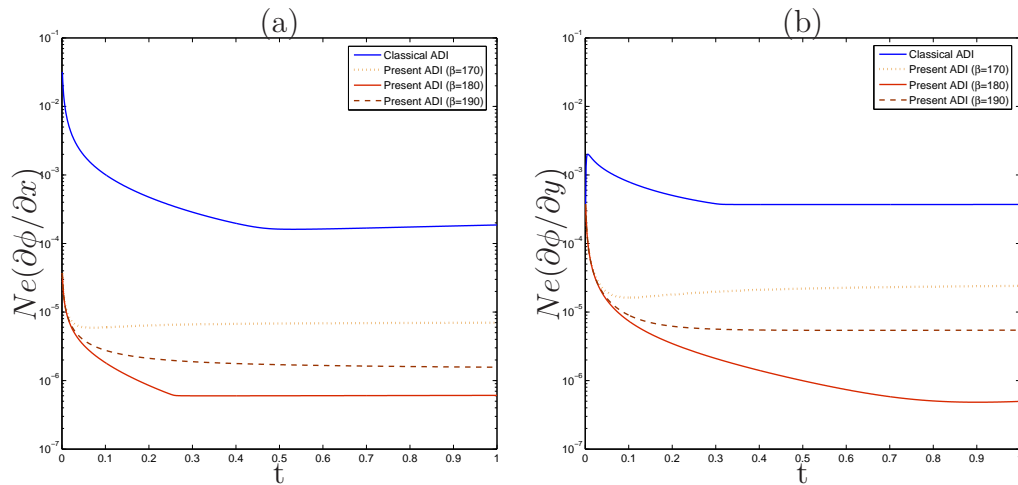


Figure 5.13: Rectangular domain problem, Dirichlet and Neumann boundary conditions,  $N_x \times N_y = 22 \times 22$ ,  $\Delta t = 0.001$ : Comparison of the accuracy of the first derivatives at each time level between the classical ADI method and the present ADI method. For the latter, three values of  $\beta$ , i.e. 170, 180 and 190, are employed.

*Dirichlet and Neumann boundary conditions:* We choose to impose the Dirichlet conditions  $\phi = 0$  and  $\phi = \sin x \sin 1 \sin t$  at  $y = 0$  and  $y = 1$ , respectively, and the Neumann conditions  $\partial\phi/\partial x = \sin y \sin t$  and  $\partial\phi/\partial x = \cos 1 \sin y \sin t$  at  $x = 0$  and  $x = 1$ , respectively. Figures 5.12 and 5.13 present a comparison of the accuracy between the present method and the classical ADI for the field variable and its first derivatives at different time levels using a grid of  $22 \times 22$ . Much more accurate results are obtained at all time levels using good  $\beta$  values. At  $\beta = 180$  and  $t = 1$ , about 3 orders of magnitude improvements are obtained for both the field variable and its first derivatives.

### 5.4.3 Example 3: circular domain problem

Consider equation (5.52) with

$$f = \sin(2\pi x) \sinh(2y) [\cos t + 4 \sin t(\pi^2 - 1)] + \cosh(4x) \cos(4\pi y) [\cos t + 16 \sin t(\pi^2 - 1)],$$

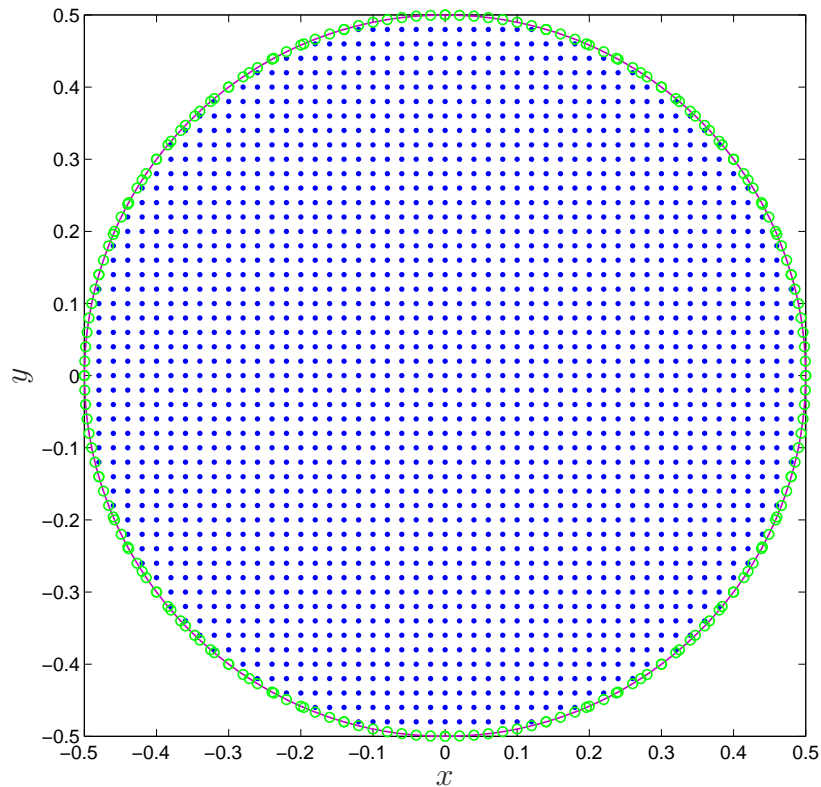


Figure 5.14: Circular domain problem: Geometry and discretisation. Boundary nodes denoted by  $\circ$  are generated by the intersection of the grid lines and the boundary.

on a circular domain of radius  $1/2$ . The domain centre is located at the origin as shown in Figure 5.14. The exact solution is

$$\phi^{(e)}(x, y, t) = [\sin(2\pi x) \sinh(2y) + \cosh(4x) \cos(4y)] \sin t, \quad (5.80)$$

from which the boundary conditions for  $\phi$  are easily derived. Figure 5.15 shows the exact solution at a time instant  $t = \pi/8$  over an extended domain  $-1/2 \leq x, y \leq 1/2$ .

In estimation of the right hand sides of (5.72) and (5.73), the boundary derivative values of  $\phi$  in grid-line directions are obtained by 1D-IRBF approximation (Mai-Duy and Tanner 2007). The boundary values of normal derivative to the

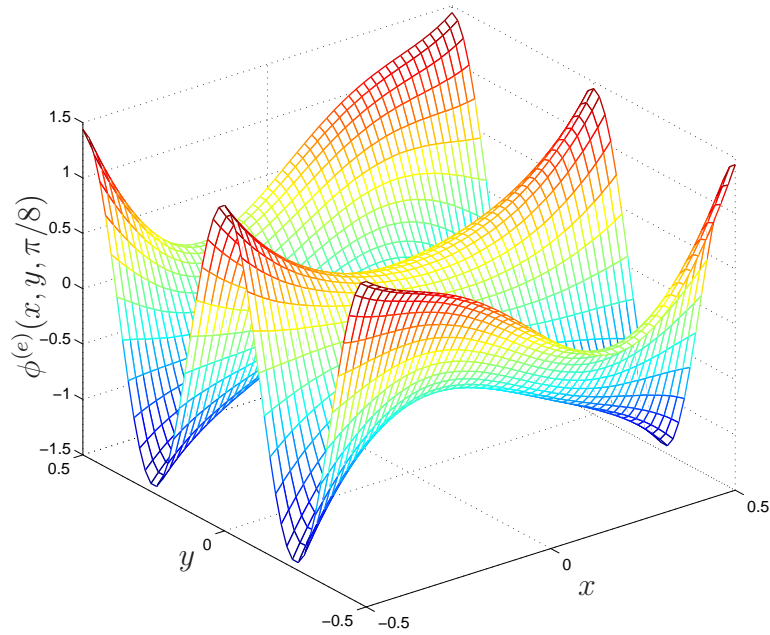


Figure 5.15: Circular domain problem: Exact solution over an extended domain.

grid-line directions are obtained by 1D-IRBF extrapolation. We employ the nonuniform grid scheme, i.e. (5.51), for the stencils at the boundaries while the uniform grid scheme, i.e. (5.35), is employed at interior stencils.

Calculations are carried out with grids of  $(21 \times 21, 23 \times 23, \dots, 51 \times 51)$  to study the grid size convergence. Table 5.4 presents the results of convergence rates and the maximum grid-line matrix condition at  $t = 0.05$  using a time step of 0.001 and  $\beta = 330$  by the present ADI method. It can be seen that very low matrix condition numbers and high average convergence rate of 4.23 are obtained. The accuracies at each time level of the last three grids, i.e.  $(47 \times 47, 49 \times 49, \text{ and } 51 \times 51)$ , are present in Figure 5.16. It can be seen that the solutions converge well as the grids are refined.

Figure 5.17 displays a contour plot of the present ADI method solution using a grid of  $141 \times 141$  and  $\beta = 25$  at  $t = 1$  where smooth contours are obtained.

Table 5.4: Circular domain problem,  $N_x \times N_y = (21 \times 21, 23 \times 23, \dots, 51 \times 51)$ ,  $\Delta t = 0.001$ : maximum condition numbers of the system matrix on a grid line and relative  $L_2$  errors of the approximate solution  $\phi$  at  $t = 0.05$  for various values of  $h$  by the present compact 2-point IRBF method ( $\beta = 330$ ). LCR stands for local convergence rate.

$h$	$\text{cond}(A)_{max}$	$Ne(\phi)$	LCR
$5.00e - 2$	$1.41e + 1$	$2.01e - 2$	
$4.55e - 2$	$8.01e + 0$	$1.57e - 2$	2.56
$4.17e - 2$	$5.34e + 0$	$1.29e - 2$	2.29
$3.85e - 2$	$8.72e + 0$	$1.05e - 2$	2.58
$3.57e - 2$	$7.62e + 1$	$8.19e - 3$	3.31
$3.33e - 2$	$2.82e + 1$	$6.80e - 3$	2.68
$3.13e - 2$	$1.78e + 1$	$5.51e - 3$	3.26
$2.94e - 2$	$3.55e + 2$	$2.85e - 2$	-27.11
$2.78e - 2$	$5.02e + 1$	$3.56e - 3$	36.41
$2.63e - 2$	$1.18e + 2$	$4.13e - 3$	2.77
$2.50e - 2$	$1.43e + 2$	$2.19e - 3$	12.41
$2.38e - 2$	$6.72e + 1$	$1.64e - 3$	5.86
$2.27e - 2$	$3.74e + 2$	$1.12e - 3$	8.26
$2.17e - 2$	$4.77e + 1$	$7.65e - 4$	8.56
$2.08e - 2$	$4.75e + 1$	$4.55e - 4$	12.21
$2.00e - 2$	$3.73e + 1$	$2.95e - 4$	10.60
		$O(h^{4.23})$	

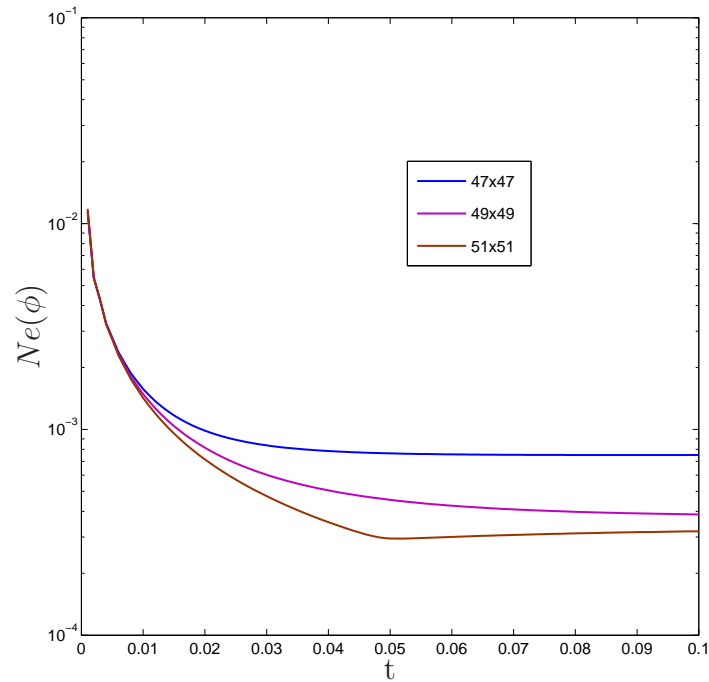


Figure 5.16: Circular domain problem,  $\Delta t = 0.001$ ,  $\beta = 330$ : The accuracy at each time level by the present ADI method using three grids.

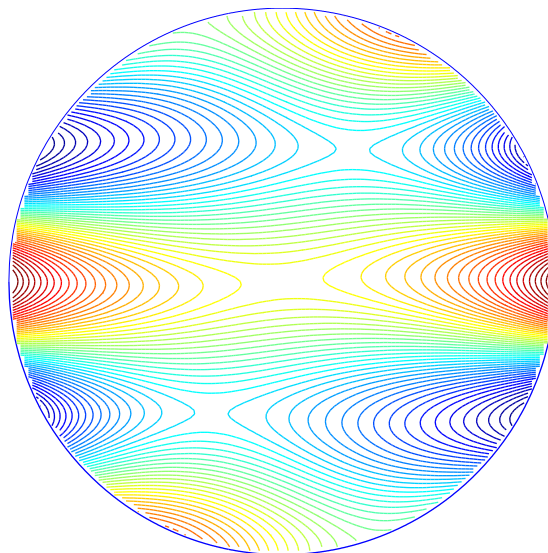


Figure 5.17: Circular domain problem,  $N_x \times N_y = 141 \times 141$ ,  $\Delta t = 0.001$ ,  $\beta = 25$ : Contour plot of the present ADI method solution at  $t = 1$ .

#### 5.4.4 Example 4: a non-linear problem

An example of a non-linear parabolic problem here is the vorticity transport equation in the Navier-Stokes equations of the form

$$-\omega = \frac{\partial^2 \psi}{\partial x^2} + \frac{\partial^2 \psi}{\partial y^2}, \quad (5.81)$$

$$\frac{\partial \omega}{\partial t} = \frac{\partial^2 \omega}{\partial x^2} + \frac{\partial^2 \omega}{\partial y^2} - Re \left( \frac{\partial \psi}{\partial y} \frac{\partial \omega}{\partial x} - \frac{\partial \psi}{\partial x} \frac{\partial \omega}{\partial y} \right), \quad (5.82)$$

where  $\psi$  is the streamfunction,  $\omega$  the vorticity,  $Re$  the Reynolds number. The velocity components  $u$  and  $v$  in  $x$ - and  $y$ -directions, respectively, are defined by

$$u = \frac{\partial \psi}{\partial y}, \quad v = -\frac{\partial \psi}{\partial x}. \quad (5.83)$$

We will solve (5.81) and (5.82) to obtain the structure of the steady flow in a lid-driven cavity which is a very useful benchmark problem for the validation of new numerical methods in CFD. The cavity is taken to be a unit square, with the lid sliding from left to right at a unit velocity. The boundary conditions can be specified as

$$\begin{aligned} \psi = 0, \quad \partial\psi/\partial x = 0, \quad x = 0, \quad x = 1, \\ \psi = 0, \quad \partial\psi/\partial y = 0, \quad y = 0, \\ \psi = 0, \quad \partial\psi/\partial y = 1, \quad y = 1. \end{aligned}$$

It can be seen that the velocity field is singular at the two top corners of the cavity. In an early paper by Ghia et al. (1982), the flow was simulated by a multigrid finite-difference method using very fine grids (i.e.  $129 \times 129$  and  $257 \times 257$ ). The obtained results are very accurate and widely cited in the literature for comparison purposes. In a later work by Botella and Peyret (1998), the regular and singular parts of the solution are handled by a Chebyshev collocation and an analytic method respectively. Benchmark spectral results were reported for the flow at  $Re = 100$  and  $Re = 1000$ .

In this study, we propose two separate procedures to discretise equations (5.81) and (5.82). Consider a grid point  $P$  and its neighboring nodes as shown in Figure 5.2. Collocating equations (5.81) and (5.82) at  $P$  we get

$$-\omega_P = \frac{\partial^2 \psi_P}{\partial x^2} + \frac{\partial^2 \psi_P}{\partial y^2}, \quad (5.84)$$

$$\frac{\partial \omega_P}{\partial t} = \frac{\partial^2 \omega_P}{\partial x^2} + \frac{\partial^2 \omega_P}{\partial y^2} - Re \left( \frac{\partial \psi_P}{\partial y} \frac{\partial \omega_P}{\partial x} - \frac{\partial \psi_P}{\partial x} \frac{\partial \omega_P}{\partial y} \right). \quad (5.85)$$

**Streamfunction equation procedure:** At a time step  $n$ , (5.84) becomes

$$-\omega_P^{n-1} = \frac{\partial^2 \psi_P^n}{\partial x^2} + \frac{\partial^2 \psi_P^n}{\partial y^2}. \quad (5.86)$$

As in Figure 5.2,  $\partial^2 \psi_P^n / \partial x^2$  can be approximated by either element  $WP$  or  $PE$  and similarly either element  $SP$  or  $PN$  can be used to give the approximation for  $\partial^2 \psi_P^n / \partial y^2$  via (3.13). It will be shown later that these options will give the same approximation for  $\partial^2 \psi_P^n / \partial x^2$  and  $\partial^2 \psi_P^n / \partial y^2$  since  $C^2$ -continuous conditions are imposed at  $P$  in both  $x$ - and  $y$ -directions. Assume that the elements  $WP$  and  $SP$  are used with the abbreviation (5.20), we have

$$\frac{\partial^2 \psi_P^n}{\partial x^2} = \nu_1 \psi_W^n + \nu_2 \psi_P^n + \nu_3 \frac{\partial \psi_W^n}{\partial x} + \nu_4 \frac{\partial \psi_P^n}{\partial x}, \quad (5.87)$$

$$\frac{\partial^2 \psi_P^n}{\partial y^2} = \nu_1 \psi_S^n + \nu_2 \psi_P^n + \nu_3 \frac{\partial \psi_S^n}{\partial y} + \nu_4 \frac{\partial \psi_P^n}{\partial y}. \quad (5.88)$$

Substituting (5.87) and (5.88) into (5.86) results in

$$\nu_1 (\psi_W^n + \psi_S^n) + 2\nu_2 \psi_P^n + \nu_3 \left( \frac{\partial \psi_W^n}{\partial x} + \frac{\partial \psi_S^n}{\partial y} \right) + \nu_4 \left( \frac{\partial \psi_P^n}{\partial x} + \frac{\partial \psi_P^n}{\partial y} \right) + \omega_P^{n-1} = 0. \quad (5.89)$$

It can be seen in (5.89) that there are three unknowns at a grid point  $P$ , namely  $\psi_P^n$ ,  $\partial \psi_P^n / \partial x$  and  $\partial \psi_P^n / \partial y$ . To solve (5.89) two more equations have to be created at a grid point  $P$  and they are devised here by applying (5.29) ( $C^2$ -continuity

conditions) at  $P$  with  $\eta \equiv x$  and  $\eta \equiv y$ , respectively

$$\frac{\partial \psi_W^n}{\partial x} + 2 \left( \frac{\mu_3}{\mu_4} \right) \frac{\partial \psi_P^n}{\partial x} + \frac{\partial \psi_E^n}{\partial x} = \frac{\mu_1}{\mu_4} (\psi_E^n - \psi_W^n), \quad (5.90)$$

$$\frac{\partial \psi_S^n}{\partial y} + 2 \left( \frac{\mu_3}{\mu_4} \right) \frac{\partial \psi_P^n}{\partial y} + \frac{\partial \psi_N^n}{\partial y} = \frac{\mu_1}{\mu_4} (\psi_N^n - \psi_S^n). \quad (5.91)$$

Collection of equations (5.89), (5.90) and (5.91) at  $(N_x - 2) \times (N_y - 2)$  interior grid points leads to a system of  $3(N_x - 2) \times (N_y - 2)$  algebraic equations for  $3(N_x - 2) \times (N_y - 2)$  unknowns. Unlike conventional discretisation procedures, nodal values of first derivatives of the streamfunction in Cartesian directions (nodal velocities) constitute a part of the solution. As a result the velocity field is explicitly given without the need of a reconstruction step for use in the vorticity equation (5.82). Unlike in previous IRBFE works (An-Vo et al. 2011b, 2013), the present procedure can involve not only the streamfunction values but also its normal derivative values at the boundary.

**Vorticity equation procedure:** We employ the ADI procedure in (5.65) and (5.66) to relax the time derivative in (5.85), i.e.

$$\frac{\omega_P^{n-1/2} - \omega_P^{n-1}}{\Delta t/2} = \frac{\partial^2 \omega_P^{n-1/2}}{\partial x^2} + \frac{\partial^2 \omega_P^{n-1}}{\partial y^2} - Re \left( \frac{\partial \psi_P^n}{\partial y} \frac{\partial \omega_P^{n-1/2}}{\partial x} - \frac{\partial \psi_P^n}{\partial x} \frac{\partial \omega_P^{n-1}}{\partial y} \right), \quad (5.92)$$

$$\frac{\omega_P^n - \omega_P^{n-1/2}}{\Delta t/2} = \frac{\partial^2 \omega_P^{n-1/2}}{\partial x^2} + \frac{\partial^2 \omega_P^n}{\partial y^2} - Re \left( \frac{\partial \psi_P^n}{\partial y} \frac{\partial \omega_P^{n-1/2}}{\partial x} - \frac{\partial \psi_P^n}{\partial x} \frac{\partial \omega_P^n}{\partial y} \right). \quad (5.93)$$

Applying (5.92) at  $W$  and  $E$  give us

$$\frac{\omega_W^{n-1/2} - \omega_W^{n-1}}{\Delta t/2} = \frac{\partial^2 \omega_W^{n-1/2}}{\partial x^2} + \frac{\partial^2 \omega_W^{n-1}}{\partial y^2} - Re \left( \frac{\partial \psi_W^n}{\partial y} \frac{\partial \omega_W^{n-1/2}}{\partial x} - \frac{\partial \psi_W^n}{\partial x} \frac{\partial \omega_W^{n-1}}{\partial y} \right), \quad (5.94)$$

$$\frac{\omega_E^{n-1/2} - \omega_E^{n-1}}{\Delta t/2} = \frac{\partial^2 \omega_E^{n-1/2}}{\partial x^2} + \frac{\partial^2 \omega_E^{n-1}}{\partial y^2} - Re \left( \frac{\partial \psi_E^n}{\partial y} \frac{\partial \omega_E^{n-1/2}}{\partial x} - \frac{\partial \psi_E^n}{\partial x} \frac{\partial \omega_E^{n-1}}{\partial y} \right). \quad (5.95)$$





noting (5.19) and (5.20) as follows.

$$\omega_b = -\frac{\partial^2 \psi_b}{\partial \eta^2} = -\left( \mu_1 \psi_b + \mu_2 \psi_g + \mu_3 \frac{\partial \psi_b}{\partial \eta} + \mu_4 \frac{\partial \psi_g}{\partial \eta} \right),$$

$$x = 0 \text{ and } y = 0, \quad 1 \equiv b \text{ and } 2 \equiv g; \quad (5.104)$$

$$\omega_b = -\frac{\partial^2 \psi_b}{\partial \eta^2} = -\left( \nu_1 \psi_g + \nu_2 \psi_b + \nu_3 \frac{\partial \psi_g}{\partial \eta} + \nu_4 \frac{\partial \psi_b}{\partial \eta} \right),$$

$$x = 1 \text{ and } y = 1, \quad 1 \equiv g \text{ and } 2 \equiv b. \quad (5.105)$$

where  $\eta$  represents  $x$  and  $y$ ;  $\psi_b$  and  $\partial \psi_b / \partial \eta$  are the Dirichlet and Neumann boundary conditions of  $\psi$ , and  $\psi_g$  and  $\partial \psi_g / \partial \eta$  are the known values taken from the solution of the streamfunction equation. It is noted that (i) all given boundary conditions are imposed in an exact manner; and (ii) this technique only requires the local values of  $\psi$  and  $\partial \psi / \partial \eta$  at the boundary node and its adjacent grid node to estimate the Dirichlet boundary conditions for the vorticity equation.

We employ the proposed procedures, i.e. (5.89)-(5.91) to solve (5.81) and (5.100)-(5.101) to solve (5.82) for a wide range of  $Re$ . The solution procedure involves the following steps

(1) Guess the initial distributions of the streamfunction and vorticity in the case of Stokes flow. Otherwise, take the solution of a lower Reynolds number as an initial guess.

(2) Discretise the streamfunction equation by (5.89)-(5.91) for all interior grid nodes and then apply the LU technique to factorise the system matrix into two triangular matrices. It is noted that the factorisation needs to be done only once.

(3) Solve (5.86) subjects to boundary conditions for the new streamfunction field. Note that both the Dirichlet and Neumann conditions of the streamfunction at boundary are imposed in this step.

(4) Estimate boundary conditions for the vorticity equation via (5.104) and (5.105) and construct the system matrices for vorticity equation in (5.100) and (5.101).

(5) Compute the first- and second-order derivatives of vorticity on the boundaries by applying the global 1D-IRBF approximations. For interior grid nodes, the derivatives are computed by using (5.31) and (5.37). The results are used to compute the right hand sides in (5.100) and (5.101).

(5) Solve (5.100) and (5.101) for the new vorticity field.

(6) Check to see whether the solution has reached a steady state through

$$CM(\psi) = \frac{\sqrt{\sum_{i=1}^N (\psi_i - \psi_i^0)^2}}{\sqrt{\sum_{i=1}^N \psi_i^2}} < 10^{-9}, \quad (5.106)$$

where  $N$  is the total number of grid nodes.

(7) If  $CM$  is not satisfactorily small, advance pseudo-time and repeat from step (3). Otherwise, stop the computation and output the results.

Simulation is carried out for a wide range of  $Re$ , namely (100, 400, 1000, 3200, 5000, 7500) with  $\beta$  chosen to be 1. Grid convergence is also studied and the numerical results are compared with those of the benchmark FD (Ghia et al. 1982) and spectral (Botella and Peyret 1998) solutions to assess the accuracy of the present method. The performance of the present high-order ADI method is also monitored via comparisons with a conventional ADI method where streamfunction and vorticity are discretised by a three-node central difference (CD) scheme. We denote this method as CD-ADI. It is noted that the method of deriving computational vorticity boundary conditions, i.e. (5.104) and (5.105), is also used in CD-ADI method.

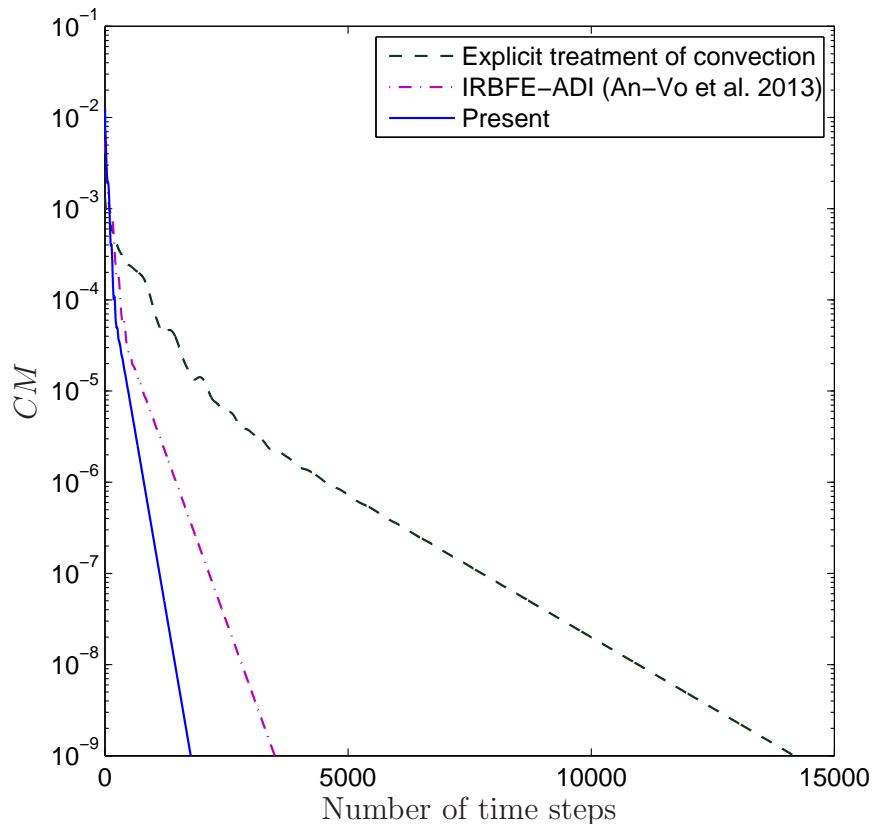


Figure 5.18: Lid-driven cavity flow,  $Re = 1000$ , grid =  $61 \times 61$ , solution at  $Re = 400$  used as initial guess: Convergence behaviour. Present method using a time step of  $1 \times 10^{-4}$  converges faster than the IRBFE-ADI method using a time step of  $5 \times 10^{-5}$  and the explicit treatment of convection method (ETCM) using a time step of  $1 \times 10^{-5}$ . It is noted that the IRBFE-ADI and the ETCM diverge for the time steps greater than  $5 \times 10^{-5}$  and  $1 \times 10^{-5}$  respectively.

**Time-stepping convergence:** To show the benefits of (i) the implicit treatment of convection and (ii) the involvement of boundary derivative values in the present method, we compare the convergence behaviours with those of (i) a method similar to the present method with an explicit treatment of convection and (ii) the IRBFE-ADI method (An-Vo et al. 2013) where semi-interior elements are employed at the boundaries, respectively. Figure 5.18 displays the convergence behaviours of the three methods for the case of  $Re = 1000$  using a grid of  $61 \times 61$ . It can be seen that solution converge faster and larger time steps can be used for the present method. The number of iterations are about 1750, 3500 and 14200 to reach  $CM < 10^{-9}$  for the present method, IRBFE-ADI

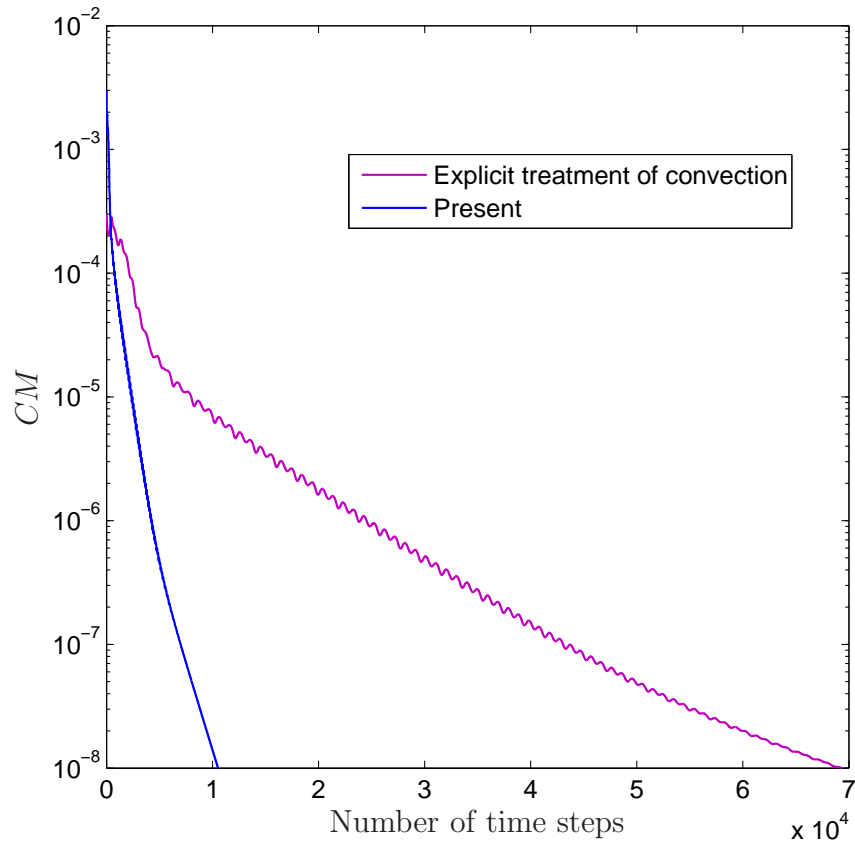


Figure 5.19: Lid-driven cavity flow,  $Re = 3200$ , grid =  $91 \times 91$ , solution at  $Re = 1000$  used as initial guess: Convergence behaviour. Present method using a time step of  $1 \times 10^{-5}$  converges faster than the explicit treatment of convection method (ETCM) using a time step of  $1 \times 10^{-6}$ . It is noted that the ETCM diverges for the time steps greater than  $1 \times 10^{-6}$ .

method and the explicit treatment of convection method (ETCM), respectively. In the case of  $Re = 3200$  and a grid of  $91 \times 91$  (Figure 5.19), the present method using a time step of  $1 \times 10^{-5}$  takes about 10500 to reach  $CM < 10^{-8}$  while the ETCM using a time step of  $1 \times 10^{-6}$  requires about 69320 to reach the same  $CM$ . The implicit treatment of convection thus allows much larger time steps can be used and hence is much more efficient especially for highly non-linear flows. The involvement of first derivative boundary values also help improve the stability where larger time steps compared to those of IRBFE-ADI method can be used.

Table 5.5: Lid-driven cavity flow: extrema of the vertical and horizontal velocity profiles along the centrelines of the cavity. % denotes percentage errors relative to the benchmark spectral results (Botella and Peyret 1998). Results of the FDM are taken from Ghia et al. (1982).

$Re$	Method	Grid	$u_{min}$	%	$v_{max}$	%	$v_{min}$	%
100	CD-ADI	11x11	-0.15242	28.79	0.10823	39.73	-0.14355	43.44
	Present	11x11	-0.21755	1.64	0.19104	6.39	-0.28096	10.70
	CD-ADI	21x21	-0.19725	7.84	0.16069	10.51	-0.22401	11.74
	Present	21x21	-0.21488	0.39	0.18056	0.55	-0.25323	0.22
	FDM ( $\psi - \omega$ )	129x129	-0.21090	1.47	0.17527	2.40	-0.24533	3.34
	Benchmark		-0.21404		0.17957		-0.25380	
	CD-ADI	31x31	-0.26073	32.90	0.24723	34.41	-0.36708	30.36
	Present	31x31	-0.42144	8.46	0.40478	7.39	-0.57783	9.63
	CD-ADI	41x41	-0.30741	20.89	0.29382	22.05	-0.42451	19.46
	Present	41x41	-0.40862	5.16	0.39505	4.80	-0.55927	6.11
1000	CD-ADI	51x51	-0.33242	14.45	0.31932	15.29	-0.45556	13.57
	Present	51x51	-0.40172	3.38	0.38888	3.17	-0.54761	3.90
	CD-ADI	61x61	-0.34772	10.51	0.33502	11.12	-0.47488	9.90
	Present	61x61	-0.39735	2.26	0.38491	2.11	-0.54060	2.57
	CD-ADI	71x71	-0.35770	7.94	0.34528	8.40	-0.48760	7.49
	Present	71x71	-0.39446	1.52	0.38219	1.39	-0.53620	1.73
	CD-ADI	81x81	-0.36452	6.19	0.35228	6.54	-0.49633	5.83
	Present	81x81	-0.39254	1.02	0.38035	0.90	-0.53331	1.18
	CD-ADI	91x91	-0.36981	4.83	0.35772	5.10	-0.50308	4.55
	Present	91x91	-0.39120	0.68	0.37905	0.56	-0.53134	0.81
	CD-ADI	101x101	-0.37333	3.92	0.36134	4.14	-0.50760	3.70
	Present	101x101	-0.39022	0.42	0.37808	0.30	-0.52994	0.54
	CD-ADI	111x111	-0.37597	3.24	0.36405	3.42	-0.51099	3.05
	Present	111x111	-0.38947	0.23	0.37738	0.12	-0.52892	0.35
	CD-ADI	121x121	-0.37800	2.72	0.36613	2.87	-0.51359	2.56
	Present	121x121	-0.38890	0.08	0.37684	0.03	-0.52816	0.20
	FDM ( $\psi - \omega$ )	129x129	-0.38289	1.46	0.37095	1.59	-0.51550	2.20
	Benchmark		-0.38857		0.37694		-0.52708	

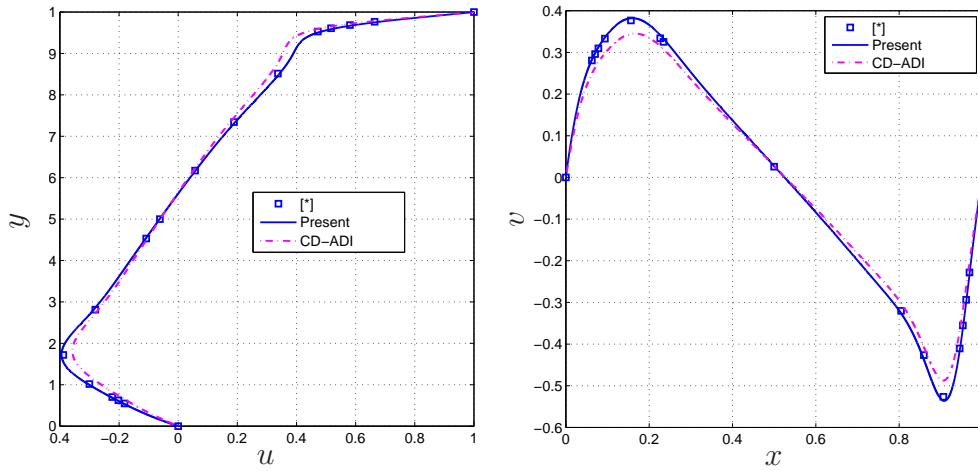


Figure 5.20: Lid-driven cavity flow,  $Re = 1000$ , grid =  $71 \times 71$ : velocity profiles along the vertical and horizontal centrelines. [\*] is Botella and Peyret (1998).

**Grid-size convergence:** The convergence of extrema of the vertical and horizontal velocity profiles along the centrelines of the cavity with respect to grid refinement is presented in Table 5.5. It can be seen that (i) errors relative to the benchmark spectral results are consistently reduced as the grid is refined; and (ii) the present results, even at relatively coarse grids, are closer to the benchmark spectral results than the FD ones. The errors are less than 1% for  $Re = 100$  using a grid of  $21 \times 21$  and for  $Re = 1000$  using a grid of  $91 \times 91$ .

**Solution quality:** Figure 5.20 displays velocity profiles on the vertical and horizontal centrelines by benchmark spectral method (Botella and Peyret 1998), CD-ADI and the present method. It can be seen that the profiles of the present method are in good agreement with those of the benchmark spectral method. The profiles of CD-ADI method, however, have clear deviations from the benchmark profiles. Contour plots are presented in Figures 5.21-5.24 which look feasible when compared with those by the pseudospectral technique (Botella and Peyret 1998) and the FDM (Ghia et al. 1982). Figure 5.21 shows that smooth contours are obtained for both the streamfunction and vorticity fields and the corner eddies are clearly captured with relatively coarse grids for  $Re = (0, 100, 400, 1000)$ .

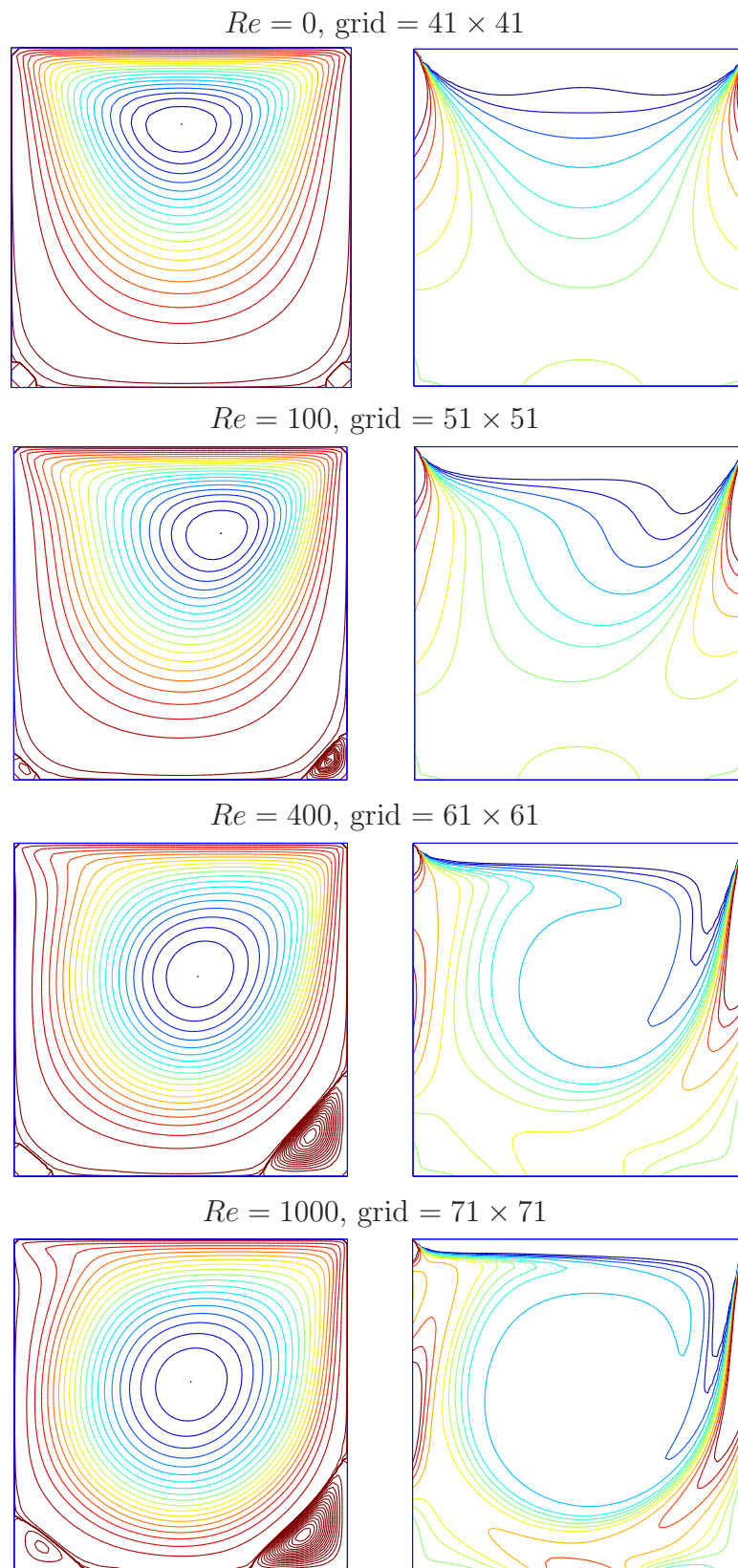


Figure 5.21: Lid-driven cavity flow: contour plots of streamfunction (left) and vorticity (right) for several values of  $Re$ . The iso-vorticity lines are taken as  $0, \pm 0.5, \pm 1, \pm 2, \pm 3, \pm 4, \pm 5$ .

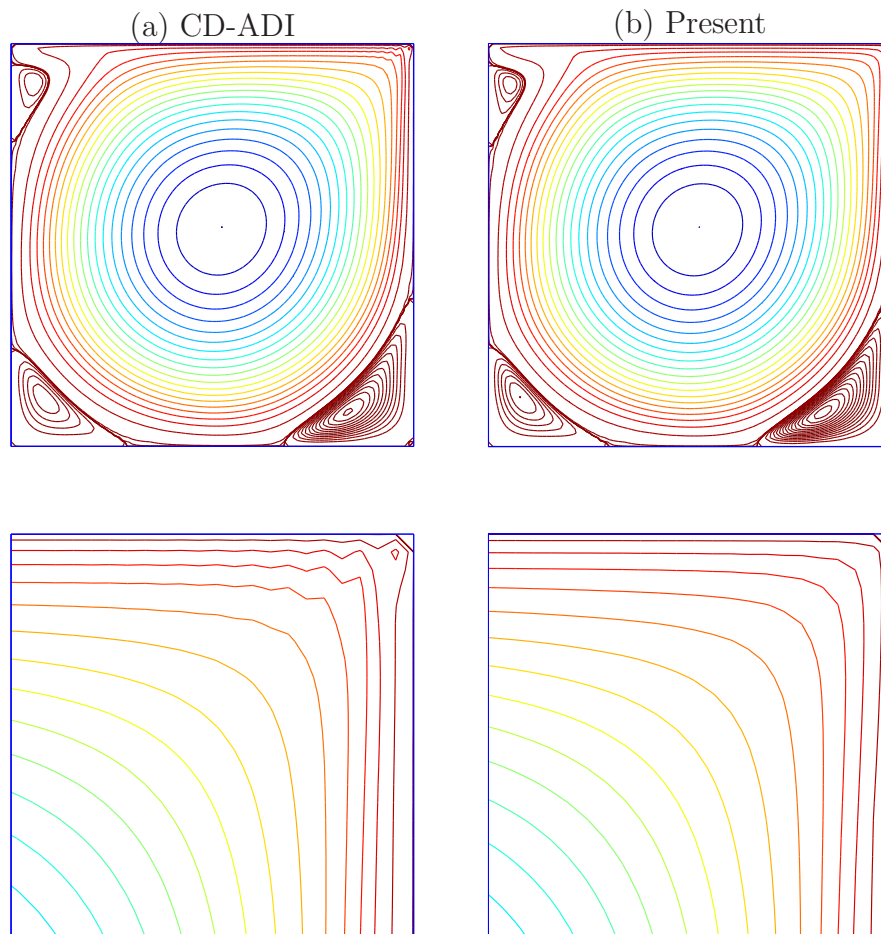


Figure 5.22: Lid-driven cavity flow,  $Re = 3200$ , grid=  $91 \times 91$ : overall stream lines (upper figures) and a magnified view of those in the upper right corner. The contour values for CD-ADI method and the present method plots are the same.

At  $Re = 3200$ , there are oscillations in streamfunction (Figure 5.22) and vorticity (Figure 5.23) fields obtained by the CD-ADI method with a grid of  $91 \times 91$ . Much finer grids are required in the CD-ADI method to capture properly the flow physics at high  $Re$ . Figure 5.24 presents the contour plots of the present method at  $Re = 5000$  and  $Re = 7500$  where smooth contours are obtained with grids of  $111 \times 111$  and  $131 \times 131$ , respectively.

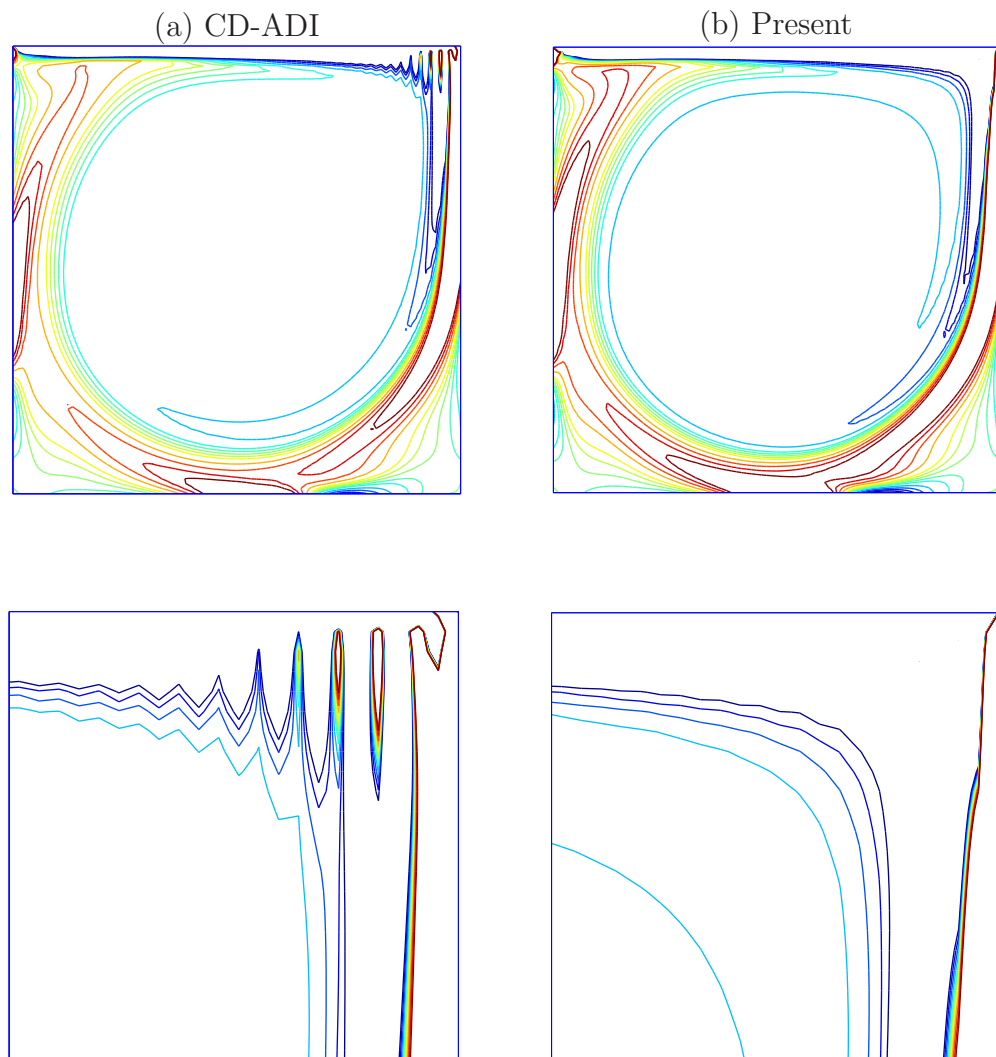
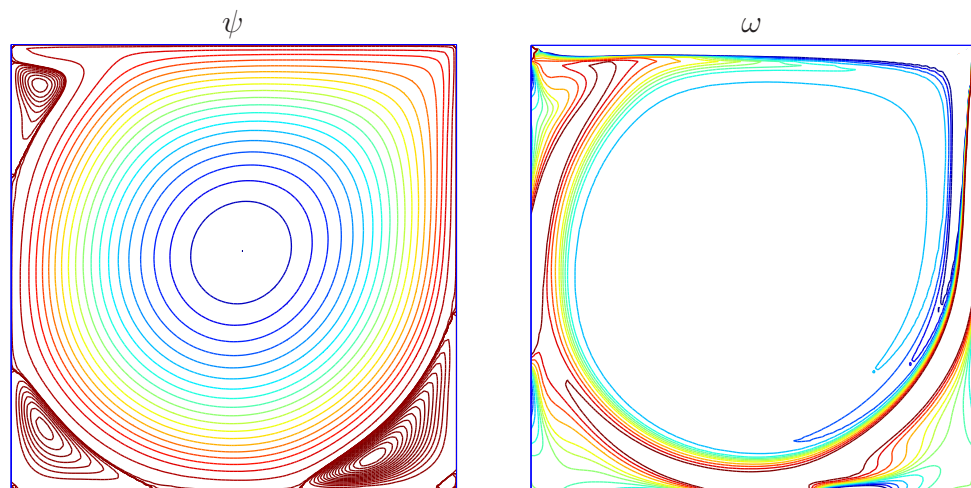


Figure 5.23: Lid-driven cavity flow,  $Re = 3200$ , grid =  $91 \times 91$ : overall isovorticity lines (upper figures) and a magnified view of those in the upper right corner. The contour values are taken as  $0, \pm 0.5, \pm 1, \pm 2, \pm 3, \pm 4, \pm 5$ .

(a)  $Re = 5000$ , grid =  $111 \times 111$



(b)  $Re = 7500$ , grid =  $131 \times 131$

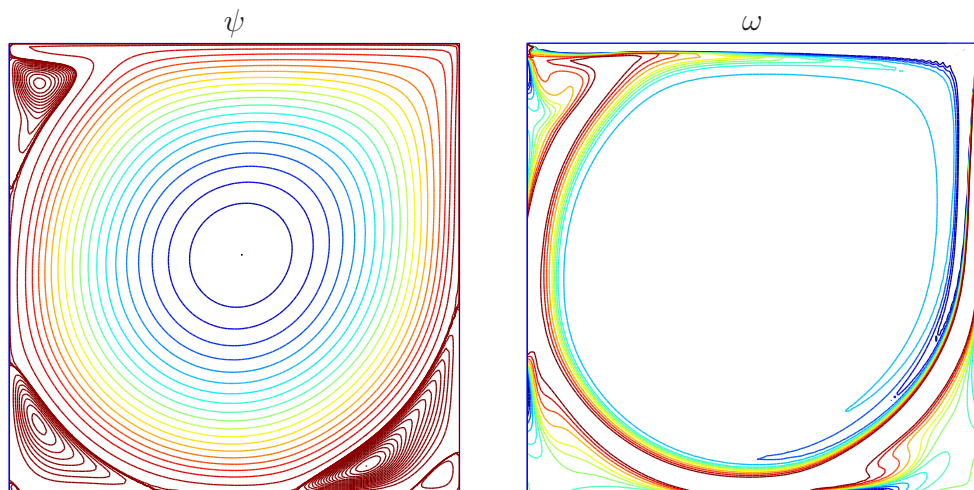


Figure 5.24: Lid-driven cavity flow: stream and iso-vorticity lines by the present method for  $Re = 5000$  and  $Re = 7500$ . The iso-vorticity lines are taken as  $0, \pm 0.5, \pm 1, \pm 2, \pm 3, \pm 4, \pm 5$ .

## 5.5 Discussion

To the best of our knowledge, the proposed compact schemes are the first closed form MQ-based compact schemes. Their coefficients depend on the factor  $\beta$  and can be considered as generalised compact finite difference schemes (at the limit of  $\beta$  MQs become polynomials). The schemes on a nonuniform grid are obtained conveniently without the need of coordinate transformation. Distinguishing features of the proposed compact schemes on uniform grids compared to the three-point compact FD scheme (Lele 1992) are (i)  $C^2$ -continuous solutions are guaranteed; and (ii) the consistence of the first and second derivative schemes, i.e. (5.29)/(5.30) and (5.35)/(5.36), respectively, wherein the coefficients on the left-hand sides are the same. The latter is very useful for solving problems involving both first- and second-order derivatives such as the vorticity transport equation in example 4. In such problems, the present schemes can treat the convection terms implicitly leading to stable solutions at high  $Re$  while maintain the efficiency of the present proposed ADI method as those in the conventional ADI method (Peaceman and Rachford 1955), i.e. tridiagonal system matrices are achieved on each and every grid line. In this scenario, a desirable solution method with accuracy, stability, and efficiency is possible. It is noted that consistent first and second derivative compact FD schemes have been proposed recently by Ma et al. (2012). However, the accuracy of the second derivative scheme is only second order.

## 5.6 Concluding remarks

Novel  $C^2$ -continuous compact schemes using 2-node integrated radial basis function elements (IRBFEs) are presented and successfully applied to the linear parabolic equations on rectangular and non-rectangular domains and the incompressible Navier-Stokes equation. The accuracy and stability of the pro-

---

posed method are verified via the numerical examples. Attractive features of the proposed compact implicit methods include (i) efficient tridiagonal system matrices; and (ii) a higher order of continuity across grid nodes.

# Chapter 6

## RBF-based multiscale control volume method for second order elliptic problems with oscillatory coefficients

Many important engineering problems have multiple-scale solutions. Thermal conductivity of composite materials, flow in porous media, and turbulent transport in high Reynolds number flows are examples of this type. Direct numerical simulations for these problems typically require extremely large amounts of CPU time and computer memory, which may be too expensive or impossible on the present supercomputers. In this chapter, we develop a high order computational method, based on multiscale basis function approach and integrated radial-basis-function (IRBF) approximant, for the solution of multiscale elliptic problems with reduced computational cost. Unlike other methods based on multiscale basis function approach, sets of basis and correction functions here are obtained through  $C^2$ -continuous IRBF element formulations. High accuracy and efficiency of this method are demonstrated by several one- and

two-dimensional examples.

## 6.1 Introduction

In composite materials, the presence of particles/fibres in the resin gives rise to the multiscale fluctuations in the thermal or electrical conductivity. In porous media, formation properties, e.g. permeability, have a very high degree of spatial variability. These effects are typically captured at scales that are too fine for direct numerical simulation. To enable the solution of these problems, a number of advanced numerical methods have been developed. Examples include those based on the homogenisation theory (e.g. Dykaar and Kitanidis 1992), upscaling methods (e.g. McCarthy 1995) and multiscale methods (e.g. Hou and Wu 1997). The homogenisation-theory-based methods have been successfully applied for the prediction of effective properties and statistical correlation lengths for multicomponent random media. However, restrictive assumptions on the media, such as scale separation and periodicity, limit their range of application. Furthermore, when dealing with problems having many separate scales, they become very expensive because their computational cost increases exponentially with the number of scales. For upscaling methods, their design principle is based on simple physical and/or mathematical motivations. A heterogeneous medium is replaced by a homogeneous medium characterised by equivalent properties, and coarse scale equations are prescribed in explicit form. Although upscaling techniques are effective, most of their applications have been reported for the case of periodic structures. As opposed to upscaling, multiscale methods consider the full problem with the original resolution. The coarse scale equations are formed and solved numerically, where one constructs the basis functions from the leading order homogeneous elliptic equation in coarse scale elements. The idea of using the non-polynomial multiscale approximation space rather than the standard piecewise polynomial space was first introduced by Babuška et al. (1994) for one-dimensional problems and by Hou and Wu (1997), Hou

et al. (1999) for two-dimensional elliptic problems. These methods have the ability to capture accurately the effects of fine scale variations without the need for using global fine meshes. Multiscale methods can be categorised into multiscale finite-element methods (MFEM) (e.g. Allaire and Brizzi 2005, Hou 2005), mixed MFEM (e.g. Aarnes et al. 2005, Arbogast 2002) and multiscale finite-volume methods (MFVM) (e.g. Chu et al. 2008, Jenny et al. 2003). Typically, there are two different meshes used: a fine mesh for computing locally the basis function space, and a coarse mesh for computing globally the solution of an elliptic partial differential equation (PDE). The multiscale bases are independent of each other and their constructions can thus be conducted in parallel. In solving the elliptic PDE, one may only need to employ a mesh that today's computing resources can efficiently and effectively handle. For two-scale periodic structures, Hou et al. (1999) have proved that the MFEM indeed converges to the correct solution independent of the small scale in the homogenisation limit. Multiscale techniques require the solutions of elliptic PDEs which are achieved by means of discretisation schemes.

Radial-basis-function networks (RBFNs) are known as a powerful tool for the approximation of scattered data. Their application to the solution of PDEs has received a great deal of attention over the last 20 years (e.g. Fasshauer (2007) and references therein). It is easy to implement RBF collocation methods and such methods can give a high order convergence solution. RBF-based approximants can be constructed through a conventional differentiation process (e.g. Kansa 1990), or an integration process (IRBF) (e.g. Mai-Duy and Tran-Cong 2001, 2003). The latter (a smoothing operator) has several advantages over the former, including (i) to avoid the reduction in convergence rate caused by differentiation and (ii) to improve the numerical stability of a discrete solution. A number of IRBF approaches, based on local approximations (Mai-Duy and Tran-Cong 2009a), domain decompositions (Mai-Duy and Tran-Cong 2008) and preconditioning schemes (Mai-Duy and Tran-Cong 2010b), have been presented towards the solution of large-scale problems. Recently, a local high order ap-

proximant based on 2-node IRBF elements (a smallest IRBF set ever used for constructing approximants) has been proposed by An-Vo et al. (2010, 2011a). It was shown that such IRBF elements (IRBFEs) lead to a  $C^2$ -continuous solution rather than the usual  $C^0$ -continuous solution. IRBFEs have been successfully incorporated into the subregion-collocation (An-Vo et al. 2011b) and point-collocation (An-Vo et al. 2011b, 2013) formulation for simulating highly nonlinear flows accurately and effectively. We also use IRBFEs to model strain localisation in (An-Vo et al. 2012).

This chapter is concerned with the incorporation of IRBFEs and subregion collocation (i.e. control volume (CV) formulation) into the non-polynomial approximation space approach for solving one- and two-dimensional multiscale elliptic problems. Unlike other multiscale CV methods in the literature, sets of basis and correction functions in the present RBF-based multiscale CV method are obtained through highly accurate  $C^2$ -continuous IRBFE-CV formulations. As a result, not only the field variable but also its first derivatives are reconstructed directly with high accuracy. This is an important issue since the first derivatives contain information of great practical interest, such as the stress distribution and heat flux in composite materials or the flow velocity field in porous media.

The remainder of this chapter is organised as follows. Section 6.2 defines the problem. Section 6.3 and 6.4 briefly review the multiscale finite element and finite volume methods, respectively, for the problem. The proposed method is described in Section 6.5 and numerical results are discussed in Section 6.6. Section 6.7 concludes the chapter.

## 6.2 Problem definition

We consider the following multiscale elliptic problem

$$-\nabla \cdot (\lambda \nabla u) = f \text{ in } \Omega, \quad (6.1)$$

with appropriate boundary conditions.  $\lambda$  is a complex multiscale coefficient tensor;  $f$  a given function. Assume that the finest scale in  $\lambda$  is represented by  $\varepsilon$ .

## 6.3 Multiscale finite-element methods (MFEM)

Conventional discretisation techniques using piecewise polynomial approximation spaces can be applied to solve (6.1). However, it would require the mesh size  $h$  be much smaller than the finest scale, i.e.  $h \ll \varepsilon$ . In contrast, the multiscale computational framework which was firstly proposed by Hou and Wu (1997), Hou et al. (1999) uses a coarse grid of size  $h > \varepsilon$  and basis functions which aim to adapt to the small-scale features of the oscillatory coefficient tensor  $\lambda$ . The formulation of Hou and Wu (1997), Hou et al. (1999), namely the multiscale finite element method (MFEM), is based on a finite element framework where both the local and global problems are solved by a linear finite element method (LFEM). The MFEM is highly efficient and capable of capturing the large scale solution without resolving all the small scale details. For the case of two-scale periodic structures, it has been proved in Hou et al. (1999) that the MFEM indeed converges to the correct solution independent of the small scale in the homogenisation limit. However, for general cases e.g. non-periodic and random-scale media, the convergence of MFEM is not always guaranteed. In addition, there is an error gap between the MFEM solution and a corresponding fine scale reference solution. This error gap typically comes from two sources: (i) reduced problem boundary conditions for solving basis functions which is

empirical even though an over-sampling technique has been proposed (Hou and Wu 1997); and (ii) local homogeneous elliptic problems for basis functions. Due to the latter the basis functions do not involve effects of the right hand side field  $f$ . The right hand side, in a manner similar to that in the MFVM (discussed next), is only considered in the global coarse mesh system.

## 6.4 Multiscale finite volume method (MFVM)

Based on the multiscale basis function approach (Hou and Wu 1997, Hou et al. 1999), Jenny et al. (2003) and Chu et al. (2008) proposed the MFVM for elliptic problems in subsurface flow simulation. Equation (6.1) governs the pressure field  $p$  as

$$-\nabla \cdot (\lambda \nabla p) = f \text{ in } \Omega, \quad (6.2)$$

with the boundary conditions  $\nabla p \cdot \mathbf{n} = q$  and  $p(\mathbf{x}) = g$  on  $\partial\Omega_1$  and  $\partial\Omega_2$ , respectively. Note that  $\partial\Omega = \partial\Omega_1 \cup \partial\Omega_2$  is the whole boundary of the domain  $\Omega$  and  $\mathbf{n}$  is the outward unit vector normal to  $\partial\Omega$ . The mobility tensor  $\lambda$  (permeability,  $\mathbf{K}$ , divided by the fluid viscosity,  $\mu$ ) is positive definite and the right-hand side  $f$ ,  $q$ , and  $g$  are specified fields. The permeability heterogeneity is a dominant factor in dictating the flow behavior in natural porous formations. The heterogeneity of  $\mathbf{K}$  is usually represented as a complex multiscale function of space. Resolving the spatial correlation structures and capturing the variability of permeability requires highly detailed description.

The MFVM aims to efficiently compute the approximate solution of problem (6.2) for highly heterogeneous coefficient  $\lambda$  and source term  $f$ . The method can be explained as a cell-centered finite-volume method (Jenny et al. 2003) or a vertex-centered finite-volume method (Chu et al. 2008). We present the latter here. A Cartesian grid of  $N \times N$  is employed to represent the problem

domain  $\Omega$  (solid lines in Figure 6.1), from which  $I$  ( $I = (N - 2) \times (N - 2)$ ) non-overlapping control volumes  $\bar{\Omega}_k$  associated with  $I$  interior grid points  $\mathbf{x}_k$  ( $k \in [1, I]$ ) are formed. This set of control volumes constitutes a grid which is referred to as the coarse grid (dashed black lines in Figure 6.1). In addition, let  $\tilde{\Omega}$  be a collection of  $J$  cells  $\tilde{\Omega}^l$  ( $l \in [1, J]$ ,  $J = (N - 1) \times (N - 1)$ ) defined by the original  $N \times N$  Cartesian grid (solid lines in Figure 6.1). This set of  $J$  cells is referred to as the dual coarse grid. Note that these two grids can be much coarser than the underlying fine grid (dashed green lines in Figure 6.1) wherein each dual cell  $\tilde{\Omega}^l$  is discretised by a local fine grid of  $n \times n$ ) on which the mobility field is represented. On each dual cell  $\tilde{\Omega}^l$ , we seek the approximate solution  $\tilde{p}$  of  $p$  in the form

$$p^l \approx \tilde{p}^l = \sum_{i=1}^4 p_i^l \phi_i^l, \quad (6.3)$$

where  $p_i^l$  and  $\phi_i^l$  are the pressure value at and the basis function associated with the node  $x_i^l$ , respectively, of the dual coarse cell  $\tilde{\Omega}^l$ .

Unlike conventional discretisation methods, these basis functions  $\{\phi_i^l\}_{i=1}^4$  are generated from solving the following leading order homogeneous elliptic equations on the dual coarse cell  $\tilde{\Omega}^l$ ,

$$\nabla \cdot (\lambda \nabla \phi_i^l) = 0 \quad \text{in } \tilde{\Omega}^l. \quad (6.4)$$

Boundary conditions for (6.4) are derived from the requirement that  $\phi_i^l(\mathbf{x}_j^l) = \delta_{ij}$  ( $i, j \in [1, 4]$ ) and (6.4) be well-posed problems. Jenny et al. (2003) employed the proposition in (Hou et al. 1999) by solving reduced local one-dimensional problems to specify the boundary conditions for (6.4). The elliptic problems (6.4) in  $\tilde{\Omega}^l$  with such boundary conditions can be solved by any appropriate numerical method. In order to obtain a solution that depends linearly on the nodal pressures  $p_i^l$  as in (6.3), we solve four elliptic problems, one for each nodal pressure.

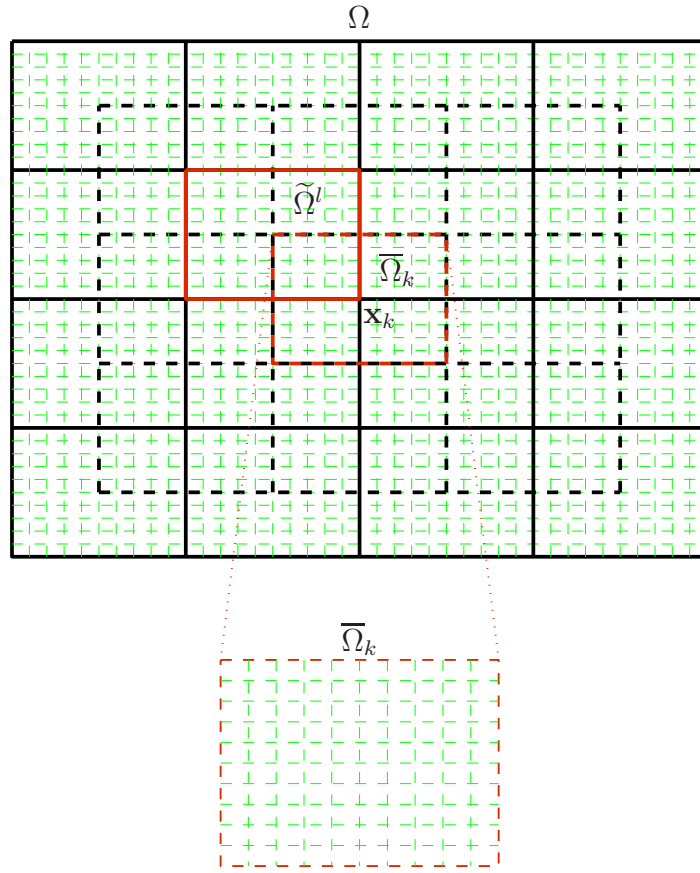


Figure 6.1: A computational domain  $\Omega$  with the coarse grid (black dashed lines) and dual coarse grid (black solid lines); dashed and solid red lines indicate a selected control volume  $\bar{\Omega}_k$  and a selected dual coarse cell  $\tilde{\Omega}^l$ , respectively. Shown underneath is an enlarged control volume, on which is imposed a  $n \times n = 11 \times 11$  local fine grid. It can be seen that the size of global fine grid (dashed green lines) is  $41 \times 41$ .

To derive a linear system for the nodal pressure values  $p_k$ , we substitute expressions (6.3) for  $\tilde{p}$  in the four dual cells associated with  $\mathbf{x}_k$  into equation (6.2) and integrate over  $\bar{\Omega}_k$ , which leads to

$$-\int_{\bar{\Omega}_k} \nabla \cdot (\lambda \nabla \tilde{p}) d\Omega = -\int_{\bar{\Omega}_k} \nabla \cdot \left( \lambda \nabla \left( \sum_{l=1}^4 \sum_{i=1}^9 \phi_i^l p_i \right) \right) d\Omega = \int_{\bar{\Omega}_k} f d\Omega, \quad (6.5)$$

where the indices  $l$  and  $i$  refer to local dual cells and local nodal points, respectively, associated with  $\mathbf{x}_k$  and  $\mathbf{x}_k \equiv \mathbf{x}_1$  as shown in Figure 6.2. Note that in the summation  $\sum_{i=1}^9 \phi_i^l p_i$  the index  $i$  of the basis functions  $\phi_i^l$  only takes on the four values relevant to  $\tilde{\Omega}^l$  (i.e.  $\phi_i^l = 0$  otherwise). Applying the Gauss theorem

to equation (6.5), one obtains

$$-\int_{\partial\bar{\Omega}_k} \left( \lambda \nabla \left( \sum_{l=1}^4 \sum_{i=1}^9 \phi_i^l p_i \right) \right) \cdot \mathbf{n}_k d\Gamma = \sum_{i=1}^9 p_i \sum_{l=1}^4 \int_{\partial\bar{\Omega}_k} (-\lambda \nabla \phi_i^l) \cdot \mathbf{n}_k d\Gamma = \int_{\bar{\Omega}_k} f d\Omega, \quad (6.6)$$

where  $\mathbf{n}_k$  is the outward unit vector normal to  $\partial\bar{\Omega}_k$ . Equations (6.6) at a nodal point  $\mathbf{x}_k$  ( $k \in [1, I]$ ) can be written in matrix form as

$$A_{ki} p_i = b_k \quad (6.7)$$

for the nodal pressure values  $p_k$  with

$$A_{ki} = \sum_{l=1}^4 \int_{\partial\bar{\Omega}_k} (-\lambda \nabla \phi_i^l) \cdot \mathbf{n}_k d\Gamma \quad (6.8)$$

and

$$b_k = \int_{\bar{\Omega}_k} f d\Omega. \quad (6.9)$$

We can reconstruct the fine scale pressure  $\tilde{p}^l$  in each dual coarse cell  $\tilde{\Omega}^l$  with  $p_k$  and the approximation (6.3). Implementing the reconstruction on the whole problem domain  $\Omega$  one obtains the fine scale pressure  $\tilde{p}$ , which is an approximation of the pressure field  $p$ . Although the MFV approach strongly resembles the multiscale finite element method by Hou et al. (1999), i.e. the construction of the basis functions is almost identical, the MFV is a finite-volume method and hence conservative. In some applications such as single and multiphase flows through porous media one is also interested in accurately representing the small-scale velocity field. Chen and Hou (2002) provide clear evidences that a locally conservative fine scale velocity field is a necessary requirement for accurate modeling of fluid transport. To construct the fine scale flow field, a straightforward way would be to use the basis functions in (6.3), but then the reconstructed fine scale velocity field is in general discontinuous at the interfaces

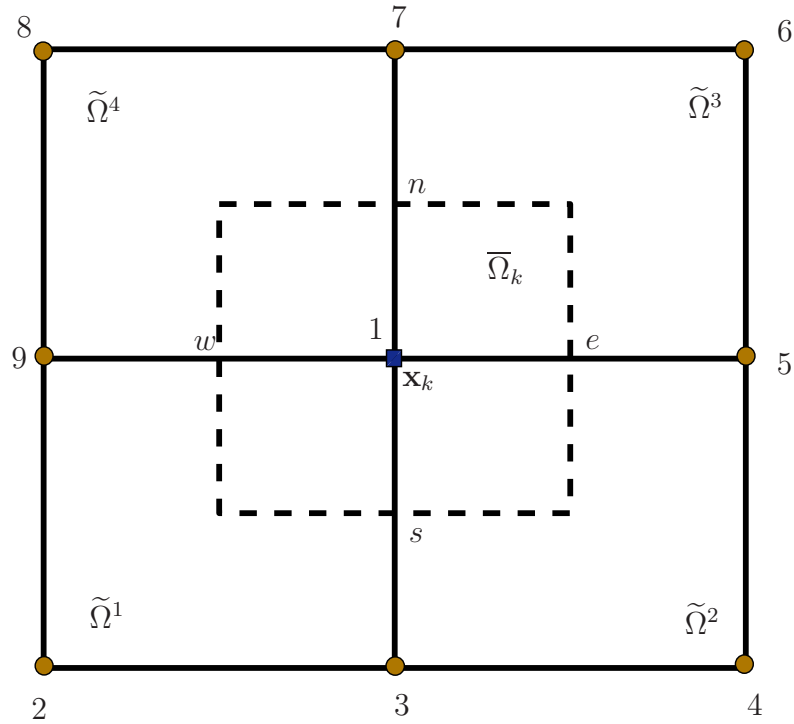


Figure 6.2: Local indices of dual cells and nodal points associated with a coarse grid node  $\mathbf{x}_k$  and  $\mathbf{x}_k \equiv \mathbf{x}_1$ .

of the dual cells. Therefore, large errors can occur in the divergence field, and local mass balance is violated. Jenny et al. (2003) describe how to reconstruct a conservative fine scale velocity field through the obtained pressure field  $\tilde{p}$ . The reader is referred to this work for more details.

The efficiency of the MFV method for large scale problems comes from the fact that fine scale details are captured through solving local problems (6.4) on small dual cells for basis functions. This step is a preprocessing step and has to be done once only. Furthermore, the construction of the fine scale basis functions is independent from cell to cell and therefore perfectly suited for parallel computation.

The MFV method was firstly used for solving single-phase flow in homogeneous and heterogenous permeability fields in Jenny et al. (2003). Jenny et al. (2004) and Jenny et al. (2006) extended the method to time dependent problems in

incompressible two-phase flows where the explicit and implicit time integrations were presented respectively. Lunati and Jenny relaxed the incompressible constraint in Lunati and Jenny (2006a) and compressible multiphase flow models were solved. It is important to note that until this stage of development the MFV method basically was not designed to solve elliptic problems with complex source terms and not appropriate to account for gravity and capillary pressure effects. The reason is that the basis functions and their linear combinations are solutions of local homogenous elliptic problems (6.4). The right hand side of the governing equation (6.2) is only taken into account in the coarse grid linear system (6.7). This led to the idea of introducing correction functions in Lunati and Jenny (2006b, 2008). Unlike basis functions  $\phi_i^l$ , correction functions  $p_c^l$  are the solutions of local elliptic problems on the dual cells with the right hand side  $f$ , i.e.

$$\nabla \cdot (\lambda \nabla p_c^l) = f \text{ in } \tilde{\Omega}^l. \quad (6.10)$$

At the grid nodes  $\mathbf{x}_k$  which belong to  $\tilde{\Omega}^l$ , we impose  $p_c^l(\mathbf{x}_k) = 0$ . The boundary conditions of (6.10) on the edge segments of the dual cell can be obtained in a manner similar to those in (6.4), i.e. by solving reduced local one-dimensional problems. It has been shown for a wide range of challenging test cases that these reduced problem boundary conditions provide a good localisation assumption. There exist scenarios, however, which demonstrate some limitations of these boundary conditions. Specifically, the MFV solution with correction functions and global fine scale reference solution  $p_f$  ( $p_f$  is an approximation of  $p$  on the global fine grid) are identical only if the basis and correction functions happen to capture the exact fine scale pressure solution on the interfaces of the dual coarse cells, i.e.

$$p_f^l = \sum_{i=1}^4 p_i^l \phi_i^l + p_c^l \text{ on } \partial \tilde{\Omega}^l. \quad (6.11)$$

It is desirable to approach boundary conditions for local elliptic problems via

(6.11) instead of the reduced problem boundary conditions. Hajibeygi et al. (2008) made it possible through an iterative framework based on a two-grid algorithm. At a step  $n$  with an initial pressure field  $\tilde{p}^{(n)}$ , they perform several smoothing steps on the global fine grid to obtain a temporary reference solution  $\tilde{p}_s^{(n)}$ . This smoothed pressure field yields the boundary values of correction functions on each dual cell through (6.11) with  $p_f^l$  replaced by  $\tilde{p}_s^{(n)}$ , i.e.

$$p_c^l = \tilde{p}_s^{(n)} - \sum_{i=1}^4 p_i^l \phi_i^l \text{ on } \partial\tilde{\Omega}^l, \quad (6.12)$$

where the boundary values of the basis functions  $\phi_i^l$  on the dual cells are still obtained from the reduced problem boundary conditions. The boundary conditions (6.12) serve to solve the local problems (6.10) on the dual cells for the correction functions at step  $n$ . Then the nodal pressures  $p_k$  are obtained through the solution of a coarse grid system (Hajibeygi et al. 2008) and a new pressure field  $\tilde{p}^{(n+1)}$  is constructed via

$$\tilde{p}^{(n+1)} = \sum_{i=1}^4 p_i^l \phi_i^l + p_c^l \text{ in } \tilde{\Omega}^l. \quad (6.13)$$

Again, we smooth  $\tilde{p}^{(n+1)}$  to yield a new smoothed field  $\tilde{p}_s^{(n+1)}$  and repeat the iteration until convergence. It was shown by a series of examples in Hajibeygi et al. (2008) that this iterative MFV (iMFV) method converges to the fine scale reference solution  $p_f$ .

The iMFV method relatively maintains the efficiency of MFV method and has the possibility to approach the accuracy of corresponding fine scale solver. This method has been successfully applied to incompressible (Hajibeygi et al. 2008) and compressible (Hajibeygi and Jenny 2009) multiphase flow in porous media. Recently, it is used adaptively (Hajibeygi and Jenny 2011) and extended to simulate multiphase flow in fractured porous media (Hajibeygi et al. 2011).

## 6.5 Proposed RBF-based multiscale control volume method

In this work we are interested in a one-parameter ( $\varepsilon$ ) form of the multiscale elliptic problem (6.1), i.e.

$$-\nabla \cdot (\mathbf{a}^\varepsilon(\mathbf{x})\nabla u(\mathbf{x})) = f(\mathbf{x}) \text{ in } \Omega \quad (6.14)$$

with the boundary conditions  $\nabla u \cdot \mathbf{n} = b$  and  $u(\mathbf{x}) = g$  on  $\partial\Omega_1$  and  $\partial\Omega_2$ , respectively. Note that  $\partial\Omega = \partial\Omega_1 \cup \partial\Omega_2$  and  $\mathbf{n}$  is the outward unit vector normal to  $\partial\Omega$ .  $\mathbf{a}^\varepsilon$  is the coefficient tensor which is positive-definite with upper and lower bounds and involving a small scale  $\varepsilon$ , and  $f, b$  and  $g$  are specified fields. This elliptic problem usually arises in modeling composite materials and porous media flows. In the case of heat conduction in composite materials,  $u$  and  $\mathbf{a}$  represent the temperature and thermal conductivity, respectively. In the case of flows in porous media,  $u$  is the pressure and  $\mathbf{a}$  is the mobility field.

For the reasons mentioned above, the MFEM is an efficient method to capture the large scale solution but cannot produce the fine scale reference solution. In addition, the method used in MFEM to determine the basis functions and solve the global coarse mesh problem is a linear finite element formulation. Note that there is an attempt to use a high-order method, e.g. the Chebyshev spectral method, to determine the basis functions in (Hou and Wu 1997, Hou et al. 1999). They found that the accuracy of the final results is relatively insensitive to the accuracy of the basis functions. On the other hand, as described above, though possessing conservative property the MFVM strongly resemble the MFEM and hence also cannot produce the fine scale reference solution. In contrast to the MFEM and the MFVM, the iMFV method (Hajibeygi et al. 2008) can produce the reference solution efficiently. However, a low order smoother has been used which results in a low-order accuracy relative to the exact solution. Moreover, like the MFVM the iMFV method requires a further reconstruction step to

obtain a continuous velocity field for the solution of transport equations. It is pointed out in (Chen and Hou 2002) that this is a compulsory step to accurately solve the flow-transport-related applications, e.g. the single and multiphase flows through porous media.

It is desirable to develop a multiscale computational framework which can produce the fine scale reference solution of elliptic problem (6.14) with high efficiency and accuracy. In the following, we propose a high-order conservative multiscale computational framework based on 2-node IRBFEs for solving (6.14). Unlike other multiscale computational frameworks, the proposed method can produce fine scale reference solutions efficiently with high accuracy. Furthermore, iterative solutions which converge to  $C^2$ -continuous reference solutions are obtained in 2D problems. As a result, intrinsically continuous velocity fields are guaranteed automatically in flow-transport-related applications without the need for a reconstruction step. Because of fundamental differences, the proposed method for 1D and 2D problems is presented independently, following a brief review of the two-node integrated-RBF elements in our discretisation scheme based on Cartesian grids.

### 6.5.1 Two-node IRBFEs

Expressions (3.11)-(3.13) are employed as interior element approximations. For convenience, in the case of  $\eta \equiv x$ , we denote

$$\mu_i = \frac{\partial \varphi_i}{\partial x} \left( \frac{x_1 + x_2}{2} \right), \quad (6.15)$$

$$\nu_i = \frac{\partial^2 \varphi_i}{\partial x^2} (x_1), \quad (6.16)$$

$$\zeta_i = \frac{\partial^2 \varphi_i}{\partial x^2} (x_2), \quad (6.17)$$

and in the case of  $\eta \equiv y$ ,

$$\theta_i = \frac{\partial \varphi_i}{\partial y} \left( \frac{y_1 + y_2}{2} \right), \quad (6.18)$$

$$\vartheta_i = \frac{\partial^2 \varphi_i}{\partial y^2} (y_1), \quad (6.19)$$

$$\xi_i = \frac{\partial^2 \varphi_i}{\partial y^2} (y_2), \quad (6.20)$$

where  $i \in \{1, 2, 3, 4\}$ .

The element *IRBFE-D1* via expressions (3.14)-(3.16) is employed at Dirichlet boundary. For Neumann boundary conditions such as given surface traction or boundary pressure, other types of semi-interior elements have been proposed in Chapter 2 to which the reader is referred for details.

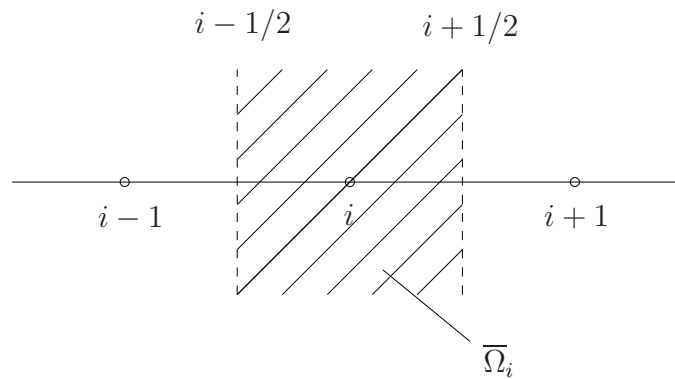


Figure 6.3: A CV discretisation scheme in 1D: node  $i$  and its associated control volume. The circles represent the nodes, and the vertical dash lines represent the faces of the control volume.

### 6.5.2 Proposed method for 1D problems

In a 1D domain, problem (6.14) reduces to

$$-\frac{d}{dx} \left( a^\varepsilon(x) \frac{du(x)}{dx} \right) = f(x), \quad x \in \Omega, \quad (6.21)$$

where  $a^\varepsilon(x)$  is a single variable function involving a small scale parameter  $\varepsilon$ . The problem domain is represented using a set of  $N$  nodal points, called a global coarse scale grid. This grid is used to obtain the coarse scale solution of problem (6.21). On each interval or coarse cell  $\tilde{\Omega}^l$ ,  $\tilde{\Omega}^l = [x_{i-1}, x_i]$  with  $i \in [2, N]$  and  $l \in [1, N - 1]$ , an approximation to the field variable  $u$  is sought in the form

$$u^l(x) = \phi_{i-1}^l(x)u_{i-1} + \phi_i^l(x)u_i + u_c^l(x), \quad (6.22)$$

where  $x \in \tilde{\Omega}^l$ ,  $u_{i-1} = u(x_{i-1})$ ,  $u_i = u(x_i)$ ,  $\phi_{i-1}^l(x)$  and  $\phi_i^l(x)$  are the basis functions associated with the nodes  $x_{i-1}$  and  $x_i$  respectively on the coarse cell  $\tilde{\Omega}^l$ , and  $u_c^l(x)$  is the correction function associated with the coarse cell  $\tilde{\Omega}^l$ .

We employ subregion collocation to discretise (6.21). Each node  $x_i$  with  $i \in [2, N - 1]$  is surrounded by a control volume  $\bar{\Omega}_i$ ,  $\bar{\Omega}_i = [x_{i-1/2}, x_{i+1/2}]$  as shown in Figure 6.3. Integrating (6.21) over a control volume  $\bar{\Omega}_i$ , one has

$$a^\varepsilon(x_{i+1/2})\frac{du}{dx}(x_{i+1/2}) - a^\varepsilon(x_{i-1/2})\frac{du}{dx}(x_{i-1/2}) + \int_{x_{i-1/2}}^{x_{i+1/2}} f dx = 0. \quad (6.23)$$

Taking (6.22) into account, one can express first derivatives in (6.23) in terms of nodal values of  $u$ . Unlike traditional discretisation methods, the basis functions  $\phi_{i-1}^l(x)$  and  $\phi_i^l(x)$  on a coarse cell  $\tilde{\Omega}^l$  are not analytic functions (e.g. not polynomials), but local numerical solutions to the following differential equation

$$\frac{d}{dx} \left( a^\varepsilon \frac{d\phi_k^l}{dx} \right) = 0 \quad (6.24)$$

with  $k \in \{i - 1, i\}$  and  $x \in \tilde{\Omega}^l$ . Boundary conditions for (6.24) are specified using the condition  $\phi_k^l(x_j) = \delta_{kj}$  with  $j \in \{i - 1, i\}$ . Likewise, the correction function  $u_c^l(x)$  is a numerical solution to the following differential equation

$$-\frac{d}{dx} \left( a^\varepsilon \frac{du_c^l}{dx} \right) = f \quad (6.25)$$

with homogeneous boundary conditions  $u_c^l(x_j) = 0$ ,  $j \in \{i - 1, i\}$ . Unlike (6.24)

the right hand side  $f$  of the governing equation (6.21) is involved in (6.25). Equation (6.24) needs to be solved twice while equation (6.25) needs to be solved once for the determination of the two basis functions and the correction function respectively on each coarse cell. A coarse cell  $\tilde{\Omega}^l$  is discretised by a set of  $n$  points, called local fine scale grid. Such a grid is used to capture the fine scale structure information of the solution. Let  $\{\eta_1 = x_{i-1}, \eta_2, \dots, \eta_n = x_i\}$  be a set of nodes of the local fine scale grid. Similar to a coarse scale node, each fine scale node  $\eta_m$  with  $m \in [2, n-1]$  is surrounded by a local control volume  $\bar{\Omega}_m$ ,  $\bar{\Omega}_m = [\eta_{m-1/2}, \eta_{m+1/2}]$ . Integrating (6.24) and (6.25) over  $\bar{\Omega}_m$ , one has respectively

$$a^\varepsilon(\eta_{m+1/2}) \frac{d\phi_k^l}{dx}(\eta_{m+1/2}) - a^\varepsilon(\eta_{m-1/2}) \frac{d\phi_k^l}{dx}(\eta_{m-1/2}) = 0, \quad (6.26)$$

$$a^\varepsilon(\eta_{m+1/2}) \frac{du_c^l}{dx}(\eta_{m+1/2}) - a^\varepsilon(\eta_{m-1/2}) \frac{du_c^l}{dx}(\eta_{m-1/2}) + \int_{\eta_{m-1/2}}^{\eta_{m+1/2}} f d\eta = 0. \quad (6.27)$$

We propose to approximate the first-order derivatives in (6.26) and (6.27) by a 2-node IRBFE scheme, i.e. equation (3.12). Assuming that  $\eta_{m-1}$  and  $\eta_{m+1}$  are interior fine scale nodes, we can form two interior 2-node IRBFES at  $\eta_m$ , i.e. elements  $[\eta_{m-1}, \eta_m]$  and  $[\eta_m, \eta_{m+1}]$ , to the left and right side of  $\eta_m$  respectively. Applying (3.12) with notation (6.15) to the element  $[\eta_{m-1}, \eta_m]$ , one has

$$\frac{d\phi_k^l}{dx}(\eta_{m-1/2}) = \mu_1 \phi_k^l(\eta_{m-1}) + \mu_2 \phi_k^l(\eta_m) + \mu_3 \frac{d\phi_k^l}{d\eta}(\eta_{m-1}) + \mu_4 \frac{d\phi_k^l}{d\eta}(\eta_m), \quad (6.28)$$

$$\frac{du_c^l}{dx}(\eta_{m-1/2}) = \mu_1 u_c^l(\eta_{m-1}) + \mu_2 u_c^l(\eta_m) + \mu_3 \frac{du_c^l}{d\eta}(\eta_{m-1}) + \mu_4 \frac{du_c^l}{d\eta}(\eta_m). \quad (6.29)$$

Similarly, to the element  $[\eta_m, \eta_{m+1}]$ , one has

$$\frac{d\phi_k^l}{dx}(\eta_{m+1/2}) = \mu_1\phi_k^l(\eta_m) + \mu_2\phi_k^l(\eta_{m+1}) + \mu_3\frac{d\phi_k^l}{d\eta}(\eta_m) + \mu_4\frac{d\phi_k^l}{d\eta}(\eta_{m+1}), \quad (6.30)$$

$$\frac{du_c^l}{dx}(\eta_{m+1/2}) = \mu_1u_c^l(\eta_m) + \mu_2u_c^l(\eta_{m+1}) + \mu_3\frac{du_c^l}{d\eta}(\eta_m) + \mu_4\frac{du_c^l}{d\eta}(\eta_{m+1}). \quad (6.31)$$

Note that (6.28)-(6.31) will be slightly different at the coarse cell boundaries (also the coarse scale nodes) where (3.15) for semi-interior elements is used instead of (3.12). Substituting (6.28) and (6.30) into (6.26) yields

$$\begin{aligned} & a^\varepsilon(\eta_{m+1/2})\mu_2\phi_k^l(\eta_{m+1}) + [a^\varepsilon(\eta_{m+1/2})\mu_1 - a^\varepsilon(\eta_{m-1/2})\mu_2] \phi_k^l(\eta_m) \\ & - a^\varepsilon(\eta_{m-1/2})\mu_1\phi_k^l(\eta_{m-1}) + a^\varepsilon(\eta_{m+1/2})\mu_4\frac{d\phi_k^l}{d\eta}(\eta_{m+1}) \\ & + [a^\varepsilon(\eta_{m+1/2})\mu_3 - a^\varepsilon(\eta_{m-1/2})\mu_4] \frac{d\phi_k^l}{d\eta}(\eta_m) - a^\varepsilon(\eta_{m-1/2})\mu_3\frac{d\phi_k^l}{d\eta}(\eta_{m-1}) = 0. \end{aligned} \quad (6.32)$$

It can be seen from (6.32) that there are two unknowns, namely  $\phi_k^l(\eta_m)$  and  $d\phi_k^l/d\eta(\eta_m)$ , associated with each nodal points  $\eta_m$  ( $m \in [2, n-1]$ ). Collection of (6.32) at all nodal points leads to a system of  $n-2$  equations for  $2 \times (n-2)$  unknowns. For the algebraic system to be solvable one more equation needs to be added at each and every nodal points  $\eta_m$ , which is here achieved by imposing  $C^2$ -continuous condition at  $\eta_m$ , i.e.

$$\left[ \frac{d^2\phi_k^l}{d\eta^2}(\eta_m) \right]_L = \left[ \frac{d^2\phi_k^l}{d\eta^2}(\eta_m) \right]_R, \quad (6.33)$$

where  $(\cdot)_L$  indicates that the computation of  $(\cdot)$  is based on the element to the left of  $\eta_m$ , i.e. element  $[\eta_{m-1}, \eta_m]$ , and similarly subscript  $R$  denotes the right element  $[\eta_m, \eta_{m+1}]$ . The left and the right of equation (6.33) are obtained via

expression (3.13), noting (6.17) and (6.16) respectively, yielding

$$\begin{aligned} \zeta_1 \phi_k^l(\eta_{m-1}) + \zeta_2 \phi_k^l(\eta_m) + \zeta_3 \frac{d\phi_k^l}{d\eta}(\eta_{m-1}) + \zeta_4 \frac{d\phi_k^l}{d\eta}(\eta_m) = \\ \nu_1 \phi_k^l(\eta_m) + \nu_2 \phi_k^l(\eta_{m+1}) + \nu_3 \frac{d\phi_k^l}{d\eta}(\eta_m) + \nu_4 \frac{d\phi_k^l}{d\eta}(\eta_{m+1}). \end{aligned} \quad (6.34)$$

Collection of equations (6.32) and (6.34) at each and every fine scale nodes  $\eta_m$  ( $m \in [2, n-1]$ ) with the associated boundary conditions leads to two systems of  $2 \times (n-2)$  equations for  $2 \times (n-2)$  unknowns. These two systems are solved for the two basis functions on  $\tilde{\Omega}^l$ . Unlike other conventional discretisation techniques, both the field variable and its first-derivative are considered in the present proposed technique, resulting  $C^2$ -continuous solutions for the basis functions.

Similarly, at each fine scale node  $\eta_m$ , substituting (6.29) and (6.31) into (6.27) and imposing  $C^2$ -continuous condition at  $\eta_m$  lead to two equations for two unknowns associated with  $\eta_m$ . Collection of these equations at all fine scale nodes with the homogeneous boundary conditions results in a system of  $2 \times (n-1)$  equations for  $2 \times (n-1)$  unknowns. This system is solved for the correction function  $u_c^l$  associated with the coarse cell  $\tilde{\Omega}^l$ .

The set of basis and correction functions of the whole domain  $\Omega$  is used to represent the first derivatives in (6.23) in terms of coarse scale nodal values  $u_i$  ( $i \in [2, N-1]$ ). Collection of equation (6.23) at all coarse scale nodes with the associated boundary conditions lead to a coarse scale system of  $N-2$  equations for  $N-2$  coarse scale nodal values of  $u$ . Consequently, the complete solution of problem (6.21) is constructed on each and every coarse cell  $\tilde{\Omega}^l$  via (6.22). It can be seen that the presently proposed multiscale method is conservative for both local and global problems.

### 6.5.3 Proposed method for 2D problems

We consider the coefficient tensor  $\mathbf{a}^\varepsilon$  in the following form

$$\mathbf{a}^\varepsilon = \begin{pmatrix} a^\varepsilon(x) & 0 \\ 0 & b^\varepsilon(y) \end{pmatrix}, \quad (6.35)$$

where  $a^\varepsilon(x)$  and  $b^\varepsilon(y)$  are oscillatory functions involving a small scale  $\varepsilon$ . It is noted that the periodicity and scale separation assumptions of  $a^\varepsilon(x)$  and  $b^\varepsilon(y)$  are not necessary here. The two-dimensional equation (6.14) becomes

$$-\frac{\partial}{\partial x} \left( a^\varepsilon(x) \frac{\partial u}{\partial x} \right) - \frac{\partial}{\partial y} \left( b^\varepsilon(y) \frac{\partial u}{\partial y} \right) = f(x, y). \quad (6.36)$$

Here we are considering a particular class (6.36) of the general problem (6.14) for the convenience of presenting the main features of the proposed method. Extension of the proposed method to the general problem where  $\mathbf{a}^\varepsilon$  is a full tensor requires consideration of a mixed derivative term and will be reported in an up-coming work. Nevertheless, the multiscale problem (6.36) does have important application in, e.g. two-dimensional semi-conductor quantum devices wherein there is a specific direction oscillation of the coefficients at each location in space and time. The readers are referred to (Wang and Shu 2009) for the application of such device models in one-dimension.

A Cartesian grid system is employed to represent the problem domain  $\Omega$  in a manner similar to that in the MFV method (e.g. Figure 6.1). Integrating (6.36) over a control volume  $\overline{\Omega}_k$  and then applying the Green's theorem in plane, one has

$$\begin{aligned} - \int_{\overline{\Omega}_k} \left[ \frac{\partial}{\partial x} \left( a^\varepsilon(x) \frac{\partial u}{\partial x} \right) + \frac{\partial}{\partial y} \left( b^\varepsilon(y) \frac{\partial u}{\partial y} \right) \right] d\Omega = \\ - \int_{\partial\overline{\Omega}_k} a^\varepsilon(x) \frac{\partial u}{\partial x} dy + \int_{\partial\overline{\Omega}_k} b^\varepsilon(y) \frac{\partial u}{\partial y} dx = A_k f_k, \end{aligned} \quad (6.37)$$

where  $A_k$  is the area of  $\bar{\Omega}_k$  and

$$f_k = \frac{1}{A_k} \int_{\bar{\Omega}_k} f d\Omega. \quad (6.38)$$

Approximating the line integrals in (6.37) by the midpoint rule, one obtains

$$- \left[ \left( a^\varepsilon(x) \frac{\partial u}{\partial x} \right)_e - \left( a^\varepsilon(x) \frac{\partial u}{\partial x} \right)_w \right] \Delta_y - \left[ \left( b^\varepsilon(y) \frac{\partial u}{\partial y} \right)_n - \left( b^\varepsilon(y) \frac{\partial u}{\partial y} \right)_s \right] \Delta_x = A_k f_k, \quad (6.39)$$

where  $\Delta_x$  and  $\Delta_y$  are the coarse grid spacing in  $x$  and  $y$  direction respectively; and the subscripts  $e, w, n$  and  $s$  are used to indicate that the flux is estimated at the intersections of the dual grid lines with the east, west, north and south faces of the control volume  $\bar{\Omega}_k$ , respectively (Figure 6.2).

To estimate the first-order derivatives of  $u$  in (6.39) we consider the dual coarse cells  $\tilde{\Omega}^l$  in a 2D computational domain as shown in Figure 6.1. We seek the approximation for the field variable  $u$  on each  $\tilde{\Omega}^l$  in the form

$$u^l(\mathbf{x}) = \sum_{i=1}^4 \phi_i^l(\mathbf{x}) u_i + u_c^l(\mathbf{x}), \quad (6.40)$$

where  $\phi_i^l(\mathbf{x})$  is the basis function associated with a coarse scale node  $\mathbf{x}_i$  and  $i \in [1, 4]$  is the local index of the four nodes of a coarse cell  $\tilde{\Omega}^l$ ,  $u_i = u(\mathbf{x}_i)$ , and  $u_c^l(\mathbf{x})$  is the correction function associated with a coarse cell  $\tilde{\Omega}^l$ . As explained earlier via (6.4) and (6.10), these basis functions and correction function are similarly local numerical solutions of problem (6.36) on  $\tilde{\Omega}^l$  without and with right-hand side, respectively, i.e.

$$- \frac{\partial}{\partial x} \left( a^\varepsilon(x) \frac{\partial \phi_i^l}{\partial x} \right) - \frac{\partial}{\partial y} \left( b^\varepsilon(y) \frac{\partial \phi_i^l}{\partial y} \right) = 0, \quad (6.41)$$

$$- \frac{\partial}{\partial x} \left( a^\varepsilon(x) \frac{\partial u_c^l}{\partial x} \right) - \frac{\partial}{\partial y} \left( b^\varepsilon(y) \frac{\partial u_c^l}{\partial y} \right) = f(x, y). \quad (6.42)$$

Boundary conditions for (6.41) are

$$\frac{\partial}{\partial x} \left( a^\varepsilon(x) \frac{\partial \phi_i^l}{\partial x} \right) = 0 \quad \text{on } \partial\tilde{\Omega}_x^l, \quad (6.43)$$

$$\frac{\partial}{\partial y} \left( b^\varepsilon(y) \frac{\partial \phi_i^l}{\partial y} \right) = 0 \quad \text{on } \partial\tilde{\Omega}_y^l, \quad (6.44)$$

and for (6.42) are

$$\frac{\partial}{\partial x} \left( a^\varepsilon(x) \frac{\partial u_c^l}{\partial x} \right) = \frac{\partial}{\partial x} \left( a^\varepsilon(x) \frac{\partial u_f}{\partial x} \right) \quad \text{on } \partial\tilde{\Omega}_x^l, \quad (6.45)$$

$$\frac{\partial}{\partial y} \left( b^\varepsilon(y) \frac{\partial u_c^l}{\partial y} \right) = \frac{\partial}{\partial y} \left( b^\varepsilon(y) \frac{\partial u_f}{\partial y} \right) \quad \text{on } \partial\tilde{\Omega}_y^l, \quad (6.46)$$

where  $\partial\tilde{\Omega}_x^l$  and  $\partial\tilde{\Omega}_y^l$  denote the  $x$ - and  $y$ -segments, respectively, of the boundary of a dual cell  $\tilde{\Omega}^l$  and  $u_f$  is a reference solution on the global fine scale grid. A method to create a fine scale reference solution  $u_f$  will be presented in the following section. At the dual-grid nodes  $\mathbf{x}_i$  which belong to  $\tilde{\Omega}^l$ ,  $\phi_j^l(\mathbf{x}_i) = \delta_{ji}$  ( $j \in [1, 4]$ ) and  $u_c^l(\mathbf{x}_i) = 0$ . Note that outside  $\tilde{\Omega}^l$  the  $\phi_j^l$  and  $u_c^l$  are set to zero. In the present approach, a  $C^2$ -continuous IRBFE based control volume method (An-Vo et al. 2011a) is used to solve the local problems (6.41) and (6.42) with the associated boundary conditions for the basis functions and correction functions respectively.

The first-order derivatives of  $u$  in (6.39) can now be estimated by using expressions (6.40) for  $u^l$  in the four dual coarse cells associated with a grid node  $\mathbf{x}_k$  (Figure 6.2). Specifically, we use local indices of  $l$  ( $l \in [1, 4]$ ) and  $i$  ( $i \in [1, 9]$ ) for local dual coarse cells and local coarse nodes, respectively, associated with  $\mathbf{x}_k$  and  $\mathbf{x}_k \equiv \mathbf{x}_1$  (Figure 6.2) to obtain

$$\begin{aligned} \left( \frac{\partial u}{\partial x} \right)_e &= \frac{\partial \phi_1^2}{\partial x}(x_e) u_1 + \frac{\partial \phi_5^2}{\partial x}(x_e) u_5 + \frac{\partial u_c^2}{\partial x}(x_e) = \\ & \frac{\partial \phi_1^3}{\partial x}(x_e) u_1 + \frac{\partial \phi_5^3}{\partial x}(x_e) u_5 + \frac{\partial u_c^3}{\partial x}(x_e), \quad (6.47) \end{aligned}$$

$$\begin{aligned} \left(\frac{\partial u}{\partial x}\right)_w &= \frac{\partial \phi_9^1}{\partial x}(x_w) u_9 + \frac{\partial \phi_1^1}{\partial x}(x_w) u_1 + \frac{\partial u_c^1}{\partial x}(x_w) = \\ & \frac{\partial \phi_9^4}{\partial x}(x_w) u_9 + \frac{\partial \phi_1^4}{\partial x}(x_w) u_1 + \frac{\partial u_c^4}{\partial x}(x_w), \end{aligned} \quad (6.48)$$

$$\begin{aligned} \left(\frac{\partial u}{\partial y}\right)_n &= \frac{\partial \phi_1^3}{\partial y}(y_n) u_1 + \frac{\partial \phi_7^3}{\partial y}(y_n) u_7 + \frac{\partial u_c^3}{\partial y}(y_n) = \\ & \frac{\partial \phi_1^4}{\partial y}(y_n) u_1 + \frac{\partial \phi_7^4}{\partial y}(y_n) u_7 + \frac{\partial u_c^4}{\partial y}(y_n), \end{aligned} \quad (6.49)$$

$$\begin{aligned} \left(\frac{\partial u}{\partial y}\right)_s &= \frac{\partial \phi_3^1}{\partial y}(y_s) u_3 + \frac{\partial \phi_1^1}{\partial y}(y_s) u_1 + \frac{\partial u_c^1}{\partial y}(y_s) = \\ & \frac{\partial \phi_3^2}{\partial y}(y_s) u_3 + \frac{\partial \phi_1^2}{\partial y}(y_s) u_1 + \frac{\partial u_c^2}{\partial y}(y_s). \end{aligned} \quad (6.50)$$

We substitute (6.47)-(6.50) into (6.39) to obtain the discretised equation at a coarse node  $\mathbf{x}_k$ . Collection of the discretised equations at all coarse nodes leads to a linear system to be solved for the coarse scale nodal values  $u_k$ ,  $k \in [1, N - 2 \times N - 2]$ . Consequently, the solution for  $u$  in each dual coarse cell  $\tilde{\Omega}^l$  is reconstructed via  $u_k$  and the approximation (6.40). By implementing the reconstruction on the whole problem domain  $\Omega$ , the global solution for  $u$  is obtained.

It should be noted that the current computational framework for  $u$  depends strongly on the boundary conditions of local problems for the determination of the correction functions, i.e. (6.45) and (6.46), which unfortunately require a priori knowledge of  $u_f$ . To obtain the fine scale reference solution  $u_f$  one typically has to directly resolve all the small scale features of a multiscale problem. In the following section, we avoid this costly and even impossible task by proposing a conservative fine scale solver based on 2-node IRBFEs.

### Fine scale $C^2$ -continuous conservative solver

Consider problem (6.36) on a global fine scale grid. Each fine scale node, similar to a coarse scale node, is surrounded by a control volume. Integrating (6.36)

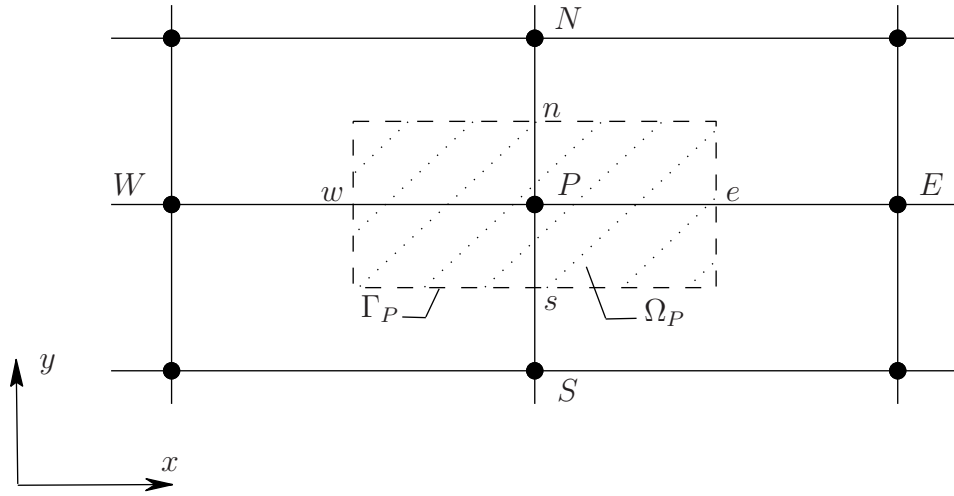


Figure 6.4: Schematic outline for a 2D control volume on the fine scale grid.

over the control volume  $\Omega_P$  of a fine scale interior grid node  $P$  (Figure 6.4) by a similar procedure in obtaining (6.39), one has

$$-\left[\left(a^\varepsilon(x)\frac{\partial u}{\partial x}\right)_e - \left(a^\varepsilon(x)\frac{\partial u}{\partial x}\right)_w\right]\delta_y - \left[\left(b^\varepsilon(y)\frac{\partial u}{\partial y}\right)_n - \left(b^\varepsilon(y)\frac{\partial u}{\partial y}\right)_s\right]\delta_x = A_P f_P, \quad (6.51)$$

where  $\delta_x$  and  $\delta_y$  are fine grid spacing in  $x$  and  $y$  direction respectively; the subscripts  $e, w, n$  and  $s$  are now used to indicate that the flux is estimated at the intersections of the fine grid lines with the east, west, north and south faces of the control volume  $\Omega_P$ , respectively (Figure 6.4); and  $A_P$  is the area of  $\Omega_P$  and  $f_P = \frac{1}{A_P} \int_{\Omega_P} f d\Omega$ . Unlike (6.47)-(6.50), the fluxes are presently computed via 2-node IRBFs defined over line segments between  $P$  and its neighbouring grid nodes ( $E, W, N$  and  $S$ ). There are 4 IRBFs associated with a control volume  $\Omega_P$ . Assuming that  $PE, WP$  are interior elements and making use of

(3.12), noting (6.15), one obtains fluxes in the  $x$ -direction as

$$\left(\frac{\partial u}{\partial x}\right)_e = \mu_1 u_P + \mu_2 u_E + \mu_3 \frac{\partial u_P}{\partial x} + \mu_4 \frac{\partial u_E}{\partial x} \quad \text{with } x_1 \equiv x_P \text{ and } x_2 \equiv x_E, \quad (6.52)$$

$$\left(\frac{\partial u}{\partial x}\right)_w = \mu_1 u_W + \mu_2 u_P + \mu_3 \frac{\partial u_W}{\partial x} + \mu_4 \frac{\partial u_P}{\partial x} \quad \text{with } x_1 \equiv x_W \text{ and } x_2 \equiv x_P. \quad (6.53)$$

Expressions for the flux at the faces  $y = y_n$  and  $y = y_s$  are of similar forms obtained by using  $PN$  and  $SP$ , assumed as interior elements, and making use of (3.12), noting (6.18),

$$\left(\frac{\partial u}{\partial y}\right)_n = \theta_1 u_P + \theta_2 u_N + \theta_3 \frac{\partial u_P}{\partial y} + \theta_4 \frac{\partial u_N}{\partial y} \quad \text{with } y_1 \equiv y_P \text{ and } y_2 \equiv y_N, \quad (6.54)$$

$$\left(\frac{\partial u}{\partial y}\right)_s = \theta_1 u_S + \theta_2 u_P + \theta_3 \frac{\partial u_S}{\partial y} + \theta_4 \frac{\partial u_P}{\partial y} \quad \text{with } y_1 \equiv y_S \text{ and } y_2 \equiv y_P. \quad (6.55)$$

(6.52)-(6.55) may change if  $PE$ ,  $WP$ ,  $PN$ , and  $SP$  are semi-interior elements where (3.15) is used instead of (3.12).

Substituting (6.52)-(6.55) into (6.51), one has

$$G^{[x]} \begin{bmatrix} u_W \\ u_P \\ u_E \end{bmatrix} + G^{[y]} \begin{bmatrix} u_S \\ u_P \\ u_N \end{bmatrix} + D^{[x]} \begin{bmatrix} \frac{\partial u_W}{\partial x} \\ \frac{\partial u_P}{\partial x} \\ \frac{\partial u_E}{\partial x} \end{bmatrix} + D^{[y]} \begin{bmatrix} \frac{\partial u_S}{\partial y} \\ \frac{\partial u_P}{\partial y} \\ \frac{\partial u_N}{\partial y} \end{bmatrix} = A_P f_P, \quad (6.56)$$

where

$$G^{[x]} = - \begin{bmatrix} -a^\varepsilon(x_w)\mu_1 & a^\varepsilon(x_e)\mu_1 - a^\varepsilon(x_w)\mu_2 & a^\varepsilon(x_e)\mu_2 \end{bmatrix} \delta_y, \quad (6.57)$$

$$G^{[y]} = - \begin{bmatrix} -b^\varepsilon(y_s)\theta_1 & b^\varepsilon(y_n)\theta_1 - b^\varepsilon(y_s)\theta_2 & b^\varepsilon(y_n)\theta_2 \end{bmatrix} \delta_x, \quad (6.58)$$

$$D^{[x]} = - \begin{bmatrix} -a^\varepsilon(x_w)\mu_3 & a^\varepsilon(x_e)\mu_3 - a^\varepsilon(x_w)\mu_4 & a^\varepsilon(x_e)\mu_4 \end{bmatrix} \delta_y, \quad (6.59)$$

$$D^{[y]} = - \begin{bmatrix} -b^\varepsilon(y_s)\theta_3 & b^\varepsilon(y_n)\theta_3 - b^\varepsilon(y_s)\theta_4 & b^\varepsilon(y_n)\theta_4 \end{bmatrix} \delta_x. \quad (6.60)$$

It can be seen from (6.56), there are three unknowns, namely  $u_P$ ,  $\partial u_P/\partial x$  and  $\partial u_P/\partial y$ , at a grid node  $P$ . To solve (6.56), two additional equations are needed and devised here by enforcing  $C^2$ -continuity condition at  $P$  in  $x$ - and  $y$ -directions, i.e.

$$\left( \frac{\partial^2 u_P}{\partial x^2} \right)_L = \left( \frac{\partial^2 u_P}{\partial x^2} \right)_R, \quad (6.61)$$

$$\left( \frac{\partial^2 u_P}{\partial y^2} \right)_B = \left( \frac{\partial^2 u_P}{\partial y^2} \right)_T, \quad (6.62)$$

where  $(\cdot)_L$  indicates that the computation of  $(\cdot)$  is based on the element to the left of  $P$ , i.e. element  $WP$ , and similarly subscripts  $R, B, T$  denote the right ( $PE$ ), bottom ( $SP$ ) and top ( $PN$ ) elements. Making use of (3.13) with noting (6.16) and (6.17) for (6.61) and (6.19) and (6.20) for (6.62), one has

$$\zeta_1 u_W + \zeta_2 u_P + \zeta_3 \frac{\partial u_W}{\partial x} + \zeta_4 \frac{\partial u_P}{\partial x} = \nu_1 u_P + \nu_2 u_E + \nu_3 \frac{\partial u_P}{\partial x} + \nu_4 \frac{\partial u_E}{\partial x}, \quad (6.63)$$

$$\xi_1 u_S + \xi_2 u_P + \xi_3 \frac{\partial u_S}{\partial y} + \xi_4 \frac{\partial u_P}{\partial y} = \vartheta_1 u_P + \vartheta_2 u_N + \vartheta_3 \frac{\partial u_P}{\partial y} + \vartheta_4 \frac{\partial u_N}{\partial y}. \quad (6.64)$$

In compact forms, (6.63) and (6.64) can be rewritten as

$$C^{[x]} \begin{bmatrix} u_W & u_P & u_E & \frac{\partial u_W}{\partial x} & \frac{\partial u_P}{\partial x} & \frac{\partial u_E}{\partial x} \end{bmatrix}^T = 0, \quad (6.65)$$

$$C^{[y]} \begin{bmatrix} u_S & u_P & u_N & \frac{\partial u_S}{\partial y} & \frac{\partial u_P}{\partial y} & \frac{\partial u_N}{\partial y} \end{bmatrix}^T = 0, \quad (6.66)$$

with

$$C^{[x]} = [ \zeta_1 \quad \zeta_2 - \nu_1 \quad -\nu_2 \quad \zeta_3 \quad \zeta_4 - \nu_3 \quad -\nu_4 ], \quad (6.67)$$

$$C^{[y]} = [ \xi_1 \quad \xi_2 - \vartheta_1 \quad -\vartheta_2 \quad \xi_3 \quad \xi_4 - \vartheta_3 \quad -\vartheta_4 ]. \quad (6.68)$$

Collection of equations (6.56), (6.63) and (6.64) at all interior nodal points of the global fine grid leads to a global fine scale system,

$$\begin{bmatrix} \mathbf{G}^{[x]} + \mathbf{G}^{[y]} & \mathbf{D}^{[x]} & \mathbf{D}^{[y]} \end{bmatrix} \begin{bmatrix} \mathbf{u} \\ \mathbf{u}_x \\ \mathbf{u}_y \end{bmatrix} = \mathbf{R}, \quad (6.69)$$

$$\mathbf{C}^{[x]} \begin{bmatrix} \mathbf{u} \\ \mathbf{u}_x \end{bmatrix} = \mathbf{0}, \quad (6.70)$$

$$\mathbf{C}^{[y]} \begin{bmatrix} \mathbf{u} \\ \mathbf{u}_y \end{bmatrix} = \mathbf{0}, \quad (6.71)$$

where  $\mathbf{G}^{[\bullet]}$ ,  $\mathbf{D}^{[\bullet]}$  and  $\mathbf{C}^{[\bullet]}$  result from the assembly of  $G^{[\bullet]}$ ,  $D^{[\bullet]}$  and  $C^{[\bullet]}$  respectively;  $\mathbf{u}$ ,  $\mathbf{u}_x$  and  $\mathbf{u}_y$  are global vectors of values of  $u$  at all nodal points and its  $x$ - and  $y$ -partial derivatives at interior grid nodes; and  $\mathbf{R}$  collects the right hand side of (6.56), which results from the application of (6.56) at fine scale interior grid nodes.

Instead of directly solving the large fine scale system (6.69)-(6.71) for the fine scale reference solution  $u_f$ , we propose a line-relaxation (LR) scheme to smooth a temporarily guessed approximate fine grid solution. Assuming that  $\mathbf{u}^{(t)}$  and  $\mathbf{u}_y^{(t)}$  are a temporarily guessed solution, an iterative strategy in two stages for

smoothing is proposed as

$$\begin{bmatrix} \mathbf{G}^{[x]} + \text{diag}(\mathbf{G}^{[y]}) & \mathbf{D}^{[x]} \\ & \mathbf{C}^{[x]} \end{bmatrix} \begin{bmatrix} \mathbf{u} \\ \mathbf{u}_x \end{bmatrix}^{\gamma+1/2} = \begin{bmatrix} \mathbf{R} - \begin{bmatrix} \mathbf{G}^{[y]} - \text{diag}(\mathbf{G}^{[y]}) & \mathbf{D}^{[y]} \end{bmatrix} \begin{bmatrix} \mathbf{u} \\ \mathbf{u}_y \end{bmatrix}^{\gamma} \\ \mathbf{0} \end{bmatrix}, \quad (6.72)$$

$$\begin{bmatrix} \mathbf{G}^{[y]} + \text{diag}(\mathbf{G}^{[x]}) & \mathbf{D}^{[y]} \\ & \mathbf{C}^{[y]} \end{bmatrix} \begin{bmatrix} \mathbf{u} \\ \mathbf{u}_y \end{bmatrix}^{\gamma+1} = \begin{bmatrix} \mathbf{R} - \begin{bmatrix} \mathbf{G}^{[x]} - \text{diag}(\mathbf{G}^{[x]}) & \mathbf{D}^{[x]} \end{bmatrix} \begin{bmatrix} \mathbf{u} \\ \mathbf{u}_x \end{bmatrix}^{\gamma+1/2} \\ \mathbf{0} \end{bmatrix}, \quad (6.73)$$

where  $[\mathbf{u} \ \mathbf{u}_x \ \mathbf{u}_y]^\gamma$  is the approximate solution after the  $\gamma$  smoothing step and  $[\mathbf{u} \ \mathbf{u}_y]^0 = [\mathbf{u}^{(t)} \ \mathbf{u}_y^{(t)}]$ ,  $\text{diag}(\mathbf{G}^{[x]})$  is the diagonal of  $\mathbf{G}^{[x]}$ . Owing to the fact that 2-node IRBFE flux approximation is used, the linear systems in (6.72) and (6.73) are very sparse. Moreover, these systems can be further split into independent linear systems for each grid line, which is an important property for the implementation of massively parallel computation. Note that the present  $C^2$ -continuous IRBFE-LR solver is convergent, but for large problem the rate is extremely slow. In our framework, however, only a few LR-steps are required to smooth the temporarily guessed approximate solution. The smoothed fine grid solution then serve to estimate temporary boundary conditions for correction functions via (6.45) and (6.46) instead of the fine scale reference solution  $u_f$ . To ensure that these temporary boundary conditions approach the conditions (6.45) and (6.46) an iterative algorithm is used. Such an algorithm is presented next.

### Iterative algorithm

We present here an iterative algorithm to improve the localised boundary conditions of the correction functions. Such boundary conditions do not depend on  $u_f$ . Instead of requirements (6.45) and (6.46), we employ an iterative improvement

$$\frac{\partial}{\partial x} \left( a^\varepsilon(x) \frac{\partial u_c^{l(t)}}{\partial x} \right) = \frac{\partial}{\partial x} \left( a^\varepsilon(x) \frac{\partial u_s^{(t)}}{\partial x} \right) \quad \text{on } \partial\tilde{\Omega}_x^l, \quad (6.74)$$

$$\frac{\partial}{\partial y} \left( b^\varepsilon(y) \frac{\partial u_c^{l(t)}}{\partial y} \right) = \frac{\partial}{\partial y} \left( b^\varepsilon(y) \frac{\partial u_s^{(t)}}{\partial y} \right) \quad \text{on } \partial\tilde{\Omega}_y^l \quad \forall l \in [1, J]. \quad (6.75)$$

The superscript  $(t)$  denotes an iterative step and

$$\left[ \begin{array}{c} u_s^{(t)} \\ \frac{\partial u_s^{(t)}}{\partial x} \\ \frac{\partial u_s^{(t)}}{\partial y} \end{array} \right] = \mathbf{S}^{n_s} \left( \left[ \begin{array}{c} u^{(t)} \\ \frac{\partial u^{(t)}}{\partial x} \\ \frac{\partial u^{(t)}}{\partial y} \end{array} \right] \right) \quad (6.76)$$

is a smoothed fine scale approximate solution, where  $\mathbf{S}$  is the proposed  $C^2$ -continuous IRBFE-LR smoothing operator, i.e. (6.72) and (6.73),  $n_s$  the number of smoothing steps, and

$$\left[ \begin{array}{c} u^{(t)} \\ \frac{\partial u^{(t)}}{\partial x} \\ \frac{\partial u^{(t)}}{\partial y} \end{array} \right]$$

is the temporary solution which is constructed on each dual coarse cell  $\tilde{\Omega}^l$  as

$$u^{l(t)} = \sum_{i=1}^4 \phi_i^l u_i^{(t)} + u_c^{l(t-1)}, \quad (6.77)$$

$$\frac{\partial u^{l(t)}}{\partial x} = \sum_{i=1}^4 \frac{\partial \phi_i^l}{\partial x} u_i^{(t)} + \frac{\partial u_c^{l(t-1)}}{\partial x}, \quad (6.78)$$

$$\frac{\partial u^{l(t)}}{\partial y} = \sum_{i=1}^4 \frac{\partial \phi_i^l}{\partial y} u_i^{(t)} + \frac{\partial u_c^{l(t-1)}}{\partial y} \quad \forall l \in [1, J]. \quad (6.79)$$

Note that the correction functions  $u_c^{l(t-1)}$  are obtained based on local boundary conditions (6.74) and (6.75) with  $u_s^{(t)}$  replaced by  $u_s^{(t-1)}$ . A pseudocode of the iterative algorithm is given below.

- 
- (1) Initialise  $\left[ \mathbf{u}^{(t=0)} \quad \mathbf{u}_x^{(t=0)} \quad \mathbf{u}_y^{(t=0)} \right]$
- (2)  $\forall l, \forall i$ : compute basis functions  $\phi_i^l$ , equations (6.41) with boundary conditions (6.43), (6.44) by a  $C^2$ -continuous IRBFE-CV method (An-Vo et al. 2011a)
- (3) for  $t = 1$  to number of iterations {
- (3i)  $\left[ \mathbf{u}_s^{(t-1)} \quad \mathbf{u}_{x_s}^{(t-1)} \quad \mathbf{u}_{y_s}^{(t-1)} \right] = \left[ \mathbf{u}^{(t-1)} \quad \mathbf{u}_x^{(t-1)} \quad \mathbf{u}_y^{(t-1)} \right]$
- (3ii) for  $i = 1$  to  $n_s$  {
- $\left[ \mathbf{u}_s^{(t-1)} \quad \mathbf{u}_{x_s}^{(t-1)} \quad \mathbf{u}_{y_s}^{(t-1)} \right] = \mathbf{S} \left( \left[ \mathbf{u}_s^{(t-1)} \quad \mathbf{u}_{x_s}^{(t-1)} \quad \mathbf{u}_{y_s}^{(t-1)} \right] \right)$ ; smoothing step
- }
- (3iii)  $\forall l$ : compute correction functions  $u_c^{l(t-1)}$ ; based on  $\mathbf{u}_s^{(t-1)}$ , equations (6.42) with boundary conditions (6.74) and (6.75) by a  $C^2$ -continuous IRBFE-CV method (An-Vo et al. 2011a)
- (3iv) Calculate right hand side of the coarse grid discretised system
- (3v) Solve coarse system
- (3vi) Reconstruct  $\left[ \mathbf{u}^{(t)} \quad \mathbf{u}_x^{(t)} \quad \mathbf{u}_y^{(t)} \right]$ , equations (6.77)-(6.79)
- (3vii) Calculate convergence measures ( $CM$ s) through
- $$CM(\mathbf{u}) = \frac{\| \mathbf{u}^{(t)} - \mathbf{u}_f \|_2}{\| \mathbf{u}_f \|_2}$$
- $$CM(\mathbf{u}_x) = \frac{\| \mathbf{u}_x^{(t)} - \mathbf{u}_{x_f} \|_2}{\| \mathbf{u}_{x_f} \|_2}$$
- $$CM(\mathbf{u}_y) = \frac{\| \mathbf{u}_y^{(t)} - \mathbf{u}_{y_f} \|_2}{\| \mathbf{u}_{y_f} \|_2}$$
- }
- 

First, the fine scale field is initialised to zero. Then, all basis functions are computed and the right-hand side of equation (6.36) is integrated over each coarse volume. These steps have to be performed only once and are followed by the main iteration loop. At the beginning of each iteration,  $n_s$  smoothing

steps are applied and the smoothed fine scale field is employed to compute the correction functions. The right hand side of the coarse linear system for coarse nodal values also includes induced terms from these correction functions. At the end of each iteration, the coarse system is solved and a new fine scale field is reconstructed.

### Deferred correction of coarse grid fluxes

In the coarse grid flux expressions, namely (6.47)-(6.50), there are required first-derivative values of basis functions and correction functions at the control volume faces. The former needs to be computed only once at the preprocessing stage and be fixed throughout the iteration loop. The latter, however, need to be updated at each iteration via the numerical differentiation of correction functions. This differentiation is usually resulted in a considerable numerical error. Here we propose a deferred correction strategy to obtain the coarse grid fluxes accurately without the need of the numerical differentiation of correction functions. Consider an east control volume face at an iteration level  $t$ , instead of using (6.47) we compute the flux value as

$$\begin{aligned} \left(\frac{\partial u}{\partial x}\right)_e^{(t)} &= \frac{\partial \phi_1^2}{\partial x}(x_e) u_1^{(t)} + \frac{\partial \phi_5^2}{\partial x}(x_e) u_5^{(t)} + \Delta f_e^{(t-1)} \\ &= \frac{\partial \phi_1^3}{\partial x}(x_e) u_1^{(t)} + \frac{\partial \phi_5^3}{\partial x}(x_e) u_5^{(t)} + \Delta f_e^{(t-1)}, \end{aligned} \quad (6.80)$$

where  $\Delta f_e^{(t-1)}$  is the correction term at  $e$  which is a known value derived from the smoothed fine scale field, i.e.

$$\begin{aligned} \Delta f_e^{(t-1)} &= \left(\frac{\partial u}{\partial x}\right)_e^{(t-1)} - \left(\frac{\partial \phi_1^2}{\partial x}(x_e) u_1^{(t-1)} + \frac{\partial \phi_5^2}{\partial x}(x_e) u_5^{(t-1)}\right) \\ &= \left(\frac{\partial u}{\partial x}\right)_e^{(t-1)} - \left(\frac{\partial \phi_1^3}{\partial x}(x_e) u_1^{(t-1)} + \frac{\partial \phi_5^3}{\partial x}(x_e) u_5^{(t-1)}\right). \end{aligned} \quad (6.81)$$

Since the proposed  $C^2$ -continuous fine scale solver is used the smoothed fine scale field includes not only the field variable but also its first partial deriva-

tives. As a result, the value  $(\partial u / \partial x)_e^{(t-1)}$  is explicitly given without the need of numerical differentiation. The flux values at other control volume faces can be computed in a similar manner. It can be seen that via this correction strategy the coarse grid fluxes are matched with the fine scale smoothed field.

## 6.6 Numerical results

The proposed method is verified by solving several problems in one and two dimension. We refer to the size of a coarse grid as  $N$  in 1D problems and  $N \times N$  in 2D problems and the size of a fine grid on a coarse cell as  $n$  and  $n \times n$  in 1D and 2D respectively. The fine grid on a coarse cell also referred to as the local fine grid. The fine grid on the whole problem domain is called the global fine grid. In 2D problems, the smoothing system is constructed on the global fine grid. The coarse grid spacing is denoted as  $H$  which is also the size of a coarse cell in this study. The local fine grids on the coarse cells are mapped to  $[0, 1]$  in 1D problems and  $[0, 1]^2$  in 2D problems and the grid spacing is denoted as  $h$ .

In each problem, two grid refinement strategies are employed. The first strategy, Strategy 1, keeps the coarse grid fixed while refining the local fine grids. In contrast, the second strategy, Strategy 2, keeps the local fine grids fixed while refining the coarse grid. The numerical results are compared with those obtained by the MFEM (Hou et al. 1999).

The factor of the MQ-width is chosen as  $\beta = 15$  throughout the computation. We assess the numerical performance of the proposed method through two measures: (i) the relative discrete  $L_2$  error defined as

$$Ne(\alpha) = \frac{\sqrt{\sum_{i=1}^M (\alpha_i - \alpha_i^{(e)})^2}}{\sqrt{\sum_{i=1}^M (\alpha_i^{(e)})^2}} \quad (6.82)$$

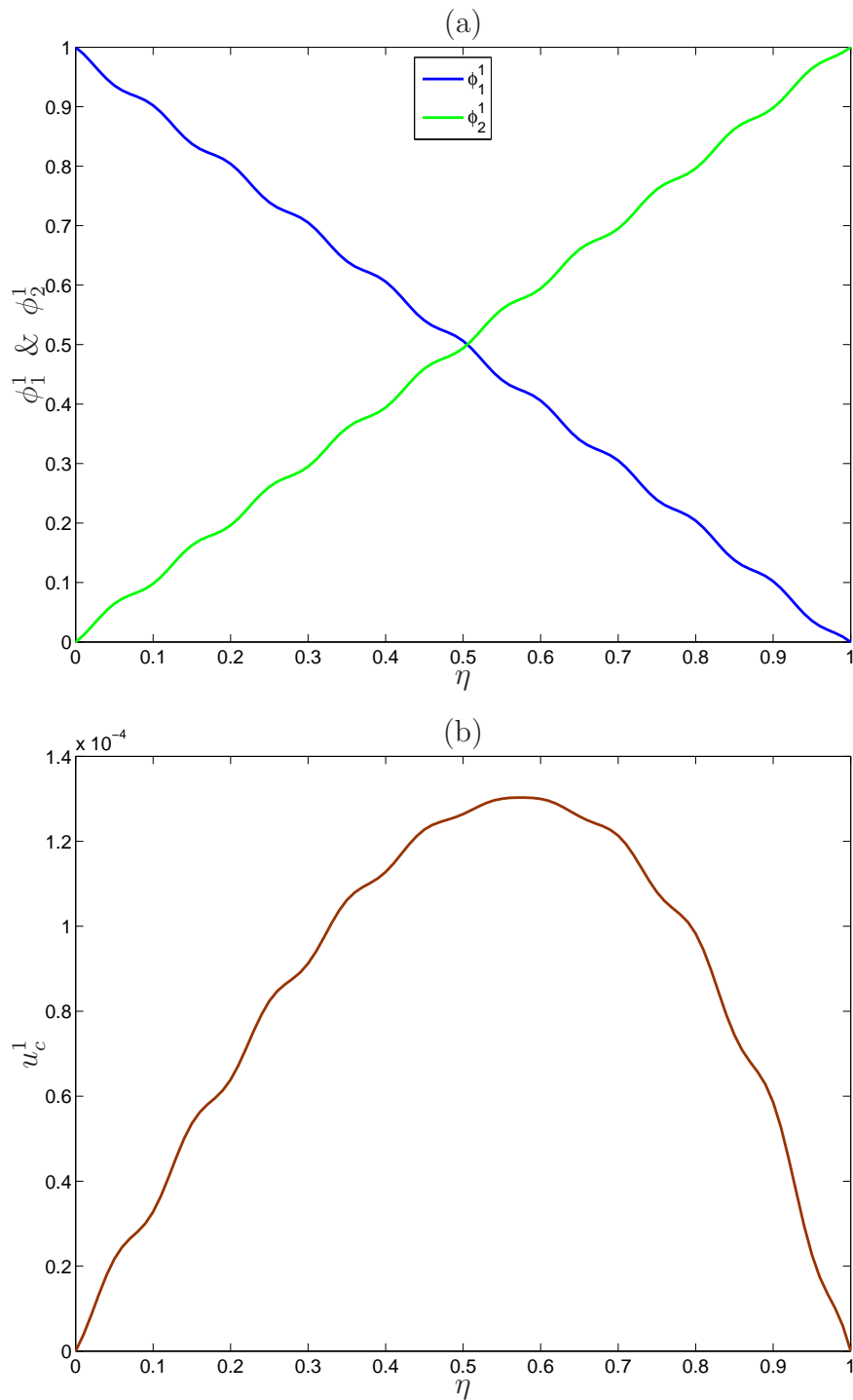


Figure 6.5: One-dimensional example 1,  $\varepsilon = 0.01$ ,  $N = 11$ ,  $n = 101$ : basis functions (a) and correction function (b) associated with the first coarse cell ( $l = 1$ ). It is noted that the coarse cell is mapped to a unit length.

where  $M$  is the number of test points,  $\alpha$  denotes the field variable  $u$  and its derivatives and (ii) the convergence rates  $\gamma$  with respect to the two grid refinement strategies defined via the error norm behaviours  $O(h^\gamma)$  and  $O(H^\gamma)$  for the Strategy 1 and 2 respectively. The convergence rates are calculated over 2 successive grids (point-wise rate) and also over the whole set of grids used (average rate).

### 6.6.1 One-dimensional examples

#### Example 1

Consider a model 1D problem (6.21) with

$$a^\epsilon(x) = \frac{1}{2 + x + \sin(2\pi x/\epsilon)}, \quad f = x, \quad \Omega = [0, 1], \quad (6.83)$$

and homogeneous Dirichlet boundary conditions  $u(0) = u(1) = 0$ .

The problem domain is discretised using a series of uniform coarse elements and the shape functions and correction functions that capture the fine scale physics in the coarse elements are numerically obtained by our  $C^2$ -continuous IRBFE-Control Volume (IRBFE-CV) method. Figure 6.5 shows the basis functions and correction function associated with a typical coarse element. Unlike conventional basis functions, the present basis functions are highly oscillatory since they adapt to the small scale information within each element (Figure 6.5(a)). The correction function is also highly oscillatory and its scale is small as shown in Figure 6.5(b). Figure 6.6 displays the convergence behaviour of a numerical shape function on a typical coarse element obtained by our IRBFE-CVM and the linear FEM. IRBFE-CVM and linear FEM give convergence rates of 4.0267 and 2.0253 respectively. It can be seen that the use of high order approximants in the form of IRBFES thus helps capture the fine scale physics and hence produce highly accurate solutions.

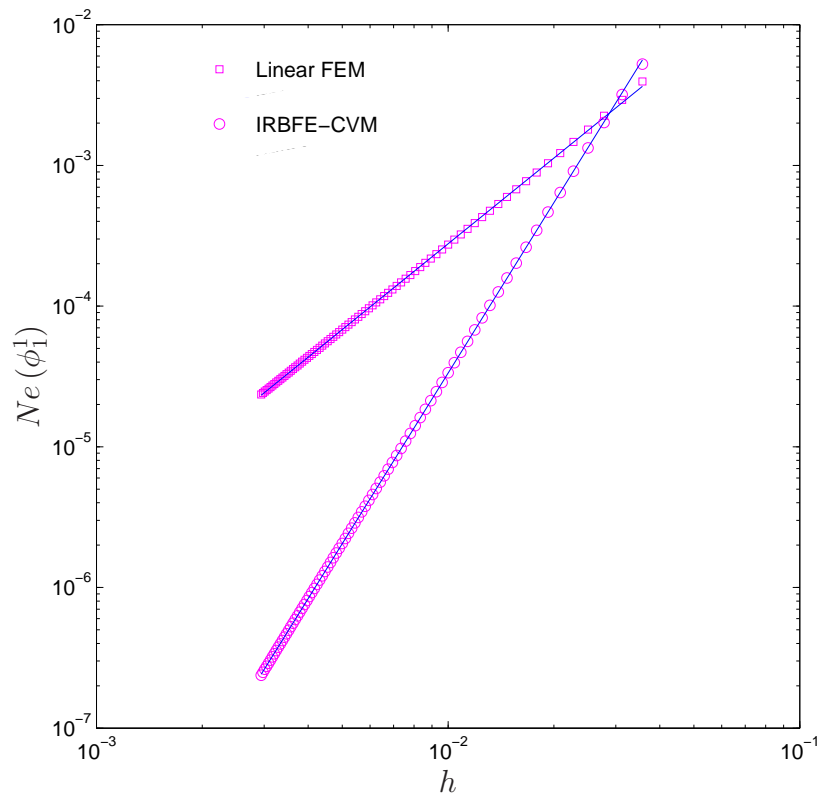


Figure 6.6: One-dimensional example 1: mesh convergence of a basis function.

The coarse scale solution at the coarse grid points is obtained by a conservative CV method where the fluxes are estimated by the obtained shape and correction functions. In order to have a good consistent measure of accuracy, error norms in all cases are computed using the same 10,001 test points where the fine scale solution is recovered via (6.22). Table 6.1 presents convergence behaviour associated with Strategy 1 where a fixed coarse scale grid of 10 elements and a series of 21, 41,  $\dots$ , 181 local fine grids are used. The present method converges monotonically while MFEM does not converge. It was pointed out in (Hou and Wu 1997, Hou et al. 1999) that the accuracy of the shape functions does not have much effect on the overall accuracy of MFEM. The present approach achieves convergence rates of 3.91, 3.16, and 2.09 for the field variable, its first, and second derivatives respectively. In comparison to multiscale discontinuous

Galerkin method proposed by Wang et al. (2011), in terms of  $L_2$  error, the present method yields two orders of magnitude improvement for the field variable and one order of magnitude improvement for the first derivative by using a local fine grid of  $n = 181$ . Note that exact shape functions have been used in Wang et al. (2011). Table 6.2 presents convergence behaviour associated with Strategy 2 where a fixed local fine grid of 27 nodes and a series of 10, 20,  $\dots$ , 100 uniform coarse elements (i.e. 11, 21,  $\dots$ , 101 nodes) are used. Both the present method and the MFEM converge well with refinement of the coarse grids. The present approach achieves convergence rates of 3.03, 2.51, and 1.47 for the field variable, its first, and second derivatives respectively while the MFEM achieves a value of 1.61 for the field variable. These results show superior performance of the present approach indicated by (i) high rates of convergence not only for the field variable but also for the first and second derivatives; (ii) working for both grid refinement strategies. One can thus either keep fine scale or coarse scale grid fixed and obtain convergence by refining the other scale grid.

Figure 6.7 displays the recovered fine scale results for the field variable  $u(x)$  and its first derivative by the present method, MFEM and exact solution. It can be seen that the present method has captured the exact solution much better than MFEM. In addition, the present method can produce approximation of derivatives up to second order as shown in Figure 6.8.

### Example 2

In this example, we consider a model 1D problem with highly oscillatory solution at both macro- and micro-scales. The multiscale problem (6.21) is specifically defined with

$$a^\epsilon(x) = \frac{1}{2 + x + \sin(10\pi x/\epsilon)}, \quad f = 300 \sin(10\pi x), \quad \Omega = [0, 1], \quad (6.84)$$

and homogeneous Dirichlet boundary conditions  $u(0) = u(1) = 0$ .

Table 6.1: One-dimensional example 1,  $\varepsilon = 0.01$ , Strategy 1:  $L_2$  errors of the field variable, its first and second derivatives. It is noted that the set of test nodes contains 10,001 uniformly distributed points. LCR stands for local convergence rate.

$\varepsilon = 0.01, N = 11$								
Local fine grid ( $n$ )	MFEM		Present method					
	$Ne(u)$	LCR	$Ne(u)$	LCR	$Ne(du/dx)$	LCR	$Ne(d^2u/dx^2)$	LCR
21	1.30E-02	-	4.10E-03	-	1.16E-01	-	5.37E-01	-
41	1.22E-02	0.09	3.60E-04	3.51	2.44E-02	2.25	2.19E-01	1.29
61	1.21E-02	0.02	6.76E-05	4.12	5.80E-03	3.54	8.21E-02	2.42
81	1.21E-02	0.00	2.11E-05	4.05	2.13E-03	3.48	4.14E-02	2.38
101	1.21E-02	0.00	8.63E-06	4.01	9.90E-04	3.43	2.50E-02	2.26
121	1.21E-02	0.00	4.18E-06	3.98	5.34E-04	3.39	1.62E-02	2.38
141	1.21E-02	0.00	2.28E-06	3.93	3.18E-04	3.36	1.16E-02	2.17
161	1.21E-02	0.00	1.35E-06	3.92	2.04E-04	3.32	8.47E-03	2.36
181	1.21E-02	0.00	8.53E-07	3.90	1.39E-04	3.26	6.56E-03	2.17
	$O(h^{0.03})$		$O(h^{3.91})$		$O(h^{3.16})$		$O(h^{2.09})$	
Wang et al. (2011) ( $S^1$ )			1.03E-03		4.73E-02			
Wang et al. (2011) ( $S^2$ )			1.16E-05		1.01E-03			

Table 6.2: One-dimensional example 1,  $\varepsilon = 0.01$ , Strategy 2:  $L_2$  errors of the field variable, its first and second derivatives. It is noted that the set of test nodes contains 10,001 uniformly distributed points. LCR stands for local convergence rate

$\varepsilon = 0.01, n = 27$								
Coarse grid ( $N$ )	MFEM		Present method					
	$Ne(u)$	LCR	$Ne(u)$	LCR	$Ne(du/dx)$	LCR	$Ne(d^2u/dx^2)$	LCR
11	1.25E-2	-	2.06E-3	-	1.09E-1	-	5.90E-1	-
21	2.63E-3	2.25	8.91E-5	4.53	1.26E-2	3.11	1.49E-1	1.99
31	1.66E-3	1.14	3.52E-4	-3.39	5.97E-3	1.84	1.09E-1	0.77
41	9.63E-4	1.89	1.98E-4	2.00	1.65E-3	4.47	3.64E-2	3.80
51	7.36E-4	1.20	3.93E-6	17.57	7.79E-4	3.37	2.32E-2	2.02
61	3.71E-4	3.76	2.40E-5	-9.92	1.43E-3	-3.33	5.26E-2	-4.49
71	2.74E-4	1.98	1.43E-5	3.36	9.88E-4	2.40	4.38E-2	1.18
81	2.12E-4	1.93	8.44E-6	3.94	8.42E-4	1.20	3.96E-2	0.76
91	1.83E-4	1.22	6.86E-6	1.76	6.13E-4	2.70	3.44E-2	1.19
101	9.12E-4	-15.24	2.53E-7	31.31	1.01E-4	17.12	5.82E-3	16.86
	$O(H^{1.61})$		$O(H^{3.03})$		$O(H^{2.51})$		$O(H^{1.47})$	

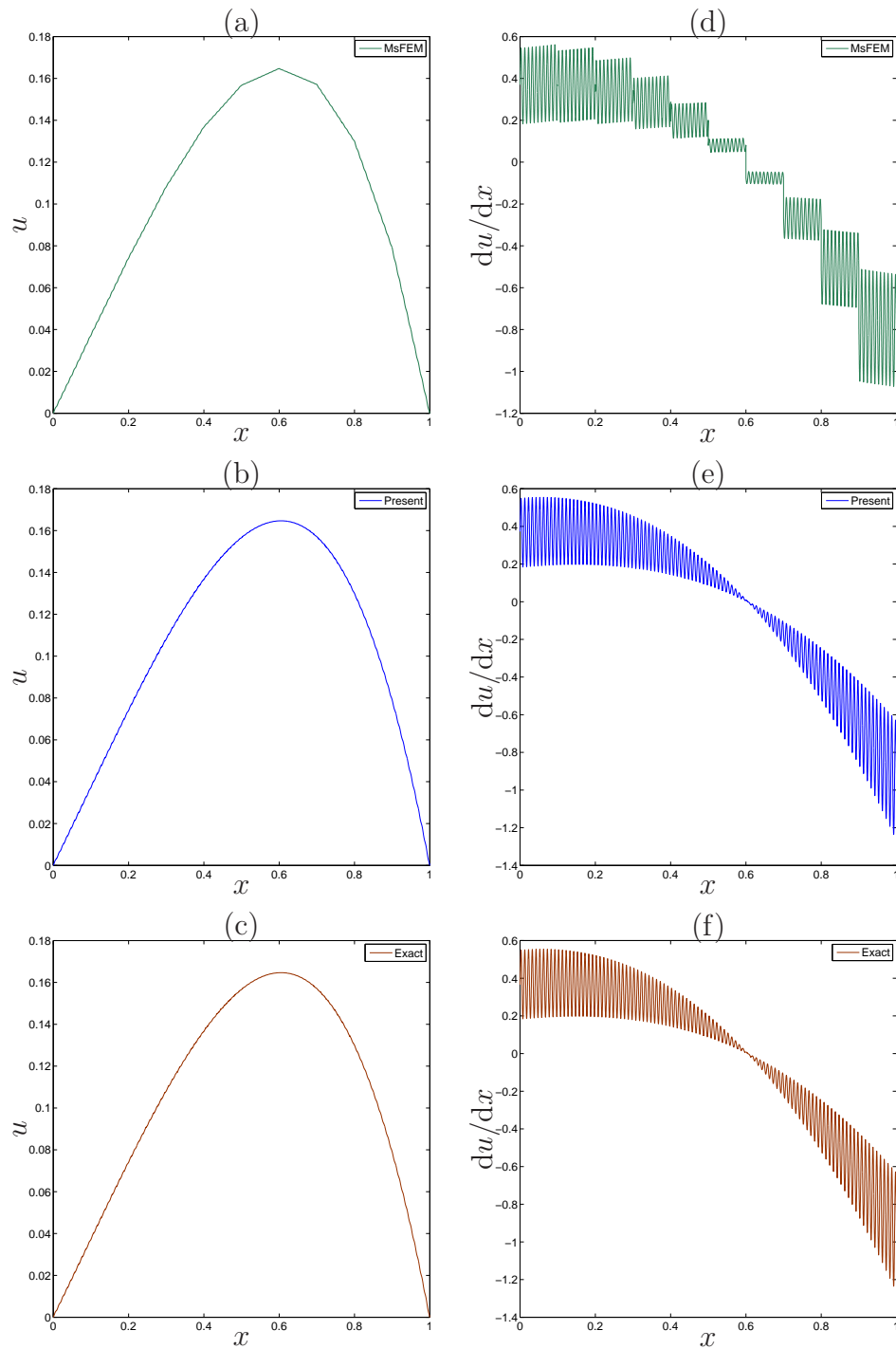


Figure 6.7: One-dimensional example 1,  $\varepsilon = 0.01$ ,  $N = 11$ ,  $n = 101$ : field variable and its first derivatives obtained by the present method in comparison with those obtained by MFEM and the exact solution.

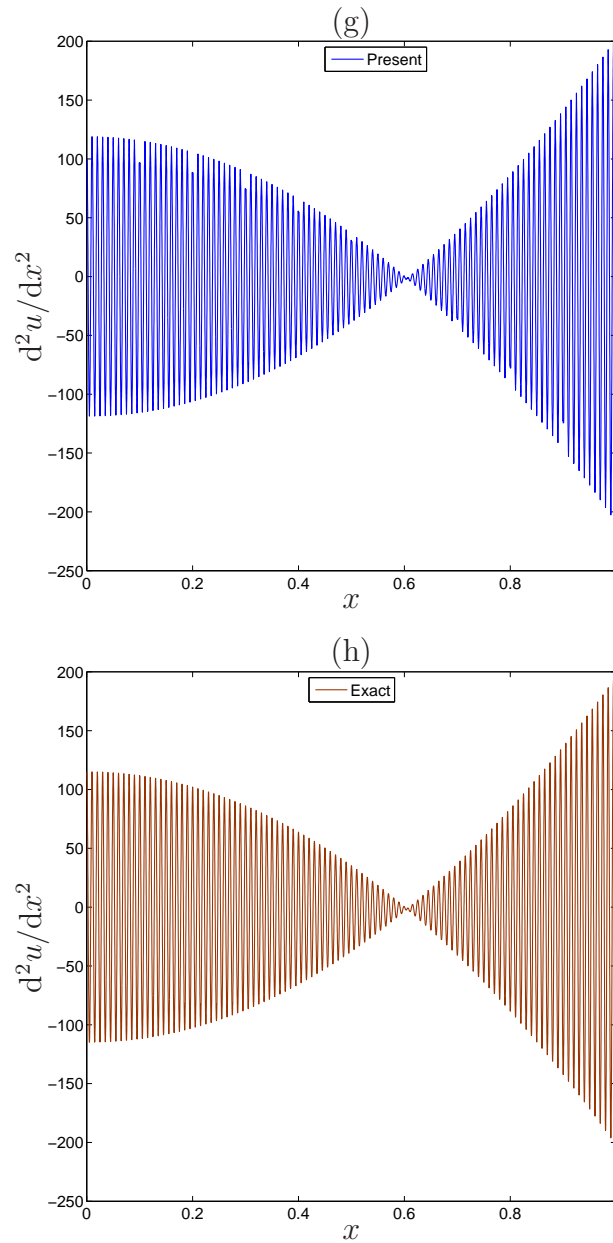


Figure 6.8: One-dimensional example 1,  $\varepsilon = 0.01$ ,  $N = 11$ ,  $n = 101$ : second derivatives obtained by the present method in comparison with that obtained by the exact solution.

Similar to example 1, two strategies of grid refinement are implemented here. Table 6.3 presents the convergence behaviour associated with Strategy 1 where a fixed coarse scale grid of 50 elements and a series of 21, 41,  $\dots$ , 281 local fine grids are used. Present method converges monotonically as in the case of example 1. The convergence rates are 3.91, 3.24, and 2.13 for the field variable, its first, and second derivatives respectively. Table 6.4 presents convergence behaviour associated with Strategy 2 where fixed local fine grids of 101 nodes and a series of 10, 20,  $\dots$ , 100 uniform coarse elements (i.e. 11, 21,  $\dots$ , 101 nodes) are used. The present method converges well with refinement of the coarse grids. The convergence rates are 3.71, 2.55, and 1.49 for the field variable, its first, and second derivatives respectively.

Figure 6.9 displays the recovered fine scale solution for the field variable  $u(x)$ , its first, and second derivatives by the present method and the exact solution. The solutions by the present method are in excellent agreement with the exact solution.

## 6.6.2 Two-dimensional examples

We demonstrate that the proposed iterative algorithm for 2D problems converges to the fine scale reference solution. In the following discussion, by “smoother” we mean one iteration of the fine scale solver. By “the present method” we mean a two-grid method where the smoother is invoked for only a few cycles within the iterative algorithm. Computational efficiency of the present method is assessed via a convergence acceleration in comparison with the fine scale solver. The acceleration is estimated by comparing the computational time to achieve a certain convergence measure ( $CM$ ).

Table 6.3: One-dimensional example 2,  $\varepsilon = 0.01$ , Strategy 1:  $L_2$  errors of the field variable, its first and second derivatives by the present method. It is noted that the set of test nodes contains 100,001 uniformly distributed points. LCR stands for local convergence rate.

Local fine grid ( $n$ )	$\varepsilon = 0.01, N = 51$					
	$Ne(u)$	LCR	$Ne(du/dx)$	LCR	$Ne(d^2u/dx^2)$	LCR
21	2.59E-2	-	1.18E-1	-	5.33E-1	-
41	2.19E-3	3.56	2.45E-2	2.27	2.16E-1	1.30
61	4.02E-4	4.18	5.77E-3	3.57	8.07E-2	2.43
81	1.25E-4	4.06	2.10E-3	3.51	4.07E-2	2.38
101	5.11E-5	4.01	9.69E-4	3.47	2.42E-2	2.33
121	2.49E-5	3.94	5.19E-4	3.42	1.59E-2	2.30
141	1.36E-5	3.92	3.07E-4	3.41	1.12E-2	2.27
161	8.09E-6	3.89	1.96E-4	3.36	8.32E-3	2.23
181	5.14E-6	3.85	1.32E-4	3.36	6.44E-3	2.17
201	3.43E-6	3.84	9.30E-5	3.32	5.23E-3	1.98
241	1.72E-6	3.79	5.11E-5	3.28	3.46E-3	2.27
281	9.62E-7	3.77	3.11E-5	3.22	2.50E-3	2.11
	$O(h^{3.91})$		$O(h^{3.24})$		$O(h^{2.13})$	

Table 6.4: One-dimensional example 2,  $\varepsilon = 0.01$ , Strategy 2:  $L_2$  errors of the field variable, its first and second derivatives by the present method. It is noted that the set of test nodes contains 100,001 uniformly distributed points. LCR stands for local convergence rate.

Coarse grid ( $N$ )	$\varepsilon = 0.01, n = 101$					
	$Ne(u)$	LCR	$Ne(du/dx)$	LCR	$Ne(d^2u/dx^2)$	LCR
11	3.66E-2	-	7.81E-2	-	3.53E-1	-
21	1.35E-3	4.76	1.83E-2	2.09	1.66E-1	1.09
31	5.86E-3	-3.62	6.85E-3	2.42	7.72E-2	1.89
41	1.18E-3	5.57	2.58E-3	3.39	3.82E-2	2.45
51	5.11E-5	14.07	9.69E-4	4.39	2.42E-2	2.05
61	1.72E-4	-6.66	1.29E-3	-1.57	3.60E-2	-2.18
71	1.13E-4	2.73	9.39E-4	2.06	3.06E-2	1.05
81	5.82E-5	4.97	7.20E-4	1.99	2.66E-2	1.05
91	2.71E-5	6.49	4.08E-4	4.82	1.74E-2	3.60
101	7.86E-7	33.60	1.20E-4	11.62	6.16E-3	9.86
	$O(H^{3.71})$		$O(H^{2.55})$		$O(H^{1.49})$	

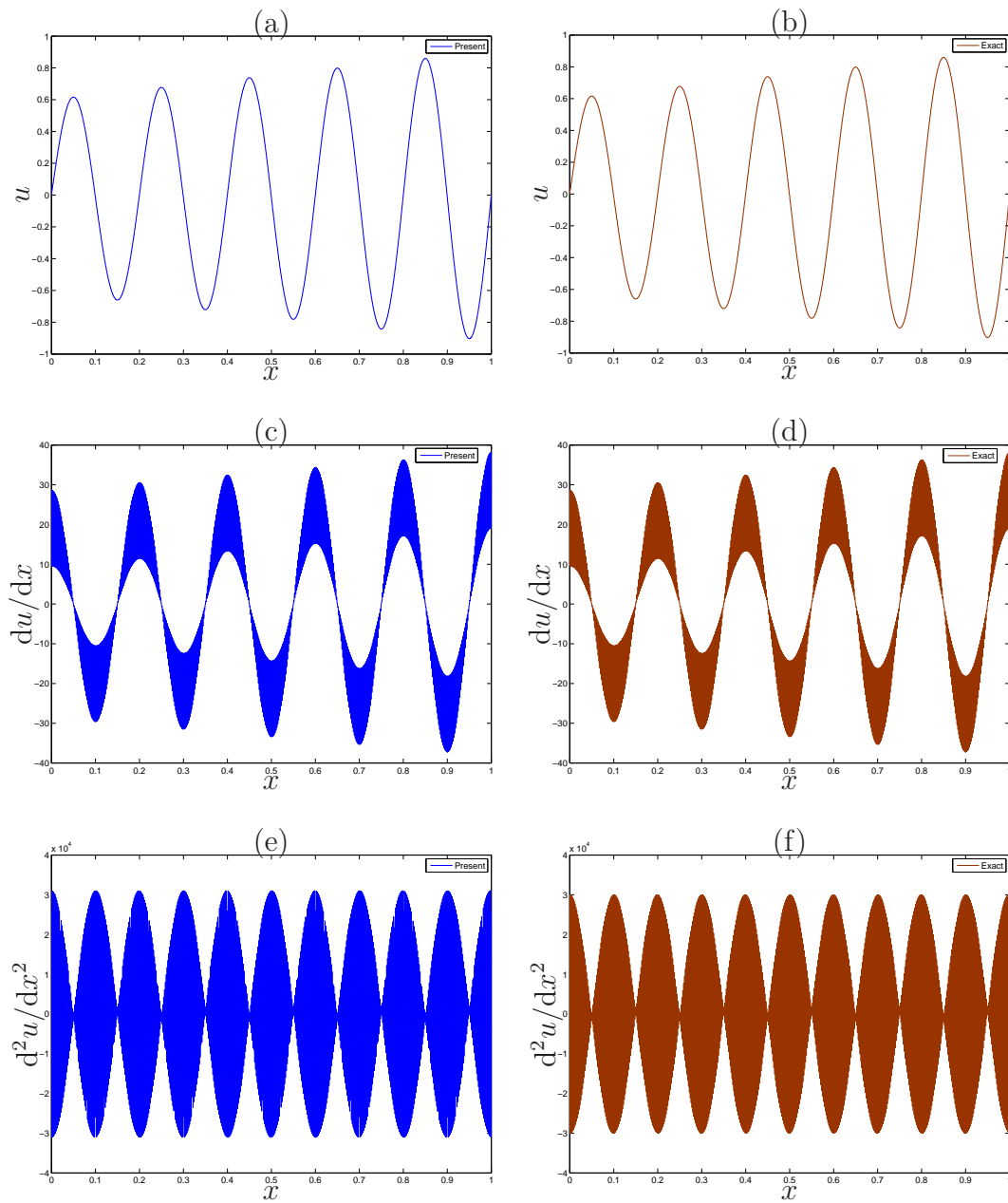


Figure 6.9: One-dimensional example 2,  $\varepsilon = 0.01$ ,  $N = 51$ ,  $n = 101$ : field variable, its first and second derivatives obtained by the present method in comparison with the exact solution.

**Example 1**

We consider a special case of equation (6.36) with  $a^\varepsilon(x) = b^\varepsilon(y) = 1$  as follows.

$$\frac{\partial^2 u}{\partial x^2} + \frac{\partial^2 u}{\partial y^2} = -2\pi^2 \cos(\pi x) \cos(\pi y), \quad (6.85)$$

on a square domain  $0 \leq x, y \leq 1$  with boundary conditions:

$$\begin{aligned} u &= \cos(\pi y) & \text{for } x &= 0, 0 \leq y \leq 1; \\ u &= -\cos(\pi y) & \text{for } x &= 1, 0 \leq y \leq 1; \\ u &= \cos(\pi x) & \text{for } y &= 0, 0 \leq x \leq 1; \\ u &= -\cos(\pi x) & \text{for } y &= 1, 0 \leq x \leq 1. \end{aligned}$$

The exact solution to this problem can be verified to be

$$u^{(e)}(x, y) = \cos(\pi x) \cos(\pi y). \quad (6.86)$$

It can be seen that the basis functions on each coarse cell are simply those of a linear 2D rectangular element in FEM and the MFEM is identical to the conventional FEM. We also utilise these exact basis functions in the present method. The correction functions are numerically obtained via our  $C^2$ -continuous CVM (An-Vo et al. 2011a) with the iteratively improved boundary conditions. Figure 6.10 shows a typical set of converged correction functions on the problem domain.

**Iterative convergence:** Figure 6.11 displays the convergence to the reference solution as a function of iterations and smoothing steps (per iteration),  $n_s$ , for two grid systems. The first grid system includes a coarse grid of  $N \times N = 5 \times 5$  and local fine grids on each coarse cells of  $n \times n = 81 \times 81$ . The other grid system includes a coarse grid of  $N \times N = 33 \times 33$  and local fine grids of  $n \times n = 11 \times 11$ . Note that these two grid systems have the same size in terms of the global fine grid of  $321 \times 321$ . It can be seen that for both grid systems the smoothing steps

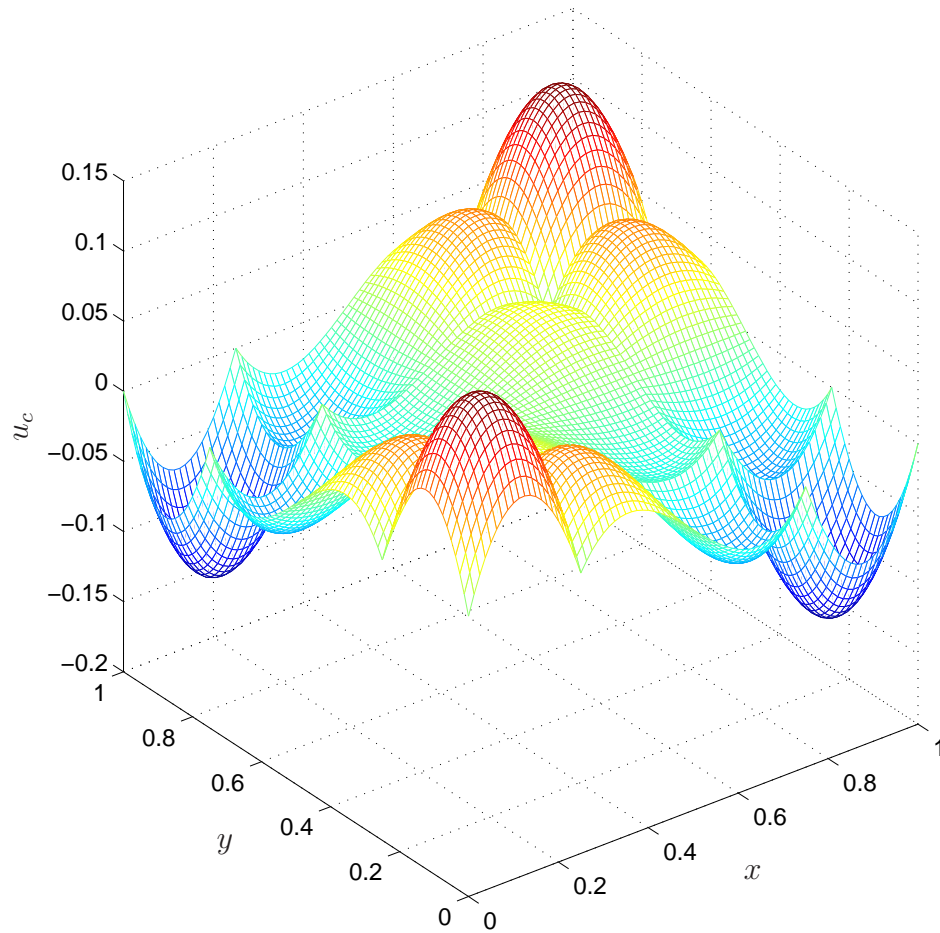


Figure 6.10: Two-dimensional example 1: collection of all correction functions on the problem domain obtained with a grid system of  $N \times N = 5 \times 5$ ,  $n \times n = 21 \times 21$ .

have a significant effect on the convergence behaviours. Increasing  $n_s$  helps reduce the iterations. In addition, the present method converges well even with only one smoothing step. This robustness is very useful for large scale problems where one smoothing step could require a significant computational load. The convergence behaviours of the first derivatives are similar to those of the field variable. Comparing between the two grid systems (with the same smoothing operation), the use of a larger coarse grid helps reduce the iterations remarkably. For instance with  $n_s = 4$ , the first grid system (smaller coarse grid) requires about 200 iterations to converge to the reference solution while the other grid system (larger coarse grid) requires only about 20 iterations.

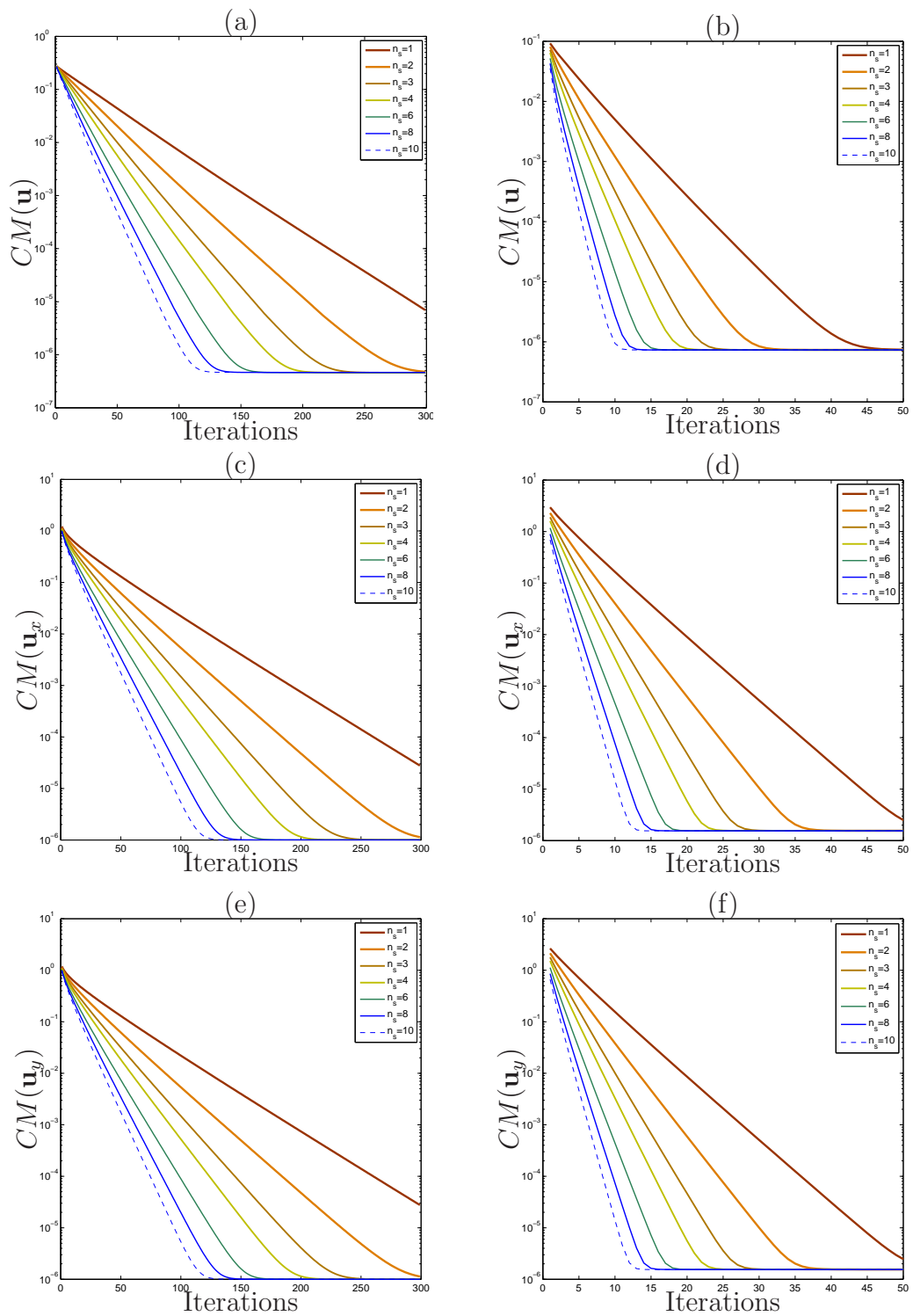


Figure 6.11: Two-dimensional example 1,  $N \times N = 5 \times 5$ ,  $n \times n = 81 \times 81$  (left) and  $N \times N = 33 \times 33$ ,  $n \times n = 11 \times 11$  (right): effect of the number of smoothing steps  $n_s$  on the convergence behaviour.

Table 6.5: Two-dimensional example 1:  $L_2$  errors of the field variable, its first and second derivatives. LCR stands for local convergence rate.

Strategy 1, $N \times N = 5 \times 5$								
Fine scale grid ( $n \times n$ )	MFEM		Present method					
	$Ne(u)$	LCR	$Ne(u)$	LCR	$Ne(\partial u/\partial x)$	LCR	$Ne(\partial u/\partial y)$	LCR
$11 \times 11$	5.54E-2	-	1.73E-5	-	5.48E-5	-	5.49E-5	-
$21 \times 21$	5.54E-2	0.00	4.76E-6	1.86	1.47E-5	1.90	1.46E-5	1.91
$31 \times 31$	5.54E-2	0.00	2.21E-6	1.89	6.68E-6	1.94	6.68E-6	1.94
$41 \times 41$	5.54E-2	0.00	1.28E-6	1.91	3.81E-6	1.95	3.81E-6	1.95
$51 \times 51$	5.54E-2	0.00	8.30E-7	1.93	2.46E-6	1.96	2.46E-6	1.96
$61 \times 61$	5.54E-2	0.00	5.83E-7	1.94	1.72E-6	1.97	1.72E-6	1.97
$71 \times 71$	5.54E-2	0.00	4.32E-7	1.94	1.27E-6	1.97	1.27E-6	1.97
$81 \times 81$	5.54E-2	0.00	3.33E-7	1.95	9.75E-7	1.97	9.75E-7	1.97
$91 \times 91$	5.54E-2	0.00	2.65E-7	1.94	7.75E-7	1.96	7.75E-7	1.96
	$O(h^{0.00})$		$O(h^{1.90})$		$O(h^{1.94})$		$O(h^{1.94})$	
Strategy 2, $n \times n = 11 \times 11$								
Coarse grid ( $N \times N$ )	$Ne(u)$	LCR	$Ne(u)$	LCR	$Ne(\partial u/\partial x)$	LCR	$Ne(\partial u/\partial y)$	LCR
$5 \times 5$	5.54E-2	-	1.73E-5	-	5.48E-5	-	5.49E-5	-
$9 \times 9$	1.40E-2	1.99	1.09E-6	3.99	6.99E-6	2.97	6.99E-6	2.97
$13 \times 13$	6.23E-3	2.00	2.09E-7	4.07	2.31E-6	2.73	2.31E-6	2.73
$17 \times 17$	3.51E-3	2.00	6.54E-8	4.04	1.33E-6	1.92	1.33E-6	1.92
$21 \times 21$	2.25E-3	2.00	2.67E-8	4.01	1.03E-6	1.15	1.03E-6	1.15
$25 \times 25$	1.56E-3	2.00	1.29E-8	3.99	8.85E-7	0.83	8.85E-7	0.83
$29 \times 29$	1.15E-3	2.00	7.04E-9	3.93	7.86E-7	0.77	7.86E-7	0.77
$33 \times 33$	8.78E-4	2.00	4.17E-9	3.92	7.04E-7	0.83	7.04E-7	0.83
$37 \times 37$	6.94E-4	2.00	2.63E-9	3.91	6.33E-7	0.90	6.33E-7	0.90
	$O(H^{2.00})$		$O(H^{4.01})$		$O(H^{1.97})$		$O(H^{1.97})$	

**Grid refinement convergence:** Two grid refinement strategies are presented in Table 6.5. In Strategy 1, a fixed coarse grid of  $N \times N = 5 \times 5$  is used while the local fine grids on coarse cells  $n \times n$  are refined in a series of  $11 \times 11, 21 \times 21, \dots, 91 \times 91$ . In contrast, Strategy 2 utilises a series of refined coarse grids of  $N \times N = 5 \times 5, 9 \times 9, \dots, 37 \times 37$  while keeping the size of local fine grids on coarse cells fixed as  $n \times n = 11 \times 11$ . The present method converges well with both grid refinement strategies while the MFEM does not converge with Strategy 1. Note that exact basis functions are employed in both MFEM and the present method. The convergence rates of the present method are 1.90 and 1.94 for the field variable and its first derivatives respectively in Strategy 1. A high convergence rate of 4.01 for the field variable is obtained with Strategy 2 where the convergence rate of the MFEM is 2.00.

**Solution accuracy:** Table 6.5 also presents the  $L_2$  error norm of the present method in comparison with those of MFEM. Very high levels of accuracy are obtained in the present method. With a small grid system, i.e.  $N \times N = 5 \times 5$  and  $n \times n = 11 \times 11$ , the error is  $1.73 \times 10^{-5}$  and with a relatively larger grid system, i.e.  $N \times N = 37 \times 37$  and  $n \times n = 11 \times 11$ , the error is  $2.63 \times 10^{-9}$ . Compared to the errors of the MFEM, with the same grid systems, the present errors are 3 and 5 orders of magnitude better respectively.

## Example 2

Consider a multiscale elliptic problem on a domain  $\Omega = [-1, 1]^2$  governed by

$$-\frac{\partial}{\partial x} \left( a^\varepsilon(x) \frac{\partial u}{\partial x} \right) - \frac{\partial}{\partial y} \left( b^\varepsilon(y) \frac{\partial u}{\partial y} \right) = xu^\varepsilon(y) + yu^\varepsilon(x) \quad (6.87)$$

with homogeneous Dirichlet boundary condition, where

$$a^\varepsilon(x) = \frac{1}{4 + x + \sin\left(\frac{x}{\varepsilon}\right)}, \quad b^\varepsilon(y) = \frac{1}{4 + y + \sin\left(\frac{y}{\varepsilon}\right)}, \quad (6.88)$$

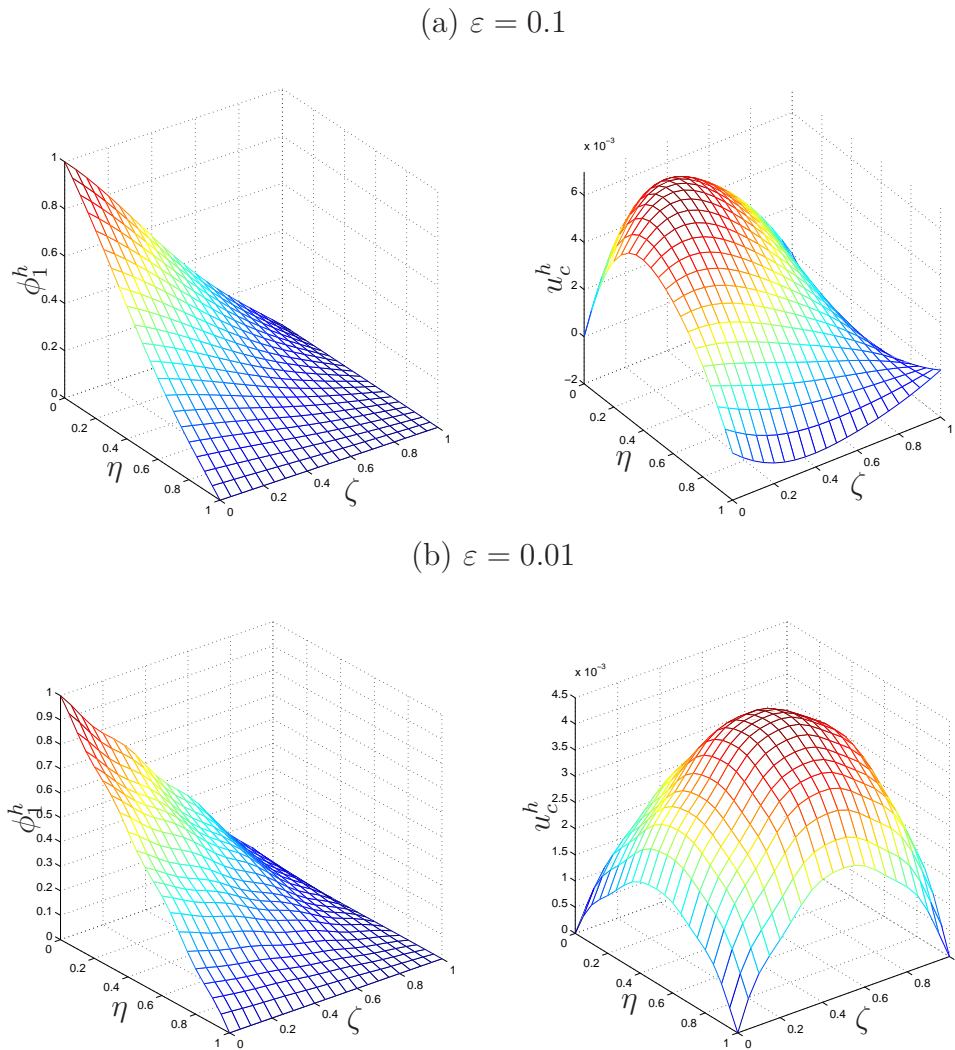


Figure 6.12: Two-dimensional example 2: typical basis and correction functions for the cases of  $\varepsilon = 0.1$  using a grid system of  $N \times N = 5 \times 5$ ,  $n \times n = 21 \times 21$  and  $\varepsilon = 0.01$  using a grid system of  $N \times N = 11 \times 11$ ,  $n \times n = 21 \times 21$ .

and  $u^e(x)$  is the exact solution of the 1D problem  $-d(a^\varepsilon(x)du/dx)/dx = x$  with  $a^\varepsilon(x)$  as in (6.88) (note that  $b^\varepsilon(x) = a^\varepsilon(x)$ ). The exact solution of (6.87) has the form

$$u(x, y) = u^e(x)u^e(y). \quad (6.89)$$

Both the basis and correction functions are numerically obtained by our  $C^2$ -continuous CVM (An-Vo et al. 2011a) in the present method. The basis functions in MFEM are obtained by a linear FEM. Figure 6.12 shows typical basis

and correction functions in the present method for two cases of small scale parameter, i.e.  $\varepsilon = 0.1$  and  $\varepsilon = 0.01$ . Typical sets of correction functions on the problem domain for these two values of small scale parameter are displayed by contour plots in Figure 6.13.

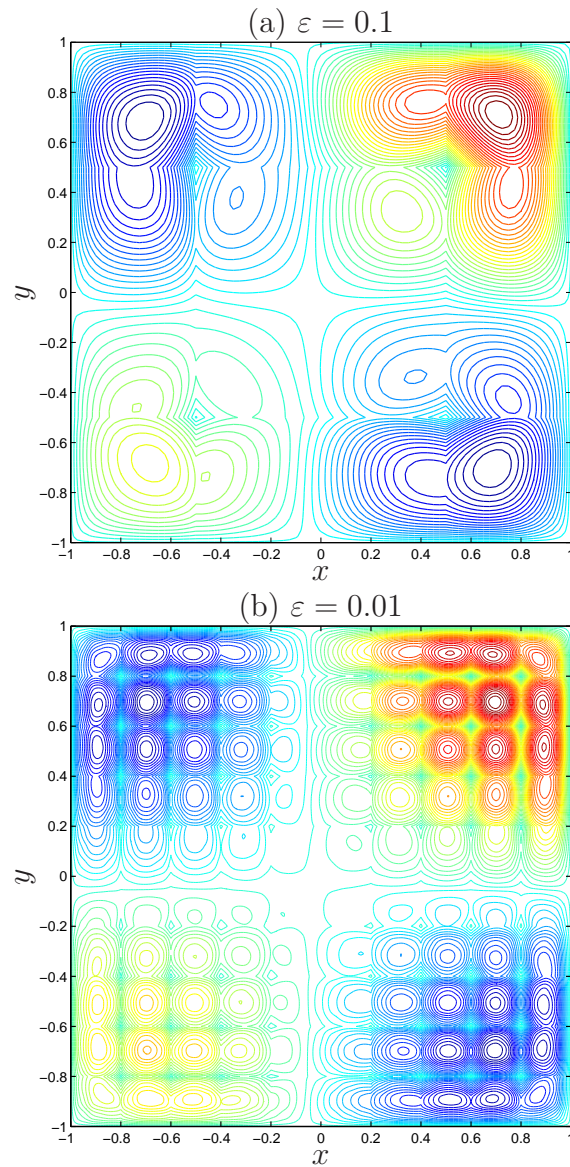


Figure 6.13: Two-dimensional example 2: contour plots of correction functions on the problem domain for the cases of  $\varepsilon = 0.1$  using a grid system of  $N \times N = 5 \times 5$ ,  $n \times n = 21 \times 21$  and  $\varepsilon = 0.01$  using a grid system of  $N \times N = 11 \times 11$ ,  $n \times n = 21 \times 21$ .

**Iterative convergence:** Figures 6.14 and 6.15 display the convergence to the

reference solution of the present method in cases of  $\varepsilon = 0.1$  and  $\varepsilon = 0.01$  respectively. Two grid systems are employed to study the effect of smoothing steps  $n_s$  on the convergence behaviours in each case of  $\varepsilon$  values. As in example 1, the smoothing steps have a significant effect on the convergence behaviours and we can reduce the number of iterations by increasing  $n_s$ . With the same smoothing systems, i.e.  $241 \times 241$  in the case of  $\varepsilon = 0.1$  in Figure 6.14 and  $701 \times 701$  in the case of  $\varepsilon = 0.01$  in Figure 6.15, the use of larger coarse grids reduces the iterations remarkably. Computational efficiency is assessed in Figure 6.16 where the convergence behaviours of the present method ( $n_s = 1$ ) and the fine scale solver (FSS) are presented. It can be seen in Figure 6.16(a) that the FSS requires about  $3.4 \times 10^4$  cycles to converge to  $CM = 10^{-8}$  in the case of grid 1. By using the smoothing system of grid 1 and with a coarse grid of  $5 \times 5$  the present method converges to  $CM = 10^{-8}$  after about 330 iterations (Figure 6.16(b)). The number of iterations can reduce to about 42 when a coarse grid of  $25 \times 25$  is used as shown in Figure 6.14(b). By using this  $25 \times 25$  coarse grid, the computational time of each iteration is measured to be 5.24 s on average which include the time of a smoothing cycle, for obtaining correction functions, and for solving the coarse grid system. The computational time of a smoothing cycle is measured to be 4.31 s. It can be seen that the time of a smoothing cycle dominates the time of an iteration. The present method hence has the potential of roughly 1000 times more efficient than the FSS. Furthermore, when we increase the size of the global fine grid to grid 2 and grid 3, the number of cycles of the smoother increases very fast compared to that of the present method (Figure 6.16(a)).

**Grid refinement convergence:** The two grid refinement strategies for  $\varepsilon = 0.1$  and  $\varepsilon = 0.01$  are presented in Tables 6.6 and 6.7 respectively. For  $\varepsilon = 0.1$ , Strategy 1 uses a fixed coarse grid of  $5 \times 5$  and a series of refined local fine grids of  $11 \times 11, 21 \times 21, \dots, 91 \times 91$ . Strategy 2 uses fixed local fine grids of  $11 \times 11$  and a series of refined coarse grids of  $5 \times 5, 9 \times 9, \dots, 37 \times 37$ . The convergence rates of the present method are 3.24 and 3.05 for the field variable

and its first derivatives respectively in Strategy 1. It can be seen that MFEM does not converge in Strategy 1. In Strategy 2, the convergence rates of the present method are 3.38 and 1.40 for the field variable and its first derivative respectively. MFEM converges at the rate of 1.95 for the field variable.

For  $\varepsilon = 0.01$ , Strategy 1 uses a fixed coarse grid of  $11 \times 11$  and a series of refined local fine grids of  $11 \times 11, 21 \times 21, \dots, 71 \times 71$ . Strategy 2 uses a fixed local fine grid of  $11 \times 11$  and a series of refined coarse grids of  $11 \times 11, 21 \times 21, \dots, 71 \times 71$ . The convergence rates of the present method are 4.17, 3.94 and 3.95 for  $u$ ,  $\partial u/\partial x$  and  $\partial u/\partial y$  respectively in Strategy 1. These rates are especially high compared to the rate of 0.13 for the field variable in MFEM. In Strategy 2, the convergence rates of the present method are 5.12, 3.60 and 3.59 for  $u$ ,  $\partial u/\partial x$  and  $\partial u/\partial y$  respectively while MFEM gives a rate of 2.10 for the field variable.

**Solution accuracy:** Tables 6.6 and 6.7 also present the  $L_2$  error norm for  $\varepsilon = 0.1$  and  $\varepsilon = 0.01$  respectively. For  $\varepsilon = 0.1$  and Strategy 1 (Table 6.6), the present method achieves the errors of  $3.90 \times 10^{-8}$  and  $1.67 \times 10^{-7}$  for the field variable and its first derivatives respectively by using a grid system of  $N \times N = 5 \times 5$  and  $n \times n = 91 \times 91$ . The error for the field variable is 7 orders of magnitude better compared to that of MFEM by using the same grid system. In Strategy 2, the present method achieves the errors of  $2.66 \times 10^{-8}$  and  $3.84 \times 10^{-6}$  for the field variable and its first derivatives respectively by using a grid system of  $N \times N = 37 \times 37$  and  $n \times n = 11 \times 11$ . The error for the field variable is 5 orders of magnitude better compared to that of MFEM by using the same grid system.

For  $\varepsilon = 0.01$  and Strategy 1 (Table 6.7), the present method achieves the errors of  $5.73 \times 10^{-6}$  and  $1.17 \times 10^{-5}$  for the field variable and its first derivatives respectively by using a grid system of  $N \times N = 11 \times 11$  and  $n \times n = 71 \times 71$ . The error for the field variable is 4 orders of magnitude better compared to that of MFEM by using the same grid system. In Strategy 2, the present method achieves the errors of  $9.05 \times 10^{-7}$ ,  $2.31 \times 10^{-5}$  and  $2.32 \times 10^{-5}$  for  $u$ ,

$\partial u/\partial x$  and  $\partial u/\partial y$  respectively by using a grid system of  $N \times N = 71 \times 71$  and  $n \times n = 11 \times 11$ . The error for the field variable is more than 3 orders of magnitude better compared to that of MFEM by using the same grid system.

Figure 6.17 displays the contour plots of the solutions obtained by MFEM, present method and the exact one for  $\varepsilon = 0.1$  and  $\varepsilon = 0.01$ . The present result is obtained with  $N \times N = 5 \times 5, n \times n = 31 \times 31$  while the MFEM result is obtained with  $N \times N = 11 \times 11, n \times n = 31 \times 31$ . It can be seen that the solutions of the present method are in excellent agreement with the exact solution.

## 6.7 Concluding remarks

A high-order RBF-based multiscale control volume method has been successfully developed for 1D and 2D multiscale elliptic problems. To assess the performance of the methods, we use two grid refinement strategies, namely (i) fixed coarse grid and various local fine grids, and (ii) fixed local fine grid and various coarse grids. Unlike MFEM, the proposed methods work well for both grid refinement strategies. High rates of convergence and levels of accuracy are obtained. The method for 2D problems is proposed with an iterative algorithm which helps overcome the limitation of MFEM where artificial localised boundary conditions are employed. It has been demonstrated numerically that the proposed iterative algorithm converges to  $C^2$ -continuous solutions. This feature is very useful especially in subsurface flow simulations where the velocity field has to be continuous across the coarse cell interfaces to ensure a conservative flow field. The scalability and high efficiency of the proposed algorithm has been confirmed against the performance of the fine scale solver.

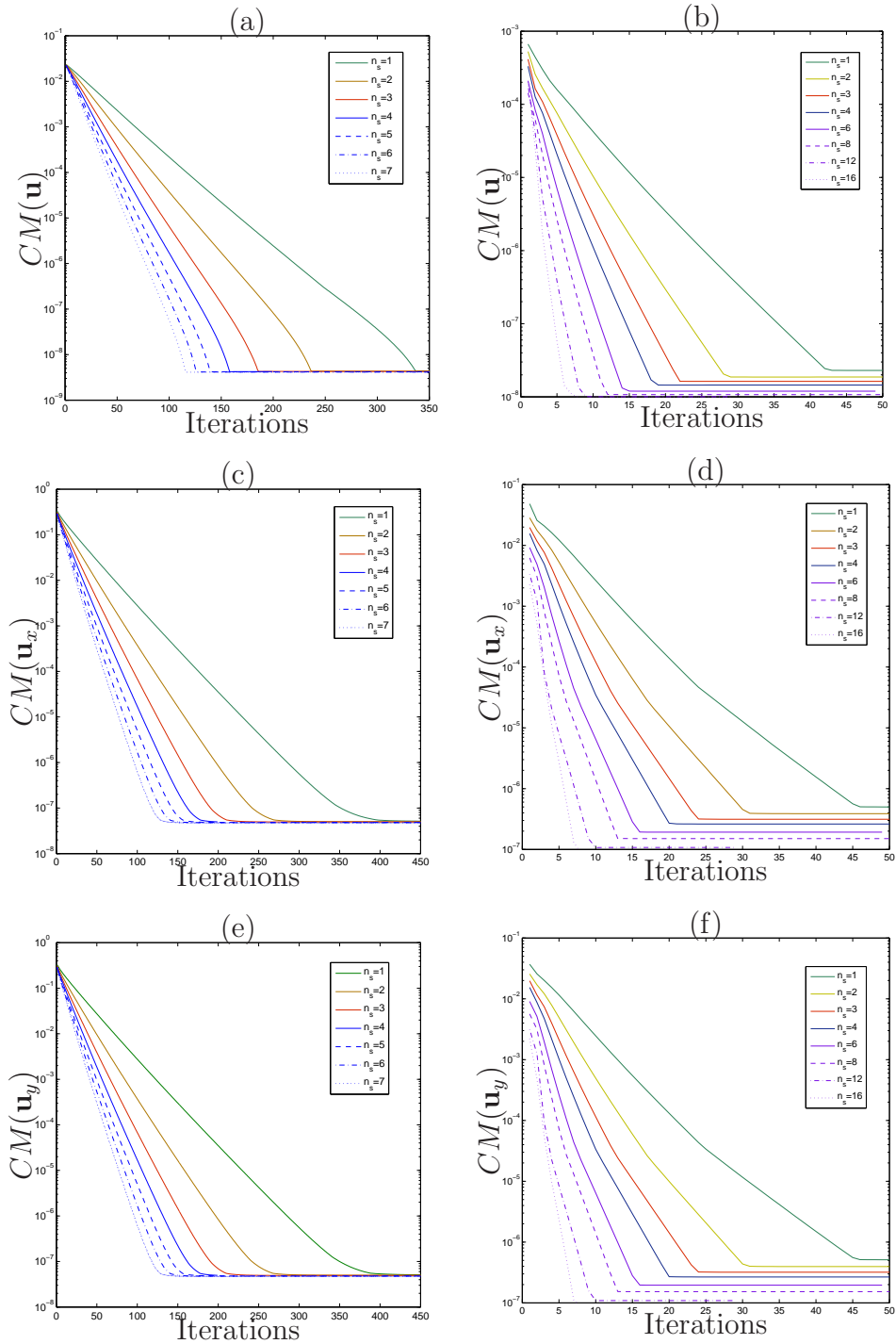


Figure 6.14: Two-dimensional example 2,  $\varepsilon = 0.1$ ,  $N \times N = 5 \times 5$ ,  $n \times n = 61 \times 61$  (left) and  $N \times N = 25 \times 25$ ,  $n \times n = 11 \times 11$  (right): effect of the number of smoothing steps  $n_s$  on the convergence behaviour.

Table 6.6: Two-dimensional example 2,  $\varepsilon = 0.1$ :  $L_2$  errors of the field variable, its first and second derivatives. LCR stands for local convergence rate.

		Strategy 1, $N \times N = 5 \times 5$							
		MFEM		Present method					
Local fine grid ( $n \times n$ )		$Ne(u)$	LCR	$Ne(u)$	LCR	$Ne(\partial u/\partial x)$	LCR	$Ne(\partial u/\partial y)$	LCR
$11 \times 11$		4.13E-1	-	5.01E-5	-	1.49E-4	-	1.49E-4	-
$21 \times 21$		4.14E-1	0.00	3.55E-6	3.82	1.14E-5	3.71	1.13E-5	3.72
$31 \times 31$		4.15E-1	0.00	8.51E-7	3.52	2.95E-6	3.33	2.95E-6	3.31
$41 \times 41$		4.15E-1	0.00	3.37E-7	3.22	1.26E-6	2.96	1.26E-6	2.96
$51 \times 51$		4.15E-1	0.00	1.75E-7	2.94	6.86E-7	2.72	6.86E-7	2.72
$61 \times 61$		4.15E-1	0.00	1.07E-7	2.70	4.33E-7	2.52	4.33E-7	2.52
$71 \times 71$		4.15E-1	0.00	7.15E-8	2.62	2.99E-7	2.40	2.99E-7	2.40
$81 \times 81$		4.15E-1	0.00	5.15E-8	2.46	2.19E-7	2.33	2.19E-7	2.33
$91 \times 91$		4.15E-1	0.00	3.90E-8	2.36	1.68E-7	2.25	1.68E-7	2.25
		$O(h^{0.00})$		$O(h^{3.24})$		$O(h^{3.05})$		$O(h^{3.05})$	
		Strategy 2, $n \times n = 11 \times 11$							
Coarse grid ( $N \times N$ )		$Ne(u)$	LCR	$Ne(u)$	LCR	$Ne(\partial u/\partial x)$	LCR	$Ne(\partial u/\partial y)$	LCR
$5 \times 5$		4.13E-1	-	5.01E-5	-	1.49E-4	-	1.49E-4	-
$9 \times 9$		1.15E-1	1.84	3.99E-6	3.65	1.06E-5	3.81	1.06E-5	3.81
$13 \times 13$		5.19E-2	1.96	7.26E-7	4.20	7.30E-6	0.92	7.29E-6	0.92
$17 \times 17$		2.94E-2	1.98	2.52E-7	3.68	6.38E-6	0.47	6.38E-6	0.46
$21 \times 21$		1.89E-2	1.98	1.21E-7	3.29	5.76E-6	0.46	5.76E-6	0.46
$25 \times 25$		1.31E-2	2.01	7.03E-8	2.98	5.22E-6	0.54	5.22E-6	0.54
$29 \times 29$		9.64E-3	1.99	6.49E-8	0.52	4.72E-6	0.65	4.71E-6	0.67
$33 \times 33$		7.39E-3	1.99	5.00E-8	1.95	4.26E-6	0.77	4.25E-6	0.77
$37 \times 37$		5.84E-3	2.00	2.66E-8	5.36	3.84E-6	0.88	3.84E-6	0.86
		$O(H^{1.95})$		$O(H^{3.38})$		$O(H^{1.40})$		$O(H^{1.40})$	

Table 6.7: Two-dimensional example 2,  $\varepsilon = 0.01$ :  $L_2$  errors of the field variable, its first and second derivatives. LCR stands for local convergence rate.

		Strategy 1, $N \times N = 11 \times 11$							
		MFEM		Present method					
Local fine grid ( $n \times n$ )		$Ne(u)$	LCR	$Ne(u)$	LCR	$Ne(\partial u/\partial x)$	LCR	$Ne(\partial u/\partial y)$	LCR
11 $\times$ 11		1.03E-1	-	1.93E-2	-	2.44E-2	-	2.44E-2	-
21 $\times$ 21		8.36E-2	0.30	9.83E-4	4.30	1.29E-3	4.24	1.29E-3	4.24
31 $\times$ 31		8.02E-2	0.10	1.80E-4	4.19	2.46E-4	4.09	2.45E-4	4.10
41 $\times$ 41		7.91E-2	0.05	5.49E-5	4.13	8.05E-5	3.88	7.80E-5	3.98
51 $\times$ 51		7.87E-2	0.02	2.20E-5	4.10	3.56E-5	3.66	3.54E-5	3.54
61 $\times$ 61		7.84E-2	0.02	1.06E-5	4.00	1.91E-5	3.42	1.90E-5	3.41
71 $\times$ 71		7.83E-2	0.01	5.73E-6	3.99	1.17E-5	3.18	1.17E-5	3.15
		$O(h^{0.13})$		$O(h^{4.17})$		$O(h^{3.94})$		$O(h^{3.95})$	
		Strategy 2, $n \times n = 11 \times 11$							
Coarse grid ( $N \times N$ )									
11 $\times$ 11		1.03E-1	-	1.93E-2	-	2.44E-2	-	2.44E-2	-
21 $\times$ 21		2.38E-2	2.11	3.91E-4	5.63	1.24E-3	4.30	1.25E-3	4.29
31 $\times$ 31		1.39E-2	1.33	1.82E-4	1.89	2.93E-4	3.56	2.92E-4	3.59
41 $\times$ 41		5.98E-3	2.93	2.08E-5	7.54	1.05E-4	3.57	1.05E-4	3.56
51 $\times$ 51		3.59E-3	2.29	5.09E-6	6.31	5.19E-5	3.16	5.22E-5	3.13
61 $\times$ 61		2.39E-3	2.23	1.63E-6	6.25	3.17E-5	2.70	3.19E-5	2.70
71 $\times$ 71		1.78E-3	1.91	9.05E-7	3.82	2.31E-5	2.05	2.32E-5	2.07
		$O(H^{2.10})$		$O(H^{5.12})$		$O(H^{3.60})$		$O(H^{3.59})$	

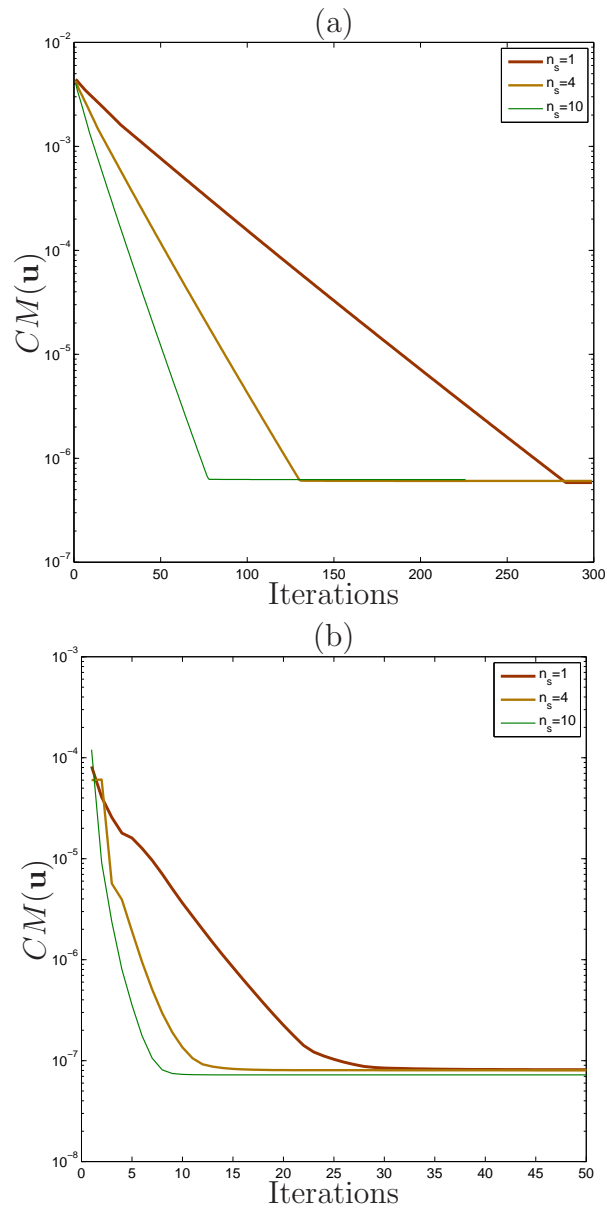


Figure 6.15: Two-dimensional example 2,  $\varepsilon = 0.01$ ,  $N \times N = 11 \times 11$ ,  $n \times n = 71 \times 71$  (a) and  $N \times N = 71 \times 71$ ,  $n \times n = 11 \times 11$  (b): effect of the number of smoothing steps  $n_s$  on the convergence behaviour.

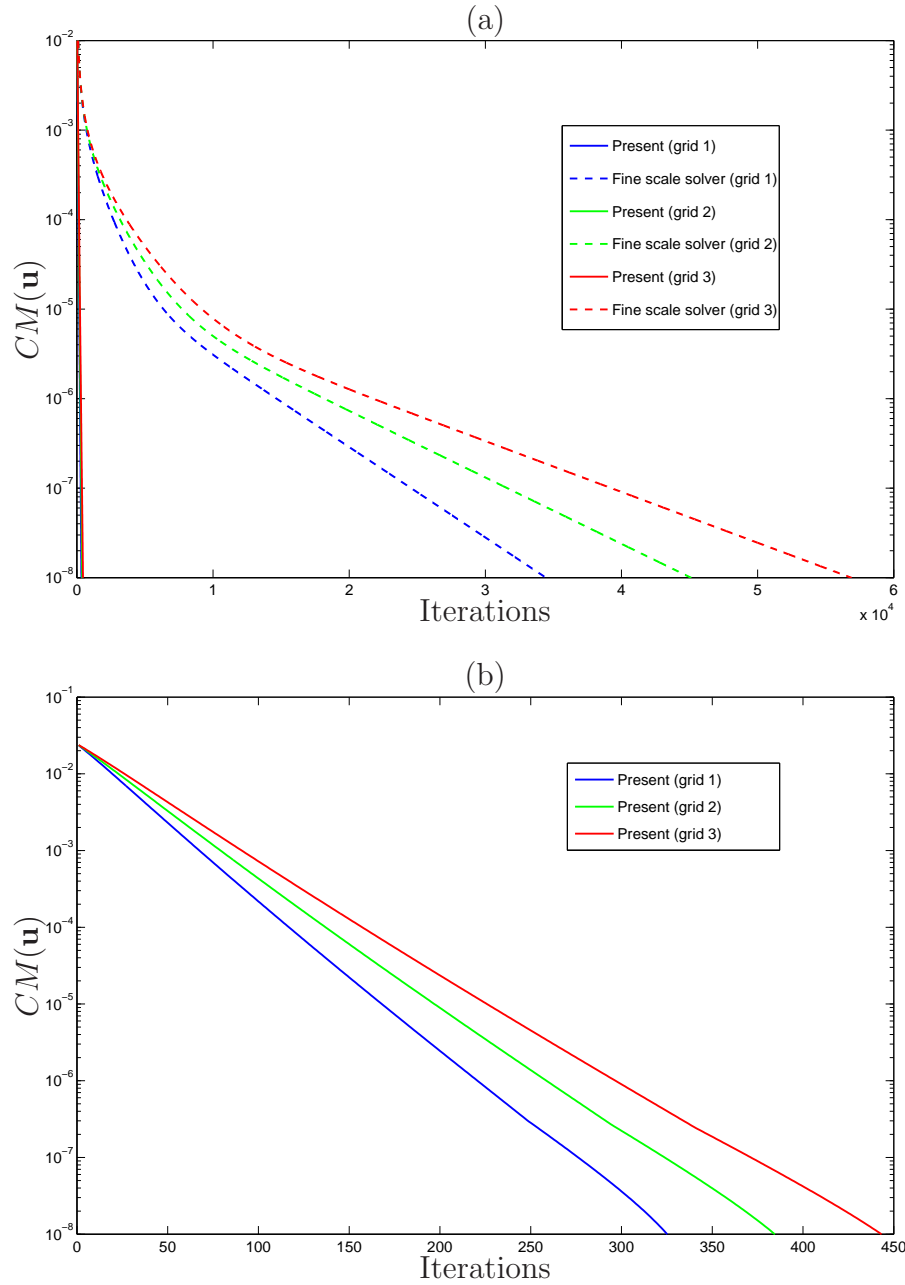


Figure 6.16: Two-dimensional example 2,  $\varepsilon = 0.1$ ,  $n_s = 1$ : convergence of the present method and the fine scale solver with increasing sizes of the global fine grid; grid 1 =  $241 \times 241$  ( $N \times N = 5 \times 5$ ,  $n \times n = 61 \times 61$ ), grid 2 =  $281 \times 281$  ( $N \times N = 5 \times 5$ ,  $n \times n = 71 \times 71$ ), grid 3 =  $321 \times 321$  ( $N \times N = 5 \times 5$ ,  $n \times n = 81 \times 81$ ).

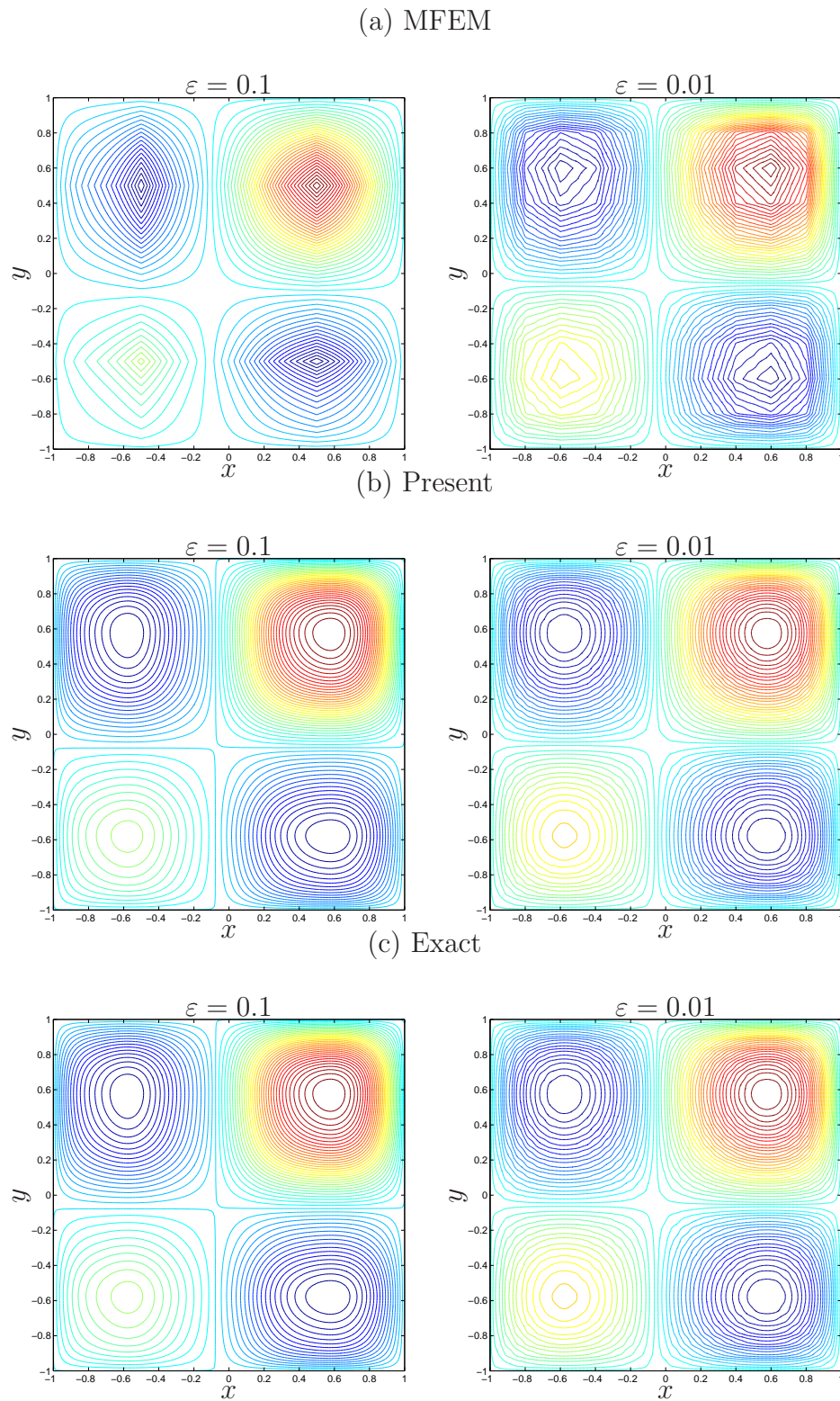


Figure 6.17: Two-dimensional example 2: contour plots of solutions for the cases of  $\varepsilon = 0.1$  and  $\varepsilon = 0.01$ , the former is obtained with  $N \times N = 5 \times 5$ ,  $n \times n = 31 \times 31$  while the latter is obtained with  $N \times N = 11 \times 11$ ,  $n \times n = 31 \times 31$ .

# Chapter 7

## Conclusions

This chapter concludes the thesis by a summary of research contributions and some suggestions for future development.

### 7.1 Research contributions

Novel local approximants based on 2-node elements and IRBF (IRBFEs), a smallest RBF set ever used for constructing approximation, have been devised which can produce curve lines between its two extremes. This can be seen as a strength of IRBFEs over linear elements used in conventional techniques. The 2-node IRBFEs have been incorporated into the subregion/point collocation formulations on Cartesian grids to create a class of  $C^2$ -continuous methods. Distinguishing features of the proposed methods include (i)  $C^2$ -continuous solution rather than the usual  $C^0$ -continuous solutions; and (ii) remarkably sparse and banded system matrices, especially tridiagonal ones, are achieved in Chapter 5. The proposed methods provide many advantages for the simulation of heat and viscous flows defined on both simply and multiply-connected domains with rectangular and non-rectangular shapes as follows.

- High levels and orders of accuracy are achieved for not only the field variables but also its first derivatives. The first derivatives contain information of great practical interest such as the heat flux or the flow velocity field.
- Both stability and high levels of accuracy are achieved for highly nonlinear flows via (i) novel high-order upwind schemes; and (ii) implicit treatments of convective terms. Larger time steps can be used leading to a faster convergence to steady state solutions. High levels of accuracy are achieved using relatively coarse grids.
- Simple preprocessing based on Cartesian grids wherein the ADI procedure are straightforwardly applied to accelerate computational processes.
- Flexible and effective implementation of derivative boundary conditions, e.g. without using ghost nodes and a simple computation of vorticity boundary conditions.

The proposed  $C^2$ -continuous IRBFE-CV method serves the development of a novel multiscale conservative computational framework in Chapter 6. The proposed multiscale CV method has been successfully applied for 1D and 2D multiscale elliptic problems arising from the modeling of composite materials and porous media flows. To the best of our knowledge, the proposed multiscale method is the first successful attempt to incorporate an RBF into a multiscale basis function approach to obtain high rates of convergence and levels of accuracy.

The contributions of each chapter can be highlighted below.

### **Novel 2-node IRBFEs and a $C^2$ -continuous control-volume method**

This achievement is presented in Chapter 2. As aforementioned, IRBF approximations are very accurate especially in regular node arrangements such as Cartesian grids. IRBF approximations are usually constructed globally on the whole domain grid or on each grid line. The global construction results in

fully populated system matrices which are highly ill-conditioned in large-scale problems. Moreover, the RBF-width, an effective mean for controlling the accuracy, is limited to small values. Local construction of RBF approximations can circumvent these difficulty. However, trade-offs include the loss of spectral accuracy and high-order continuity of the approximate solutions. 2-node IRBFEs are constructed locally using only two RBF centres (a smallest RBF set) associated with the two nodes of the elements and able to overcome the shortcomings of conventional local RBF approximations. Nodal values of both the field variable and its first derivative are involved in IRBFE approximations leading to  $C^2$ -continuous solutions. In addition, a wide range of RBF-widths can be used to effectively control the solution accuracy.

A novel  $C^2$ -continuous conservative method based on 2-node IRBFEs and Cartesian grids has been successfully developed for the solution of second-order elliptic problems in 1D and 2D. The latter can be defined on rectangular or non-rectangular domains. The use of 2-node elements guarantees consistency of the flux at CV faces as in the standard (linear) CVM (one of the four basic rules to guarantee a physically realistic solution) and leads to a sparse and banded system matrix, facilitating the employment of a large number of nodes. Unlike the standard CVM, the proposed IRBFE-CVM can give solutions with curved profiles between the two adjacent nodes. Moreover, the approximate solution is  $C^2$ -continuous on the grid lines. Its solution accuracy can be effectively controlled by means of the RBF-width ( $\beta$  up to 85) and/or grid size. Numerical results show that the method is much more accurate and faster convergent, especially for the approximation of derivatives, than the standard CVM.

### **Development of high-order upwind schemes based on 2-node IRBFEs for highly nonlinear flows**

This research work has been presented in Chapter 3. 2-node IRBFEs are further developed for the simulation of incompressible viscous flows. Advancement includes (i) the incorporation of  $C^2$ -continuous 2-node IRBFEs into the subregion

and point collocation frameworks for the discretisation of the streamfunction-vorticity formulation on Cartesian grids; and (ii) the development of high-order upwind schemes based on 2-node IRBFs for the case of convection-dominant flows. It should be emphasised that the proposed upwind schemes can achieve both stability and accuracy. The proposed  $C^2$ -continuous discretisation methods with upwind schemes are verified with the simulation of lid-driven cavity flows and flows past a circular cylinder in a channel. The structures of steady flows are obtained for a wide range of Reynolds numbers by using the method of modified dynamics or false transient. Numerical results show that (i) much larger time steps can be used with the upwind versions; and (ii) a high level of accuracy is achieved using relatively coarse grids.

### **Development of a high-order $C^2$ -continuous ADI method based on 2-node IRBFs and Cartesian grids**

This research work has been presented in Chapter 4. A novel high-order  $C^2$ -continuous ADI method is devised via the combination of the ADI procedure and the  $C^2$ -continuous 2-node IRBF collocation method. The discretisation of the streamfunction-vorticity formulation governing viscous flows is implemented on Cartesian grids. 2-node IRBFs are used for the discretisation of the diffusion terms, and then the convection terms are incorporated into system matrices by treating nodal derivatives as unknowns - an advantageous feature of IRBFs. By treating the convection terms implicitly as unknowns, the obtained matrices based on grid lines are always diagonally dominant. Unlike the solution strategy in Chapters 2 and 3, the 2D problem becomes a sequence of 1D problems following the ADI factorisation in this work. The present solution strategy consists of multiple use of a 1D sparse matrix algorithm that helps save the computational cost. The obtained systems include  $2 \times N_\eta$  equations only without the need of implicit elimination where  $N_\eta$  is the total number of interior grid nodes on an  $\eta$ -grid line. Note that the systems in Chapter 2 and 3 includes  $3 \times N$  equations where  $N$  is the total number of interior grid nodes of the

problem domain. The proposed method successfully simulates the benchmark lid-driven square and triangular cavities for a wide range of Reynolds numbers without recourse to upwind schemes. Numerical results show that larger time steps can be used and smaller number of iterations are required in comparison with the classical CD-ADI method. The computational times of the present ADI method are competitive with those of the CD-ADI where 1D tridiagonal system matrices on grid lines are solved with the Thomas algorithm.

### **Novel $C^2$ -continuous compact scheme based on 2-node IRBFEs on uniform and nonuniform grids**

This research work has been presented in Chapter 5. In recent years, compact finite difference schemes are emerging to replace the classical finite difference schemes in computational science. Similar to the classical schemes, the construction of compact derivative schemes also bases on Taylor series expansion on uniform grids. However, the derivative approximations are implicitly expressed in terms of given nodal values of the field variable. Extension of compact schemes to nonuniform grid is in active research which typically requires coordinate transformation. In present work, compact derivative schemes are constructed by the 2-node IRBFEs leading to a novel class of  $C^2$ -continuous compact schemes. The proposed schemes have been easily extended for nonuniform grids without the need of coordinate transformation. Distinguishing features of the proposed compact scheme include (i)  $C^2$ -continuous solutions across grid nodes are guaranteed; and (ii) the consistence of the first and second derivative schemes. The latter is very useful for solving problems involving both first- and second-order derivatives such as the convection diffusion type problems. The proposed  $C^2$ -continuous compact schemes have been applied to the discretisation of linear and non-linear parabolic equations in an implicit manner (ADI procedure is employed in 2D problems). The latter is the vorticity transport equation in the Navier-Stokes equations. In such problems, the present schemes can treat the convective terms implicitly leading to stable solutions

at high  $Re$  while maintain the efficiency of the present proposed ADI method as those in the conventional ADI method, i.e. tridiagonal system matrices are achieved on each and every grid line. Note that the presently obtained system matrices involve only  $N_\eta$  equations for  $N_\eta$  interior grid nodes of an  $\eta$ -grid line.

### **Development of an RBF-based multiscale control-volume method**

This achievement is presented in Chapter 6. A novel high-order multiscale computational method, based on multiscale basis function approach and IRBFEs approximant, has been developed for the solution of multiscale elliptic problems with reduced computational cost. Unlike other methods based on multiscale basis function approach, sets of basis and correction functions here are obtained through  $C^2$ -continuous IRBFE-CV formulations. The problem domain is discretised by two grids, a coarse grid to obtain coarse nodal values and a fine grid to obtain the basis and correction functions on each dual cell. In the proposed method,  $C^2$ -continuous IRBFE-CVM developed in Chapter 1 is employed to solve local problems on dual cells for the basis and correction functions. These obtained functions help the computation of the coarse grid fluxes at coarse control-volume faces for the discretisation of the governing equation on coarse grid. The coarse grid system is solved for the coarse nodal values. The complete solution is then constructed on each dual cell by the associated coarse nodal values, basis and correction functions. To avoid the artificial localised boundary conditions in 2D problems typically used by other multiscale basis function approaches, e.g. MFEM and MFVM, an iterative algorithm based on two grids and  $C^2$ -continuous IRBFE-CV line smoother is proposed. It has been proved numerically that such iterative algorithm converges to a  $C^2$ -continuous fine scale reference solution. This feature is very useful especially in subsurface flow simulations where the velocity field has to be continuous across the coarse cell interfaces to ensure a conservative flow field. Several 1D and 2D multiscale elliptic problems are solved to verify the proposed method via two grid refinement strategies. Unlike MFEM, the proposed method can work well for both

grid refinement strategies. High rate of convergence and levels of accuracy are obtained. The scalability and high efficiency of the proposed algorithm in 2D has been confirmed against the performance of the fine scale solver (FSS). The present algorithm has the potential of roughly 1000 times more efficient than the FSS.

## 7.2 Suggested work

The following works are suggested for possible further developments

- Numerical results show that RBF-width (shape parameter) can effectively control the solution accuracy. Development of strategies to optimise the RBF-width is very necessary.
- Application of ADI procedure to IRBFE-CV formulation can result in a very efficient conservative method. It is well known that conservative methods are more suitable for flow field simulation.
- The IRBFES subregion/point collocation methods are presently developed for the simulation of 2D fluid flow governed by the streamfunction-vorticity ( $\psi - \omega$ ) formulation. Extension of the method to other formulations such as velocity-pressure ( $\mathbf{u} - p$ ) or velocity-vorticity ( $\mathbf{u} - \omega$ ) is possible. Such formulations are known to suit 3D problems. Especially, it would be very interesting if the IRBFES are applied to primitive variable formulations using pressure correction type schemes on collocated (non-staggered) grids where IRBFES can be used to interpolate the pressure at control volume faces to see whether checker boarding pressure fields could be eliminated.
- The development of the proposed multiscale CV method for full tensor and 3D problems is essential. Further development can involve time dependence, nonlinear effects such as convection, compressibility, multiphase,

---

fracture media. More sophisticated applications can include porous media/subsurface flows, turbulent flows, viscoelastic flows, composite materials.

# Appendix A

## Analytic forms of integrated MQ basis functions

Analytic forms of the integrated MQ basis functions used are given below

$$I_i^{(1)}(\mathbf{x}) = \int I_i^{(2)}(\mathbf{x}) d\eta = \frac{(\eta - \eta_i)}{2} Q + \frac{S}{2} R \quad (\text{A.1})$$

$$I_i^{(0)}(\mathbf{x}) = \int I_i^{(1)}(\mathbf{x}) d\eta = \left( \frac{(\eta - \eta_i)^2}{6} - \frac{S}{3} \right) Q + \frac{S(\eta - \eta_i)}{2} R \quad (\text{A.2})$$

where  $\mathbf{x} = (\eta, \theta)^T$ ;  $\mathbf{c}_i = (\eta_i, \theta_i)^T$ ;  $r = \|\mathbf{x} - \mathbf{c}_i\|$ ;

$$Q = \sqrt{r^2 + a_i^2} \quad (\text{A.3})$$

$$R = \ln((\eta - \eta_i) + Q) \quad (\text{A.4})$$

$$S = r^2 - (\eta - \eta_i)^2 + a_i^2. \quad (\text{A.5})$$

When the analysis domain is a line segment, expressions (A.1) and (A.2) reduce to

$$I_i^{(1)}(\eta) = \frac{(\eta - \eta_i)}{2} Q + \frac{a_i^2}{2} R \quad (\text{A.6})$$

$$I_i^{(0)}(\eta) = \left( \frac{r^2}{6} - \frac{a_i^2}{3} \right) Q + \frac{a_i^2(\eta - \eta_i)}{2} R \quad (\text{A.7})$$

where  $r = \| \eta - \eta_i \|$ .

# Appendix B

## Analytic forms of 2-node IRBFE basis functions in physical space

The analytic forms of  $\{\varphi_i(\eta)\}_{i=1}^4$  and  $\{\partial\varphi_i(\eta)/\partial\eta\}_{i=1}^4$  are given below

$$\begin{aligned}\varphi_1(\eta) = \frac{1}{D}[\bar{I}_1^{(0)}(L_1 - B_2) + \bar{I}_2^{(0)}(L_2 - B_2) + (\bar{\eta} - 1)(B_2^2 - L_1L_2) \\ + (B_2 - L_2)B_1 + (B_2 - L_1)R_2] \quad (\text{B.1})\end{aligned}$$

$$\begin{aligned}\varphi_2(\eta) = \frac{1}{D}[-\bar{I}_1^{(0)}(L_1 - B_2) - \bar{I}_2^{(0)}(L_2 - B_2) - \bar{\eta}(B_2^2 - L_1L_2) \\ - (B_2 - L_1)B_1 - (B_2 - L_2)R_1] \quad (\text{B.2})\end{aligned}$$

$$\begin{aligned}\varphi_3(\eta) = \frac{h}{D}[\bar{I}_1^{(0)}(B_1 - B_2 - R_1) + \bar{I}_2^{(0)}(B_1 + L_2 - R_2) + \bar{\eta}(R_2B_2 - L_2B_1) \\ + (\bar{\eta} - 1)(R_1L_2 - B_1B_2) - B_1^2 + R_1R_2] \quad (\text{B.3})\end{aligned}$$

$$\begin{aligned}\varphi_4(\eta) = \frac{h}{D}[\bar{I}_1^{(0)}(L_1 + R_1 - B_1) + \bar{I}_2^{(0)}(B_2 + R_2 - B_1) + \bar{\eta}(B_1B_2 - R_2L_1) \\ - (\bar{\eta} - 1)(B_1L_1 + B_2R_1) + B_1^2 - R_1R_2] \quad (\text{B.4})\end{aligned}$$

$$\frac{\partial \varphi_1(\eta)}{\partial \eta} = \frac{1}{Dh} [\bar{I}_1^{(1)}(L_1 - B_2) + \bar{I}_2^{(1)}(L_2 - B_2) + B_2^2 - L_1 L_2] \quad (\text{B.5})$$

$$\frac{\partial \varphi_2(\eta)}{\partial \eta} = \frac{1}{Dh} [-\bar{I}_1^{(1)}(L_1 - B_2) - \bar{I}_2^{(1)}(L_2 - B_2) - B_2^2 + L_1 L_2] \quad (\text{B.6})$$

$$\begin{aligned} \frac{\partial \varphi_3(\eta)}{\partial \eta} = \frac{1}{D} [\bar{I}_1^{(1)}(B_1 - B_2 - R_1) + \bar{I}_2^{(1)}(B_1 + L_2 - R_2) + B_2(R_2 - B_1) \\ + L_2(R_1 - B_1)] \quad (\text{B.7}) \end{aligned}$$

$$\begin{aligned} \frac{\partial \varphi_4(\eta)}{\partial \eta} = \frac{1}{D} [\bar{I}_1^{(1)}(R_1 + L_1 - B_1) + \bar{I}_2^{(1)}(R_2 - B_1 - B_2) + B_2(B_1 - R_1) \\ + L_1(B_1 - R_2)] \quad (\text{B.8}) \end{aligned}$$

where

$$\bar{I}_1^{(0)} = \frac{1}{6} \left[ (\bar{\eta}^2 - 2\beta^2) \sqrt{\bar{\eta}^2 + \beta^2} + 3\beta^2 \bar{\eta} \ln \left( \bar{\eta} + \sqrt{\bar{\eta}^2 + \beta^2} \right) \right] \quad (\text{B.9})$$

$$\begin{aligned} \bar{I}_2^{(0)} = \frac{1}{6} [((\bar{\eta} - 1)^2 - 2\beta^2) \sqrt{(\bar{\eta} - 1)^2 + \beta^2} + \\ 3\beta^2(\bar{\eta} - 1) \ln \left( \bar{\eta} - 1 + \sqrt{(\bar{\eta} - 1)^2 + \beta^2} \right)] \quad (\text{B.10}) \end{aligned}$$

$$\bar{I}_1^{(1)} = \frac{1}{2} \left[ \bar{\eta} \sqrt{\bar{\eta}^2 + \beta^2} + \beta^2 \ln \left( \bar{\eta} + \sqrt{\bar{\eta}^2 + \beta^2} \right) \right] \quad (\text{B.11})$$

$$\begin{aligned} \bar{I}_2^{(1)} = \frac{1}{2} \left[ (\bar{\eta} - 1) \sqrt{(\bar{\eta} - 1)^2 + \beta^2} + \beta^2 \ln \left( \bar{\eta} - 1 + \sqrt{(\bar{\eta} - 1)^2 + \beta^2} \right) \right] \\ (\text{B.12}) \end{aligned}$$

# References

- Aarnes, J., Kippe, V. and Lie, K.-A. (2005). Mixed multiscale finite elements and streamline methods for reservoir simulation of large geomodels, *Advances in Water Resources* **28**: 257–271.
- Abdulle, A. (2007). Heterogenous multiscale methods with quadrilateral finite elements, *Numerical Mathematics and Advanced Applications* **20**: 743–751.
- Adam, Y. (1976). Highly accurate compact implicit methods and boundary conditions, *Journal of Computational Physics* **24**: 10–22.
- Allaire, G. and Brizzi, R. (2005). A multiscale finite element method for numerical homogenization, *Multiscale Modeling & Simulation* **43**: 790–812.
- An-Vo, D.-A., Mai-Duy, N., Tran, C.-D. and Tran-Cong, T. (2012). Modeling strain localisation in a segmented bar by a  $C^2$ -continuous two-node integrated-RBF element formulation, *Boundary Element and Other Mesh Reduction Method XXXIV* **53**: 3–13.
- An-Vo, D.-A., Mai-Duy, N., Tran, C.-D. and Tran-Cong, T. (2013). ADI method based on  $C^2$ -continuous two-node integrated-RBF elements for viscous flows, *Applied Mathematical Modelling* **37**: 5184–5203.
- An-Vo, D.-A., Mai-Duy, N. and Tran-Cong, T. (2010). Simulation of Newtonian-fluid flows with  $C^2$ -continuous two-node integrated-RBF elements, *Structural Longevity* **4(1)**: 39–45.

- An-Vo, D.-A., Mai-Duy, N. and Tran-Cong, T. (2011a). A  $C^2$ -continuous control-volume technique based on Cartesian grids and two-node integrated-RBF elements for second-order elliptic problems, *CMES: Computer Modeling in Engineering and Sciences* **72** (4): 299–334.
- An-Vo, D.-A., Mai-Duy, N. and Tran-Cong, T. (2011b). High-order upwind methods based on  $C^2$ -continuous two-node integrated-RBF elements for viscous flows, *CMES: Computer Modeling in Engineering and Sciences* **80** (2): 141–177.
- Anagnostopoulos, P. and Iliadis, G. (1996). Numerical study of the blockage effects on viscous flow past a circular cylinder, *International Journal for Numerical Methods in Fluids* **22**: 1061–1074.
- Arbogast, T. (2002). Implementation of a locally conservative numerical sub-grid upscaling scheme for two-phase Darcy flow, *Computational Geosciences* **6**: 453–481.
- Atluri, S. N., Han, Z. D. and Rajendran, A. M. (2004). A new implementation of the meshless finite volume method, through the MLPG “mixed” approach, *CMES: Computer Modeling in Engineering and Sciences* **6**: 491–514.
- Atluri, S. N. and Shen, S. (2002). *The meshless local Petrov-Galerkin (MLPG) method*, Tech Science Press.
- Babuška, I. (1976). Solution of interface problems by homogenization, part I, II, *SIAM Journal of Mathematical Analysis* **7**: 603–645.
- Babuška, I., Caloz, G. and Osborn, J. (1994). Special finite element methods for a class of second order elliptic problems with rough coefficients, *SIAM J. on Numerical Analysis* **31**: 945–981.
- Babuška, I. and Osborn, J. (1983). Generalized finite element methods: their performance and their relation to mixed methods, *SIAM Journal on Numerical Analysis* **vol. 20**: 510–536.

- Benjamin, A. S. and Denny, V. E. (1979). On the convergence of numerical solutions for 2-D flows in a cavity at large Re, *Journal of Computational Physics* **33**: 340–358.
- Benssousan, A., Lions, J. L. and Papanicolaou, G. (1978). *Asymptotic analysis for periodic structures*, North Holland: Amsterdam.
- Botella, O. and Peyret, R. (1998). Benchmark spectral results on the lid-driven cavity flow, *Computers & Fluids* **27**: 421–433.
- Burnett, D. S. (1987). *Finite element analysis from concepts to applications*, Addison-Wesley Publishing company.
- Chen, C. S., Karageorghis, A. and Smyrlis, Y. S. (2008). *The method of fundamental solutions - A meshless method*, Dynamic Publishers.
- Chen, J. H., Pritchard, W. G. and Tavener, S. J. (1995). Bifurcation for flow past a cylinder between parallel planes, *Journal of Fluid Mechanics* **284**: 23–41.
- Chen, Z. and Hou, T. Y. (2002). A mixed multiscale finite element method for elliptic problems with oscillating coefficients, *Mathematics of Computation* **72** (242): 541–576.
- Chen, Z. X. (2009). On the heterogeneous multiscale method with various macroscopic solvers, *Nonlinear Analysis* **71**: 3267–3282.
- Cheng, A. H. D., Golberg, M. A., Kansa, E. J. and Zammito, G. (2003). Exponential convergence and h-c multiquadric collocation method for partial differential equations, *Numerical Methods for Partial Differential Equations* **19**: 571–594.
- Chu, J., Efendiev, Y., Ginting, V. and Hou, T. (2008). Flow based oversampling technique for multiscale finite element methods, *Advances in Water Resources* **31**: 599–608.

- Collatz, L. (1960). *The numerical treatment of differential equations*, Springer-Verlag, Berlin.
- Courant, R., Isaacson, E. and Rees, M. (1952). On the solution of non-linear hyperbolic differential equations by finite differences, *Communications on Pure and Applied Mathematics* **5**: 243.
- Divo, E. and Kassab, A. J. (2007). An efficient localized radial basis function meshless method for fluid flow and conjugate heat transfer, *Journal of Heat Transfer* **129**: 124–136.
- Douglas, J. and Gunn, J. E. (1964). A General Formulation of Alternating Direction Methods Part I. Parabolic and Hyperbolic Problems, *Numerische Mathematik* **6**: 428–453.
- Douglas, J. and Kim, S. (2001). Improved accuracy for locally one-dimensional methods for parabolic equations, *Mathematical Models and Methods in Applied Sciences* **11(9)**: 1563–1579.
- Dykaar, B. B. and Kitanidis, P. K. (1992). Determination of the effective hydraulic conductivity for heterogeneous porous media using a numerical spectral approach 1. method., *Water Resources Research* **28**: 1155–1166.
- E, W. and Engquist, B. (2003a). Multiscale modeling and computation, *Notices of the AMS* **50**: 1062–1070.
- E, W. and Engquist, B. (2003b). The heterogeneous multiscale methods, *Communications in Mathematical Sciences* **1**: 87–132.
- E, W. and Engquist, B. (2005). Analysis of the heterogeneous multiscale method for elliptic homogenization problems, *Journal of American Mathematical Society* **18**: 121–156.
- E, W. and Engquist, B. (2006). The heterogeneous multi-scale method for homogenization problems, *Lecture notes in computational science and engineering: Multiscale Methods in Science and Engineering* **44**: 89–110.

- E, W., Engquist, B., Li, X., Ren, W. and Vanden-Eijnden, E. (2007). The heterogeneous multiscale method: A review, *Communications in Computational Physics* **2**: 367–450.
- Efendiev, Y. and Hou, T. (2007). Multiscale finite element methods for porous media flows and their applications, *Applied Numerical Mathematics* **57**: 577–596.
- Efendiev, Y. R., Hou, T. Y. and Wu, X.-H. (2000). Convergence of a non-conforming multiscale finite element method, *SIAM Journal of Numerical Analysis* **37**: 888–910.
- Erturk, E. and Gokcol, O. (2007). Fine grid numerical solutions of triangular cavity flow, *The European Physical Journal - Applied Physics* **38**: 97–105.
- Fasshauer, G. E. (2007). *Meshfree approximation methods with Matlab*, Interdisciplinary mathematical sciences, vol. 6. Singapore: World Scientific Publishers.
- Fedoseyev, A. I., Friedman, M. J. and Kansa, E. J. (2002). Improved multi-quadric method for elliptic partial differential equations via PDE collocation on the boundary, *Computers and Mathematics with Applications* **43**: 439–455.
- Fish, J. and Belsky, V. (1995a). Multigrid method for a periodic heterogeneous medium part I: convergence studies for one-dimensional case, *Computer Methods in Applied Mechanics and Engineering* **126**: 17–38.
- Fish, J. and Belsky, V. (1995b). Multigrid method for a periodic heterogeneous medium part II: multiscale modeling and quality control in multidimensional case, *Computer Methods in Applied Mechanics and Engineering* **126**: 17–38.
- Fish, J. and Yuan, Z. (2005). Multiscale enrichment based on partition of unity, *International Journal for Numerical Methods in Engineering* **62**: 1341–1359.
- Fletcher, C. A. J. (1991). *Computational techniques for fluid dynamics*, Springer-Verlag.

- Franke, R. (1982). Scattered data interpolation: tests of some methods, *Mathematics of Computation* **38**: 182–200.
- Gentry, R. A., Martin, R. E. and Daly, B. J. (1966). An Eulerian differencing method for unsteady compressible flow problems, *Journal of Computational Physics* **1**: 87–118.
- Ghia, U., Ghia, K. N. and Shin, C. (1982). High-Re Solutions for Incompressible Flow Using the Navier-Stokes equations and a Multigrid method, *Journal of Computational Physics* **48**: 387–411.
- Guedes, J. M. and Kikuchi, N. (1990). Pre and post processing for materials based on the homogenization method with adaptive finite element methods, *Computer Methods in Applied Mechanics and Engineering* **83**: 143–198.
- Hajibeygi, H., Bonfigli, G., Hesse, M. A. and Jenny, P. (2008). Iterative multiscale finite-volume method, *Journal of Computational Physics* **227**: 8604–8621.
- Hajibeygi, H. and Jenny, P. (2009). Multiscale finite-volume method for parabolic problems arising from compressible multiphase flow in porous media, *Journal of Computational Physics* **228(14)**: 5129–5147.
- Hajibeygi, H. and Jenny, P. (2011). Adaptive iterative multiscale finite volume method, *Journal of Computational Physics* **230(3)**: 628–643.
- Hajibeygi, H., Karvounis, D. and Jenny, P. (2011). A hierarchical fracture model for the iterative multiscale finite volume method, *Journal of Computational Physics* **230(24)**: 8729–8743.
- Hassani, B. and Hinton, E. (1998). A review of homogenization and topology optimization I - homogenization theory for media with periodic structure, *Computers and Structures* **69**: 707–717.

- Hirsh, R. S. (1975). Higher order accurate difference solution of fluid mechanics problems by a compact differencing technique, *Journal of Computational Physics* **19**: 90–109.
- Ho-Minh, D., Mai-Duy, N. and Tran-Cong, T. (2009). A Galerkin-RBF approach for the streamfunction-vorticity-temperature formulation of natural convection in 2D enclosed domains, *CMES: Computer Modeling in Engineering and Sciences* **44**: 219–248.
- Holdeman, J. T. (2009). A Hermite finite element method for incompressible fluid flow, *International Journal for Numerical Methods in Fluids* **00**: 1–33.
- Hou, T. Y. (2005). Multiscale modelling and computation of fluid flow, *Int. J. for Numerical Methods in Fluids* **47**: 707–719.
- Hou, T. Y. and Wu, X.-H. (1997). A multiscale finite element method for elliptic problems in composite materials and porous media, *Journal of Computational Physics* **134**: 169–189.
- Hou, T. Y., Wu, X.-H. and Cai, Z. (1999). Convergence of a multiscale finite element method for elliptic problems with rapidly oscillating coefficients, *Mathematics of Computation* **68 (227)**: 913–943.
- Huang, C.-S., Lee, C.-F. and Cheng, A.-D. (2007). Error estimate, optimal shape factor, and high precision computation of multiquadric collocation method, *Engineering Analysis with Boundary Elements* **31**: 614–623.
- Huang, J. and Greengard, L. (2000). A fast direct solver for elliptic partial differential equations on adaptively refined meshes, *SIAM Journal on Scientific Computing* **21**: 1551–1566.
- Huilgol, R. and Phan-Thien, N. (1997). *Fluid mechanics of viscoelasticity*, Elsevier: Amsterdam.
- Jenny, P., Lee, S. H. and Tchelepi, H. A. (2003). Multi-scale finite-volume

- method for elliptic problems in subsurface flow simulation, *Journal of Computational Physics* **187**: 47–67.
- Jenny, P., Lee, S. H. and Tchelepi, H. A. (2004). Adaptive multiscale finite-volume method for multiphase flow and transport in porous media, *Multiscale Modelling and Simulation* **3 (1)**: 50–64.
- Jenny, P., Lee, S. H. and Tchelepi, H. A. (2006). Adaptive fully implicit multi-scale finite-volume method for multi-phase flow and transport in heterogenous porous media, *Journal of Computational Physics* **217(2)**: 627–641.
- Jyotsna, R. and Vanka, S. P. (1995). Multigrid calculation of steady, viscous flow in a triangular cavity, *Journal of Computational Physics* **122**: 107–117.
- Kalamkarov, A. L., Adrianov, I. V. and Danishevs'ky, V. V. (2009). Asymptotic homogenization of composite materials and structures, *Applied Mechanics Reviews* **62**: 1–20.
- Kansa, E. (1990). Multiquadrics-a scattered data approximation scheme with applications to computational fluid-dynamics-II, *Computers & Mathematics with Applications* **19**: 147–161.
- Karaa, S. (2007). High-order ADI method for stream-function vorticity equations, *PMMA: Proceedings in Applied Mathematics and Mechanics* **7**: 1025601–1025602.
- Karaa, S. and Zhang, J. (2004). High order ADI method for solving unsteady convection-diffusion problems, *Journal of Computational Physics* **198**: 1–9.
- Khosla, P. K. and Rubin, S. G. (1974). A diagonally dominant second-order accurate implicit scheme, *Computers and Fluids* **2 (2)**: 207–209.
- Kohno, H. and Bathe, K. (2006). A flow-condition-based interpolation finite element procedure for triangular grids, *International Journal for Numerical Method in Fluids* **51**: 673–699.

- Le-Cao, K., Mai-Duy, N. and Tran-Cong, T. (2009). An effective intergrated-RBFN Cartesian-grid discretization for the stream function-vorticity-temperature formulation in nonrectangular domains, *Numerical Heat Transfer, Part B: Fundamentals* **55**: 480 – 502.
- Lee, C. K., Liu, X. and Fan, S. C. (2003). Local multiquadric approximation for solving boundary value problems, *Computational Mechanics* **30**: 396–409.
- Lele, S. K. (1992). Compact finite difference schemes with spectral-like resolution, *Journal of Computational Physics* **103**: 16–42.
- Leonard, B. P. (1979). A stable and accurate convective modelling procedure based on quadratic upstream interpolation, *Computer Methods in Applied Mechanics and Engineering* **19**: 59–98.
- Li, J. and Hon, Y. C. (2004). Domain decomposition for radial basis meshless methods, *Numerical Methods for Partial Differential Equations* **20**: 450–462.
- Li, M. and Tang, T. (1996). Steady viscous flow in a triangular cavity by efficient numerical techniques, *Computers and Mathematics with Applications* **31(10)**: 55–65.
- Libre, N. A., Emdadi, A., Kansa, E. J., Rahimian, M. and Shekarchi, M. (2008). A stabilized RBF collocation scheme for Neumann type boundary value problems, *CMES: Computer Modeling in Engineering and Sciences* **24**: 61–80.
- Lunati, I. and Jenny, P. (2006a). Multiscale finite-volume method for compressible multiphase flow in porous media, *Journal of Computational Physics* **216**: 616–636.
- Lunati, I. and Jenny, P. (2006b). The multiscale finite-volume method - a flexible tool to model physically complex flow in porous media, *10<sup>th</sup> European Conference on the Mathematics of Oil Recovery*.
- Lunati, I. and Jenny, P. (2008). Multiscale finite-volume method for density-driven flow in porous media, *Computational Geosciences* **12**: 337–350.

- Ma, Y., Sun, C.-P., Haake, D. A., Churchill, B. M. and Ho, C.-M. (2012). A high-order alternating direction implicit method for the unsteady convection-dominated diffusion problem, *International Journal for Numerical Methods in Fluids* **70**: 703–712.
- Madych, W. R. (1992). Miscellaneous error bounds for multiquadric and related interpolators, *Computers and Mathematics with Applications* **24**: 121–138.
- Mai-Duy, N., Le-Cao, K. and Tran-Cong, T. (2008). A Cartesian grid technique based on one-dimensional integrated radial basis function networks for natural convection in concentric annuli, *International Journal for Numerical Methods in Fluids* **57**: 1709–1730.
- Mai-Duy, N. and Tanner, R. I. (2005). Solving high order partial differential equations with indirect radial basis function networks, *International Journal for Numerical Methods in Engineering* **63**: 1636–1654.
- Mai-Duy, N. and Tanner, R. I. (2007). A collocation method based on one-dimensional RBF interpolation scheme for solving PDEs, *International Journal for Numerical Methods for Heat & Fluid Flow* **17(2)**: 165–186.
- Mai-Duy, N. and Tran-Cong, T. (2001). Numerical solution of differential equations using multiquadric radial basis function networks, *Neural Networks* **14**: 185–199.
- Mai-Duy, N. and Tran-Cong, T. (2003). Approximation of function and its derivatives using radial basis function network methods, *Applied Mathematical Modelling* **27**: 197–220.
- Mai-Duy, N. and Tran-Cong, T. (2005). An effective indirect RBFN-based method for numerical solution of PDEs, *Numerical Methods for Partial Differential Equations* **21**: 770–790.
- Mai-Duy, N. and Tran-Cong, T. (2007). A Cartesian-grid collocation method based on radial-basis-function networks for solving PDEs in irregular domains, *Numerical Methods for Partial Differential Equations* **23**: 1192–1210.

- Mai-Duy, N. and Tran-Cong, T. (2008). A multidomain integrated-radial-basis-function collocation method for elliptic problems, *Numerical Methods for Partial Differential Equations* **24**: 1301–1320.
- Mai-Duy, N. and Tran-Cong, T. (2009a). A Cartesian-grid discretisation scheme based on local integrated RBFNs for two-dimensional elliptic problems, *CMES: Computer Modeling in Engineering and Sciences* **51**: 213–238.
- Mai-Duy, N. and Tran-Cong, T. (2009b). Integrated radial-basis-function networks for computing Newtonian and non-Newtonian fluid flows, *Computers & Structures* **87**: 642–650.
- Mai-Duy, N. and Tran-Cong, T. (2010a). A control volume technique based on integrated RBFNs for the convection-diffusion equation, *Numerical Methods for Partial Differential Equations* **26**: 426–447.
- Mai-Duy, N. and Tran-Cong, T. (2010b). A numerical study of 2D integrated RBFNs incorporating Cartesian grids for solving 2D elliptic differential problems, *Numerical Methods for Partial Differential Equations* **26 (6)**: 1443–1462.
- Mai-Duy, N. and Tran-Cong, T. (2011a). A high-order upwind control-volume method based on integrated RBFs for fluid-flow problems, *International Journal for Numerical Methods in Fluids* **67**: 1973–1992.
- Mai-Duy, N. and Tran-Cong, T. (2011b). Compact local integrated-RBF approximations for second-order elliptic differential problems, *Journal of Computational Physics* **230(12)**: 4772–4794.
- Mai-Duy, N. and Tran-Cong, T. (2013). A compact five-point stencil based on integrated RBFs for 2D second-order differential problems, *Journal of Computational Physics* **235**: 302–321.
- Mallinson, G. D. and Davis, G. D. V. (1973). The method of the false transient for the solution of coupled elliptic equations, *Journal of Computational Physics* **12**: 435–461.

- McCarthy, J. (1995). Comparison of fast algorithms for estimating large-scale permeabilities of heterogeneous media, *Transport in Porous Media* **19**: 123–137.
- Ming, P. B. and Zhang, P. W. (2007). Analysis of the heterogeneous multiscale method for parabolic homogenization problems, *Mathematics of Computation* **76**: 153–177.
- Ming, P. and Yue, X. (2006). Numerical methods for multiscale elliptic problems, *Journal of Computational Physics* **214**: 421–445.
- Moffat, H. K. (1963). Viscous and resistive eddies near a sharp corner, *Journal of Fluid Mechanics* **18**: 1–18.
- Mohammadi, M. H. (2008). Stabilized meshless local Petrov-Galerkin (MLPG) method for incompressible viscous fluid flows, *CMES: Computer Modeling in Engineering and Sciences* **29**: 75–94.
- Ngo-Cong, D., Mai-Duy, N., Karunasena, W. and Tran-Cong, T. (2011). Free vibration analysis of laminated composite plates based on FSDT using one-dimensional IRBFN method, *Computers and Structures* **89**: 1–13.
- Oden, J. T. and Vemaganti, K. S. (2000). Estimation of local modeling error and global-oriented adaptive modeling of heterogeneous materials I: error estimates and adaptive algorithms, *Journal of Computational Physics* **164**: 22–47.
- Oleinik, O., Shamaev, A. S. and Yosifian, G. A. (1992). *Mathematical problems in elasticity and homogenization*, North Holland: Amsterdam.
- Orsini, P., Power, H. and Morvan, H. (2008). Improving volume element methods by meshless radial basis function techniques, *CMES: Computer Modeling in Engineering and Sciences* **23**: 187–208.
- Patankar, S. V. (1980). *Numerical heat transfer and fluid flow*, Taylor & Francis.

- Patankar, S. V. (1981). A calculation procedure for two-dimensional elliptic situations, *Numerical Heat Transfer, Part B* **4**: 409–425.
- Peaceman, D. W. and Rachford, H. H. (1955). The numerical solution of parabolic and elliptic differential equations, *Journal of the Society for Industrial and Applied Mathematics* **3(1)**: 28–41.
- Pozrikidis, C. (1997). *Introduction to theoretical and computational fluid dynamics*, Oxford University Press.
- Qiu, J. and Shu, C.-W. (2003). Hermite WENO schemes and their application as limiters for Runge-Kutta discontinuous Galerkin method: one-dimensional case, *Journal of Computational Physics* **193**: 115–135.
- Qiu, J. and Shu, C.-W. (2005). Hermite WENO schemes and their application as limiters for Runge-Kutta discontinuous Galerkin method II: Two dimensional case, *Computers & Fluids* **34**: 642–663.
- Ribbens, C. J., Watson, L. T. and Wang, C.-Y. (1994). Steady viscous flow in a triangular cavity, *Journal of Computational Physics* **112(1)**: 173–181.
- Roache, P. J. (1998). *Fundamentals of Computational Fluid Dynamics*, Hermosa Publishers, Albuquerque.
- Sahin, M. and Owens, R. G. (2003). A novel fully implicit finite volume method applied to the lid-driven cavity problem - Part I: High Reynolds number flow calculations, *International Journal for Numerical Method in Fluids* **42**: 57–77.
- Sahin, M. and Owens, R. G. (2004). A numerical investigation of wall effects up to high blockage ratios on two-dimensional flow past a confined circular cylinder, *Physics of Fluids* **16**: 1305–1320.
- Sangalli, G. (2003). Capturing small scales in elliptic problems using a residual free bubbles finite element method, *Multiscale Modeling and Simulation* **1**: 485–503.

- Sanyasiraju, Y. V. S. S. and Chandhini, G. (2008). Local radial basis function based gridfree scheme for unsteady incompressible viscous flows, *Journal of Computational Physics* **227**: 8922–8948.
- Sarler, B. (2005). A radial basis function collocation approach in computational fluid dynamics, *CMES: Computer Modeling in Engineering and Sciences* **7**: 185–194.
- Sellountos, E. J. and Sequeira, A. (2008). A hybrid multi-region BEM/LBIE-RBF velocity-vorticity scheme for the two-dimensional Navier-Stokes equations, *CMES: Computer Modeling in Engineering and Sciences* **23**: 127–148.
- Shu, C., Ding, H. and Yeo, K. S. (2003). Local radial basis function-based differential quadrature method and its application to solve two-dimensional incompressible Navier-Stokes equations, *Computer Methods in Applied Mechanics and Engineering* **192**: 941–954.
- Singha, S. and Sinhamahapatra, K. P. (2010). Flow past a circular cylinder between parallel walls at low Reynolds numbers, *Ocean Engineering* **37**: 757–769.
- Spalding, D. B. (1972). A novel finite-difference formulation for differential expression involving both first and second derivatives, *International Journal for Numerical Method in Engineering* **4**: 551–559.
- Takano, N., Zako, M. and Ishizono, M. (2000). Multi-scale computational method for elastic bodies with global and local heterogeneity, *Journal of Computer-Aided Materials Design* **7**: 111–132.
- Thompson, J. F., Soni, B. K. and Weatherill, N. P. (1999). *Handbook of grid generation*, CRC Press.
- Tian, Z. and Ge, Y. (2003). A fourth-order compact finite difference scheme for the steady stream function-vorticity formulation of the Navier-Stokes/Boussinesq equations, *International Journal for Numerical Method in Fluids* **41**: 495–518.

- Tolstykh, A. I. and Shirobokov, D. A. (2003). On using radial basis functions in “finite difference mode” with applications to elasticity problems, *Computational Mechanics* **33**: 68–79.
- Šarler, B. and Vertnik, R. (2006). Meshfree explicit local radial basis function collocation method for diffusion problems, *Computers and Mathematics with Applications* **51**: 1269–1282.
- Wang, W., Guzman, J. and Shu, C.-W. (2011). The multiscale discontinuous Galerkin method for solving a class of second order elliptic problems with rough coefficients, *International Journal of Numerical Analysis and Modeling* **8 (1)**: 28–47.
- Wang, W. and Shu, C.-W. (2009). The WKB local discontinuous Galerkin method for the simulation of Schrödinger equation in a resonant tunneling diode, *Journal of Scientific Computing* **40**: 360–374.
- Watkins, D. S. (1976). On the construction of conforming rectangular plate elements, *International Journal for Numerical Method in Engineering* **10**: 925–933.
- Wright, G. B. and Fornberg, B. (2006). Scattered node compact finite difference-type formulas generated from radial basis functions, *Journal of Computational Physics* **212(1)**: 99–123.
- Xing, Y. F., Yang, Y. and Wang, X. M. (2010). A multiscale eigenelement method and its application to periodic composite structures, *Composite Structures* **92**: 2265–2275.
- You, D. A. (2006). A high order Pade ADI method for unsteady convection-diffusion equations, *Journal of Computational Physics* **214**: 1–11.
- Yuan, L. and Shu, C. W. (2008). Discontinuous Galerkin method for a class of elliptic multi-scale problems, *International Journal for Numerical Methods in Fluids* **56**: 1017–1032.

- Yue, X. and E, W. (2007). The local microscale problem in the multiscale modeling of strongly heterogeneous media: Effects of boundary conditions and cell size, *Journal of Computational Physics* **222**: 556–572.
- Zerroukat, M., Power, H. and Chen, C. S. (1998). A numerical method for heat transfer problems using collocation and radial basis functions, *International Journal for Numerical Methods in Engineering* **42**: 1263–1278.
- Zhang, H. W., Fu, Z. D. and Wu, J. K. (2009). Coupling multiscale finite element method for consolidation analysis of heterogeneous saturated porous media, *Advanced Water Resources* **32**: 268–279.
- Zienkiewicz, O. C. (1971). *The finite element method in engineering science*, McGraw-Hill, London.